Photoelectrochemical Kolbe Coupling at Bismuth Vanadate Photoelectrodes under Visible-Light Irradiation

William Anthony Swansborough-Aston

Doctor of Philosophy

University of York

Chemistry

March 2022

Abstract

Semiconductor photoelectrocatalysis is a promising tool for the development of synthetic methodologies utilising renewable energy sources. However, development is still in its infancy and thorough understanding of photoelectrochemical reactions is lacking. Oxidative decarboxylation, the focus of this thesis, represents an interesting model reaction as a one electron process that has been extensively studied electrochemically and has potential application in C-X coupling reactions.

In this work, bismuth vanadate is used as a photoelectrode material due to its visible-light absorption and prominence in water splitting reactions, as well as some initial photoelectrosynthesis. Photoelectrodes are prepared by electrostatic spray pyrolysis and optimised based on photocurrent density generated for the oxidation of phenylacetic acid solutions. Electrodes prepared by deposition of bismuth 2-ethylhexanoate and vanadyl acetylacetonate in a mixed ethyl acetate:dimethylsulfoxide solvent system yields reproducible photocurrent density up to 1.6 mA cm^{-2} at 1.0 V vs ferrocene.

After optimisation of photoelectrodes, optimisation of reaction conditions including electrolytic cell, substrate concentrations and applied potential were investigated. Once an optimised PEC system had been developed, substrate effects of substituted phenylacetic acids on carboxylate oxidation were investigated, as well as the effects of supporting electrolytes in low acid concentration media. We suggest that an intramolecular dissociative electron transfer mechanism dominates for the oxidation of phenylacetic acid at bismuth vanadate electrodes. Electrolyses of 1 M phenylacetic acid solutions partially neutralised by triethylamine (0.05 equiv) with optimised photoelectrodes yields bibenzyl at up to 88% selectivity at mild anodic potentials (<0.5 V vs Fc/Fc^{+}). The photoelectrochemical system developed in this thesis is a significant improvement on the >5 V potentials required for similar electrochemical transformations at metallic electrodes. Electrolysis of phenylacetic acid derivatives shows dimer selectivity (74% - >99%) correlates well with time-averaged photocurrent density, with no dimer observed for aliphatic acids.

In 50 mM acid solutions containing a supporting electrolyte, a significant drop in dimer selectivity is observed (~5%). Our studies indicate that an excess of carboxylate is crucial in determining the selectivity by influencing the adsorption-desorption equilibrium of the intermediate radical.

Table of Contents

List of Figures

List of Schemes

List of Tables

Acknowledgements

Initial thanks must be given to the Engineering and Physical Sciences research council for funding the research, as well as the University of York for teaching opportunities and 8 (and a bit) wonderful years. Thanks must also go to my supervisors, Richard Douthwaite and Victor Chechik – your guidance and input has been invaluable over the past 4 years and I have learnt so much from you both in that time.

I would like to extend my gratitude to several members of the Chemistry department, including Scott Hicks, Abigail Mortimer, Chris Rhodes, Mark Roper, Tim Ayers, Karl Heaton, Ben Coulson and Heather Fish for technical support.

I would like to acknowledge all members, past and present, of the RED and VC research groups for making the day-to-day experiences enjoyable and their general advice and feedback. Specific thanks must go to Joyashish Debgupta, for always being happy to answer my questions – no matter how ridiculous - on all things electrochemistry. To Luisa Ciano for starting off the coffee addiction, and to Nik Vagkidis and Jonathan Churchill for ensuring the addiction didn't fade. You both proved vital to my sanity during the latter parts of this degree and throughout the Coronavirus pandemic. Finally to Ben Coulson, Nina Leeb and Chris Goult for providing consistent lunch breaks, Wednesday evening dinner plans and support through the difficult times.

Outside of the department and academia, I would like to truly thank my family and friends for their unwavering support throughout the last few years. To my mum, Helen, and dad, Anthony, thank you for 26 years of love and support, words on a page can't do justice to how grateful I am. To my sister, Grace, thank you for being a lifelong cheerleader and friend. Sam Bates and Ben O'Keeffe, thank you both for the comic relief and over a decade of friendship. Thanks also to my emotional support animals, Geoff and Colin.

I would like to use the final words to thank my partner, Rosie, for making the last few years feel a breeze even when things were at their most stressful. I think I would need an entire other thesis to detail just how grateful I am for the love and support you have given me and how reciprocated that is.

Declaration

The work presented in this thesis was carried out at the University of York between October 2017 and March 2021. To the best of my knowledge, this work is original and my own, excluding:

Gas Chromatography and High-Performance Liquid Chromatography were carried out in part by Dr Scott Hicks

Mass Spectrometry and Gas Chromatography-Mass Spectrometry were carried out by Mr Karl Heaton

X-ray Photoelectron Spectroscopy, Ultra-Violet Photoelectron Spectroscopy and some X-ray Diffraction was carried out by Dr Ben Coulson

Preparation of glassware for electrolytic cells was carried out by Ms Abigail Mortimer

3D Printing of electrospray components was carried out by Mr Mark Roper or Roboze S.P.A., Italy.

I declare that this thesis is a presentation of original work and that I am the sole author. This thesis has not been submitted for any other degree at this University or any other. All sources are acknowledged as references.

1. Introduction

Molecular transformations underpin chemical production in major industries, such as agriculture, pharmaceuticals and cosmetics.[1] Common to a number of these processes is the use of unsustainable or expensive synthetic methods. The use of precious metal catalysts, strong oxidising and reducing agents or excessive thermal energy mean that many existing industrial synthetic procedures do not comply with aims of reducing the global environmental impact of the chemical industry.[1, 2] By comparison, the energy sector has made progress with the use of renewable sources such as solar and wind power to begin reducing its environmental impact.[3-5] The use of irradiation in chemical transformation is not a new phenomenon, dating back to the early 20th century, with seminal work by Ciamician.[6, 7] In 1912, he postulated that "*glass buildings will rise everywhere; inside of these will take place the photo-chemical processes that hitherto have been the guarded secret of the plants*" – a notion that one day, industrial scale synthesis will be based predominantly in photochemistry.[8]

Although still a long way from Ciamician's ideal, the field of photocatalysis has progressed tremendously over the past 50 years. Significant advances in both homo- and heterogeneous photochemistry have created a diverse library of redox transformations, based predominantly in single electron transfer (SET).[9-12]

Unlike the diversity in homogeneous examples, heterogeneous photocatalysis with semiconductor materials has been relatively localised on the 'Holy Grail' of solar fuel generation from CO_2 and water.[13-15] In 1972, Honda and Fujishima showed the photocatalytic oxidation of water at titanium dioxide (TiO_2) photoelectrodes under applied potential. Further work has since focussed on efficiency improvements, visible-light active materials and mechanistic understanding.[13, 15-17] At a similar time, Bard and coworkers used TiO_2 photoelectrodes for the decarboxylative oxidation of acetate anions and further C-C cross coupling of the radicals. This work seemingly gained less traction than Honda and Fujishima's in spite of its relevance to useful synthetic transformations.[18-20] These reactions were an adaptation of Kolbe's work in the 19th century – electrochemical decarboxylation of organic acids and radical dimerization.[21] Development of Bard's work then led to the use of colloidal photocatalyst suspensions for the same transformation.[19, 22]

Although distinct approaches to synthetic problems, photoelectrochemistry and photocatalysis are reliant on the same physical processes within the semiconductor: photon absorption, photogeneration of electron-hole pairs, charge migration to the material surface and electron transfer to/from the substrate. Despite this, the two fields have diverged somewhat. Photoelectrochemical approaches typically focus on characterisation and modification of the electrode material, with in-depth analysis of defect states and their role in the catalysis of the mechanistically complex water splitting reaction.[13, 16, 23-25] Conversely, selective photocatalysis has centred more on the useful transformations of substrates after electron transfer events.[12, 26, 27] It is rare that photocatalyst powders are characterised electrochemically and thus little to no comment on the impact of defect states on reactivity, quantum yield or selectivity is made. Additionally, by suspending a semiconductor photocatalyst on a conducting substrate, the oxidising/reducing power of charge carriers can be manipulated through varying the applied potential.

A combination of the two general approaches may lead to clearer understanding of phenomena common to both. Selective photocatalysis would benefit from deeper characterisation of the photocatalyst powders using electrochemical techniques such as electrochemical impedance spectroscopy (EIS). Conversely, simplification of redox reactions at photoelectrode surfaces may lead to clearer definition of surface state concentrations, energies and reactivities and enable its application to organic synthetic problems. Discussion of the key similarities and differences of the two approaches in the literature should identify scope for further research into the role of defect states in photocatalysis. An initial description of the photophysics and chemistry and the semiconductor-liquid interface will be given, followed by a discussion of the use of in situ analytical techniques to determine key reactive species such as reaction intermediates and semiconductor surface states. The final sections of the review will cover existing transformations at semiconductor photoelectrodes in the literature and the scope for photoelectrochemical oxidative decarboxylation as a route to carbon-centred radicals. Discussion of oxidative decarboxylation will be given in the context of existing electrochemical works.

1.1 Photophysics and Chemistry of Semiconductor-Liquid Interfaces

The electronic properties of semiconductors have been well documented, with the development of the band model widely accepted and described elsewhere.[28, 29] The physical processes of electron-hole pair generation and separation across the electronic band gap upon irradiation are the defining principles of photocatalysis and photoelectrochemistry. In a perfect

vacuum, for an ideal semiconductor, the conduction and valence band edges are isoenergetic across the entire semiconductor crystal, independent of location in the bulk or at the surface. In reality, surface terminations, and adsorption of species creates interfaces between phases, impacting the electronic structure of the material.[30-32] The key interface with respect to photocatalysis is that of the semiconductor and liquid, with charge transfer processes heavily dependent upon the structure and energetics of this interface.[33-36] The formation of a semiconductor-liquid junction, SCLJ, results in changes to the internal electric field of the semiconductor, as well as the electric potential, V, and potential energy, E, of the charge carriers. The internal electric field is defined as the force exerted on charge carriers within the semiconductor. With respect to this internal electric field, the electric potential of charge carriers can be defined as the work done on a unit charge to a specific point within an electric field, and the electric potential energy, E, is the energy required to move the unit charge against the electric field. The two parameters are related, as E can be calculated as the differential of V.

When the semiconductor is first brought into contact with a solution containing a redox active species, there is a mismatch of electronic potentials. The Fermi level of the semiconductor, E_F, must equilibrate with the equilibrium potential of the redox couple, E_{redox}. E_{redox} is defined as the intersection between the Gaussian energy distributions of the reduced and oxidised forms of the adsorbate.[31] The potentials for reduction and oxidation are termed E_{red} and E_{ox} respectively.

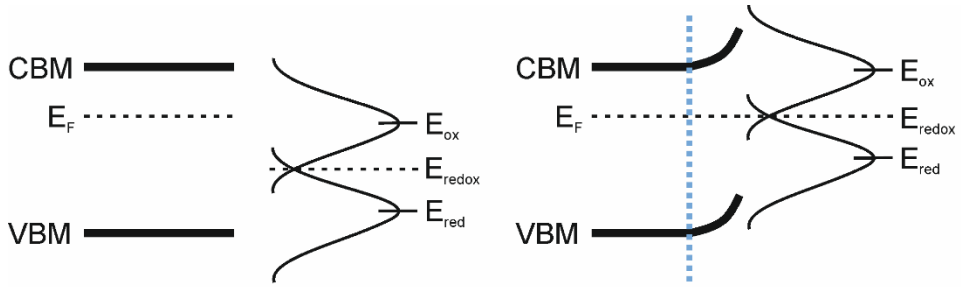

Figure 1.1: Formation of a semiconductor-liquid junction for an n-type semiconductor and a redox couple in solution – the donor band in the mid gap is omitted for clarity. The dotted blue line indicates the onset of the space-charge region. CBM and VBM represent the conduction band minimum and valence band maximum respectively.

As electron transfer occurs between the semiconductor and adsorbate, the energies of the conduction and valence bands change to accommodate the accumulation of charge at the

interface. For an n-type semiconductor, the Fermi level will lie closer to the conduction band minimum (CBM) because of the donor states in the mid gap. If this n-type semiconductor is brought into contact with a redox couple with a more positive potential versus vacuum, E_F and E_{redox} will need to equilibrate (Figure 1.1). As such, electrons will flow from the semiconductor to the adsorbate, creating a linear potential gradient towards the surface of the semiconductor and a parabolic potential gradient (Figure 1.2). The change in potential causes bending of the band energies in the opposite direction – upward in the case of an n-type semiconductor. This change in energy is observed over a distance from the semiconductor surface – the space charge region. The space charge region is specific to semiconductors and insulators as the relatively low number of free carriers (~ 10^{17} cm^{-3} for semiconductors versus ~ 10^{22} cm^{-3} for metals) results in poor screening of charge accumulated at the surface.[32, 36] The screening of an electric field within a semiconductor is caused by conduction electrons dampening the electric field acting on ions in the crystal lattice. Since semiconductors have very low numbers of conduction electrons, the screening effect is diminished compared to more conductive materials such as metals.

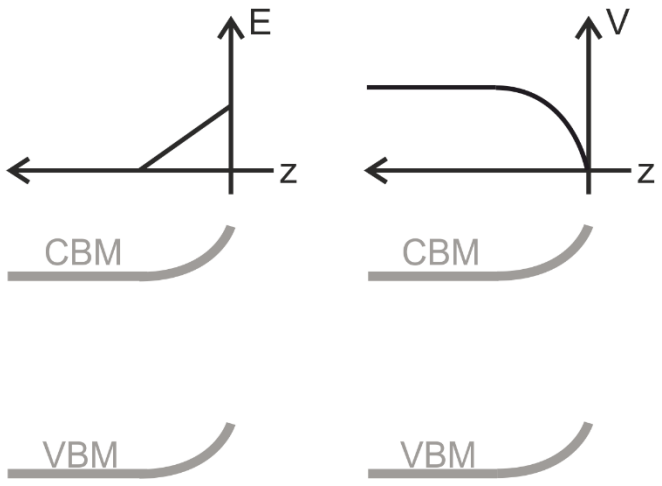

Figure 1.2: Electric field (left) and potential (right) changes across the space charge region for a semiconductor under depletion conditions.

The space charge region is an important factor in charge separation, as the potential gradient creates a driving force for the separation of electrons and holes at the material surface. The direction and extent of the band bending will be dependent upon both the nature of the adsorbate as well as the electronic structure of the semiconductor.[37] For upward band bending, holes will accumulate at the surface, increasing minority carrier concentration for an n-type semiconductor. As this region would be depleted of majority carriers, electrons for an

n-type material, it is termed a 'depletion region'. Conversely, should downward band bending be observed, electrons will accumulate at the surface and form an 'accumulation region'. The accumulation of charge carriers at the surface is an important factor in semiconductor photocatalysis as the rates of oxidative and reductive processes will be dependent upon surface concentrations of holes and electrons, respectively and their energies.[38]

The structure of the semiconductor-liquid interface outlined above is still a somewhat idealised picture – assuming a 'perfect' semiconductor crystal free from defects and surface states. In real systems, however, defects are common in both the bulk and at the surface as their formation is entropically driven. These defects cause not only structural abnormalities but form electronic states with the potential to trap charge carriers on an atomistic scale.[39-42] Electronic states created by crystal defects can actually contribute to the bulk electronic structure of materials – semiconductors such as TiO_2 and tin oxide, SnO_2, are n-doped due to oxygen vacancies in the crystal lattice.[43, 44]

Whilst bulk defects can play an important role in charge-carrier recombination and mobility, it is surface defects that will exhibit greater influence on redox reactions with semiconducting photocatalysts.[37, 38, 45, 46] At a material surface, the termination of the crystal unit cell leaves coordinatively unsaturated sites with 'dangling bonds'. The electron density associated with these dangling bonds will form electronic states in between the valence and conduction bands. These new states will occupy the mid-gap in addition to existing p- or n-type doping of the semiconductor. Commonly, these surface states will be terminated by -OH or -H groups due to adsorption of atmospheric water vapour. As they create separate electronic energy levels in the mid gap, surface states can impact band bending, charge carrier recombination and thus photocatalysis.[25, 47] As with the 'ideal' semiconductor without surface states, the surface states will be affected by adsorption of species from solution.[37] There are two main arguments as to the role of surface states within semiconductor photocatalysis and photoelectrochemistry – as either centres for recombination of the electron-hole pairs or as non-innocent sites within a catalytic cycle.[48, 49]

Recombination in semiconductors can occur throughout the crystal, either in the bulk or at the surface. In the bulk, electrons in the conduction band can relax directly to the valence band edge or can relax into electronic states created by bulk defects.[42, 47, 50-52] At the surface, the recombination pathways are affected by the space charge region as the band bending creates an impetus for electron-hole separation. However, as with bulk defects, the electronic states in the mid gap created by surface defects provide relaxation pathways for conduction

band electrons. Surface state-mediated recombination is also known as Shockley-Read-Hall recombination.[40, 41] In a photocatalyst, the recombination pathways will be in direct competition with charge extraction by oxidation or reduction of a substrate. This competition means that surface states can have a detrimental impact on photocatalyst activity, reducing quantum yield (Figure 1.3).

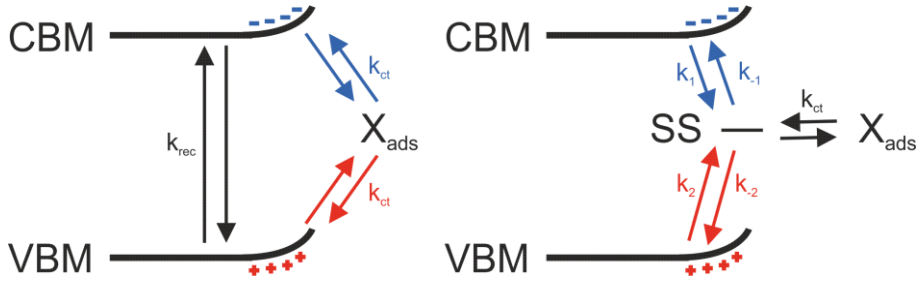

Figure 1.3: Direct band to band or band to substrate transitions of electrons and holes (left) compared with surface state (SS) mediated processes (right). k_{rec} signifies direct electron-hole recombination between bands, k_{ct} represents charge transfer from either band edges or the surface state. k_1, k_{-1}, k_2 and k_{-2} represent electron/hole capture by and injection from the surface state respectively. Hole transfer processes are represented by red arrows, electron transfer by blue.

Whilst suggested as a significant limitation of semiconductor photocatalysis, there are few reports of attempting to reduce surface recombination rates for synthetically relevant photocatalytic reactions.[12, 53] In contrast, photoelectrochemistry focusses heavily on the role of surface states and the importance of recombination rates when reporting water oxidation at photoelectrodes.[25, 50, 54-56] As both bulk and surface recombination rates directly affect photocatalyst efficiency, it is important to differentiate the key steps in mechanism and alleviate the trapping of charge carriers.

1.1.1 Semiconductor-Metal Interfaces in Selective Photocatalysis

One method typically used to reduce recombination rates in semiconductor photocatalyst powders is decoration of the particle surface with noble metal nanoparticles. When the semiconductor is brought into contact with a metal, there is again an equilibration of Fermi levels, E_F. The equilibration results in the pinning of the semiconductor Fermi level due to the much larger number of states at E_F for the metal and enables the metal nanoparticle to act as an electron sink (Figure 1.4).

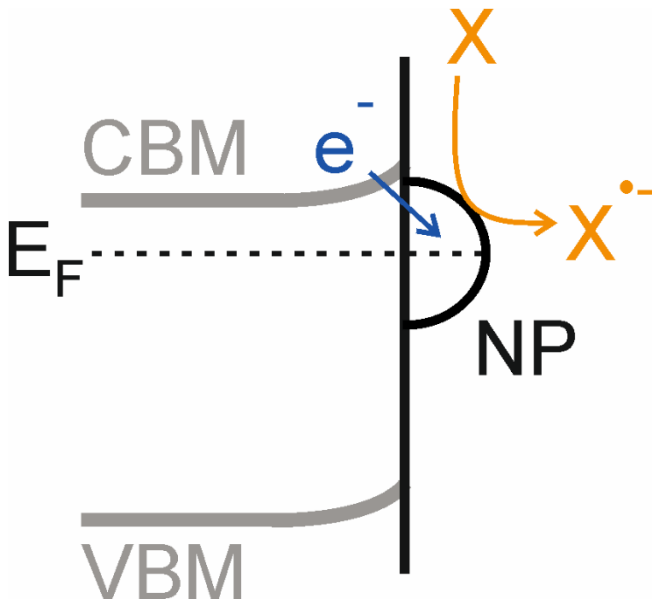

Figure 1.4: Schematic of a semiconductor-metal nanoparticle interface. Electron transfer to the metal nanoparticle, NP, and subsequent reduction of a substrate, X, is also shown.

A major benefit of decoration with metal nanoparticles is the facilitation of reduction reactions. Typically, platinum nanoparticles are employed to enhance the proton reduction reaction, which is commonly the complementary process to oxidative transformations.[46] Supported palladium nanoparticles have been used to support more complex chemistry such as Sonogoshira C-C coupling of phenylacetylene and iodobenzene.[57]

1.1.2 Photoelectrochemistry of Semiconductor Photocatalysts

Charge carrier recombination rates can also be reduced through the application of a bias potential, provided the semiconductor is suspended on a conducting substrate. For an n-type semiconductor as an increasingly anodic potential is applied, the extent of band bending increases. Due to the relatively low number of bulk carriers in a semiconductor, screening of the applied potential is poor and so all potential changes appear over the space charge region of the semiconductor. For metallic electrodes, this potential change is usually observed over the Helmholtz layer.

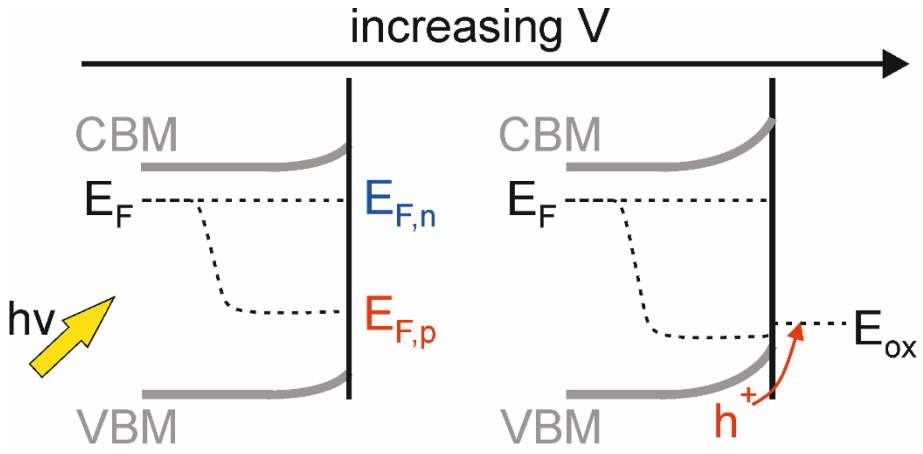

Figure 1.5: Splitting of the semiconductor Fermi level, E_F, into quasi-Fermi levels for electrons, $E_{F,n}$, and holes, $E_{F,p}$, under illumination. As anodic bias is increased $E_{F,p}$ drops below the oxidation potential of the substrate, E_{ox}, and hole transfer occurs.

In the absence of illumination and under a sufficient bias, band bending causes the Fermi level to reside within the conduction or the valence band, making the semiconductor degenerate and causing metallic behaviour. Under these conditions electrons flow between the semiconductor and the substrate as they would at a metallic electrode.

Under illumination, the semiconductor Fermi level splits into two quasi-Fermi levels for holes, $E_{F,p}$, and electrons, $E_{F,n}$, independently (Figure 1.5). As bias is increased, band bending eventually causes $E_{F,p}$ to drop below the oxidation potential of the substrate and electrons can be transferred from the electrolyte to the valence band of the photocatalyst. In addition to adjusting the oxidation potential of holes, the increased band bending acts to improve electron-hole separation in the space charge region of the semiconductor. As applied potential is increased, the width of the space charge region increases, enhancing electron-hole separation by increasing the electric field gradient between the bulk and surface of the semiconductor (Figure 1.6). The improved charge separation results in reduced surface recombination rates at mid-gap surface states and gives spatial separation between the bulk electron and the surface hole.

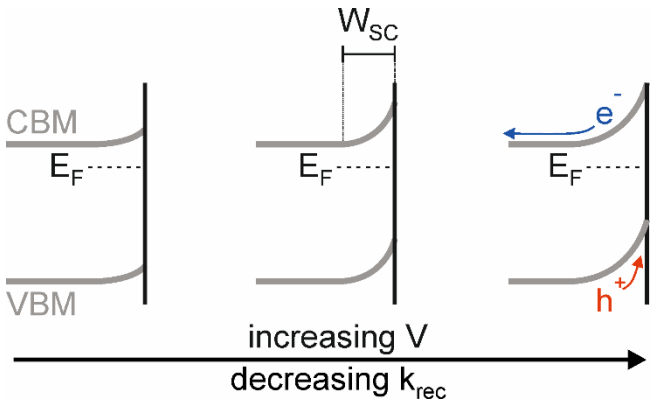

Figure 1.6: Changes to the electronic structure of an n-type semiconductor under an increasingly anodic bias. Increased band bending of the conduction band minimum (CBM) and valence band maximum (VBM), combined with an increased space-charge width (W_{SC}) reduce electron-hole recombination rate, k_{rec}.

Suspension of a semiconductor photocatalyst onto a conducting substrate can be used as a method of reducing charge carrier recombination, but it also enables the use of operando electrochemical characterisation methods. Techniques such as voltammetry, amperometry and electrochemical impedance spectroscopy (EIS) can be used to understand charge carrier behaviours in the semiconductor in real time and under reaction conditions.[58, 59] Understanding charge carrier behaviours and the photophysics of the semiconductor surface are key in probing reaction mechanism and optimising photocatalysts to their application.

1.2 Operando and In Situ Characterisation of Semiconductor Photocatalysts and Reaction Intermediates

The structural and energetic characterisation of semiconductor photocatalysts and reaction intermediates is key to elucidating mechanism of photocatalytic transformations. Unlike molecular photocatalysts, such as $[Ru(bpy)_3]^{2+}$, semiconductor crystallites are more difficult to characterise. Often, semiconductor photocatalysts are polycrystalline, containing a variety of exposed facets at the surface, each with a unique composition, electronic structure, and reactivity. Additionally, the presence of surface states complicates understanding as their role in photocatalytic transformations is unclear and their characterisation difficult. Typically, outer sphere electron transfer mechanisms are assumed, but coordinatively unsaturated surface states can affect substrate adsorption or ligation to the semiconductor surface. Operando and in situ methods are useful probes of photocatalysis mechanisms through

characterisation of reactive intermediates and charge carrier behaviours at the photocatalyst surface.

1.2.1 Electrochemical Impedance Spectroscopy

In much of the photoelectrochemical literature it is common to employ electrochemical perturbation methods alongside typical d.c. methods such as cyclic/linear voltammetry and chronoamperometry.[51, 60, 61] Access to perturbation techniques is difficult for photocatalyst powders in a suspension and so these studies are lacking in selective photocatalysis. For analysis of charge transfer and recombination rate constants, deposition onto a suitable electrode substrate is required. In perturbation techniques a small, sinusoidal change is applied to the system, the frequency of which is varied. The perturbation shifts the system away from equilibrium and so a current or resistance response is generated. It is important that this perturbation is small enough to ensure a linear response from the system. The plotting of this response against frequency allows the determination of charge carrier kinetics through simulation of an 'equivalent cell'. The equivalent cell is simply an electrical circuit of resistors and capacitors modelled on charge transfer processes within the electrode and cell.

The two main perturbation techniques utilised in photoelectrochemistry are the electrochemical impedance method (EIS) and intensity-modulated photocurrent spectroscopy (IMPS).[62] In EIS, the perturbation takes the form of an applied voltage small enough to not significantly remove the system from equilibrium. This impedance can be broken down into real and imaginary components, which are then plotted to give a Nyquist plot – a common representation of impedance in the literature. These semi-circular plots can be simulated as an electrical circuit and model resistances and capacitances within the electrode. The simplest form of a Nyquist plot is the Randles circuit – a model of a metallic electrode in an electrolyte solution (Figure 1.7).

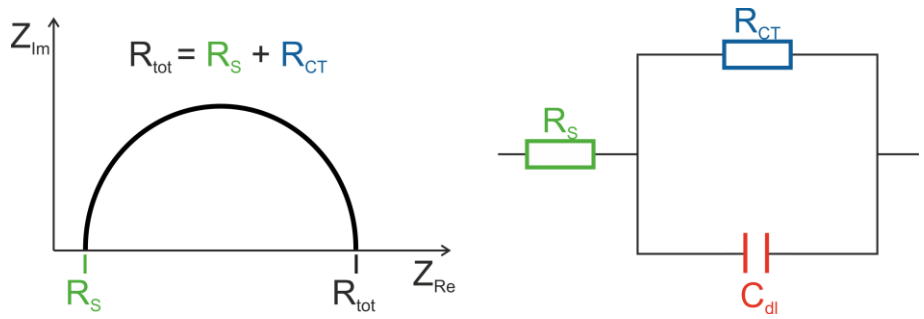

Figure 1.7: Simplified Nyquist plot (left) and equivalent cell (right) of a Randles circuit. R_S denotes the solution resistance, R_{CT} the resistance to charge transfer and C_{dl} the double layer capacitance. The total resistance can be calculated as the sum of individual resistances within the cell.

Semiconductor photoelectrodes and photocatalysts introduce more complexity to the impedance analysis due to the unique photophysics at the semiconductor-liquid junction.[24, 63] Any changes in applied potential will appear predominantly over the space-charge region due to poor shielding of charge by the limited number of free carriers, around 10^{18} cm^{-3}. Due to differences in bulk and surface electronic structure, more components of the equivalent cell are necessary to model charge carrier behaviours.[42, 59] By increasing the complexity of the model, it is also possible to probe the impedance associated with charge trapping and reactions at surface states. The key benefit of these techniques is that they are in situ probes of charge carrier behaviour in the semiconductor. An in-depth analysis of charge transfer to and from surface states of silicon surfaces is provided by Hoffmann *et al*., who model rate constants for these processes using EIS.[64] As most theoretical treatments of impedance assume microscopically flat surfaces - the Hoffmann example is based on pure Si (111) surfaces – the analysis of porous electrodes and powders is more difficult. Contributions to the impedance from mass transport and multi-directional electron transfer in pores at multiple surfaces complicate the interrogation of 'real', porous systems.[65, 66]

The application of surface state models to water splitting is shown in investigations by Klahr *et al*. Using EIS, they have related changes in surface state capacitance of hematite (Fe_2O_3) to improved catalysis in the water oxidation reaction.[48, 49] A comparison between the oxidation of the ferricyanide redox couple, $[Fe(CN)_6]^{3-/4-}$, and water was made due to their different charge transfer kinetics. As the ferricyanide couple has been shown to efficiently scavenge holes, any changes in current-voltage characteristics should arise from differences in hole collection efficiencies at the surface.[67] Linear sweep voltammograms of ferricyanide (Figure 1.8) show a significant cathodic shift in onset potential as well as larger photocurrent

density at all potentials. The changes in voltammogram are attributed to improved charge transfer kinetics, most likely due to the relative simplicity of the one electron oxidation of ferricyanide compared to the four-electron oxidation of water.

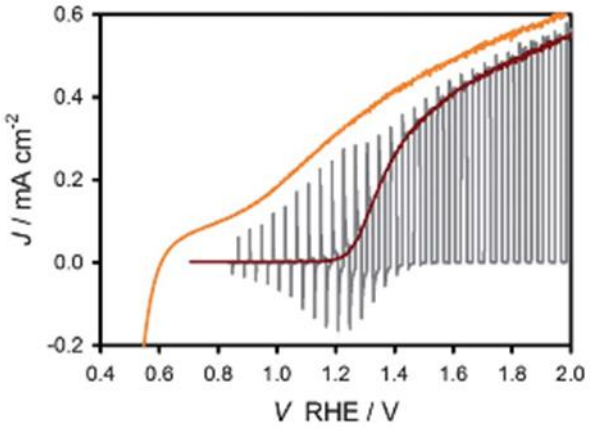

Figure 1.8: Linear sweep voltammograms under illumination of hematite photoelectrodes in ferricyanide solutions (orange) and pH 6.9 water (red). Chopped illumination is shown by the grey line. Figure was taken from Klahr et al., Energ. Environ. Soc., 2012.[48]

This was corroborated by EIS measurements that show an additional feature at high frequency in the Nyquist plot for water oxidation (Figure 1.9), attributed to changes in surface state capacitance. For the ferricyanide couple, the fitting with a simples Randle's circuit implies charge transfer directly from the band edge. The validity of the measurements is confirmed by comparison of the total resistance of the hematite electrode by linear sweep voltammetry and EIS.[49] Further probing of water oxidation under various pH and illumination conditions revealed that surface state capacitance plays a key role in water oxidation. It is important to note that resistances and capacitances derived in the equivalent cell have little to no physical meaning. The changes to surface capacitance do not reveal any mechanistic information about the water oxidation but simply provide a correlation between surface capacitance and rate of oxidation. The electrodes studied were prepared by atomic layer deposition to give compact hematite films. Electrodes also showed poor catalytic performance for water oxidation, which may be attributed to low porosity or lack of nanostructuring. As such, the impedance analysis of surface states may not be applicable to many relevant materials for large scale water oxidation, or electrodes prepared by other methods.

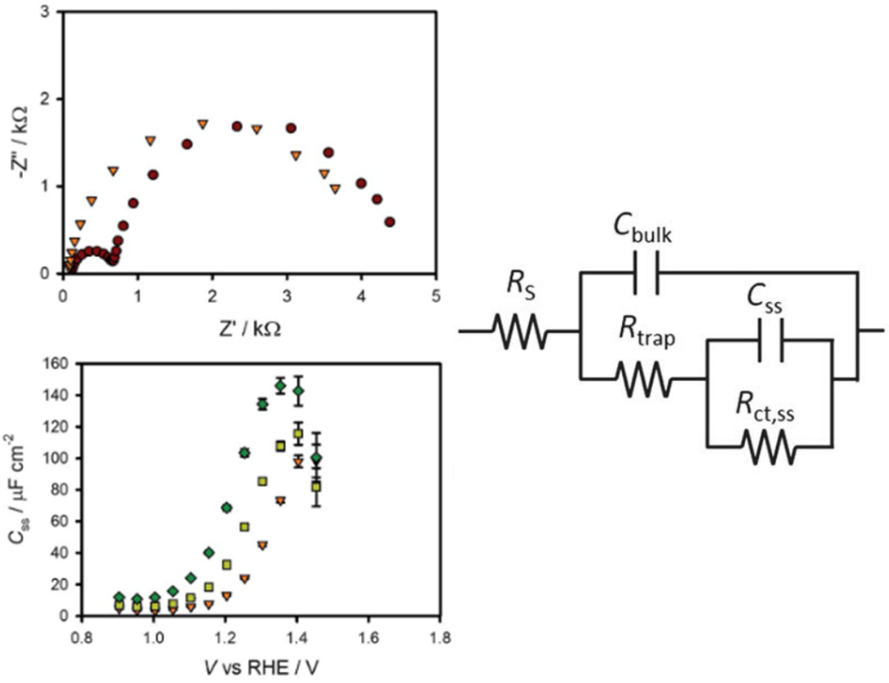

Figure 1.9: Nyquist plots of hematite electrodes in ferricyanide (orange triangles) and pH 6.9 water (red circles) solutions (top). Surface state capacitance as a function of potential for hematite photoelectrodes at 0.1 (orange triangles), 0.33 (yellow squares) and 1 (green diamonds) sun illumination (bottom). The equivalent cell used to fit Nyquist plots for water oxidation is shown on the right. Figure was taken from Klahr et al., Energ. Environ. Soc., 2012.[48]

The impedance analysis of porous films can be achieved using a 'transmission line' model to simulate the impedance response at varying depths in well-defined pore structures. Alternatively, a constant phase element (CPE) can be used in the simulation of EIS data to account for the non-ideal behaviour of surface capacitance with changing frequency.[65] The transmission line model has successfully been applied to Li and H-doped TiO_2 nanorod electrodes in water splitting applications, however no explicit rate information was extracted.[68] Instead, it was hypothesised that a decrease in the charge transfer resistance was indicative of reduced electron-hole combination from passivation by Li/H dopant. The use of CPEs has been shown in the impedance analysis of $BiVO_4$ for water splitting also. Hernandez *et al*. propose the use of CPEs to account for frequency dispersions caused by electrode porosity as they compare compact and porous electrodes. Whilst a useful fitting tool, CPEs are limited as they have no physical meaning. The real capacitance can be extracted from CPE values but preferably impedance responses should be mapped by ideal capacitors.

A derivative of EIS, Mott-Schottky analysis, is a useful tool for characterisation of the flat-band potential, E_{fb}, and donor density, N_D, of semiconductor materials.[69] These parameters are important for the understanding of the electronic structure of the semiconductor at the electrode-electrolyte interface. E_{fb} measurements can be used to understand the band-bending of the semiconductor at equilibrium, whilst N_D is a measure of majority carriers within the material which dictates the number of photogenerated charge carriers under illumination.[31] N_D is a useful measure for the comparison of doped and undoped materials, for example, Mo doping of $BiVO_4$ has been shown to increase N_D by an order of magnitude, from 10^{19} to 10^{20}.[70]

1.2.2 Intensity Modulated Photocurrent Spectroscopy

Another form of perturbation analysis employs small modulations of light intensity to probe charge transfer kinetics. The theoretical treatment of these techniques was mainly considered by Laurie Peter in the 90s.[62, 71] The modulation of light intensity brings about a current and a voltage response which are probed by intensity modulated photocurrent spectroscopy (IMPS) and intensity modulated photovoltage spectroscopy (IMVS) respectively.[72, 73] With these measurements it is important that the incident intensity is low, as theoretical assumptions include constant space charge capacitance and majority carrier concentration. Similarly to EIS, techniques utilising the modulation of light intensity give information on charge transfer processes within the semiconductor. Unlike impedance spectroscopy, however, these techniques are not limited by the frequency constraints of the potentiostat (high frequency limits are usually in the MHz range) and so can probe faster processes within the electrode.[62]

In the treatment of IMPS data, it is assumed that charge transfer and recombination processes can be modelled with pseudo-first order kinetics due to the much greater concentration of recombination centres relative to charge carriers.[71-73] This assumption allows the calculation of the rate constants associated with charge transfer processes in the semiconductor. As with impedance data, IMPS and IMVS outputs are commonly represented in Nyquist plots detailing real and imaginary components of the response. As IMPS data are treated in terms of a charge transfer rate (k_{ct}) and a recombination rate (k_{rec}) the Nyquist plots can be broadly separated into a 'charge transfer' semicircle and a 'recombination' semicircle. The recombination semicircle is represented in the complex quadrant at high frequency with charge transfer processes observed in the real quadrant at lower frequency. In IMPS/IMVS,

bulk processes are assumed to be invisible, therefore only surface processes contribute to the Nyquist plot.

Whilst many applications of IMPS have related to carrier transport in dye sensitized solar cells, there have been recent developments on its use as a mechanistic probe for water splitting reactions. The role of the common 'co-catalyst' for water oxidation, CoPi, on $BiVO_4$ surfaces was recently elucidated through IMPS.[25] Improvements to PEC performance on decoration of CoPi were rationalised by suppression of recombination rates by passivation of surface defects, as opposed to improved catalysis at the CoPi surface.

An important distinction between the IMPS and EIS studies is sensitivity to the morphology of the electrode being studied. For EIS, the electrode is required to be compact with a microscopically 'flat' surface in order to eliminate contributions from frequency dispersions associated with porosity.[65, 66] Klahr *et al*. prepared hematite films by ALD for analysis by EIS, whereas the $BiVO_4$ film used by Zachäus *et al*. for IMPS analysis was prepared by spray pyrolysis resulting in a comparatively 'rough' electrode surface.[25, 49] In IMPS and IMVS, as the illumination is modulated, responses are only generated across the space charge layer of the semiconductor. This means that contributions from the Helmholtz layer and frequency dispersions are less significant.[71] As such, it seems much easier to extract recombination and charge transfer information for porous films using light intensity modulation techniques. However, light penetration and modulation of the light intensity through the porous electrode can complicate analysis.

1.2.3 In Situ Spectroscopy for Characterisation of Reaction Intermediates

Perturbation techniques as described in sections 1.2.1 and 1.2.2 are probes of the whole electrode and therefore no chemical information is obtained about surface states or key reactive intermediates. For example, the IMPS analysis of $BiVO_4$ reveals Fermi level pinning by populated surface states but it is impossible to understand the chemical composition of these states without using local probes such as electron paramagnetic resonance spectroscopy, EPR, infra-red and X-ray spectroscopies.[74-79] Spectroscopic techniques can be used in situ to identify key intermediates at the semiconductor-liquid interface, as shown by IR characterisation of reactive species in water oxidation.[78, 80]

Single electron transfer between photocatalysts and substrates forms radical intermediates, therefore it is possible to follow reactions by EPR.[81] In the same way, the

paramagnetic nature of defect states allows characterisation of trapped charge carriers, though this is an ex situ study due to the low temperatures needed to trap charge carriers.[82-85] It is possible to obtain information on defect symmetry and lattice structure through analysis of the anisotropic g and A tensors of the EPR signal.[86] EPR spectroscopy of photoactive metal oxides and their interaction with adsorbates was pioneered in the 1980s, predominantly with studies on TiO_2 due to its popularity in water-splitting research.[82, 87, 88]

For bulk and surface states in the semiconductor, in depth characterisation often includes anisotropic magnetic properties of the EPR signal. The anisotropy of paramagnetic species in the solid means that through analysis of the g and A tensors it is possible to identify the symmetry of the site. Symmetry can inform on the coordination sphere of the trapped charge carrier.

As with examples of cross coupling photocatalysis, the majority of EPR studies on semiconductors have been focussed on TiO_2 powders owing to their utility in solar cells, water oxidation and the interesting properties of doped materials.[89-91] For many visible-light absorbing materials of interest, such as bismuth vanadate and tungsten trioxide, in-depth EPR characterisation is lacking. For bismuth vanadate specifically, vanadyl (VO^{2+}) impurities can dominate the EPR signal.[85] As such, there is limited understanding of the structure of surface states and their roles in photocatalysis. As with many physical properties of photocatalysts, it is possible defect concentration and composition vary with synthetic methods employed.[92, 93] EPR studies of PEC systems add an extra level of complexity to experimental design as EPR cells must be narrow enough to allow transmission of microwaves, yet spacious enough to accommodate a 3-electrode set-up.[94, 95]

More elaborate methods, such as X-ray (XAS) and transient absorption spectroscopy (TAS) have been used to identify key Fe(IV) intermediates in the photoelectrochemical oxidation of water at hematite electrodes.[96, 97] Using TAS, a unique multi-hole mechanistic step for water oxidation at hematite electrodes was revealed. The rate law under a sufficient bias for PEC water oxidation is third order with respect to surface holes, indicating a hole accumulation step in the mechanism, similar to systems in biological photosynthesis. XAS has been used to determine the nature of the rate determining O-O bond formation in water oxidation.

In the field of photoelectrochemistry, most spectroscopic and electrochemical techniques have found main applications in water splitting and water remediation.[98] Very few

examples of these techniques applied to non-aqueous systems or organic transformations exist in the literature. For complete characterisation of a photocatalytic system, a combination of in situ techniques are necessary to understand the mechanistic steps from light absorption to eventual reaction. The correlation of structure and reactivity by in situ and operando methods is becoming more commonplace in PEC water splitting literature – the same treatment is required to fully understand selective photo- and photoelectrocatalysis using semiconductor powders or electrodes.

1.3 Selective Organic Transformations at Semiconductor Photoelectrodes

Heterogeneous photocatalysis in organic synthesis has seen increasing applications due to constantly expanding libraries of possible transformations. In recent years, several review articles have been published discussing the application of semiconductor photocatalysts to organic synthesis problems, with most research utilising TiO_2 powders in some form.[12, 99] Although ubiquitous in heterogeneous photocatalysis research, the large band gap of TiO_2 - E_g = 3.2 eV for anatase - means UV irradiation is required.[91] Combinatorial approaches employing a semiconductor photocatalyst and homogeneous co-catalyst have been developed, with carbon nitride (C_3N_4), cadmium sulfide (CdS) and lead halide perovskites such as $CsPbBr_3$ employed alongside nickel catalysts in C-X bond forming reactions (X = C, N, O).[100-103]

There has also been interest in utilising semiconductor photoelectrochemistry to remediate issues associated with powdered photocatalysts such as insufficient oxidation potential of surface holes and high recombination rates.[31, 104] These PEC systems can be differentiated based on the nature of the substrate-semiconductor interactions. Synthetic systems in which the electrochemical and photochemical pathways are independent of one and other are referred to as decoupled PEC (d-PEC). These decoupled systems include those such as semiconductor photoelectrodes coupled with redox mediators or homogeneous catalysts. Systems where photon absorption, electrochemical bias and substrate transformation all occur at the same electrode are referred to as interfacial PEC (i-PEC). Coupling all components of a PEC system into one electrode reduces the need for expensive co-catalysts and separations and enables the use of some characterisation methods detailed in section 1.2. Despite these benefits, i-PEC is limited by poor understanding of surface chemistry at semiconductor photoelectrodes and the relatively low number of available carriers for redox reactions compared to metallic electrodes.

Interfacial photoelectrochemical systems have mainly found applications in water splitting, remediation of organic pollutants in water, and fuel cells.[98] As such, much of their characterisation is focused on optimising the reactions of small molecules. As with semiconductor photocatalysis with powdered materials, i-PEC systems can be applied to organic synthesis problems concerning redox reactions as well as a variety of C-X coupling reactions or functional group interconversions.[104]

1.3.1 Alcohol Oxidation

Selective alcohol oxidation to the corresponding aldehyde is an industrially important reaction as aldehydes are useful synthetic intermediates and valuable products in the cosmetic industry.[105] Typically, a stoichiometric oxidant such as chromate or permanganate will be used in this process, however these compounds are relatively expensive and rather toxic. As such, the selective oxidation of alcohols to aldehydes is an attractive target reaction for photo- and photoelectrochemical synthesis. In 2014, Zhang *et al*. carried out the first example of photoelectrochemical benzyl alcohol oxidation, employing gold decorated CeO_2/TiO_2 photoelectrodes in aqueous solution.[106] Reactions were carried out under visible light irradiation (100 mW cm^{-2}, 420 - 800 nm) at a bias of -0.8 V vs SCE, with >99% selectivity for benzaldehyde observed. A proposed mechanism with simultaneous oxygen reduction at Au nanoparticles and benzyl alcohol oxidation at the CeO_2/TiO_2 electrode was put forward. However, due to the large cathodic potential and photocurrent, oxidation of benzyl alcohol at the photoelectrode seems unlikely as, under these conditions, it would be expected that the semiconductor is depleted of holes. Supported Au nanoparticles have been used in the thermal catalysis of alcohol oxidation reactions. Here, formation of a Au-hydride intermediate is key to oxidation, formed by β-hydride shift from the alcohol.[107] Given the -0.8 V cathodic bias applied to the CeO_2/TiO_2/Au composite in the photoelectrochemical example, it is possible that the hydride shift is catalysed at the Au nanoparticles.

Further research on benzyl alcohol oxidation was given by Sayama and coworkers in 2017, this time at a tandem $BiVO_4/WO_3$ photoelectrode in a direct oxidative reaction at the semiconductor.[108] Oxidation of several benzyl alcohol derivatives was carried out, with corresponding aldehyde yields up to 97% after 10 hours. No clear substituent effects were observed for alcohol oxidation, with oxidation potentials required to maintain a 0.2 mA cm^{-2} current density consistently around 0.7 V vs SHE. Sayama *et al*. attributed the lack of correlation in the Hammett plot to the required bias depending on the conduction band potential of the electrode, which should be effectively constant in the similar media. More

recent research has proposed a non-electrochemical pathway for benzyl alcohol oxidation at metal oxide photoelectrodes, with a singlet oxygen mediated pathway.[109] However, the requirement for UV-light irradiation to form singlet oxygen excludes this pathway from visible-light mediated reactions. Nevertheless, mechanistic studies on PEC transformations are relatively lacking and more considerations must be taken when developing new reaction systems. More in-depth mechanistic studies are required, as full understanding of the key reaction steps will allow rational design of optimised systems.

1.3.2 C-H Functionalisation

In addition to simple oxidation reactions of alcohols, C-H functionalisation in PEC systems has been demonstrated, with a range of C-X bond formations (X = C, P, N, O, halogen). C-H functionalisation reactions are an incredibly important class of reactions in fine chemical synthesis, typically catalysed by palladium complexes.[110] As with alcohol oxidations, PEC C-H functionalisation can offer a cheaper, greener alternative to traditional methods.

Several recent examples of PEC C-H functionalisation employ a redox mediator and are therefore not a result of i-PEC. However, C-P and C-O bonds have been formed in high yields for C-H/P-H coupling reactions and C-H oxidations.[111, 112] In both cases, $BiVO_4$ was employed as the photoanode, with irradiation by a blue LED array.

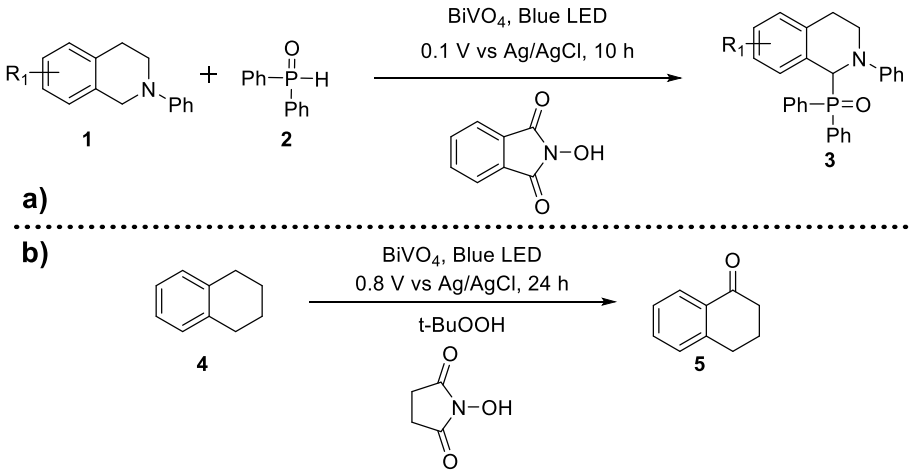

Scheme 1.1: a) PEC C-P coupling of N-phenyltetrahydroisoquinoline and diphenyl phosphine oxide at a $BiVO_4$ photoanode. b) PEC C-H oxidation of tetralin to tetralone at a $BiVO_4$ photoelectrode. Schemes adapted from a) Wang et al., Chem. Commun., 2019 and b) Li et al., Nat. Commun., 2017.[111, 112]

C-P coupling of N-phenyltetrahydroisoquinoline (**1**) to diphenylphosphine oxide (**2**) was performed in good yields (up to 99%) over 10 hours at current densities of around 2.0 mA cm^{-2} (Scheme 1.1). In this instance, initial oxidation of **1** is carried out by valence band holes at the photoelectrode. The N-hydroxyphthalimide (NHPI) redox mediator is then responsible for a second oxidation to a cationic intermediate that then couples to **2**. Addition of the redox mediator was key in forming the cationic intermediate, as shown by increased yields from 39% to 93% as well as a decrease in the required potential from 0.5 V to 0.1 V vs Ag/AgCl. The formation of some product in the absence of redox mediator shows that two-electron oxidation of **1** directly at the photoanode is possible but is limited by sluggish oxidation kinetics.

Similar importance is given to the redox mediator in the photoelectrochemical oxidation of C-H bonds to ketones.[112] Tetralone (**5**) is afforded in a 75% yield after 24-hour electrolysis of tetralin (**4**) at 0.8 V vs Ag/AgCl, with current densities of around 1.1 mA cm^{-2}. Again, a tentative mechanism is proposed, with oxidation of the N-hydroxysuccinimide (NHS) anion and subsequent hydrogen abstraction of tetralin C-H bonds. The carbon-centred radical then reacts with t-butylperoxide (t-BuOOH) to give a peroxyl intermediate that decomposes to **5** and t-butanol (t-BuOH). Further mechanistic study may have been able to elucidate the true role of t-BuOOH, as possible reduction to t-$BuO^{\bullet}$ at the cathode would enable both hydrogen abstraction of **4** and t-BuOH formation. The presence of t-BuOOH is not essential to the reaction, as oxidation of cyclohexene to cyclohexanone (>99% Faradaic efficiency) has been performed at $BiVO_4/WO_3$ photoanodes using solely NHPI as a redox mediator.[113] $BiVO_4/WO_3$ photoanodes have also been employed in the formation C-O single bonds through methoxylation of furan, using a bromide redox mediator in up to 99% yields.[114]

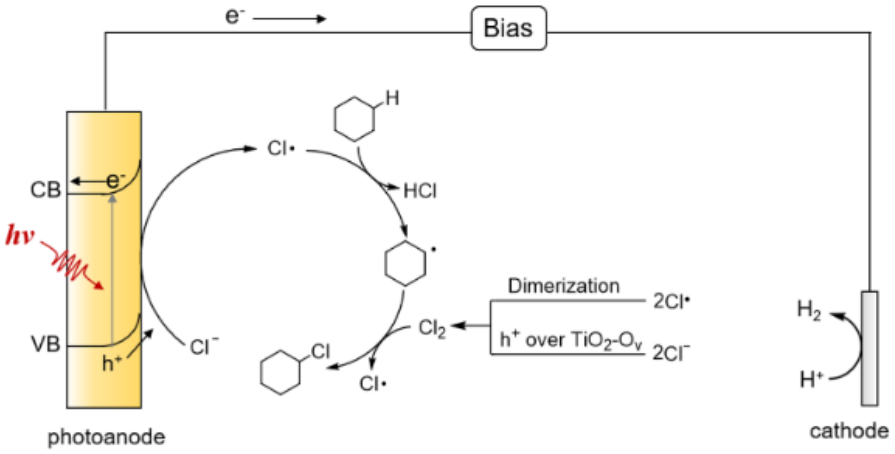

Figure 1.10: Proposed mechanism of C-H halogenation at TiO_2 photoelectrodes. The Ag/AgCl reference electrode is omitted for clarity. Figure taken from Li et al., Nat. Commun., 2021.[115]

The utilisation of halogen anions as redox agents in PEC systems has been further developed recently, with C-H halogenation of cyclohexane achieved at TiO_2 photoelectrodes in water, under AM1.5G solar simulated illumination.[115] Aromatic, heteroaromatic and aliphatic substrates were halogenated in up to 99% selectivity at applied potentials up to 1.6 V vs RHE, however conversion of acyclic hydrocarbons was extremely low. In the proposed mechanism, halide anions, provided by NaX electrolyte salts (X = Cl^-, Br^-, I^-), were oxidised to form halide radicals, which either abstract a hydrogen from cyclohexane, or recombine to the dihalide. The carbon-centred radical formed from C-H abstraction can then undergo halogenation by $X^\bullet$ radicals generated at the photoanode or by the dihalide (Figure 1.10). After initial reactions with unmodified TiO_2 photoelectrodes, the PEC system was optimised by partial reduction of the photoanode to generate oxygen vacancies, achieved through annealing in a H_2 atmosphere. The treated TiO_2 electrode exhibited a 1.9 mA cm^{-2} increase in photocurrent density at 1.6 V vs RHE, shortening reaction time and showing greater enhancements for Cl^- oxidation compared to water oxidation.

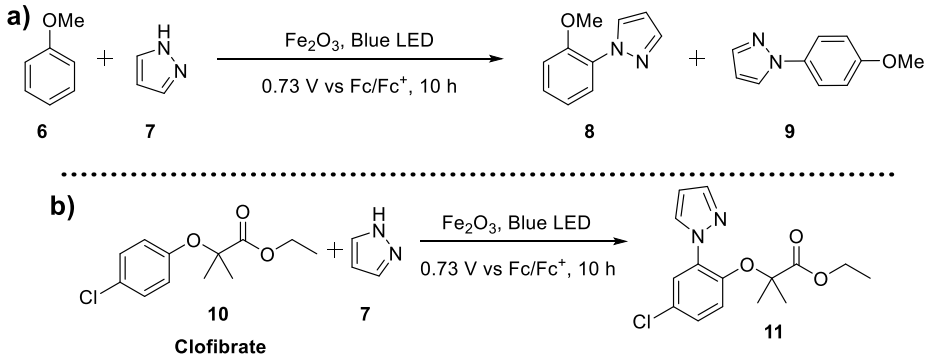

Scheme 1.2: a) C-H amination of anisole with pyrazole at Fe_2O_3 photoanodes. b) C-H amination of Clofibrate.[116] Schemes were adapted from Zhang et al., Nature Catalysis, 2019.[116]

Direct C-H functionalisation at the photoelectrode surface in the absence of redox mediators has been achieved at Fe_2O_3 photoelectrodes (Scheme 1.2).[116] Grätzel and co-workers have demonstrated ortho-amination of anisole (**6**) derivatives in good yields (41 – 86%) after 10 hours under blue LED illumination. Initial oxidation of the aryl π-system of **6** enables nucleophilic attack of pyrazole (**7**), with substitution directed to the ortho-position (**8**) by hydrogen bonding interactions with hexafluoroisopropanol solvent. Ratios up to 14:1 of **8**:**9** were observed, showing excellent ortho-selectivity. For 1,2,3-triazole derivatives, ortho:para ratio decreases to 2:1, though no comment is given as to why. In addition to exploring the substrate scope of the transformation, the C-H amination reactions were applied to the functionalisation of late-stage pharmaceuticals, such as Clofibrate (**10**) in up to 87% yields – a first example of PEC synthesis in this context. This work is also one of the few that uses impedance analysis as a probe of the photoelectrode in the system. Mott-Schottky analysis is used to determine the flat band potential and estimate a 0.12 V overpotential for the reaction.

The C-H halogenation and amination works presented represent the first steps into true optimisation of PEC synthetic systems, through photoelectrode modification and analysis by impedance methods. These methods are commonplace in the water-splitting literature and their application to selective PEC synthesis is key for optimisation and possible implementation as a sustainable synthetic methodology.[117, 118]

1.3.3 Oxygen Atom Transfer

Thorough characterisation of PEC water splitting systems has enabled oxygen atom transfer reactions at Fe_2O_3 photoelectrodes using water as an oxygen source. Operando IR studies of water oxidation have characterised a key iron-oxo (Fe(IV)=O) intermediate that can be utilised as an oxygen atom transfer catalyst.[80, 119] Zhao *et al*. demonstrate oxygenation of a range of substrates including sulfides and arsines in high selectivity (up to 99%) as well as epoxidation of unactivated alkenes in poorer yields (45.5% for cyclohexene to cyclohexene oxide).

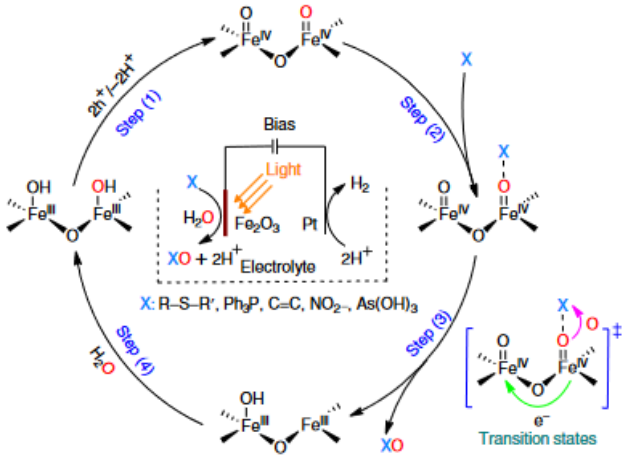

Figure 1.11: Mechanism of PEC oxygen atom transfer reactions at Fe_2O_3 photoanodes. Figure was taken from Zhao et al., Nature Catalysis, 2021.[119]

Comparison of TiO_2 and Fe_2O_3 photoanodes showed diminished selectivity at TiO_2 photoelectrodes, showing the importance of the iron-oxo intermediate. As around 10% conversion was observed at TiO_2 photoanodes, an alternate pathway may exist for these oxygen atom transfer reactions through direct oxidation of the substrate initially before reaction with water. However, it is clear that catalysis by the Fe(IV)=O intermediate enables the high substrate conversion and selectivity for the oxygenated product. Initial oxidation of water, up to 20% by volume in MeCN, forms the key Fe(IV)=O intermediate before oxygen atom transfer to the substrate (Figure 1.11). The work of Zhao *et al*. is a clear example of how thorough characterisation of PEC systems through electrochemical and operando techniques can enable not only optimisation of photoelectrosynthetic systems but the development of new transformations.

1.3.4 Oxidative Decarboxylation

Oxidative decarboxylation has proven to be a useful method for the photocatalytic generation of carbon-centred radicals. Generated radicals have then been deployed in C-C bond forming reactions through dimerization or addition to electron-deficient alkenes.[26, 120, 121] These transformations have also been called photo-Kolbe and photo-Giese reactions (for radical-radical and radical-alkene couplings respectively) due to their similarity to existing chemical transformations.[18, 122]

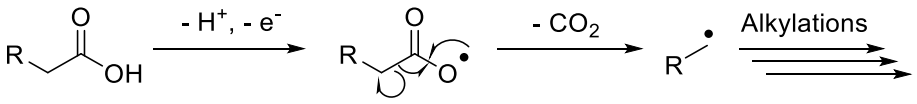

Figure 1.12: General mechanism for the oxidative decarboxylation of organic acids.

Some synthetic scope exists for these types of transformations at powdered TiO_2 photocatalysts, with dimerization and radical-alkene couplings of benzyl radicals demonstrated. Manley et al. show yields of 87% for the dimerization of benzyl radicals produced by oxidative decarboxylation of phenylacetic acid at a Pt-TiO_2 photocatalyst.[121] The scope of dimerization reactions was extended to a number of phenylacetic acid derivatives in reasonable yields (> 50%), however, for α-hydroxy and α-aminophenylacetic acids, preferential formation of alcohol/aldehyde and imine products was observed. Some attempts were also made at cross-coupling of benzylic radicals generated by oxidative decarboxylation of phenylacetic acid and triphenylacetic acid. However, only 18% yield for cross-coupled products was observed, with product distribution controlled by steric congestion of the radical.

The reactions of carbon-centred radicals with alkenes in photo-Giese type chemistry have also been demonstrated by Manley et al.[26, 120] Again, oxidative decarboxylation of phenylacetic acid and derivatives was used to produce benzylic radicals which were coupled to maleic anhydride and maleimide derivatives in up to 79% yields.

Very few photoelectrochemical examples of oxidative decarboxylation reactions exist, with only some analytical studies of acetate oxidation at TiO_2 photoelectrodes.[20] Recently, this was extended to trifluoroacetate by Grinberg and co-workers, but it's application to synthetic transformations remains limited.[123]

Despite their utility in generating carbon-centred radicals for alkylations, no examples of oxidative decarboxylation reactions at non-TiO_2 semiconductor photocatalysts have been published. This could be due to insufficient valence band potential i.e. holes are not 'oxidising' enough, or poor charge carrier separation within visible-light absorbing semiconductors. By supporting visible light photocatalysts onto an electrode, these limitations can be influenced. The application of visible-light absorbing semiconductors as photoelectrodes for oxidative decarboxylation reactions requires further study, not only for potential synthetic applications but also the understanding of key mechanistic processes at the photocatalyst surface. Factors such as substrate adsorption, applied potential and the nature of the radical intermediate have

been studied extensively for electrochemical reactions, therefore the same treatment should be applied to analogous PEC systems.[124, 125]

1.4 Electrochemical Oxidative Decarboxylation

The scope of oxidative decarboxylation reactions has been explored in much more depth using electrochemical methods. Electrochemical examples of radical-radical coupling (Kolbe), radical-alkene coupling (Giese) and reactions of electrochemically generated carbocations (non-Kolbe) have resulted in a variety of molecular transformations at metallic electrodes.[124, 126, 127] For use as model reactions to establish a photoelectrochemical system for oxidative decarboxylation reactions, the Kolbe reaction is preferable. Due to the formation of a radical product after addition to an alkene, a second reduction or oxidation step is required for Giese type chemistry which complicates the mechanism.[122] Additionally, carbocation formation is a multiple electron, stepwise process which obfuscates the reaction mechanism and can lead to side product formation.[124, 128] In contrast, Kolbe reactions proceed via a theoretically simple one-electron oxidation and subsequent decarboxylation to the carbon centred radical. Two carbon centred radicals then recombine to yield a dimerised product. As decarboxylation rate constants are typically > 10^9 s^{-1}, electron transfer is the rate determining step, simplifying correlations between electrode kinetics and product distributions.[129] Often Kolbe and non-Kolbe reactions are in direct competition, therefore tuning selectivity between the two pathways can expand the scope of these transformations.

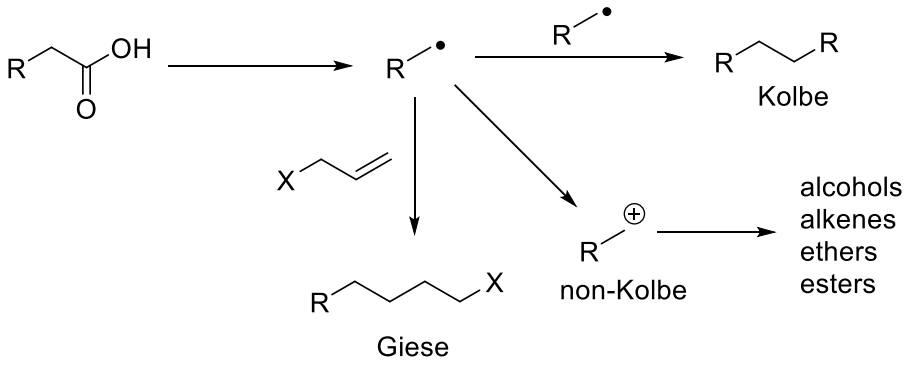

Scheme 1.3: Oxidative decarboxylation of a carboxylic acid and subsequent Kolbe, non-Kolbe and Giese chemistry of the intermediate radical.

Electrochemical Kolbe reactions are typically carried out at extremely high current densities (and thus extreme anodic potentials, often >10 V) to maximise intermediate radical concentrations and favour dimerization. Under these conditions, a 'critical potential' is

exceeded, above which oxidation of carboxylate anions is favoured over competing electrochemical reactions such as solvent or water oxidation.[130] The extreme potential ensures a defined layer of carboxylate anions is preferentially adsorbed to the electrode surface, preventing the adsorption of solvent molecules.[125] Adsorption of the carboxylate anions at the electrode surface under sufficient anodic potentials has been confirmed using isotopic labelling and rotating disk electrode measurements.[125] The strong adsorption of carboxylate anions has been corroborated by Tafel analysis of acetate and trifluoroacetate electrolysis at Pt electrodes. Extreme Tafel slopes indicated the formation of a barrier layer much thicker than a monolayer coverage of carboxylate anions, with strong interactions at the electrode surface.[131]

As carboxylate anions have significantly lower oxidation potentials (around 1.0 V lower) than the associated acids, electrolytes for Kolbe reactions typically consist of high acid concentrations and a small proportion of the carboxylate, either in the form of a salt or through partial neutralisation by addition of a base such as sodium methoxide (NaOMe) or triethylamine (Et_3N).[124, 132] Generally, Kolbe electrolysis is tolerant to a wide range of functional groups and carboxylic acids, though electron donating substituents adjacent to the carboxylate can promote carbocation formation.[124] Kolbe electrochemistry provides a reasonable pathway to the synthesis of symmetrical molecules, including as part of the total synthesis of α-onocerin.[133]

For Kolbe electrolysis, platinum is typically preferred as a working electrode material. Deployment of carbon-based electrodes can result in grafting of intermediate radicals to the electrode surface.[134] Carbon electrodes have also been shown to favour carbocation formation, such as in the synthesis of N-alkylacetamides.[135] For other metals such as gold and palladium, decarboxylation efficiencies are lower than for Pt in methanolic solutions.[136] Differences in product selectivity for the electrode materials was rationalised based on adsorption strengths of the intermediate acyloxy radical.[137] For lead oxide electrodes, ethane formation from acetic acid solutions is inhibited by even a small amount of water due its preferential adsorption onto the electrode surface.

More recent studies of electrode material for Kolbe electrolysis have utilised platinized titanium (Pt-Ti) as a means of reducing the amount of platinum required, making the reaction more cost-effective.[138] The oxidation of n-hexanoic acid in aqueous solutions was achieved with Coulombic efficiency of 48% for n-decane at Pt-Ti electrodes, which is comparable to a pure Pt electrode (55%). Despite the comparable selectivity for Kolbe products when using Pt-

Ti electrodes, their stability under operating conditions is lacking. Here, the dissolution of the Ti substrate results in Pt loss into solution and exposure of the underlying Ti (up to around 3% exposed Ti after electrolysis). The dynamic structural changes of electrodes in Kolbe electrolysis have been shown to affect recyclability of Pt and boron-doped diamond (BDD) electrodes.[139] Platinum surface roughness more than triples from 1.5 µm to 5.2 µm as measured by an optical profilometer, whilst AFM and electrochemical measurements of BDD electrodes show no clear etching but a marked decrease in electrochemical performance of the electrode. The appearance of a second voltametric wave when studying cyclic voltammetry of $Ru(NH_3)_6^{3+}$ suggested adsorption of foreign material on the electrode surface after electrolysis of hexanoic acid.

The nature of adsorption of the intermediate radicals, however, is less certain as contrasting evidence has been given for both adsorbed radicals and radicals free in solution. Characterisation of adsorbed radicals is further obfuscated by the existence of both acyloxy and alkyl radical intermediates (Scheme 1.4). Racemisation of chiral carboxylates indicates that radical-radical coupling may take place in solution, as opposed to the recombination of two surface bound radicals.[140, 141] Characterisation of adsorbed or free radicals is complicated by the existence of an adsorption-desorption equilibrium at the electrode surface, meaning a finite concentration of both species will exist during analysis.

Substrate adsorption and product selectivity have been shown to be sensitive to reaction solvents, with Kolbe electrolyses typically carried out in methanol or water despite competitive solvent oxidation. Studies using some common electrochemical solvents such as acetonitrile and DMF have shown a preference for formation of dimerised products in the case of diphenylacetic acid.[142] For acetonitrile, consideration for competing solvent oxidation is not needed due to the thermodynamically favourable carboxylate oxidation, however reactions between carbocations and solvent to form N-acylamides are a competing pathway.[143] Mixtures of acetonitrile and water can be used to promote carbocation formation, as shown by the formation of N-acylamides in Kolbe electrolyses.[144, 145] Several analytical studies on the Kolbe electrolysis have employed acetonitrile as a solvent, taking advantage of the wide potential window. Coulometric measurements reveal a stepwise mechanism, with formation of an acyloxy radical followed by sequential CO_2 loss, as opposed to a concerted mechanism (Scheme 1.4).[145, 146] Often, solvent selection depends heavily upon the carboxylate structure, as minimising the formation of carbocations is critical in maximising selectivity for the dimer.

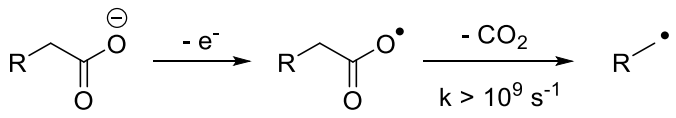

Scheme 1.4: Stepwise Kolbe decarboxylation mechanism proceeding via initial acyloxy radical formation followed by decarboxylation to the carbon-centred radical.

Despite the extreme potentials typically applied in electrochemical Kolbe reactions, the critical potential for favouring carboxylate oxidation is between 2.1 – 2.8 V vs NHE. Therefore, use of a semiconductor photoelectrode could still result in good dimer yields at low applied potentials by offsetting the critical potential with the photovoltage generated on illumination.[147] Additionally, the nature of substrate adsorption may be affected by the use of metal oxide photoelectrodes. Variation in surface structure and the concentration of surface hydroxyl species and defects may all play critical roles in the adsorption of carboxylate anions and intermediate radicals.

1.5 Conclusions

Semiconductor photoelectrochemistry is a promising technology for enabling more sustainable synthetic systems. The unique photophysics and chemistry at the semiconductor-electrolyte interface theoretically enable highly selective redox processes at mild applied potentials.[148] However, surface processes in semiconducting electrodes obscure mechanistic understanding due to difficult characterisation and the unknown role of surface states and substrate-electrode interactions.

By using semiconductor photoelectrodes, access is granted to a range of in situ and operando photoelectrochemical characterisation techniques that have seen extensive application to water splitting and water remediation systems. Techniques such as EIS allow characterisation of the semiconductor under reaction conditions and kinetic parameters relating to charge transfer can be extracted. Additionally, development of several spectroscopies has allowed characterisation of key reaction intermediates in PEC water splitting.

Since 2017, the application of semiconductor photoelectrochemistry to synthetic problems has gained traction, and several examples of selective organic transformations now exist. From these examples, it is clear that bismuth vanadate ($BiVO_4$) holds promise as a visible-light absorbing semiconductor (E_g = 2.4 eV) for these applications.

Oxidative decarboxylation reactions represent a class of transformations with a) synthetic utility in the formation of C-C and C-X bonds and b) thorough application and study under electrochemical conditions. These criteria, combined with a lack of photoelectrochemical examples, makes for an interesting model reaction for analysis and optimisation of a PEC synthetic system.

As synthetic photoelectrochemistry is in its relative infancy, a lack of in-depth characterisation of these systems is apparent. Therefore, systematic studies of a PEC synthetic system should be carried out to elucidate the key parameters affecting product selectivity, photocatalyst performance and material stability. Deploying techniques commonly seen in analysis of PEC water splitting could enable further mechanistic insights, and potentially inform on key kinetic bottlenecks. Understanding and remediation of these issues could help develop the application of powdered semiconductor photocatalysts to organic synthesis problems.

1.6 Aims

The principal goals of this work are to develop a photoelectrochemical system for oxidative decarboxylation reactions at bismuth vanadate photoelectrodes. These reactions represent an interesting route to the synthesis of new C-C bonds and extensive studies of these reactions at metallic electrodes have been carried out. However, very few photoelectrochemical examples of this reaction exist, only utilising simple carboxylic acids and non-visible-light absorbing materials. Previous photoelectrochemical examples also yielded dimerised products in very low selectivity, therefore a key aim will be to maximise the selectivity for C-C coupled product. A thorough analysis of factors affecting product selectivity will be considered and optimisation of the system carried out. Key similarities and differences between these reactions at metallic and semiconducting electrodes will be identified.

Initially, synthesis of bismuth vanadate photoelectrodes will be carried out to optimise photoelectrode performance for oxidation of carboxylic acid electrolytes. Ideally, photocurrents surpassing 1 mA cm^{-2} will be generated under illumination at reasonable anodic potentials. Electrodes will be prepared using electrostatic spray pyrolysis and key deposition parameters such as solvent system, temperature and deposition rate will be adjusted. The effects on structure and performance of varying deposition conditions will be characterised to understand aspects of the structure-function relationship of bismuth vanadate photoelectrodes. Photoelectrodes will be structurally characterised by typical methods

including electron microscopy (EM), X-ray diffraction (XRD) and X-ray photoelectron spectroscopy (XPS) to determine structure-function relationships and explain PEC behaviour.

After optimisation of the photoelectrode synthesis, photoelectrochemical Kolbe reactions of phenylacetic acid will be carried out and optimised to determine key factors defining product selectivity and reaction rate. Variables such as electrolytic cell set-up, light source, applied potential and substrate concentrations will be adjusted. These parameters are known to affect electro- and photochemical reactions independently, however their impact on the activity and selectivity of photoelectrochemical reactions is poorly understood or not considered. Additionally, substrate effects of substitution on the aryl ring and varying the chain length between the phenyl and carboxylate moieties will be investigated to elucidate mechanistic information. The effect of aryl substitution on PEC performance will be analysed by Hammett style plots to investigate electronic effects of the substituents.

Operando characterisation of the photoelectrochemical system will be carried out using EIS with the goal of determining key mechanistic processes within the semiconductor. As charge carrier behaviours are strongly influenced by the semiconductor liquid junction, the effects of applied potential and electrolyte concentration on the surface capacitance and charge transfer resistance may give insight into the kinetic bottlenecks of the photoelectrochemical Kolbe reaction.

Studies of electrode stability after electrolysis of phenylacetic acid solutions will also be carried out to determine the recyclability of photoelectrodes. $BiVO_4$ photoelectrodes are known to undergo photocorrosion during water oxidation reactions, therefore the study of these materials in non-aqueous media may result in marked changes to the material stability under applied potential and illumination. Structural and compositional changes will be analysed through electron microscopy and XPS to determine major loss mechanisms that affect PEC performance.

2. Fabrication of Bismuth Vanadate Photoelectrodes using Electrostatic Spray Pyrolysis

2.1 Introduction

Preparation of crystalline thin films for photoelectrochemical applications can be achieved through methods such as hydrothermal deposition, spin-coating, vapour deposition and spray pyrolysis.[92, 93, 149-151] Vapour deposition techniques, such as pulsed laser deposition (PLD) and chemical vapour deposition (CVD), typically require specialised equipment, high processing temperatures and gaseous precursors that can prove difficult to handle. Hydrothermal and spin-coating methods do not require such specialist equipment, however these techniques typically yield unreliable and/or irreproducible electrodes.[152, 153] Spray pyrolysis methods offer both cost-effectiveness as well as close control over film growth, and have been shown to produce high-quality and reproducible metal oxide films.[154-156] Typically, metal precursor solutions are deposited onto heated, conductive glass substrates (fluorine-doped tin oxide, FTO, or indium tin oxide, ITO), with oxidation to form the metal oxide achieved through thermal reaction with atmospheric oxygen often in a separate calcination processing step.[157]

Spray pyrolysis methods are categorised based on the source of precursor atomisation – ultrasonic, thermal/flame, and electrostatic.[157-160] Electrostatic spray pyrolysis relies on the application of a high potential to a metal capillary to efficiently disperse a flowing solution. In all cases, film thickness can often be controlled through parameters such as precursor concentration, nozzle-substrate distance and deposition time. Choice between ultrasonic and thermal atomisation comes from the vapour pressure of solvents used, with ultrasonic atomisation limited to volatile solvents such as acetone, alcohols, etc. Electrostatic spray pyrolysis (electrospray deposition), however, can be used with most solvents as the applied voltage can be tuned to overcome the surface tension and dielectric of the solvent.[161] Voltages greater than 2 kV are typically necessary to overcome the Rayleigh limit, Q_R - the charge required to overcome the surface tension of the solvent and cause droplet fission (Equation 1):

$$Q_R = 2\pi(16\sigma_l\varepsilon_0 r^3)^{0.5} \qquad \text{Equation 1}$$

where σ_l is the liquid surface tension, ε_0 is the dielectric permittivity of free space and r is the droplet radius.[158] The charged droplets disperse homogeneously as they are sprayed onto the substrate due to mutual Coulombic repulsion. Formation of droplets with

nanometre scale diameter is common when using electrospray deposition and thus nanoscale metal oxide particles are deposited onto the substrate.[162] The deposition of smaller particles, homogeneously distributed across the substrate should result in uniform films with large active surface areas.

The homogeneity of the deposited film depends heavily upon the spraying mode generated from the nozzle. Figure 2.1 shows the different types of spray mode when using electrospray deposition. Dripping modes are typically associated with an excessive flow rate or an insufficient applied voltage as the Rayleigh limit has not been exceeded. If the applied voltage is too excessive then multi-jet modes are obtained, or the cone-jet can precess about the nozzle. Formation of a cone-jet spray is desired as there is no oscillation or rotary motion and droplet fission is consistent. As well as altering flow rate and applied potential, it is possible to influence the spraying mode by adjusting solution conductivity and nozzle dimensions.

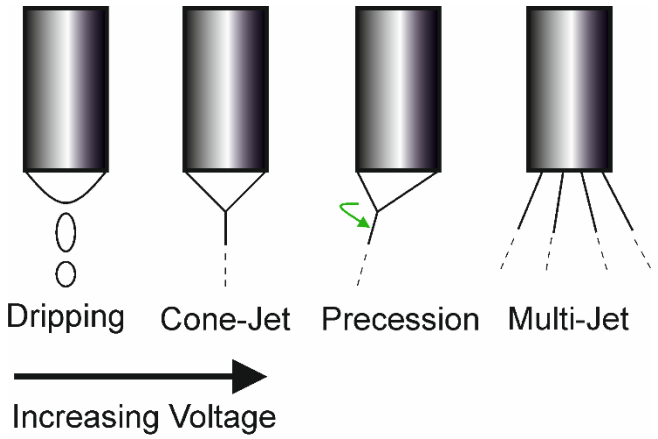

Figure 2.1: Spraying modes of electrostatic spray pyrolysis with increasing applied potential. The green arrow indicates rotation of the cone-jet mode about the normal to the nozzle.[158, 161]

Electrostatic spray pyrolysis has been utilised for electrode preparation previously, mainly for lithium-ion batteries and silicon solar cells, including metal oxide films.[163-167]

$BiVO_4$ photoelectrodes have been previously prepared by electrospray deposition from bismuth chloride ($BiCl_3$) and vanadyl acetylacetonate ($VO(acac)_2$) precursor solutions, combined *in situ* prior to spraying.[155] Film morphology and crystallinity were examined as a function of deposition temperature between 200 and 500 °C. Below 400 °C, pure monoclinic bismuth vanadate was synthesised, with higher temperature deposition yielding some tetragonal crystal phase. The as-synthesised thin films were then used as

photoanodes in the oxygen evolution reaction. The electrode deposited at 400 °C showed the highest photocurrent density of 0.5 mA cm^{-2} at 1.23 V_{RHE}, with films deposited at 200 and 300 °C giving negligible photocurrents. The difference in photocurrent densities was attributed to the compact nature of the film deposited at 400 °C compared to those deposited at lower temperatures. The compact films facilitated charge carrier separation by reducing the path length for electrons to reach the FTO substrate and holes to migrate to the surface. For electrodes prepared at 500 °C, poorer OER performance was rationalised by the presence of the tetragonal $BiVO_4$ phase in combination with the sintering of large nanoparticle clusters.

In addition to the deposition of metal precursors at high temperature, it is possible to spray metal oxide nanoparticles directly by forming a stable suspension in solution.[162, 168] The stability of the suspension is critical in achieving efficient deposition, as the concentration of nanoparticles must remain consistent throughout the deposition and sedimentation can lead to blockages in tubing. To prevent particle sedimentation and stabilise the suspension, it is common to use surfactant additives such as Triton X-100, which are often removed by combustion during processing of films.[168] The deposition of pre-prepared nanoparticles allows more thorough characterisation of the photoactive material by methods such as N_2 adsorption prior to deposition.

Due to the close control of deposition conditions and the flexibility to use both precursors and pre-prepared nanoparticles, electrospray deposition presents an attractive method for the general preparation of metal oxide photoelectrodes.

2.1.1 Aims

The main goals of this work were to develop electrostatic spray pyrolysis apparatus and methodology for the preparation of highly active and reproducible $BiVO_4$ photoelectrodes. These photoelectrodes were benchmarked using photoelectrochemical oxidation of phenylacetic acid (PAA) solutions. Optimisation of deposition parameters such as solvent system, deposition temperature and electrode precursors (pre-prepared nanoparticles or bismuth and vanadium precursor complexes) was carried out to maximise oxidative photocurrents as measured by linear sweep voltammetry (LSV).

Composition, structure, and spectroscopic characterisation of prepared $BiVO_4$ photoelectrodes was used to elucidate structure-function relationships and understand the underlying factors affecting their photoelectrochemical performance.

2.2 Electrospray Deposition of Bismuth Vanadate Photoelectrodes

2.2.1 Preparation and Electrospray Deposition of Pre-prepared Bismuth Vanadate Nanoparticles

The electrospray deposition of pre-prepared $BiVO_4$ nanoparticles with known photocatalytic activity was chosen as an initial route to highly active $BiVO_4$ photoelectrodes. Bismuth vanadate nanoparticles were synthesised hydrothermally according to a literature procedure, with bismuth (III) ions stabilised by ethylenediamine tetraacetic acid (EDTA) in solution (Scheme 2.1).[169] The surface area of the particles was measured as 11.7 $m^2\ g^{-1}$ by nitrogen porosimetry, comparable to the surface area of 10.4 $m^2\ g^{-1}$ obtained by Sun et al. (Figure 2.3).[169] This surface area was low when compared to other examples of bismuth vanadate photoelectrodes, with electrodeposition methods potentially yielding a surface area of 31.8 $m^2\ g^{-1}$.[170]

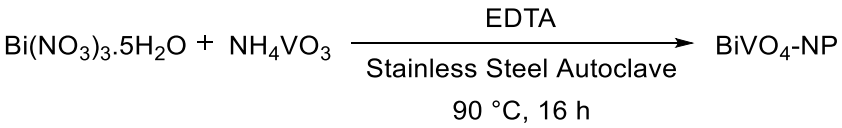

Scheme 2.1: Hydrothermal synthesis of bismuth vanadate nanoparticles.

Synthesis of crystalline monoclinic bismuth vanadate (JCPDS 14-0688) was confirmed by powder X-ray diffraction (pXRD), with all diffraction peaks consistent with the calculated pattern (Figure 2.2).

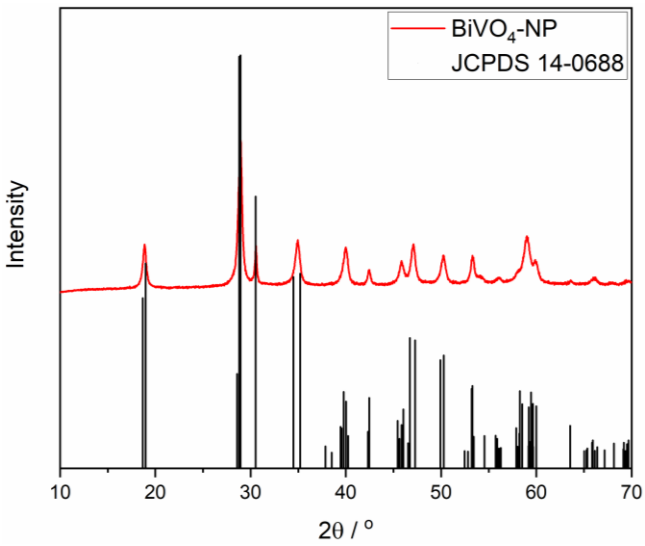

Figure 2.2: Powder X-ray diffractogram of hydrothermally-synthesised $BiVO_4$ nanoparticles (BiVO4-NP, red) prior to electrospray deposition. The diffractogram is referenced to calculated peaks for monoclinic $BiVO_4$ (JCPDS 14-0688, black).

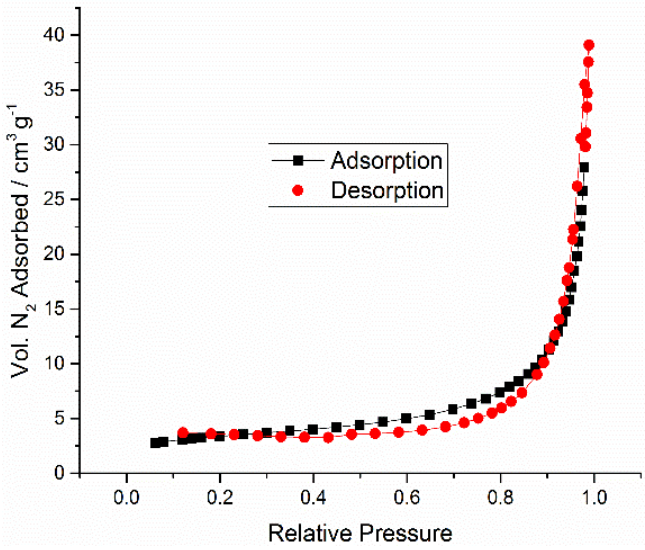

Figure 2.3: Nitrogen porosimetry of $BiVO_4$ nanoparticles before electrospray deposition onto FTO substrates.

SEM images of the prepared nanoparticles showed a range of crystallite sizes between 50 nm – 1 µm (Figure 2.4). Due to the variation in particle size, dispersion in solution was expected to vary and sedimentation of larger crystallites was likely.

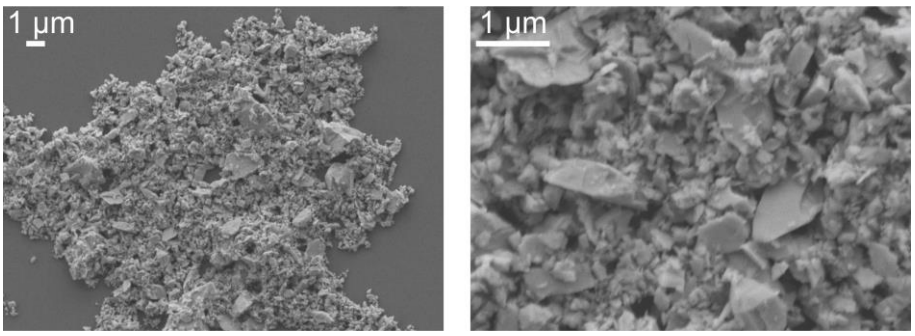

Figure 2.4: SEM images of $BiVO_4$ nanoparticles before electrospray deposition onto FTO. Images were taken at an acceleration voltage of 5 kV.

To assess the light absorption characteristics of $BiVO_4$ nanoparticles and estimate the band gap, a UV-vis diffuse reflectance spectrum (DRUVS) of the $BiVO_4$ powder was recorded (Figure 2.5).

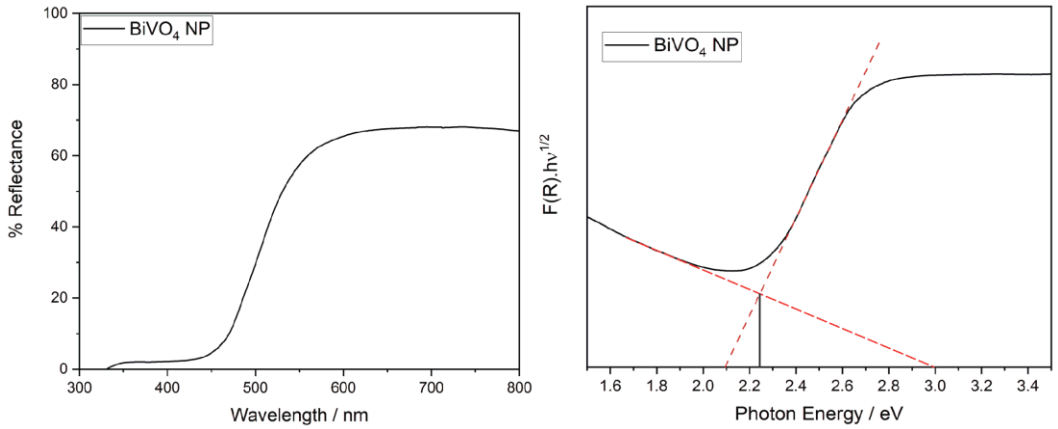

Figure 2.5: Diffuse reflectance UV-vis spectrum (left) of hydrothermally synthesised bismuth vanadate nanoparticles and corresponding Tauc plot (right) giving an estimated band gap of 2.23 eV.

Using the Tauc plot shown in Figure 2.5, the band gap of hydrothermally synthesised $BiVO_4$ nanoparticles was estimated at 2.23 eV. When compared to literature band gaps for bismuth vanadate (around 2.4 eV), this band gap value seems low, however Tauc plots only offer an approximation of the band gap due to the somewhat arbitrary nature of drawing the tangent and possible light scattering affecting reflectance measurements.[150, 169]

Once prepared and characterised, $BiVO_4$ nanoparticles were suspended in a 9:1 mixture of isopropanol:dimethyl sulfoxide (DMSO) at a concentration of 10 mg mL^{-1}. Suspensions were stable for up to 1 hour, after which some sedimentation of larger

crystallites was observed. As deposition was carried out over 30 minutes, it was likely that larger crystallites sedimented within the apparatus and therefore most deposited material consisted of smaller particles that were more stable in suspension. The suspension of particles was then deposited onto FTO glass held at 140 °C using electrospray deposition ().

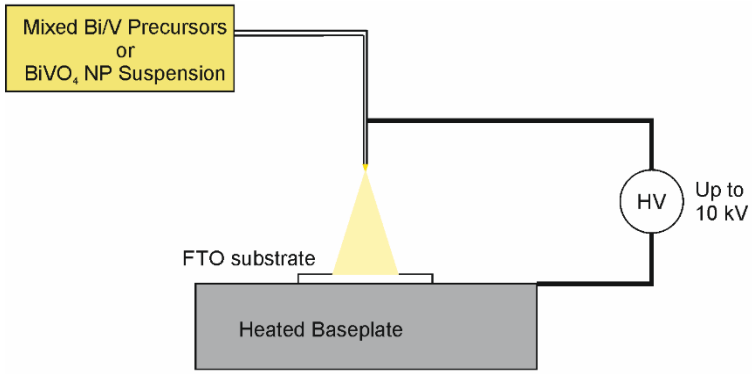

Figure 2.6: Schematic of the 1-injector electrospray apparatus used for the deposition of $BiVO_4$ nanoparticle suspensions and pre-mixed bismuth and vanadium precursors.

Initially, a flat, metal syringe needle was employed as a deposition nozzle (i.d. = 0.8 mm), however during deposition the surface tension of the iPrOH:DMSO mixture resulted in droplet formation on the side of the nozzle and an asymmetry in the cone-jet spraying mode (Figure 2.7b). To prevent the droplet forming unevenly on the nozzle, a rounded glass bead was attached to the nozzle outlet to break the surface tension of the suspension (Figure 2.7c).

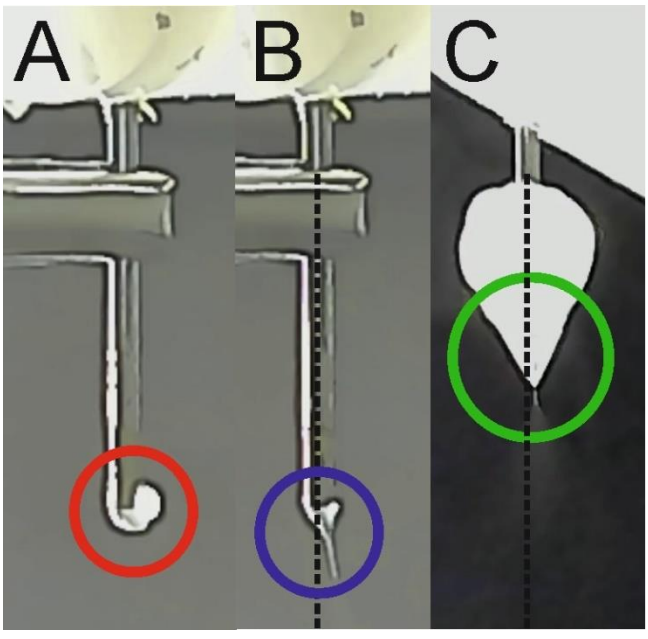

Figure 2.7: a) Asymmetric droplet formation of $BiVO_4$ nanoparticle suspensions in 9:1 iPrOH:DMSO caused by surface tension (red) and b) the resulting asymmetric cone-jet spraying mode (blue). c) a more symmetrical cone-jet mode after implementation of a glass bead at the end of the spraying nozzle. The normal to the nozzle is given by the black, dashed line.

The suspension flow rate was maintained at 0.01 mL min^{-1} and a voltage of 8.5 kV was applied between the nozzle and baseplate. The particle deposition was carried out for 30 minutes resulting in an opaque yellow film. After deposition, bismuth vanadate nanoparticle electrodes ($BiVO_4$-NP) were calcined at 450 °C for 2 hours to improve adhesion to the FTO substrate and remove organic ligands and impurities.

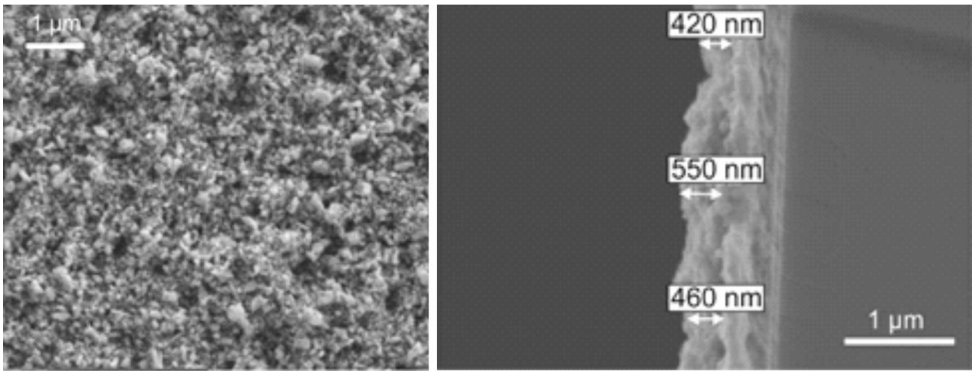

Figure 2.8: Plane (left) and cross-section (right) SEM images of $BiVO_4$ nanoparticles after deposition onto FTO.

SEM images of the particles after deposition showed no significant change of morphology after deposition, however only particles 70 nm or smaller were observed (Figure 2.8). This suggested that sedimentation of larger particulates occurred. Smaller crystallites are preferred due to increased surface-to-volume ratios and improved charge carrier extraction to the surface of the particles.[169] As-prepared $BiVO_4$ films were approximately 450 nm thick, although this varied across the electrode possibly due to areas of greater deposition caused by inhomogeneous distribution of particles in the cone-jet. This was undesirable as inhomogeneity of film thickness would have led to variable catalytic properties due to variable photon absorption and recombination rates due to the short hole diffusion lengths (~70 nm) within $BiVO_4$.[171]

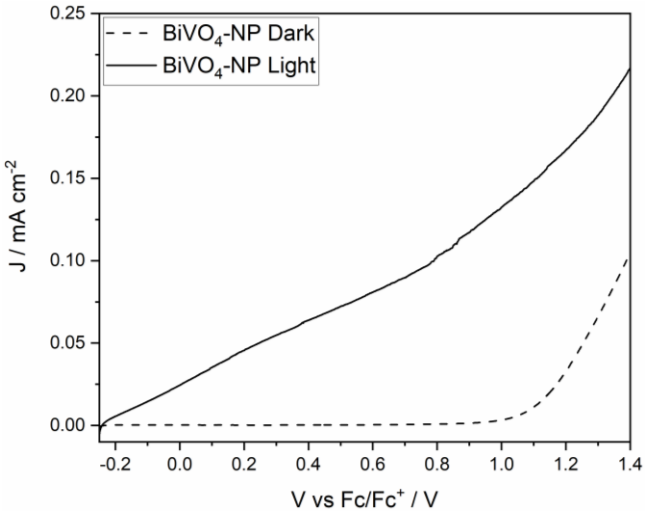

Figure 2.9: Linear sweep voltammograms of $BiVO_4$-NP electrodes prepared by electrospray deposition. Voltammograms were recorded in 1 M phenylacetic acid solutions in acetonitrile with 0.05 equiv triethylamine. Voltammograms were recorded under AM1.5G illumination (100 mW cm^{-2}, solid) and in the dark (dashed).

To assess the photocatalytic properties of $BiVO_4$-NP electrodes, linear sweep voltammograms (LSV) were recorded in 1 M phenylacetic acid solutions in acetonitrile that were partially neutralised with 0.05 equiv triethylamine, forming a non-innocent electrolyte of phenylacetate and protonated triethylammonium ions and reduced solution resistance (Figure 2.9). Electrodes were tested electrochemically in the dark and under illumination by an AM1.5G solar-simulated light source (100 mW cm^{-2}).

As shown in Figure 2.9, the dark electrochemical oxidation of phenylacetate anions occurred at potentials greater than 1.0 V vs Fc/Fc^+. On illumination, the current onset shifted cathodically to ~-0.2 V vs Fc/Fc^+. Photocurrent density increased linearly with applied potential, implying ohmic electrode behaviour. The ohmic nature of the voltammogram suggested that photocurrent was not limited by the availability of photogenerated charge carriers within $BiVO_4$, under which a plateau in photocurrent is typically observed. In addition, $BiVO_4$-NP electrodes showed rather poor photocatalytic activity for the Kolbe reaction, with low photocurrents at all potentials (Figure 2.9). The low, ohmic photocurrent was possibly due to a poor electrical contact at the FTO/$BiVO_4$ interface, therefore direct growth of $BiVO_4$ on the FTO substrate was chosen as a route to higher performance photoelectrodes.

2.2.2 Electrospray Deposition of Bismuth and Vanadium Precursors

To improve the electrical contact between FTO and $BiVO_4$, electrodes were also prepared from the electrostatic spray pyrolysis of bismuth and vanadium precursors onto a heated FTO glass substrate (Scheme 2.2).

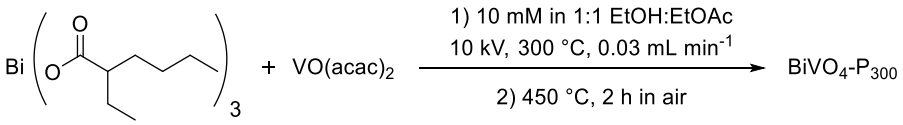

Scheme 2.2: Electrospray deposition of bismuth 2-ethylhexanoate and vanadyl acetylacetonate ($VO(acac)_2$) precursors for the preparation of $BiVO_4$ photoelectrodes.

Solutions of bismuth 2-ethylhexanoate and vanadyl acetylacetonate were combined and deposited by electrospray deposition onto FTO substrates held at 300 °C. Deposition was carried out for 1 hour at a flow rate of 0.02 mL min^{-1}, resulting in a black film that was subsequently annealed at 450 °C for 2 hours to yield the final yellow electrodes ($BiVO_4$-P_{300}).

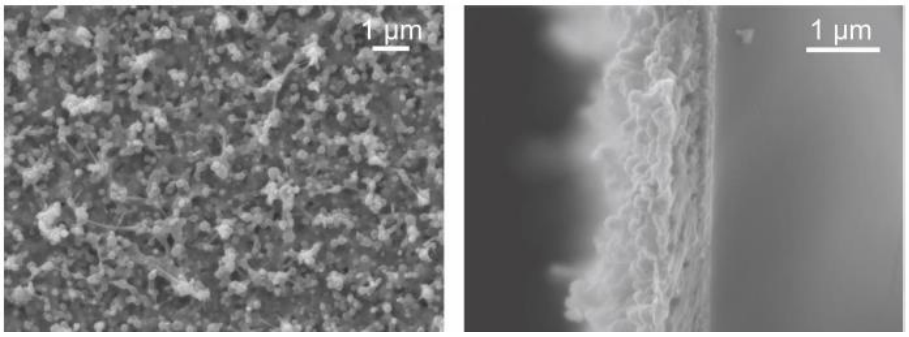

Figure 2.10: Plane (left) and cross-section (right) SEM images of $BiVO_4$ photoelectrodes prepared from the deposition of bismuth 2-ethylhexanoate and vanadyl acetylacetonate at 300 °C.

SEM images of electrodes showed crystallites around 100 nm in diameter as well as long, needle-like particles (Figure 2.10). The X-ray diffractogram shows clear peaks for monoclinic bismuth vanadate, consistent with the powder prepared hydrothermally (Figure 2.11). Peaks corresponding to the FTO substrate were also visible in the diffractogram,

which could indicate poor homogeneity of the film and exposure of the substrate (Figure 2.11). In comparison to hydrothermally synthesised powders, peaks in the diffractogram were significantly broader, owing to either poor crystallinity, instrumental broadening, or smaller average crystallite diameter.

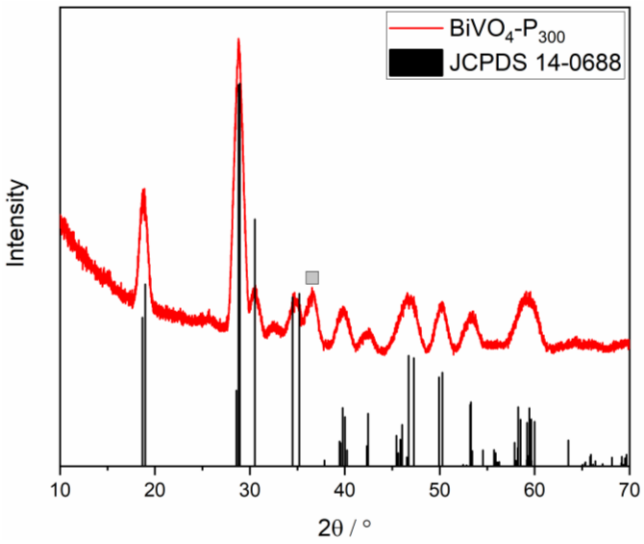

Figure 2.11: GI-XRD of a $BiVO_4$ photoelectrode prepared from the electrospray deposition of bismuth 2-ethylhexanoate and vanadyl acetylacetonate at 300 °C. Peaks are referenced to calculated diffraction peaks of monoclinic $BiVO_4$ (JCPDS 14-0688). Peaks arising from underlying FTO are denoted by the grey squares.

For precursor electrodes, above -0.5 V vs Fc/Fc^+ an oxidative current that is unaffected by illumination was observed (Figure 2.12). This suggested an oxidative process inherent to the electrode, as this feature was not observed when using electrodes prepared by deposition of nanoparticles. The observed current may have been due to oxidation of residual V^{4+} centres in bismuth vanadate by photogenerated holes, limiting photocurrent through increased recombination rate. Alternatively, it was possible that residual organic species from deposition were oxidised.

For precursor electrodes, above 0.0 V vs Fc/Fc^+ the oxidative current observed in the dark decayed to almost 0 mA cm^{-2}, indicating no oxidation of phenylacetic acid without illumination. Under illumination, a significant photocurrent density was observed, reaching approximately 0.6 mA cm^{-2} before dark oxidation of phenylacetic acid became prevalent at 0.9 V vs Fc/Fc^+. Although photocurrent densities were significantly larger than for the films made from nanoparticles, ohmic behaviour was also observed for $BiVO_4$-P_{300} electrodes. A poor electrical contact at the FTO-$BiVO_4$ interface could also have accounted for the

electrochemical behaviour of $BiVO_4$-P_{300} electrodes as low temperature deposition may leave residual organic matter at the FTO/$BiVO_4$ interface, reducing conductivity. The discrepancy in photocurrent density between the two electrodes may also have been explained by improved charge transport within the $BiVO_4$ electrode. Although many grain boundaries would have been present between individual crystallites in $BiVO_4$-NP electrodes, it has been suggested that interfacial states actually act to improve carrier lifetime and electrode activity.[172, 173] Discrepancy between precursor and nanoparticle electrode performance was thus attributed to improved conductivity at the FTO/$BiVO_4$ interface and possibly a more photoelectrochemically active surface structure.

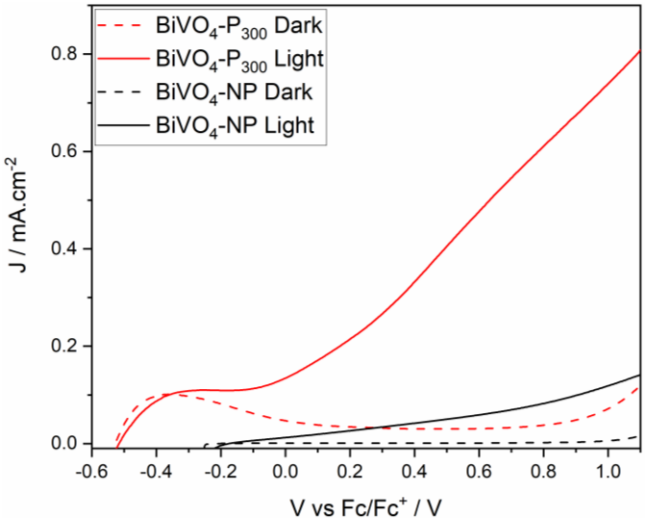

Figure 2.12: Linear sweep voltammograms of $BiVO_4$-NP (black) and $BiVO_4$-P_{300} (red) photoelectrodes. Voltammograms were recorded in 1 M phenylacetic acid solutions partially neutralised by addition of 0.05 equiv Et_3N in acetonitrile under AM1.5G illumination (solid) and in the dark (dashed).

2.2.3 High Temperature Electrospray Deposition of Bismuth and Vanadium Precursors

As residual organic matter may have been contributing to poor photoelectrode performance, electrospray pyrolysis of bismuth vanadate was conducted at 450 °C to burn off any carbonaceous material, as has been demonstrated with other spray pyrolysis methods.[155] The electrostatic spray pyrolysis set up was adapted to allow high temperature

deposition of materials by extending the length of the metal nozzle to increase distance between the heated baseplate and plastic components. After deposition, electrodes prepared at 450 °C ($BiVO_4$-P_{450}) were yellow in colour, as opposed to the black colour observed for deposition at 300 °C prior to annealing.

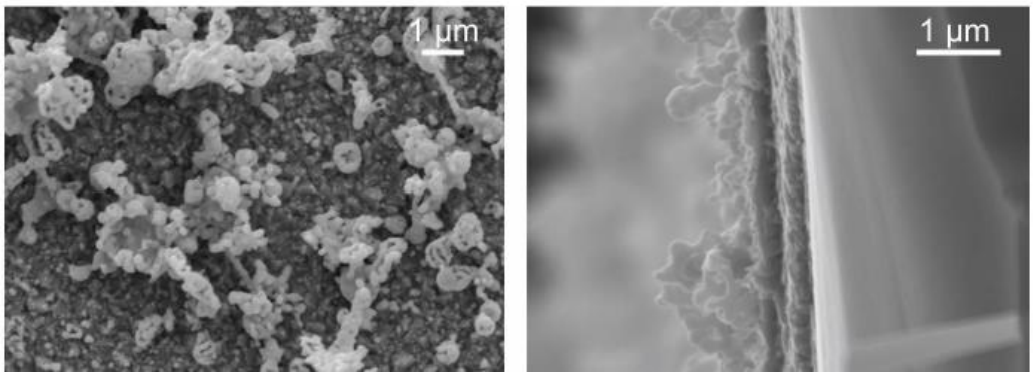

Figure 2.13: Surface (left) and cross-section (right) SEM images of $BiVO_4$ photoelectrodes prepared from precursor deposition at 450 °C.

SEM images of electrodes prepared at 450 °C showed significant structural changes compared to lower temperature deposition (Figure 2.13). Large, hierarchical structures were formed at higher temperature, with poorer surface coverage resulting in exposure of the underlying FTO substrate in some regions (Figure 2.14). These changes could have been caused by more rapid solvent loss or evaporation of volatile bismuth precursors from the surface; the latter has been shown to affect synthesis of ferroelectric materials such as $SrBi_2Ta_2O_9$.[174]

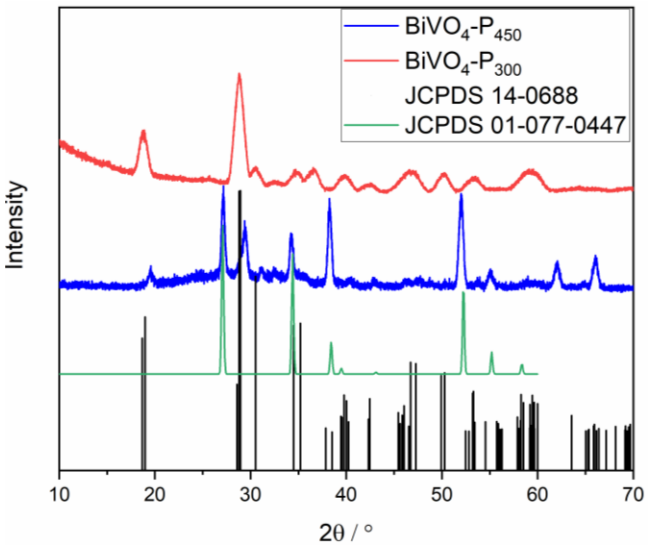

Figure 2.14: GI-XRD comparison of $BiVO_4$-P_{450} (blue) and BiVO4-P_{300} (red) photoelectrodes prepared by electrospray deposition of bismuth 2-ethylhexanoate and $VO(acac)_2$. All peaks are referenced to calculated diffraction peaks for monoclinic $BiVO_4$ (black, JCPDS 14-0688) and cassiterite SnO_2 (green, JCPDS 01-077-0447).

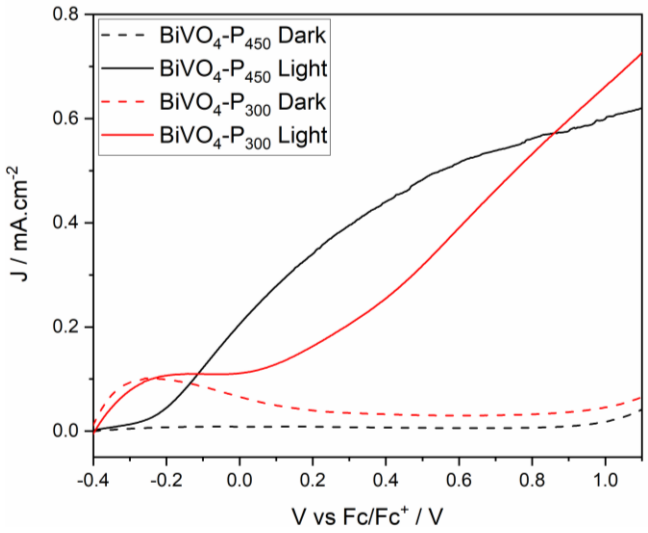

Figure 2.15: Linear sweep voltammograms of $BiVO_4$ photoelectrodes prepared from precursor deposition at 300 °C ($BiVO_4$-P_{300}, blue) and 450 °C ($BiVO_4$-P_{450}, red). Voltammograms were recorded under AM1.G illumination (solid) and in the dark (dashed) in 1 M PAA solutions partially neutralised with 0.05 equiv Et_3N in MeCN.

For electrodes prepared at 450 °C, the oxidative current around -0.5 V vs Fc/Fc^+ was no longer observed (Figure 2.15). This was attributed to complete removal of organic material from electrode interfaces at higher deposition temperatures. The material colour

change from black to yellow with increasing temperature may have been consistent with the removal of organic material during deposition and more rapid formation of $BiVO_4$.

During deposition, it was observed that the combined solution of bismuth 2-ethylhexanoate and $VO(acac)_2$ began to precipitate after approximately 30 minutes. This was attributed to spontaneous formation of a mixed bismuth-vanadium oxide over time as both bismuth 2-ethylhexanoate and $VO(acac)_2$ were stable in solution for at least 12 hours. Uncontrolled precipitation of mixed bismuth vanadium oxides may have been the source of large clusters and variable particle morphology observed in SEM images of electrodes from the same batch ($BiVO_4$-P_{450}-A and B) in Figure 2.16. Electrode $BiVO_4$-P_{450}-A showed large porous clusters present on the electrode surface, compared with the large spherical particles observed on $BiVO_4$-P_{450}-B which may have explained the significant change in electrochemical performance between the two electrodes (Figure 2.17). Additionally, as shown by the increased dark current observed for $BiVO_4$-P_{450}-B, irreproducible substrate coverage of $BiVO_4$ and exposure of the underlying FTO were responsible for variable electrode performance.

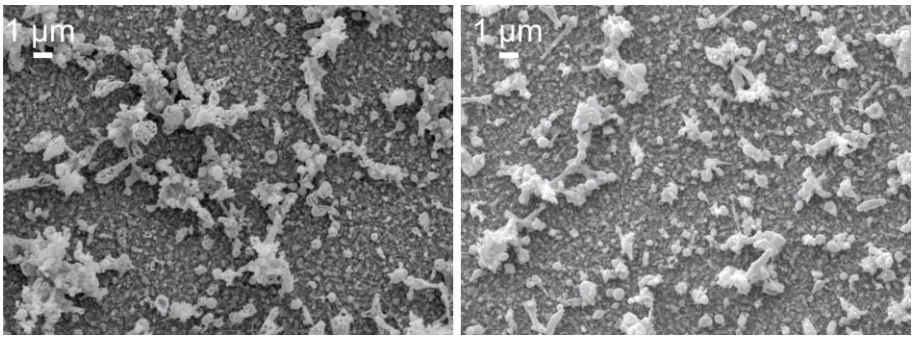

Figure 2.16: Plane SEM images of $BiVO_4$-P_{450}-A (left) and $BiVO_4$-P_{450}-B (right) electrode surfaces showing variation in cluster morphology.

LSV measurements showed significant changes to both photocurrent and dark current between electrodes despite identical deposition conditions, with $BiVO_4$-P_{450}-B showing overall ohmic behaviour and P_{450}-A showing a typical photoelectrode response (Figure 2.17). This suggested the photocatalytic performance depended heavily on the structure and morphology of clusters instead of the thin, compact $BiVO_4$ film. The surface clusters were most likely deposited from precipitates formed before cone-jet spray from the nozzle of the apparatus. The dependence of electrochemical performance on surface

clusters was a contributor to the poor reproducibility, therefore minimising precipitation before the electrospray nozzle was key to producing reproducible $BiVO_4$ electrodes.

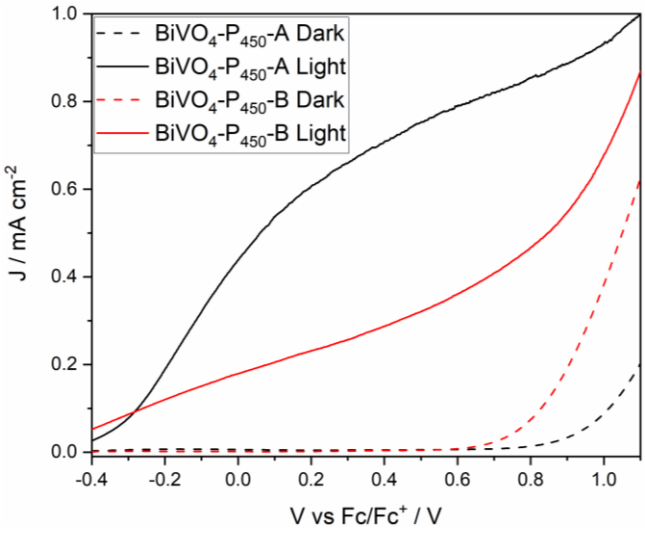

Figure 2.17: LSV comparison of electrodes prepared from 1-injector electrospray deposition of bismuth 2-ethylhexanoate and vanadyl acetylacetonate at 450 °C. LSVs were recorded in 1 M PAA solutions neutralised with 0.05 equiv Et_3N under AM1.5G illumination (solid) and in the dark (dashed).

2.2.4 2-Injector Electrospray Deposition of Bismuth Vanadate Electrodes from Precursors in 1:1 EtOAc:iPrOH

To prevent premature precipitation of $BiVO_4$ and improve reproducibility, the electrospray set up was modified to have separate injections for Bi and V precursors. Separate injection of precursors and mixing of solutions close to the nozzle was used as a method of trying to reduce precipitation before deposition. A diagram of the electrospray apparatus used is given in .

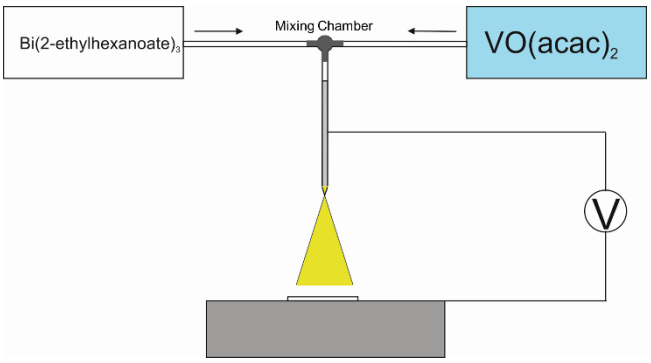

Figure 2.18: Schematic of the 2-injector electrospray apparatus used for the deposition of bismuth 2-ethylhexanoate and vanadyl acetylacetonate.

The mixing chamber was 3D printed with a 1/16th in. inner diameter to increase solution turbulence and promote mixing of the two solutions. Ethanol (EtOH) was unusable as a solvent due to degradation of the 3D printing resin over time. As a replacement for EtOH, isopropanol (iPrOH) was used to dissolve $VO(acac)_2$. $BiVO_4$ electrodes prepared by electrospray of precursors in EtOAc:iPrOH mixtures (IPA-TEMP-TIME) were deposited onto FTO held at 450 °C with deposition time and flow rate varied to vary film thickness and morphology (Table 2.1). The applied voltage was kept at 7.5 kV to maintain a consistently stable cone-jet spray.

Table 2.1: Deposition parameters for the preparation of $BiVO_4$ photoelectrodes using a 2-injection electrospray setup.

Sample	Deposition Time / min	Flow Rate / mL min^{-1}	Applied Voltage / kV
IPA-450-60	60	0.015	7.5
IPA-450-90	90	0.015	7.5
IPA-450-120	120	0.015	7.5
IPA-450-30	30	0.03	7.5
IPA-450-45	45	0.03	7.5
IPA-450-18	18	0.05	7.5
IPA-450-27	27	0.05	7.5
IPA-450-36	36	0.05	7.5

SEM images of electrodes deposited at a flow rate of 0.015 mL min^{-1} showed large clusters of $BiVO_4$, similar to the single injector deposition of precursors (Figure 2.19). As deposition time was increased, the density of large clusters increases, with no significant change in the underlying $BiVO_4$ film. This suggests a short initial period where a compact

$BiVO_4$ layer is deposited before clusters form. It was possible that the clusters were formed from insoluble $VO(acac)_2$ particulates due to poor solubility in iPrOH. During deposition, sedimentation of material in the mixing chamber was again observed which may result from insoluble $VO(acac)_2$ particulates and contribute to poor reproducibility and the cluster structures observed.

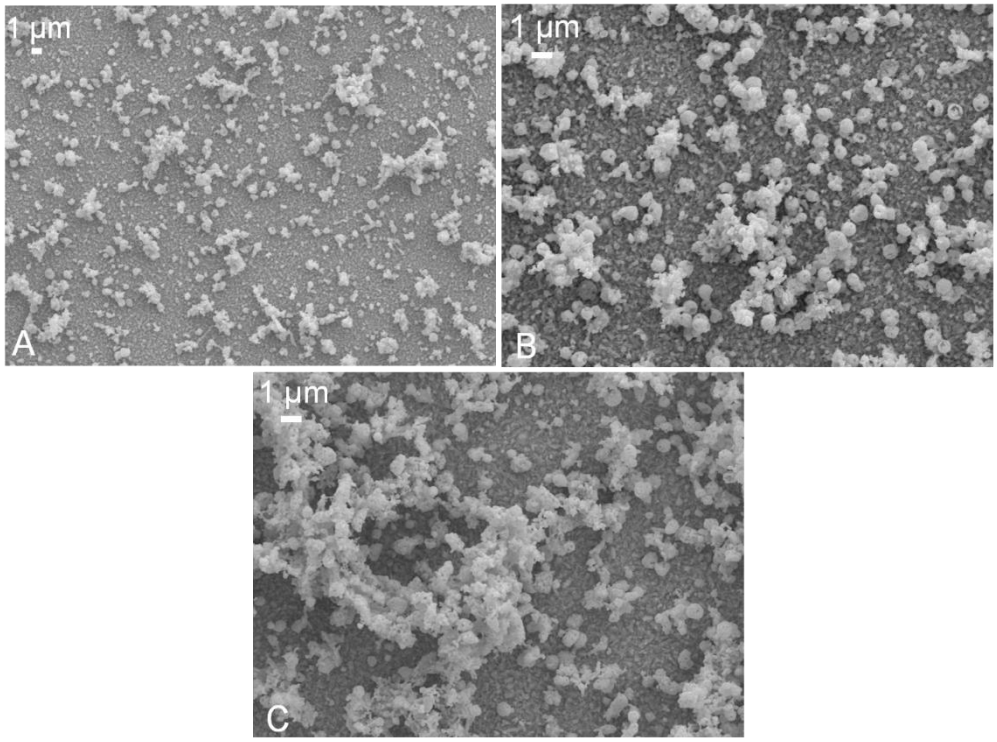

Figure 2.19: SEM images of a) IPA-450-60, b) IPA-450-90 and c) IPA-450-120 electrode surfaces. Images were taken at an acceleration voltage of 10 kV and a working distance of 10 mm.

When tested as photoelectrodes by LSV, IPA-450-60, IPA-450-90 and IPA-450-120 showed overall ohmic behaviour under illumination (Figure 2.20). Without illumination of the electrode, a significant oxidative current was observed around 0.4 V vs Fc/Fc^+. This feature was attributed to the oxidation of residual V^{4+} in the electrode material, resulting from the deposition of insoluble vanadyl clusters or from poor mixing of Bi and V precursor solutions (Table 2.2).

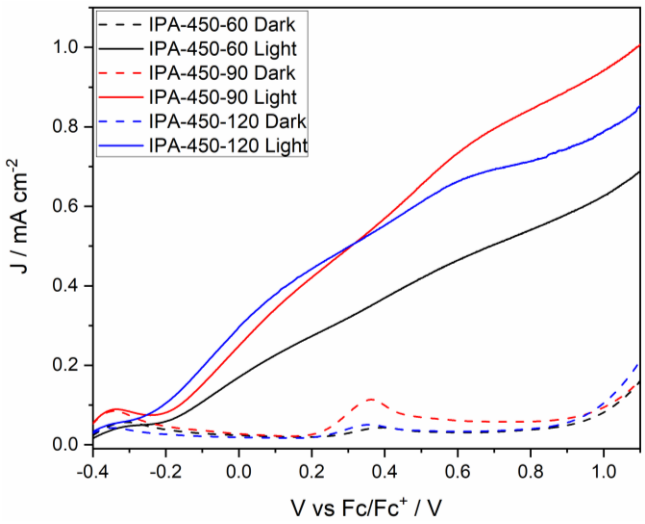

Figure 2.20: LSV of $BiVO_4$ photoelectrodes IPA-450-60 (black), IPA-450-90 (red) and IPA-450-120 (blue) under AM1.5G illumination (solid) and in the dark (dashed). Voltammograms were recorded in 1 M PAA solutions that were partially neutralised with 0.05 equiv Et_3N.

Two features were observed in the voltammograms under illumination, with small peaks at 0.1 and 0.6 V vs Fc/Fc^+. The overall ohmic behaviour suggested that the oxidative current was again not limited by surface hole concentration, most likely due to inefficient charge carrier separation and migration in the photoelectrode. The initial feature may have corresponded to the oxidation of V^{4+} centres by photogenerated holes, which could account for the 200 mV cathodic potential shift from 0.4 V vs Fc/Fc^+ in the dark.

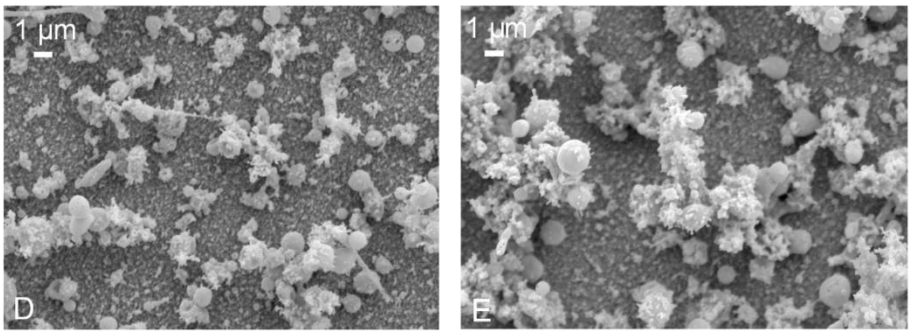

Figure 2.21: Surface SEM images of IPA-450-30 (left) and IPA-450-45 (right) $BiVO_4$ photoelectrodes. Images were taken at an acceleration voltage of 10 kV at a working distance of 10 mm.

For electrodes deposited at a flow rate of 0.03 mL min^{-1}, no significant changes in structure and morphology were observed with SEM, except for large spherical particles on the electrode surface (Figure 2.21). Similarly to deposition at low flow rate, the density of large clusters on the electrode surface increased with deposition time.

Although large cluster structures were observed on the electrode surface for samples IPA-450-30 and 450-45, the photoelectrochemical performance was significantly better (Figure 2.22). Photocurrent density at all potentials was much greater than for all other electrodes and the current-voltage relationship was more typical of a photoelectrochemical process suggesting the limting factor on photocurrent was the surface concentration of photogenerated holes.[175] As similar structural properties were observed between high and low performance electrodes, a second batch of electrodes IPA-450-30 and 450-45 were deposited.

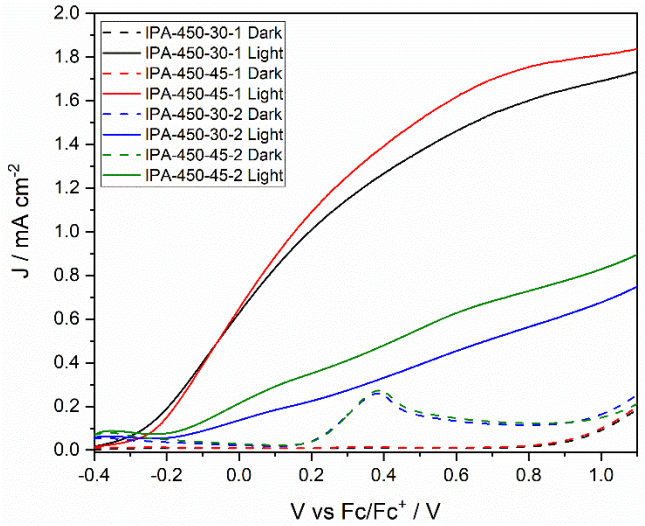

Figure 2.22: LSVs of $BiVO_4$ photoelectrodes IPA-450-30-1 (black) and IPA-450-45-1 (red) with electrodes prepared under the same depositions conditions, IPA-450-30-2 (blue) and IPA-450-45-2 (green). Voltammograms were recorded under AM1.5G illumination (solid) and in the dark (dashed).

As shown in Figure 2.22, the second batch of $BiVO_4$ electrodes deposited showed significantly poorer performance than the first. Additionally, under dark conditions, a large oxidative current peak was observed at ~0.4 V vs Fc/Fc^+ which was not observed in high performance electrodes. This peak was attributed to oxidation of residual V^{4+} resulting from deposition of insoluble $VO(acac)_2$ clusters (Table 2.2). As electrodes were illuminated over a 6 mm diameter circle, it was also possible that irreproducibility of PEC performance originated from variable activity at different points of the electrode surface. As shown in Figure 2.21, synthesised photoelectrodes comprise an inhomogeneous covering of large cluster structures. As the PEC performance was most likely dominated by the large clusters then it was rational that the PEC performance would be irreproducible when illuminating at different sites of the inhomogeneous film.

First, to ensure that electrode performance was independent of illumination area, three new electrodes were prepared using identical deposition conditions to IPA-450-30 and LSVs were recorded under 6 mm diameter and full electrode illumination (Figure 2.23).

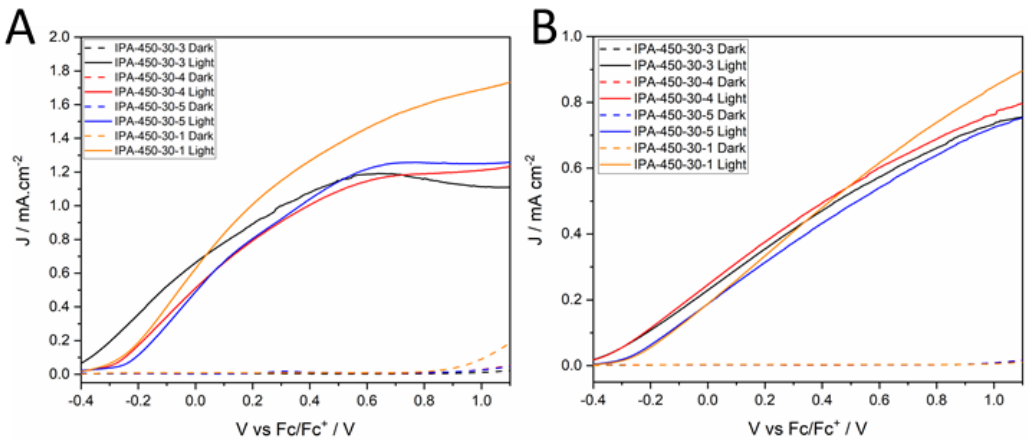

Figure 2.23: Linear sweep voltammograms of $BiVO_4$ photoelectrodes illuminated over a) a 6 mm diameter circle and b) the full electrode area (1.5 cm^2). All electrodes were prepared by electrospray deposition of bismuth 2-ethylhexanoate and $VO(acac)_2$ at 450 °C. Voltammograms were recorded under AM1.5G illumination (solid) and in the dark (dashed).

As shown in Figure 2.23, when illuminating across the whole electrode, much better reproducibility was observed in LSV measurements. The performance of the second batch of electrodes also matched very closely with the previous 'best performance' electrodes, IPA-450-30-1 – this was not seen when illuminating over a 6 mm diameter circle, which accounted for around 30% of the electrode area. Additionally, although current densities were much lower when illuminating the whole electrode, absolute photocurrents were greater, which was a much more accurate representation of the reaction rate during controlled potential experiments.

The poor reproducibility of electrodes when illuminating over a 6 mm diameter circle suggested that these electrodes had small regions with much greater photoelectrochemical activity than other regions of the same electrode. The variable performance of areas across similar electrodes was due to inhomogeneous distribution of $BiVO_4$ clusters observed on the electrode surfaces by SEM (Figure 2.21), as this would have caused inhomogeneous distribution of photocatalytic active sites for PAA oxidation. Additionally, inhomogeneous photoelectrodes made characterisation by capacitance-based methods, such as EIS, much more difficult. EIS relies heavily on assumptions that surfaces

are purely capacitive with no frequency dispersions, often caused by porosity and surface structure.[176]

To determine whether the presence of excess V^{4+} was responsible for the dark current observed at 0.3 V vs Fc/Fc^{+}, XPS analysis was carried out (Figure 2.24).

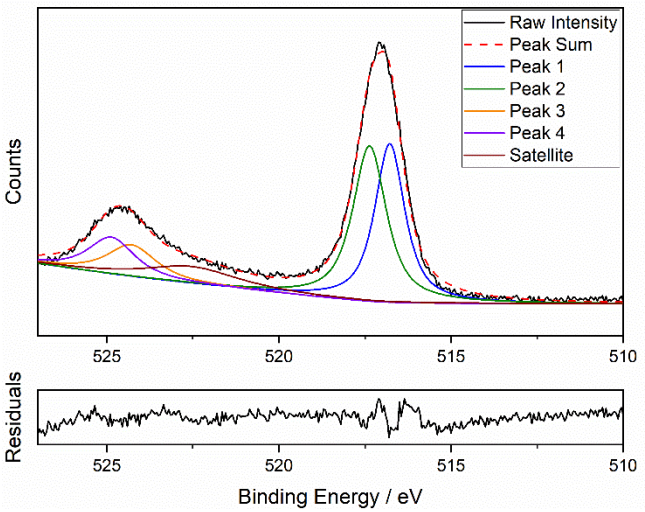

Figure 2.24: Vanadium 2p region of the XPS spectrum of a $BiVO_4$ photoanode that exhibited a dark oxidative current at 0.3 V vs Fc/Fc^{+}. Residual differences between fitted and experimental data are shown below the plot.

Deconvolution of the XPS signal showed the presence of two species which were attributed to V^{5+} and V^{4+} at the electrode surface.

Table 2.2: Summary of deconvoluted signals in the V 2p region of the XPS spectrum of a $BiVO_4$ photoanode that exhibited a dark oxidative current at 0.3 V vs Fc/Fc^{+}.

Region	Peak	Species	Peak Position / eV	Peak FWHM / eV	Percentage Integration
V 2p	1	V^{4+} $2p_{3/2}$	516.8	1.04	31.9
	2	V^{5+} $2p_{3/2}$	517.4	1.17	35
	3	V^{4+} $2p_{1/2}$	524.3	1.71	10.5
	4	V^{5+} $2p_{1/2}$	524.9	1.62	11.6
	5	Satellite	522.5	3.25	11

The presence of V^{4+} in some but not all electrodes suggested some irreproducibility in the electrode synthesis procedure. Additionally, the dark oxidative current was variable between electrodes within the same batch, and therefore stoichiometry of Bi and V

precursors was unlikely to be the origin of V^{4+}. As electrodes were prepared sequentially before annealing in air as a complete batch, some electrodes spent significant time cooling to room temperature before annealing.

During the cooling period it was possible that vanadium (IV) oxides precipitated due to an insufficient excess of atmospheric oxygen during electrospray deposition (Figure 2.25).[177]

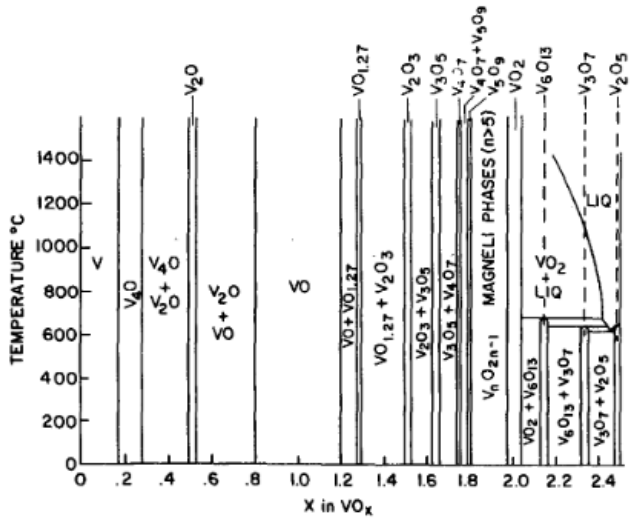

Figure 2.25: Phase diagram for mixed vanadium-oxygen compounds.[177]

Vanadium (IV) containing oxides precipitated during electrode synthesis were most likely stable at 450 °C according to phase diagrams suggested by Griffiths and Eastwood, provided the vanadium:oxygen stoichiometry was still insufficient to form pure $BiVO_4$.[177] Confirmation of the presence of V(IV) oxides was difficult as no additional peaks were observed in the GI-XRD diffractogram of $BiVO_4$ photoelectrodes (Figure 2.14). The absence of XRD peaks could suggest the presence of amorphous vanadium (IV) oxides or that these oxides were present in insufficient quantities to give reasonable signal above the baseline.

2.2.5 Electrospray Deposition of $BiVO_4$ Photoelectrodes from Precursors in 1:1 EtOAC:DMSO

The deposition of insoluble $VO(acac)_2$ in alcohol solvents led to inhomogeneous film deposition and the presence of V(IV) impurities, therefore to improve the solubility of $VO(acac)_2$, the deposition solvent system was changed from 1:1 EtOAc:iPrOH to 1:1 EtOAc:DMSO. In literature preparations of $BiVO_4$ photoelectrodes, DMSO has commonly been used to drop cast bismuth oxyiodide (BiOI) films with $VO(acac)_2$.[170] Additionally,

samples prepared from precursors in this solvent system were transferred directly to a pre-heated furnace for annealing to prevent the formation of possible mixed vanadium oxides.

Initially, deposition conditions were kept as consistent as possible with those used to prepare $BiVO_4$-IPA-450-30 and 450-45 to ensure changes to electrode structure and performance were solely due to improved $VO(acac)_2$ solubility. However, when using a nozzle height of 76 mm, no visible material deposition was observed within 1 hour of electrospray operation, therefore, the nozzle height was reduced to 36 mm and maintained at that height. Baseplate temperature and deposition time were varied (Table 2.3). Additionally, changing from iPrOH to DMSO resulted in degradation of the original 3D-printed mixing chamber, prepared from a proprietary resin. To prevent component degradation, a mixing chamber was printed from polyether ether ketone (PEEK), known for its excellent chemical resistance.

Table 2.3: Deposition parameters for electrospray deposition of $BiVO_4$ photoelectrodes from precursors in 1:1 EtOAc:DMSO.

Sample	Deposition Time / min	Applied Voltage / kV	Baseplate Temperature / °C	Flow Rate / mL min^{-1}
DMSO-350-15	15	9.5	350	0.03
DMSO-400-15	15	9.5	400	0.03
DMSO-450-15	15	9.5	450	0.03
DMSO-350-30	30	9.5	350	0.03
DMSO-350-45	45	9.5	350	0.03
DMSO-400-30	30	9.5	400	0.03
DMSO-400-45	45	9.5	400	0.03

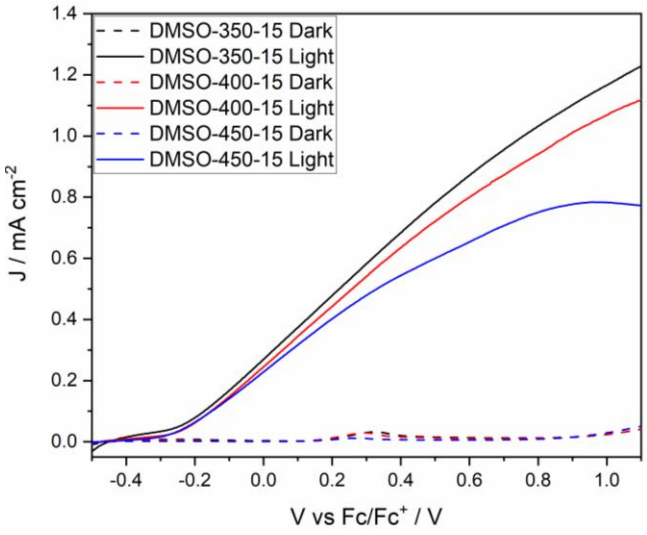

Figure 2.26: Linear sweep voltammograms of $BiVO_4$ photoelectrodes deposited for 15 minutes at 350 °C (DMSO-350-15, black), 400 °C (DMSO-400-15, red) and 450 °C (DMSO-450-15, blue). Voltammograms were recorded in 1 M PAA partially neutralised with 0.05 equiv Et_3N under AM1.5G illumination (solid) and in the dark (dashed).

For 15 minutes of precursor deposition, increased temperatures resulted in poorer PEC performance at all potentials in the LSV (Figure 2.26). No shift in the photocurrent onset potential was observed between baseplate temperatures, but photocurrent decreased slightly between 350 and 400 °C, with more significant losses at 450 °C. The lower photocurrent observed at 450 °C was due to thermal degradation of the solution, resulting in smoking of the solution at the end of the electrospray nozzle. The smoking of the solution was attributed to thermal decomposition of DMSO at high temperatures.[178, 179] The decomposition of the solvent mixture also resulted in an extremely unstable cone-jet during deposition and therefore a thinner $BiVO_4$ film, with poorer light absorption characteristics.

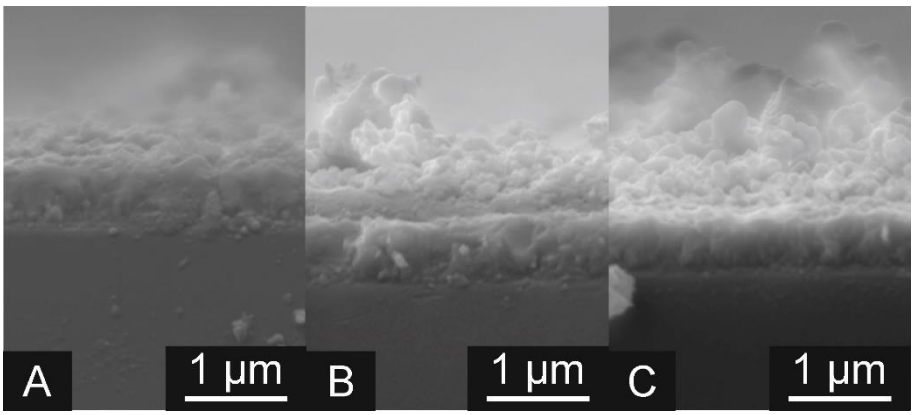

Figure 2.27: Cross section of a) DMSO-350-15, b) DMSO-400-15 and c) DMSO-450-15 photoelectrodes.

A compact 200 – 300 nm $BiVO_4$ film was deposited after 15 minutes of deposition at 350 °C (Figure 2.27). As deposition temperature was increased, cross section SEM images seemed to show an increasing film thickness, however this was attributed to surface roughness (Figure 2.28). Surface roughness changes were caused by increasing solvent evaporation rates as baseplate temperature was increased. Increased porosity in polymer films has been observed when decreasing the boiling point of the solvent system, therefore increasing deposition temperatures for a single solvent system should have the same effect.[180, 181]

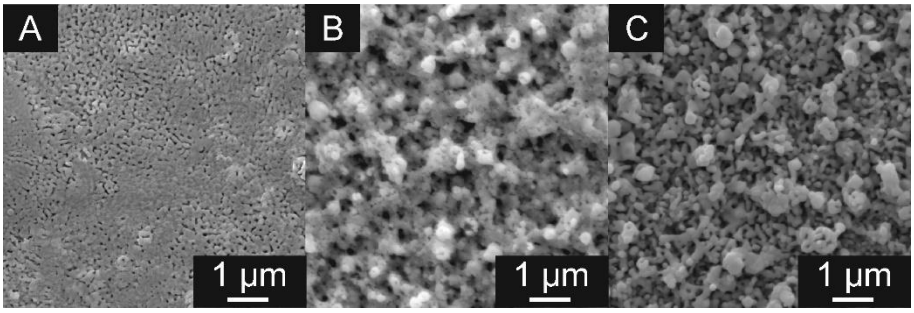

Figure 2.28: Surface SEM images of a) DMSO-350-15, b) DMSO-400-15 and c) DMSO-450-15 photoelectrodes.

Due to the instability of the cone-jet spray mode at 450 °C, deposition for longer than 15 minutes was not possible for EtOAc:DMSO solutions.

At all baseplate temperatures for deposition in EtOAc:DMSO solutions, the magnitude of the dark oxidative current at approximately 0.4 V vs Fc/Fc^+ decreased to around 0.1 mA, compared to depositions using EtOAc:iPrOH which showed up to 0.3 mA peak current (Figure 2.22). As deposition temperature was increased, it was also observed

that the magnitude of the dark oxidative current at approximately 0.4 V vs Fc/Fc^+ decreased. The loss of the oxidative peak at 0.4 V vs Fc/Fc^+ with increased temperature most likely corresponded to more complete oxidation of the V(IV) precursor to V(V) during deposition. All samples were annealed under identical conditions; therefore, the loss of the V(IV) oxidation peak must have been accounted for during deposition.

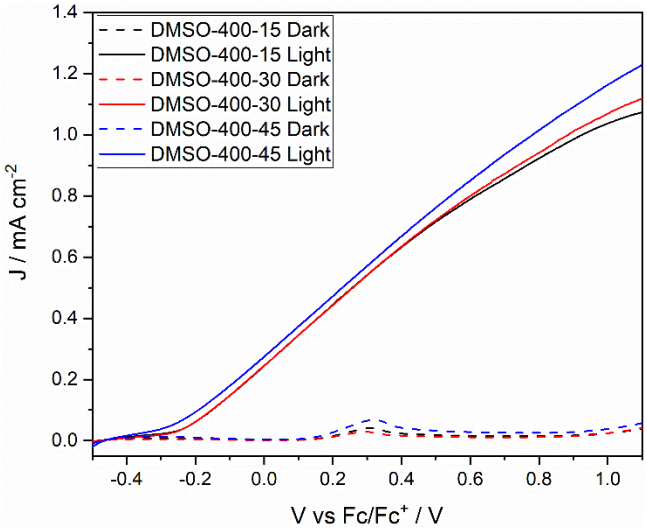

Figure 2.29: Linear sweep voltammograms of $BiVO_4$ photoelectrodes deposited at 400 °C for 15 (DMSO-400-15, black), 30 (DMSO-400-30, red) and 45 (DMSO-400-45, blue) minutes. Voltammograms were recorded in 1 M PAA solutions partially neutralised by 0.05 equiv Et_3N under AM1.5G illumination (solid) and in the dark (dashed).

Deposition time was varied between 15 – 45 minutes for both 350 and 400 °C baseplate temperatures. At 400 °C, the LSV performance of photoelectrodes under illumination showed no correlation with deposition time, with the lowest photocurrents obtained after 30 minutes of deposition, and the highest after 45 minutes (Figure 2.29). Although no clear trend was observed for varying deposition times, the photocurrent traces recorded for the electrodes were very similar at all potentials. The small changes on increasing the deposition time suggested that varying film thickness and absorption characteristics of the electrodes had little bearing on PEC performance at 400 °C. As electrodes were illuminated through the FTO substrate, this suggested that most of the electrode activity is close to the $BiVO_4$/FTO interface.

For the dark oxidative current attributed to oxidation of V(IV) to V(V), the peak current increased with deposition time, owing to more material deposited onto the substrate and thus greater V(IV) content of the electrode.

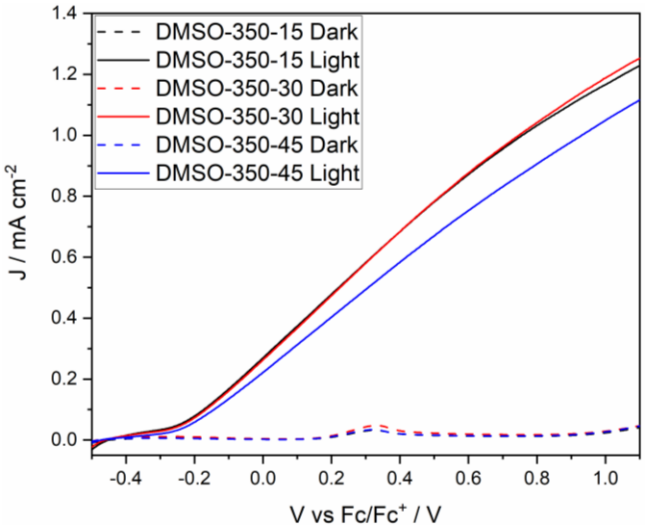

Figure 2.30: Linear sweep voltammograms of $BiVO_4$ photoelectrodes deposited at 350 °C for 15 (DMSO-350-15, black), 30 (DMSO-350-30, red) and 45 (DMSO-350-45, blue). Voltammograms were recorded in 1 M PAA solutions containing 0.05 equiv Et_3N in MeCN under AM1.5G illumination (solid) and in the dark (dashed).

Compared to deposition at 400 °C, a clearer trend in PEC performance is observed in electrodes deposited at a baseplate temperature of 350 °C. Much better stability of the cone-jet spray was observed at the lower temperature, possibly eliminating structural and performance irreproducibility caused by changeable cone-jet characteristics. Overall, only small changes to PEC performance were observed for electrodes prepared at 350 and 400 °C, though deposition for 30 minutes at 350 °C yielded the photoelectrode with the best PEC performance. Deposition of precursors for 45 minutes at 350 °C produced an electrode with poorer PEC performance than shorter depositions, with very similar PEC performance observed for 30 and 15 mintue depositions.

For DMSO-350-45, the increased thickness (1.3 µm) of the film resulted in poorer charge transport to the electrode surface due to the short hole diffusion lengths of $BiVO_4$ – around 70 nm (Figure 2.31).[171] As a result of the poor charge carrier transport in $BiVO_4$ films, a trade-off between thicker films for increased light harvesting efficiency and thinner films for improved hole migration to the electrode surface is required.[25, 182] As only small changes in PEC performance were observed based on deposition time, it was concluded that charge extraction from the electrode surface was more important than light harvesting for these $BiVO_4$ photoelectrodes.

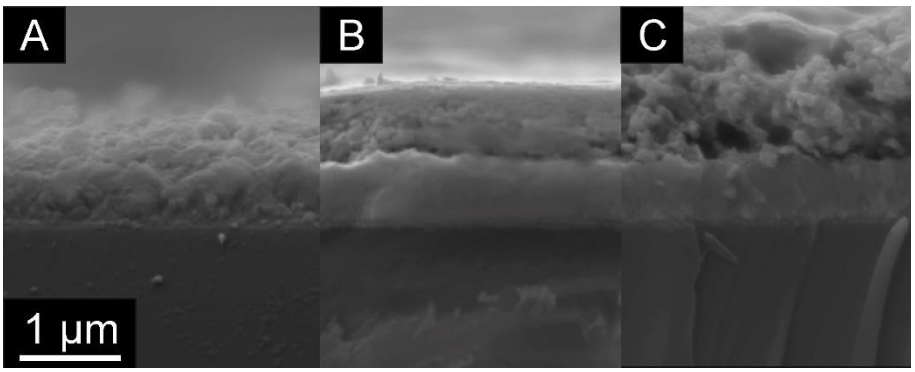

Figure 2.31: Cross section SEM images of a) DMSO-350-15, b) DMSO-350-30 and c) DMSO-350-45 photoelectrodes.

Deposition of $BiVO_4$ films at 350 °C for 30 minutes was chosen as the desired synthetic method for photoelectrodes used in PAA oxidation reactions, due to the trade-off between absorption characteristics and charge carrier transport. Elemental characterisation of a DMSO-350-45 electrode by EDS allowed glass, FTO and $BiVO_4$ layers to be determined (Figure 2.32).

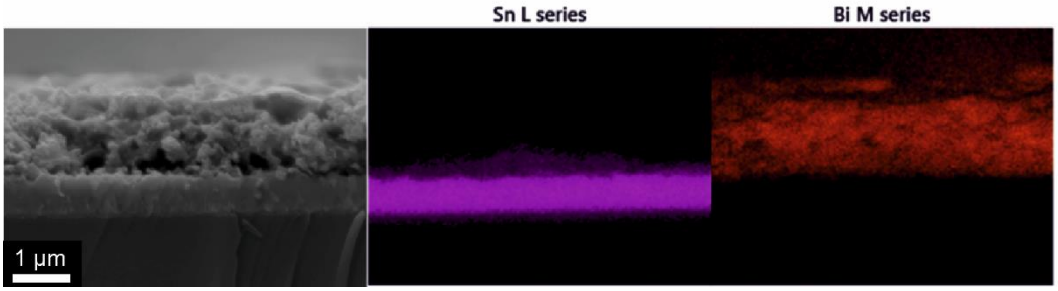

Figure 2.32: Energy dispersive X-ray spectroscopy (EDS) of a DMSO-350-45 cross-section showing the presence of tin (Sn) indicative of FTO and bismuth (Bi) indicative of $BiVO_4$.

Both FTO and $BiVO_4$ layers were clearly defined for synthesised photoelectrodes, however some Sn, Bi and V leaching was observed between the layers by linescan measurements, as shown by overlap of the elemental profiles (Figure 2.33). Ion migration of Sn into Fe_2O_3 films has been observed, however much higher annealing temperatures (>750 °C) were required.[183] Tin migration into Fe_2O_3 films has been shown to improve PEC performance for water oxidation, however due to the insufficient annealing temperatures used for $BiVO_4$ photoelectrode preparation, the overlap was attributed to the large interaction volume of electrons in EDS measurements.

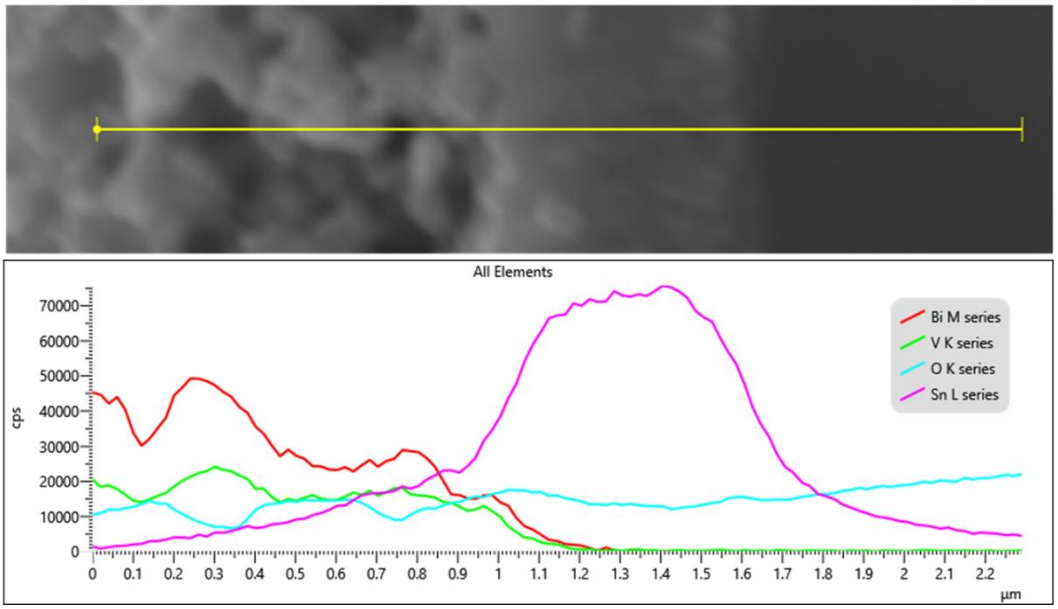

Figure 2.33: EDS linescan of a DMSO-350-45 cross section, showing the presence of bismuth (Bi, red), vanadium (V, green), oxygen (O, cyan) and tin (Sn, pink).

To assess the reproducibility of photoelectrode synthesis, multiple batches of $BiVO_4$ films were prepared.

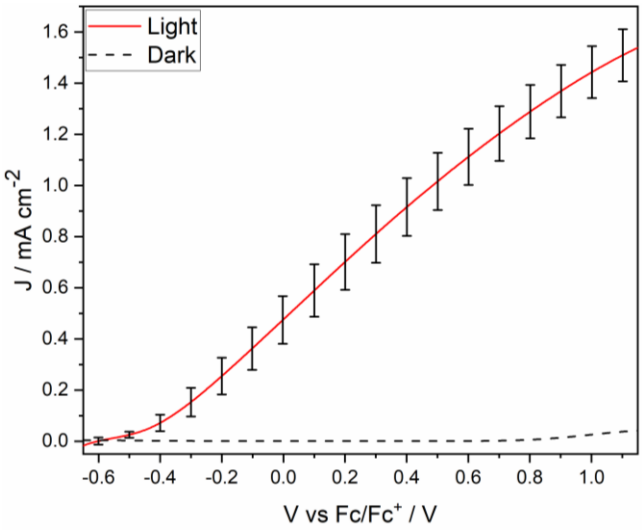

Figure 2.34: Average linear sweep voltammogram and standard deviation of 13 $BiVO_4$ photoelectrodes synthesised by electrospray deposition of bismuth 2-ethylhexanoate and $VO(acac)_2$ in 1:1 EtOAc:DMSO at 350 °C for 30 minutes. Voltammograms were recorded under AM1.5G illumination (red, solid) and in the dark (dashed, black).

As shown in Figure 2.34, $BiVO_4$ photoelectrodes showed consistent PEC performance across multiple batches as well as an absence of dark oxidative currents at

around 0.3 V vs Fc/Fc^+, with the exception of a single sample. Photocurrent onset potential varied by approximately 200 mV across all samples, suggesting some possible changes to surface chemistry between samples.[175] Any changes to surface chemistry may have arisen from inhomogeneous deposition across the electrode area, or slight inconsistencies between electrode batches. Factors such as turbulence around the precursor spray or cone-jet asymmetry could have contributed to slight variations observed by LSV.

Photocurrents at all potentials also showed some variance, with differences of up to 0.25 mA cm^{-2} at 0.5 V vs ferrocene observed between highest and lowest PEC performance electrodes. Although variances of up to 25% of maximum photocurrent was observed, electrode reproducibility was significantly better than for electrodes prepared using iPrOH:EtOAc precursor solutions.

X-ray photoelectron spectroscopy (XPS) was used to assess the surface composition of electrodes prepared by electrospray deposition from precursors in DMSO:EtOAc. An electrode from the batches prepared in Figure 2.34 that did not exhibit the dark oxidative current at approximately 0.4 V vs Fc/Fc^+ was analysed by XPS.

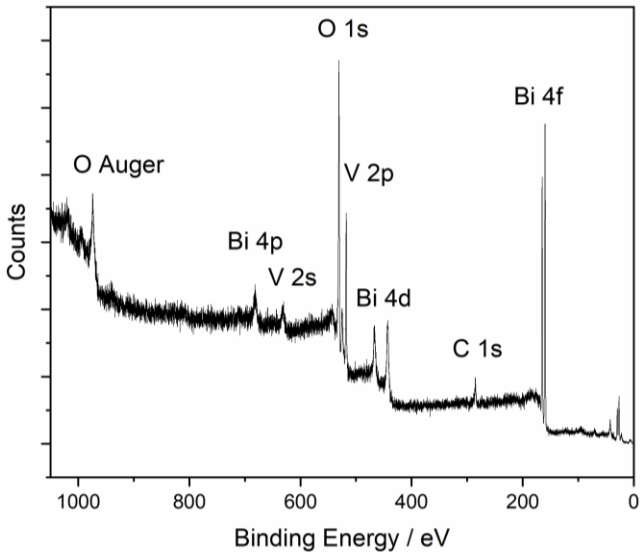

Figure 2.35: XPS survey spectrum for a $BiVO_4$ photoanode prepared by electrospray deposition from precursors in 1:1 EtOAc:DMSO solutions. The spectrum was referenced to the adventitious carbon peak at 284.8 eV.

As shown in Figure 2.35, the surface elemental composition of $BiVO_4$ photoanodes consisted solely of Bi, V, O and a small amount of adventitious carbon, which possibly originated from either sample preparation for analysis or latent organic material from

precursor ligands.(ref) Further analysis of Bi 4f and V 2p regions showed a single oxidation state of each metal - +3 for bismuth and +5 for vanadium.

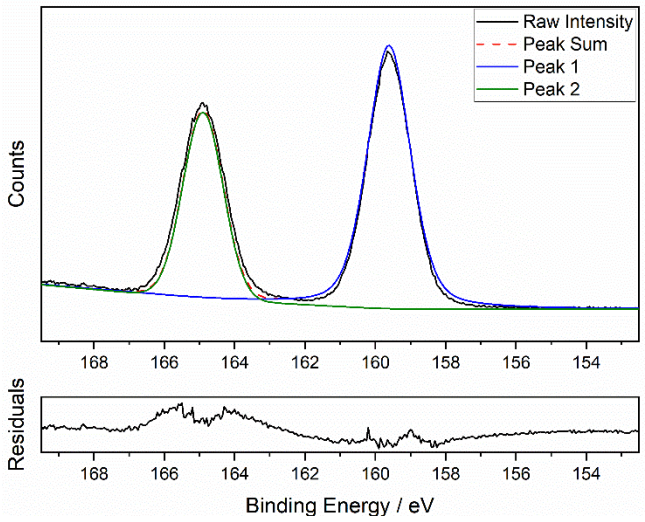

Figure 2.36: Bismuth 4f region of XPS spectrum of a $BiVO_4$ photoanode prepared by electrospray deposition from precursors in 1:1 EtOAc:DMSO solutions. Residual differences between fitted and experimental data are shown below the plot.

Table 2.4: Summary of deconvoluted signals in the Bi 4f region of the XPS spectrum of a $BiVO_4$ photoanode prepared by electrospray deposition of precursors in 1:1 EtOAc:DMSO solutions.

Region	Peak	Species	Peak Position / eV	Peak FWHM / eV	Percentage Integration
Bi 4f	1	Bi^{3+} $4f_{7/2}$	159.6	1.45	63.7
	2	Bi^{3+} $4f_{5/2}$	164.9	1.35	36.3

The Bi 4f region showed peaks at 159.6 and 164.9 eV, consistent with the presence of solely Bi^{3+} at the electrode surface and with literature examples.[150, 184] The V 2p and O 1s regions of the survey spectrum could not be separated into individual spectra and thus were fitted together (Figure 2.37).

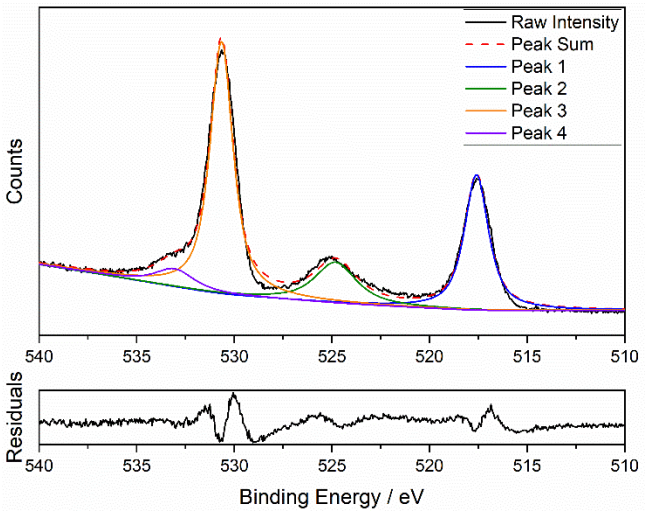

Figure 2.37: Vanadium 2p and Oxygen 1s regions of the XPS spectrum of a $BiVO_4$ photoanode prepared by electrospray deposition from precursors in 1:1 EtOAc:DMSO solutions. Residual differences between fitted and experimental data are shown below the plot.

Table 2.5: Summary of deconvoluted signals in the V 2p and O 1s regions of the XPS spectrum of a $BiVO_4$ photoanode prepared by electrospray depositon of precursors in 1:1 EtOAc:DMSO solutions

Region	Peak	Species	Peak Position / eV	Peak FWHM / eV	Percentage Integration
V 2p	1	V^{5+} $2p_{3/2}$	517.6	1.47	28.6
	2	V^{5+} $2p_{1/2}$	524.8	2.54	14.8
O 1s	3	Metal Oxide	530.7	1.4	50.6
	4	Hydroxide/Water	533.1	2.35	6.1

Fitting of the peaks in the V 2p region of the XPS spectrum confirmed the sole presence of V^{5+}, with comparable $2p_{3/2}$ and $2p_{1/2}$ peak values reported in the literature.[184] Integration of XPS signals was carried out as a method of determining surface Bi:V stoichiometry.

Table 2.6: Surface stoichiometry of an unused $BiVO_4$ photoelectrode as observed in XPS. Sensitivity factors taken from Wagner, C. D.[185]

Peak	Peak Centre / eV	Integration	Sensitivity Factor	Normalised Integration	Relative Quantity
Bi 4f	159.65	930.12	4.25	218.85	1.00
V 2p	517.60	551.68	1.30	424.37	1.94
O 1s	530.60	1138.51	0.66	1725.02	7.88
C 1s	285.00	80.71	0.25	322.82	1.48

As shown in Table 2.6, a significant excess of V(V) is observed at the electrode surface, with a Bi:V ratio of 34:66. The source of excess V(V) was not immediately obvious as precursor solutions were identical concentrations and care was taken to ensure homogeneous mixing of solutions during passage through electrospray tubing. It was possible that the surface excess of V was caused by segregation of Bi and V during deposition or annealing, however this would result in a deficiency of vanadium in the bulk material and no alternative mixed bismuth-vanadium oxides were observed by XRD. Alternatively, the surface composition may have resulted from loss of volatile bismuth compounds during annealing, which has previously been shown to affect the stoichiometry of ferroelectric materials.[174, 186] To determine the possible nature of excess V^{5+} at the electrode surface, grazing incidence X-ray diffraction (GI-XRD) was used to try and identify crystalline species in the photoelectrode.

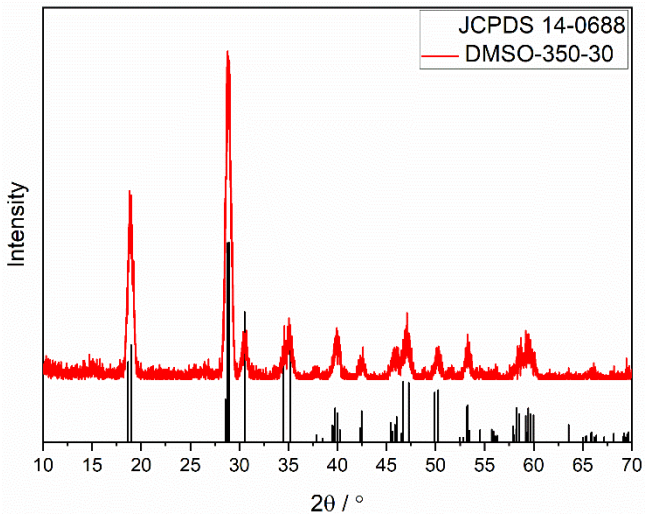

Figure 2.38: Grazing incidence XRD spectrum of an a DMSO-350-30 $BiVO_4$ photoelectrode. A computed X-ray diffractogram of monoclinic $BiVO_4$ (JCPDS 14-0688) is given as a comparison.

Although XPS analysis showed excess V(V) and oxygen at the electrode surface, no evidence for crystalline vanadium oxides was observed by GI-XRD.[187] The GI-XRD diffractogram of a DMSO-350-30 photoelectrode may not have shown any V_2O_5 peaks due to the poor signal-to-noise ratio or the formation of an amorphous vanadium oxide layer. Additionally, as film thicknesses were around 700 nm, only very small quantities of V_2O_5 would have been present and thus any XRD peak intensities would have been small, making detection more difficult.

The absence of crystalline vanadium oxides suggested that the electrode surface was intrinsically-doped and vanadium rich. Bismuth-rich surfaces have been shown to drastically improve PEC performance for single crystal $BiVO_4$ photoelectrodes, however 'V-rich' surfaces studied only had a small excess of V at the surface (Bi:V ratio 43:57).[188] The effects of V(V) enrichment at the electrode surface on photoelectrode performance was unclear and may present a route to further electrode optimisation in future research.

Deposition of bismuth 2-ethylhexanoate and $VO(acac)_2$ in ethyl acetate:DMSO mixtures produced high PEC performance, reproducible photoelectrodes. After optimisation of deposition temperature and time to 350 °C and 30 minutes respectively resulted in 700 nm thick films that showed sufficient activity for the study and optimisation of photoelectrochemical Kolbe reactions of phenylacetic acid.

2.3 Conclusions

Electrospray apparatus and methodology were developed for preparation of high PEC performance and reproducible $BiVO_4$ photoelectrodes. Electrodes prepared from deposition of metal precursors were shown to outperform those prepared from pre-synthesised nanoparticle suspensions. Ohmic behaviour and low photocurrents obtained using nanoparticle electrodes was attributed to poor electrical contact at the $BiVO_4$/FTO interface despite annealing films after deposition. Crystalline films with defined optical characteristics were prepared when using bismuth and vanadium precursors, deposited at temperatures > 300 °C. For precursor electrodes, photocurrents of up to 1.6 mA cm^{-2} at 0.7 V vs Fc/Fc^+ were obtained for both iPrOH:EtOAc and DMSO:EtOAc precursor mixtures.

Although high photocurrents were measured using iPrOH:EtOAc electrodes, reproducibility was extremely poor, owing to low solubility of $VO(acac)_2$ in iPrOH. Inhomogeneous deposition of large clusters was observed in SEM images and PEC performance was variable when illuminating different electrode areas. The presence of V^{4+}

species was evidenced by a dark oxidative current at approximately 0.3 V vs Fc/Fc^+ and confirmed using XPS analysis. Changing the solvent system to DMSO:EtOAc resulted in nanostructured films with excellent performance and reproducibility. Electrode performance and optical properties were shown to vary with deposition temperature and duration, which were optimised to 350 °C and 30 minutes, respectively.

After optimisation of $BiVO_4$ electrospray deposition, substrates were used as working electrodes in the photoelectrochemical oxidation of phenylacetic acid. Optimisation of photoelectrochemical apparatus and conditions for maximum selectivity towards C-C bond formation is outlined in Chapter 3.

3. Photoelectrochemical Kolbe Coupling of Phenylacetic Acid at $BiVO_4$ Photoelectrodes

3.1 Introduction

Electrochemical and photoelectrochemical reactions are sensitive to several reaction parameters, including electrolytic cell set-up, inter-electrode spacing, reaction solvent, supporting electrolyte and applied potential.[189, 190] Design of an electrolytic cell can be intricate, with consideration of reaction volume, number of compartments and electrode dimensions required. In some cases, separation of anodic and cathodic reactions is required due to side reactions between substrates or a parasitic oxidation or reduction of the desired product. For example, the electrolysis of water into H_2 and O_2 requires separation of oxidative and reductive reactions as proton reduction is favourable in acidic media, whilst water oxidation is suppressed.[191] Additionally, many electrocatalysts for water oxidation, such as metal oxides (RuO_2, IrO_2), are unstable in acidic media.[192]

Considerations must also be given for inter-electrode spacing, as this has a considerable effect on current generation in low conductivity media as well as product selectivity. In narrow electrochemical flow cells, C-C bond formation has been achieved free from supporting electrolyte, which is typically required to increase solution conductivity in larger electrolytic cells.[193] Additionally, for the electrochemical synthesis of alkoxycaffeine derivatives, moderate increase from 37 to 43% yield was observed on optimization of the electrode spacing.[194]

For Kolbe electrolysis specifically, product distributions have been shown to be sensitive to solvent and electrolyte compositions. In aqueous systems, oxidative decarboxylation is in direct competition with water oxidation above 1.23 V vs RHE. However, selectivity up to 50% for C-C coupled products has been observed when using applied potentials > 5 V or large current densities in controlled-current studies.[138] The suppression of solvent oxidation arises from the formation of a defined carboxylate layer at the electrode surface at high electrode potentials due to the electrostatic attraction between the net positive anode and the negatively charged carboxylate anions.[125]

When introducing a supporting electrolyte to aqueous Kolbe electrolyses, decreases in C-C coupled product yield up to 50% were observed when using 0.1 mg mL^{-1}

KNO_3, whilst no change was observed with Na_2SO_4 (93%). Reductions to Kolbe product yield with KNO_3 were attributed to the blocking of electrode active sites by NO_3^- anions and greater stabilisation of carbocation intermediates produced by over-oxidation of the radical.[195] Non-aqueous solvents have also been used for Kolbe electrolysis and are typically favoured, with most synthetic applications carried out in methanolic solutions.[196, 197] Acetonitrile is also a common solvent in electrochemical measurements and has been used in photoelectrochemical oxidation of acetate at TiO_2 photoelectrodes.[123]

As well as considerations required for electrochemical synthesis, photoelectrochemical reactions are constrained by factors that affect photochemical transformations, such as light source wavelength and intensity. These factors are crucial for not only the efficiency of electron-hole pair photogeneration, but also the concentration of electrons and holes available for reaction. As few examples of photoelectrochemical synthesis exist within the literature, thorough optimisation of reaction parameters is lacking or not clearly reported.[116, 119] Additionally, little consideration is given to the recyclability of photoelectrodes in a supposedly sustainable application.

Typically, optimisation of substrate concentrations and applied potential is performed but little comment is given on the electrolytic cell set-up and illumination source. For photoelectrocatalytic C-H amination at α-Fe_2O_3 electrodes, a significant solvent effect was observed, with no product formation in acetonitrile and methanol containing 0.1 M tetrabutylammonium hexafluorophosphate ($TBAPF_6$). When using hexafluoroisopropanol (HFIP), not only was a product yield of 75% obtained but unusual selectivity for ortho-amination was observed.[116] Here the ortho-directed amination was attributed to hydrogen bonding interactions between the radical cation intermediate and HFIP stabilising the ortho-substituted arene. Apart from substrate concentration effects, optimisation of electrochemical parameters is not discussed. In particular, the recycling and reproducibility of Fe_2O_3 is not mentioned. Mott-Schottky (MS) plots for two Fe_2O_3 photoelectrodes show similar flat band potentials but vastly different gradients. As the gradient of the MS plot should depend solely on donor density, it is possible that electrodes are not consistent between depositions.[198] Investigation of the effects of electrolysis parameters is key to developing photoelectrochemical synthesis to ensure reproducibility between systems and clearer understanding of optimisation processes.

3.1.1 Aims

The predominant aim of this work was to develop a photoelectrochemical system for radical-radical Kolbe coupling with high photocurrent densities and Kolbe product selectivity. Additional goals were to investigate the effect of electrolysis parameters on the product distribution of Kolbe electrolyses and determine key factors underlying these changes. Alterations to light source, electrolytic cell parameters, substrate concentrations, applied potential and supporting electrolyte will be investigated and their effect on photocurrent density and product selectivity determined.

In addition to interrogation of key reaction parameters, studies on the stability of $BiVO_4$ photoelectrodes to reaction conditions were to be carried out. X-ray techniques and microscopy will be used to determine structural changes to electrodes, as well as electrochemical characterisation and product selectivity to determine changes in activity.

3.2 Optimisation of Photoelectrocatalytic Kolbe Conditions

3.2.1 Cell and Illumination Source Optimisation

With an optimised synthesis of $BiVO_4$ photoelectrodes in hand, photoelectrochemical cell conditions were optimised for photocurrent generation and bibenzyl selectivity, with ideal photocurrent densities of > 0.5 mA cm^{-2} at relevant electrolysis potentials. $BiVO_4$ photoelectrodes have shown good performances for water oxidation when using AM1.5G illumination (Figure 3.1), therefore a solar-simulated light source was used initially in this work. Literature examples of water oxidation show photocurrents up to 1 mA cm^{-2} at 1.23 V vs RHE have been obtained for unmodified $BiVO_4$, with post-synthetic treatments, doping and co-catalysts employed to further enhance performance.[118, 155, 170, 199-201]

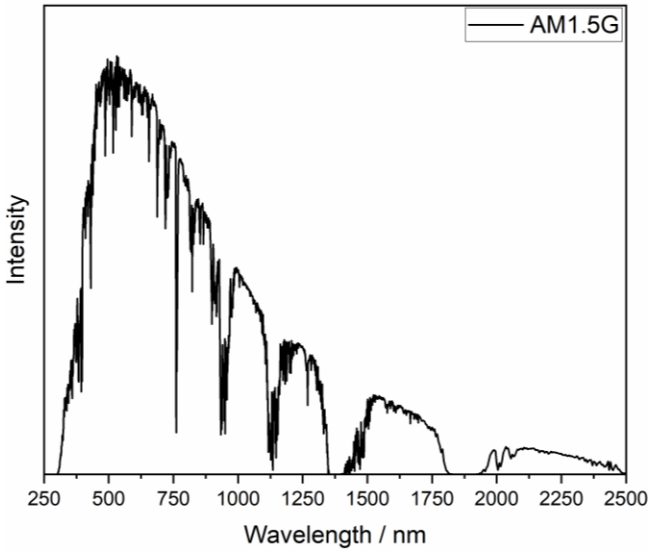

Figure 3.1: AM1.5G solar radiation emission spectrum.

Initial photoelectrochemical measurements were carried out with 1 M phenylacetic acid solutions to ensure that oxidation processes at the photoanode were not diffusion limited and were instead controlled by the surface hole concentration and charge transfer kinetics. To generate charged species, to reduce solution resistance, the carboxylic acid was partially neutralised by addition of 0.05 equiv triethylamine (Et_3N). Addition of a base to electrochemical Kolbe reactions is common as a means of generating carboxylate anions. Bases such as potassium hydroxide (KOH) and sodium methoxide (NaOMe) have been used for oxidative decarboxylation reactions previously.[202, 203] Ionic salts work well in methanol (MeOH) and can be easily separated from preparative mixtures by simple work-up, however, for analysis by GC, the high boiling points of ionic salts can result in column blockages. Other examples of electrochemical oxidative decarboxylation have also used triethylamine (Et_3N) as a base, which has a low boiling point and is suitable for GC analysis.[127, 204] For dimerization of unsaturated carboxylic acids, Knolle and Schafer demonstrated increased selectivity (31%) when using amine bases versus no partial neutralisation (8%).[205]

Although metal oxide photoelectrodes are typically unstable in acidic media, the use of non-aqueous solvents increases the pKa of phenylacetic acid. In MeCN, this increase is approximately five-fold, giving phenylacetic acid a pKa of around 20-25 – acetic and benzoic acids have pKa values of approximately 23 in MeCN.[206] The increased acid pKa, along with partial neutralisation, avoided issues of electrode degradation via acid-base reactions under ambient conditions.

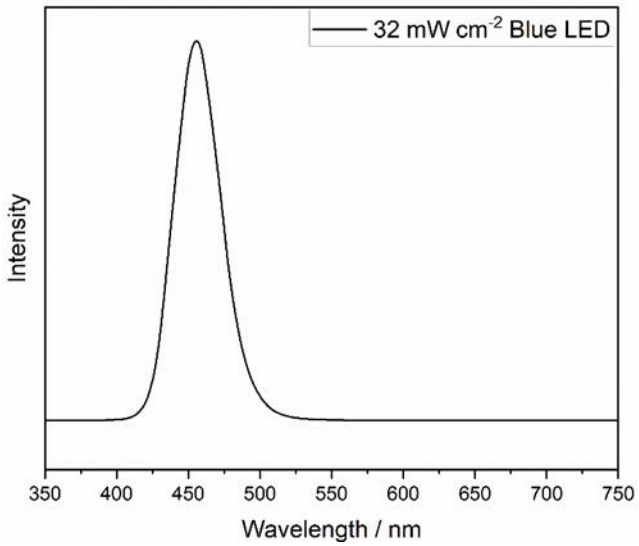

Figure 3.2: Emission spectrum of a blue LED array (32 mW cm^{-2}) used in photoelectrochemical measurements.

Although AM1.5G sources have been used for overall water splitting at semiconductor photoelectrodes, many examples of photocatalysis using semiconductor powders make use of high-irradiance, narrow wavelength range LED arrays.[116, 207-209] A blue LED array (32 mW cm^{-2}) was also used to illuminate photoelectrodes, with current density and product selectivity compared as a function of light source and irradiance. The output spectrum for AM1.5G covers virtually the entire visible spectrum, meaning that many wavelengths are too low energy to be absorbed by the semiconductor and generate electron-hole pairs. Higher energy photons with wavelengths < 300 nm can also be absorbed by the reaction solvent, possibly leading to side reactions between substrates and excited states of solvent molecules.[210] Additionally, many wavelengths emitted by AM1.5G sources are absorbed by common lab glassware, meaning quartz cells or quartz windows are required when using solar-simulated illumination (Figure 3.1). By contrast, the blue LED array had a much lower irradiance (32 mW cm^{-2}) and narrower wavelength spread between 420 – 500 nm (Figure 3.2), meaning no specialist glassware was required and excitation of solvent molecules was not a competing factor. After electrolysis, 3 main products were observed by gas chromatography (GC) – bibenzyl, benzyl alcohol (BnOH) and benzaldehyde (PhCHO). Reaction pathways for Kolbe and non-Kolbe product formations are shown in Scheme 3.1. Unless stated, initial screening for optimised cell conditions was carried out once per electrochemical cell. As GC analysis was carried out in triplicate, the errors associated with product quantification are low, therefore the most errors are

associated with the small variability in $BiVO_4$ photoelectrode performance, which was estimated at around ±0.1 mA cm^{-2} by LSV (Figure 2.34).

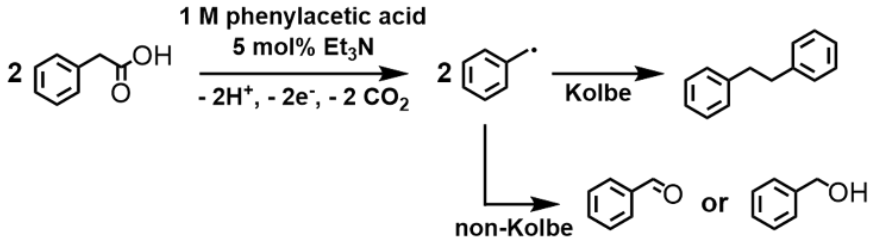

Scheme 3.1: Reaction pathways for formation of the desired Kolbe product bibenzyl, and non-Kolbe products benzyl alcohol and benzaldehyde formed by oxidation of the intermediate radical.

*Table 3.1: Optimisation of illumination sources and electrolytic cell conditions for bibenzyl selectivity measured by GC. Schematics of electrolytic cells are given in section **6.4**.*

Cell	Cell Volume / mL	Ave. Photocurrent Density / mA cm^{-2}	Illumination Source	Applied Potential / V vs Fc/Fc^+	FE Bibenzyl / %	FE Total / %
2-comp.	20+5	0.73	AM1.5G	0.54	28	102
2-comp.	20+5	0.95	Blue LED	0.54	34	98
1-comp.	20	0.34	Blue LED	0.54	55	97
1-comp.	8	0.96	Blue LED	0.09	88	100

In comparison to AM1.5G, illumination with the LED array resulted in a 0.22 mA cm^{-2} increase in photocurrent density in a 2-compartment electrolytic cell (Table 3.1, Figure 3.3). Reduction of the illumination intensity of the AM1.5G source with neutral density filters showed that photoelectrodes were not under saturation conditions from the light source. Approximately linear photocurrent density decreases with transmittance were observed (Figure 3.4). As no saturation point of irradiance was observed, photocurrent improvements on using a blue LED were attributed to the narrow emission wavelength range and thus increased percentage of absorbed photons.

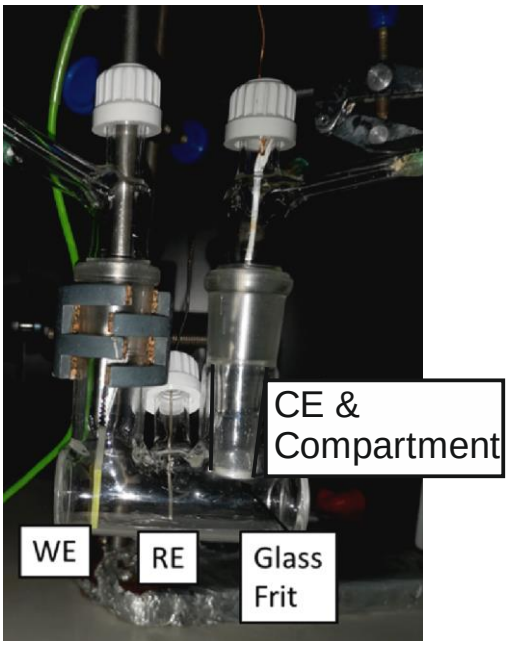

Figure 3.3: Picture of a two-compartment electrolytic cell (20 + 5 mL) used for electrolysis of phenylacetic acid solutions partially neutralised with 0.05 equiv Et_3N.

The increased photocurrent on irradiance with a blue LED array translated to only a slight increase in product selectivity for bibenzyl from 28% to 34%. This increase was attributed to the higher photocurrent density generating greater benzyl radical concentrations at the working electrode surface. An increased steady-state concentration of radicals would favour the radical-radical coupling product due to an increased likelihood of collision between two benzyl radicals.

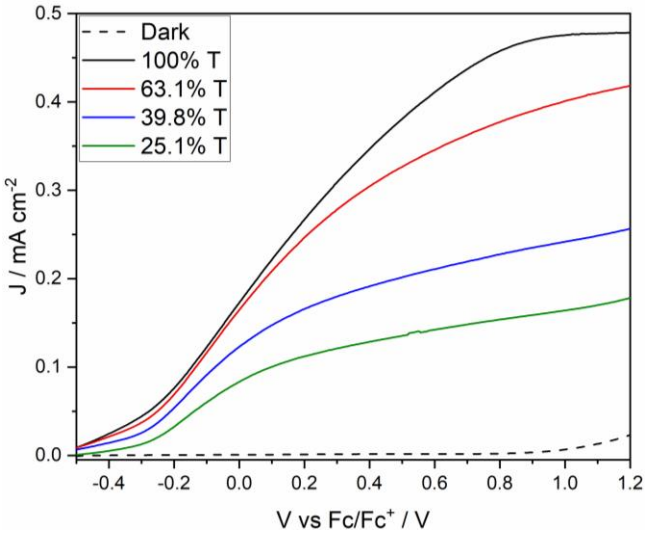

Figure 3.4: Linear sweep voltammograms of a $BiVO_4$ photoelectrode under illumination by an AM1.5G light source at 100 (black), 63.1 (red), 39.8 (blue) and 25.1 % Transmittance (green), controlled by neutral density filters. Voltammograms were recorded in 1 M PAA solutions that had been partially neutralised by addition of 0.05 equiv Et_3N.

Typically, electrochemical Kolbe syntheses have been carried out in one-compartment cells at much higher anodic potentials (>15 V), however, under these conditions, parasitic reactions of electrolysis products are possible.[147, 211] To assess possible cathodic degradation of reaction products, electrolysis was carried out with the counter electrode compartment containing 10 mM bibenzyl. No appreciable loss of bibenzyl was observed by GC, with a concentration of 9.7 mM measured after 6-hour electrolysis.

As no parasitic reduction of bibenzyl was evident, electrolysis in a 20 mL one-compartment cell was attempted by removing the cathodic compartment and submerging the counter electrode in the bulk solution (Figure 3.5). This was done to reduce electrode spacing, which has been shown to improve current density for electrochemical reactions.[212] However, when using a one-compartment, 20 mL electrolytic cell, a significant drop in photocurrent was observed (0.34 mA cm^{-2}). This may have been caused by the high solution resistance. As electrolytes were comprised predominantly of phenylacetic acid and a low concentration (around 50 mM) of carboxylate and protonated amine, the solution resistivity was large (approximately 150 Ω m), resulting in reduced photocurrents.

Figure 3.5: Picture of a one-compartment electrolytic cell (20 mL).

Although a drop in photocurrent was observed on moving to a one-compartment cell, the selectivity for bibenzyl increased significantly to 55%. Despite the corresponding decrease in steady-state radical concentration, the selectivity improvements were assigned to improved exclusion of atmospheric oxygen from the electrolytic cell. On moving from a two-compartment to a one-compartment cell, fewer glass joints were required and a rubber septum was used to seal the electrolytic cell. Lower oxygen concentrations in the one-compartment cell would not have acted to enhance radical-radical coupling rates, but instead decrease the rate of competing non-Kolbe reaction pathways that form benzyl alcohol and benzaldehyde.

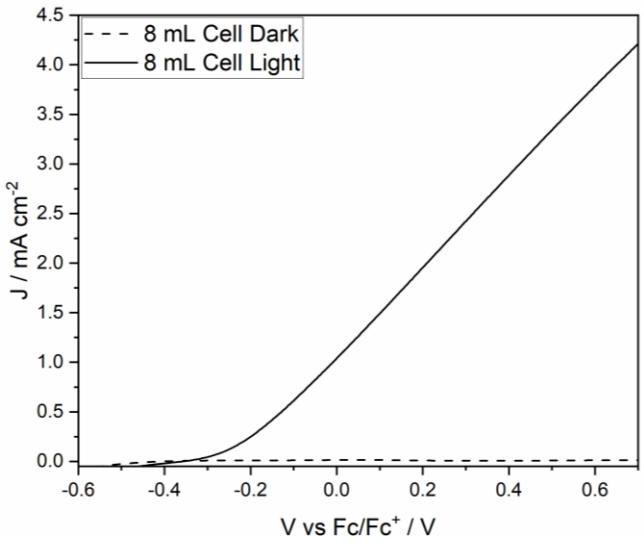

Figure 3.6: Linear sweep voltammogram of a $BiVO_4$ photoelectrode in an 8 mL one-compartment electrolytic cell containing 1 M PAA electrolyte partially neutralised with 0.05 equiv Et_3N under blue LED illumination.

After establishing that no parasitic reduction of bibenzyl occurred at the cathode, and that bibenzyl selectivity was improved by better exclusion of atmospheric oxygen, a smaller 8 mL electrolytic cell was developed (Figure 3.7).

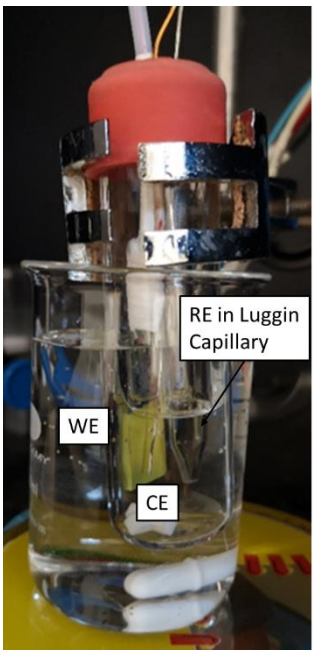

Figure 3.7: Picture of a one-compartment electrolytic cell (8 mL).

As shown in Figure 3.6, the photocurrent at the $BiVO_4$ photoanode was significantly increased to around 3.5 mA cm^{-2} at 0.54 V vs Fc/Fc^+. The enhanced photocurrents observed

thus increased the intermediate benzyl radical concentration significantly, favouring radical-radical coupling and resulting in much higher bibenzyl selectivity (88%) at less anodic potentials (+0.09 V vs Fc/Fc^+). Additionally, the formation of H_2 from proton reduction and CO_2 from decarboxylation were confirmed by GC analysis of the cell headspace.

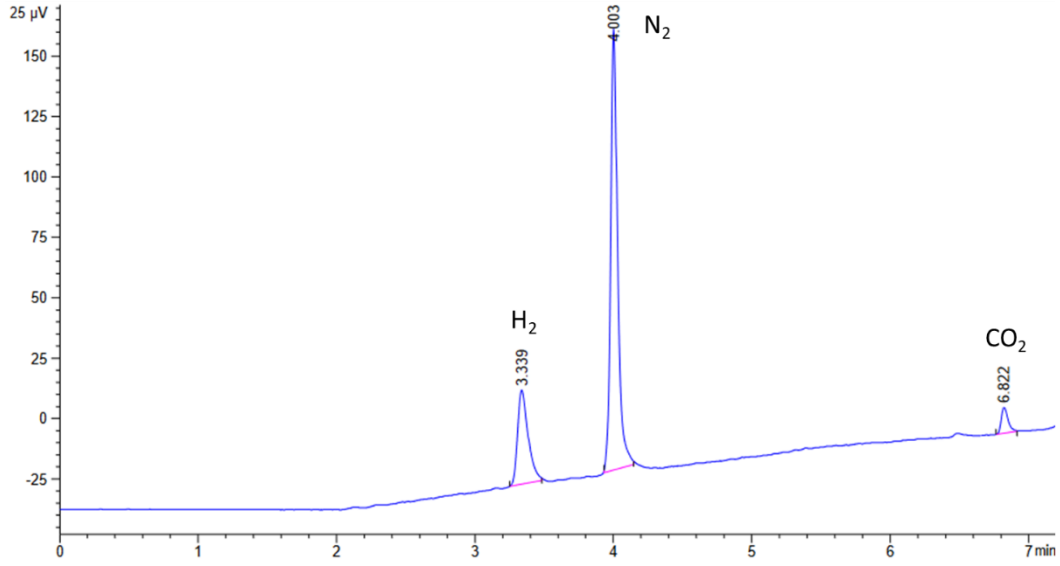

Figure 3.8: Gas chromatogram of the cell headspace after 3-hour electrolysis of 1 M PAA partially neutralised by 0.05 equiv Et_3N. Electrolysis was carried out at +0.09 V vs Fc/Fc^+.

3.2.2 Reference Electrode Stability

Although exceptional photocurrents were generated initially, a 400 mV anodic shift in the onset potential was observed during CV measurements (Figure 3.9). The loss of electrode performance was attributed to either $BiVO_4$ stability in the reaction medium under electrolysis conditions or pseudo-reference electrode instability due to extremely close electrode spacings. It was possible that the concentration gradient between the photoanode and cathode resulted in variable pseudo-reference electrode potentials. Classical reference electrodes, such as Ag/AgCl or the saturated calomel electrode (SCE), establish a fixed potential in an electrochemical system due to the thermodynamic equilibrium of a redox couple – $Ag_{(s)}/Ag^+_{(aq)}$ for Ag/AgCl electrodes and $Hg_{(l)}/Hg^+_{(aq)}$ for SCE. When using a pseudo-reference electrode, no such equilibrium exists, therefore calibration to an external reference is necessary – the ferrocene/ferrocenium redox couple (Fc/Fc^+) in this case. However, as no fixed redox couple is present when using a pseudo-reference electrode, the reference electrode potential can vary with solution composition and must

remain stable over the course of the experiment.[213, 214] Cyclic voltammograms were recorded between -0.3 – 1.0 V vs Pt wire pseudo-reference for 10 cycles under blue LED illumination (Figure 3.9). In this section, potential measurements are referenced to the metal wire for clarity.

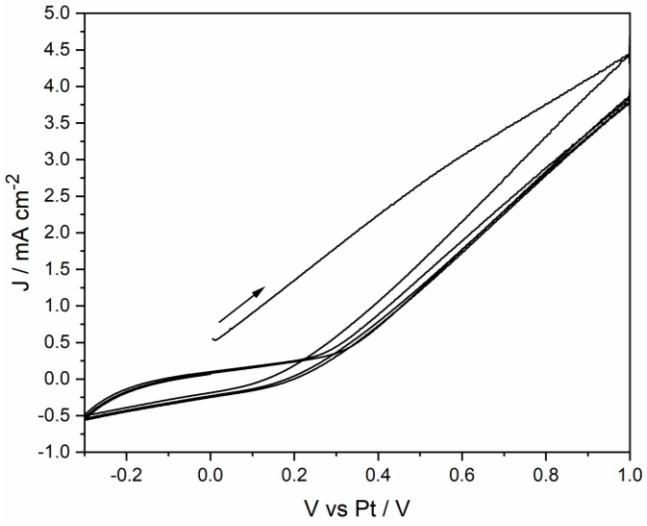

Figure 3.9: Cyclic voltammogram (3 cycles) of a $BiVO_4$ photoelectrode in 1 M PAA with 0.05 equiv Et_3N. Voltammograms were recorded in an 8 mL, one-compartment electrolytic cell with 5 mm electrode spacings under blue LED illumination.

After the initial sweep, consistent photocurrent traces suggested that electrode stability was not the cause of electrode potential changes, as no further photocurrent decay was observed. The large onset potential shift suggested a variable pseudo-reference potential, most likely caused by the concentration gradient established between the photoanode and cathode at such short electrode spacings.

To improve pseudo-reference electrode stability, various methods of isolating the platinum wire were implemented. A fritted glass housing and a Luggin capillary were used to isolate the Pt wire from the bulk solution, minimising diffusion between the bulk solution and the pseudo-reference electrode medium. The pseudo-reference electrode housings were filled with either 1 M PAA partially neutralised by addition of 0.05 equiv Et_3N or 0.1 M tetrabutylammonium hexafluorophosphate ($TBAPF_6$) electrolyte solutions.

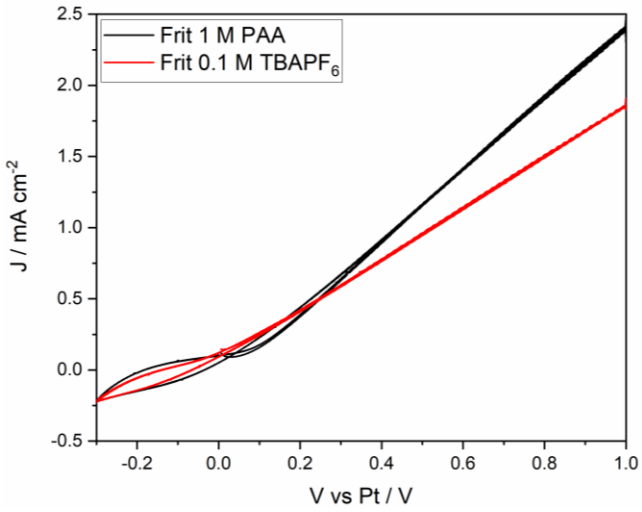

Figure 3.10: Cyclic voltammograms of a $BiVO_4$ photoanode in 1 M PAA partially neutralised by addition of 0.05 equiv Et_3N under blue LED illumination. A Pt wire pseudo-reference was isolated in a fritted tube containing PAA/Et_3N electrolyte (black) and 0.1 M tetrabutylammonium hexafluorophosphate ($TBAPF_6$, red). Scan rate 10 mV s^{-1}.

When using a fritted tube for pseudo-reference electrode isolation, a 200 mV anodic shift of photocurrent onset potential was observed relative to no isolation of the Pt wire (Figure 3.11). The increased onset potential was consistent between all scans, indicating a stable reference electrode potential. The photocurrent onset potential was also independent of the medium in which the pseudo-reference electrode was submerged, with 0.1 M $TBAPF_6$ electrolyte also giving an onset potential of around 0.0 V vs Pt wire. For isolation in 0.1 M $TBAPF_6$ electrolyte, a slight decrease in photocurrent density was observed at all potentials. The decrease was attributed to possible exchange of the bulk and reference solutions and interference of $TBAPF_6$ on the oxidation rate of PAA.

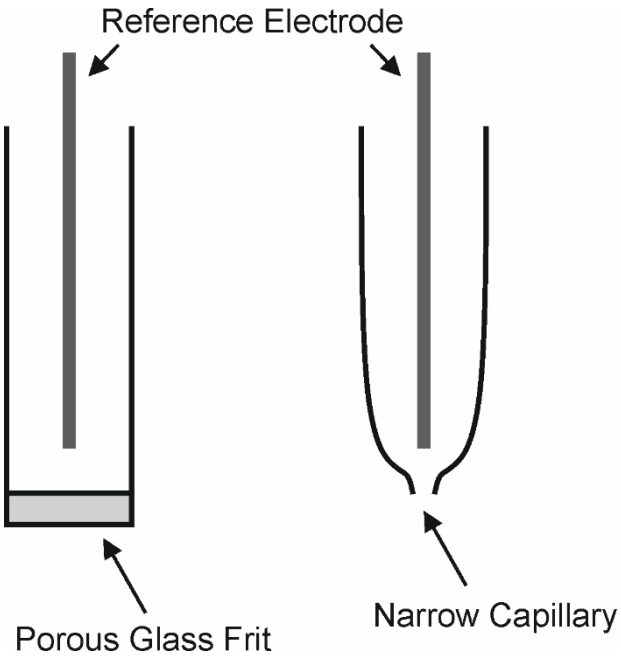

Figure 3.11: Diagram of a reference electrode isolated in a fritted tube (left) and a Luggin capillary (right).

The 200 mV shift in onset potential when using a frit was attributed to a possible potential junction across the frit. Potential junctions are common when using aqueous reference electrodes in non-aqueous systems due to the establishment of a liquid junction between the two phases.[213] Across this junction, a small but noticeable electrochemical potential is observed, possibly resulting in inaccurate potential measurements at the working electrode. Different frit materials and pore sizes have also been shown to affect potential measurements by up to 50 mV.[215] Variation of frit pore size can control the size of solvated ions able to pass between reference electrode and bulk chambers, and can also lead to increased contamination of solutions by excessive mixing of the two phases. Frit materials such as Vycor glass, polyethylene and Teflon were shown to result in variable reference electrode potential as a function of pH, salt concentration and solvent. Due to the shifted onset potential and possible exchange of reference and bulk solutions, isolation of the reference in a fritted glass tube was not selected as an appropriate fix for the instability of Pt wire pseudo-reference electrodes.

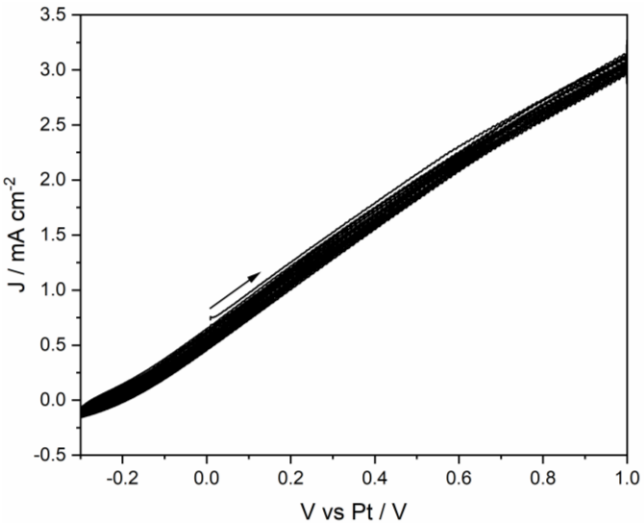

Figure 3.12: Cyclic voltammogram (10 cycles) of a $BiVO_4$ photoelectrode in 1 M PAA partially neutralised by addition of 0.05 equiv Et_3N under blue LED illumination with a Pt wire pseudo-reference electrode isolated by a Luggin capillary. Scan rate 10 mV s^{-1}.

After implementation of the Luggin capillary, cyclic voltammograms showed much more consistent photocurrent density traces across all cycles as well as a fixed photocurrent onset potential of around -0.2 V vs Pt. Unlike the fritted tube, no difference in photocurrent onset potential was observed in comparison to a reference electrode in the bulk solution, suggesting the absence of a junction potential between the reference and working electrodes. Controlled potential electrolyses were recorded at -0.26 V vs Fc/Fc^+ as decreasing photocurrent density at this potential indicated a shift in reference electrode potential (Figure 3.9). Erratic photocurrents were again observed when using the Luggin capillary housing in controlled potential electrolyses (Figure 3.13).

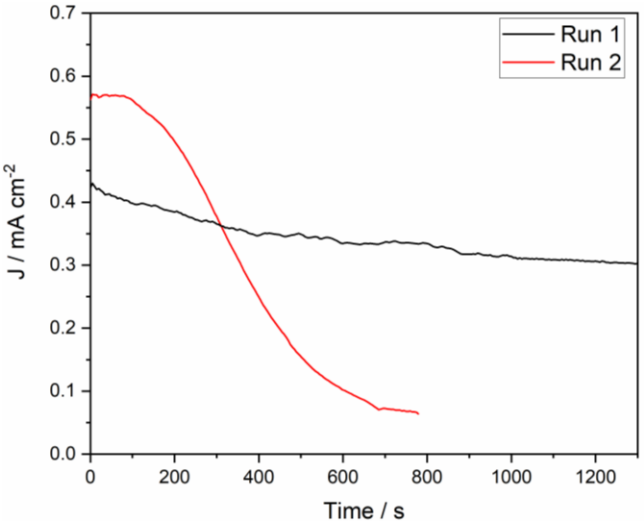

Figure 3.13: Controlled potential electrolyses at -0.26 V vs Fc/Fc^+ for a $BiVO_4$ photoelectrode in 1 M PAA partially neutralised by addition of 0.05 equiv Et_3N. The Pt wire pseudo-reference wire was housed in a Luggin capillary filled with bulk electrolyte.

As isolation of the reference electrode from the bulk solution did not result in stable current-time traces, it was possible that pseudo-reference instability was a result of the electrode material. The platinum wire pseudo-reference was switched for silver wire, resulting in a much more stable pseudo-reference electrode – as shown by photocurrent versus time traces in Figure 3.14.

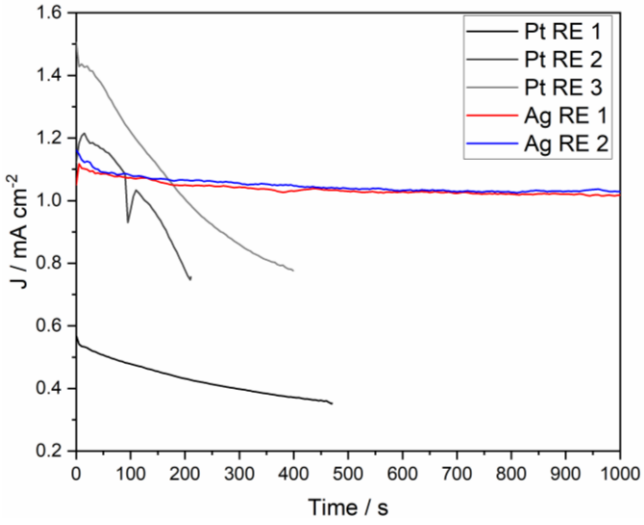

Figure 3.14: Controlled potential electrolyses at -0.26 V vs Fc/Fc^+ using different pseudo-reference electrode materials housed in a Luggin capillary. Electrolyses were carried out in 1 M PAA partially neutralised by addition of 0.05 equiv Et_3N. Individual Pt (black, dark grey, grey) and Ag (red, blue) wires were used for each electrolysis.

When using three different Pt wire reference electrodes, initial photocurrent density varied dramatically between 0.55 – 1.45 mA cm^{-2} (Figure 3.14). Additionally, the temporal changes in photocurrent were inconsistent between each sample. When switching Pt for Ag, a much more stable photocurrent trace was observed, with minimal changes between initial and final photocurrent density after 1000 s of electrolysis. The improved stability of the Ag wire was also independent of the sample, unlike Pt wire pseudo-reference electrodes, suggesting that improved stability was a result of changes to the electrode material.

The improved stability of Ag wire as a pseudo-reference electrode was tentatively attributed to a thin oxide layer at the electrode surface creating an inert barrier between the potentially reactive electrolyte and pure Ag metal electrode.[216, 217] Additionally, due to the low solubility of Ag^+ ions in acetonitrile, it was likely that no leaching of Ag^+ into solution occurred, which is a drawback of Ag/Ag^+ reference electrodes such as silver-silver nitrate.[218] The presence of surface Ag^+ ions generated a stable, thermodynamic equilibrium between Ag/Ag^+ suspended on the reference electrode, providing a much more stable reference potential. Due to the improved potential stability as a pseudo-reference electrode, Ag wires were used for all further experiments.

3.2.3 Effect of Dark Electrolysis

To confirm illumination of the photoelectrode was necessary for the selective generation of bibenzyl, electrolysis in the dark at 2.50 V vs Fc/Fc^+ was carried out.

Table 3.2: Electrolysis parameters for the oxidation of phenylacetic acid in an 8 mL electrolytic cell.

Applied Potential / V vs Fc/Fc^+	Ave. Photocurrent Density / mA cm^{-2}	Illumination Source	FE Bibenzyl / %	FE Total / %
0.09	0.96	Blue LED	88	100
2.50	0.29	-	16	74

As shown in Table 3.2, in spite of the extreme anodic potential, a significant reduction in bibenzyl selectivity is observed in the absence of illumination. This was initially attributed to the reduced current density passed at the $BiVO_4$ electrode in the absence of illumination. Current density measured by LSV was comparable to the current density

generated on illumination (Figure 3.15), however a significant decay was observed over the first 20 minutes of electrolysis (Figure 3.16).

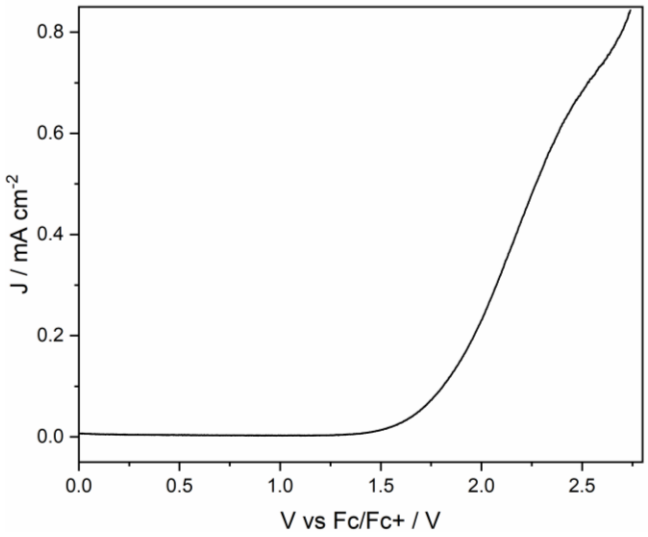

Figure 3.15: Linear sweep voltammogram of a $BiVO_4$ electrode in 1 M PAA solution partially neutralised by addition of 0.05 equiv Et_3N.

Current density increased steadily after 20 minutes but did not reach values measured by LSV. As current density was not particularly stable for dark electrolyses, and bibenzyl FE was much greater under illumination, it was clear that the blue LED light source was extremely important to the selective production of bibenzyl at low anodic potentials.

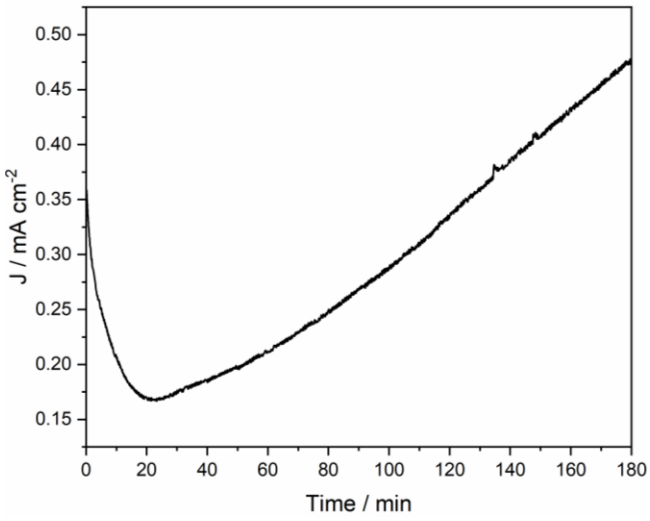

Figure 3.16: Controlled potential electrolysis of 1 M PAA solution partially neutralised by addition of 0.05 equiv Et_3N. Electrolysis was carried out at 2.50 V vs Fc/Fc^+ in the absence of illumination.

3.2.4 Effect of Applied Potential

After ensuring electrolysis conditions were stable over relevant timescales, the effect of electrolysis potential on product selectivity was investigated (Figure 3.17).

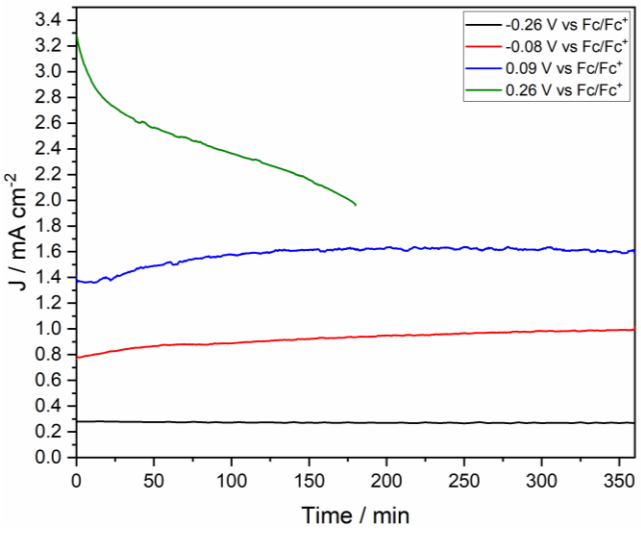

Figure 3.17: Controlled potential electrolysis of 1 M PAA electrolyte partially neutralised with 0.05 equiv Et_3N at -0.26 (black), -0.08 (red), 0.09 (blue) and 0.26 V vs Fc/Fc^+ (green). Electrolyses were carried out under blue LED illumination (32 mW cm^{-2}).

In general, as applied potential was increased, photocurrent density also increased, however, at +0.26 V vs Fc/Fc^+, a significant decay in photocurrent density was observed relative to LSV measurements. This decrease was attributed to instability of the $BiVO_4$ photoelectrode at higher applied potentials. A discussion of the photoelectrode stability is given in section 3.3.

Bibenzyl selectivity after 6 hour electrolyses mimicked photocurrent density trends up to +0.09 V vs Fc/Fc^+, with 88% FE measured for bibenzyl (Figure 3.18). Although an increased bibenzyl production rate was measured at +0.26 V vs Fc/Fc+, overall bibenzyl FE was lower (74%), which, in combination with photocurrent decay over time, suggested electrode instability at more forcing potentials.

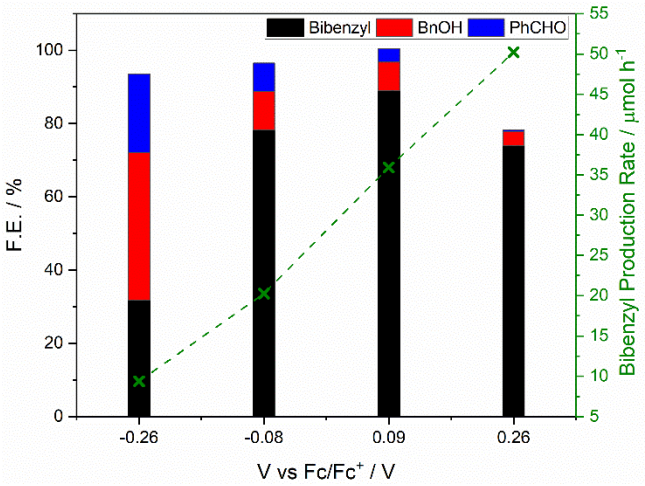

Figure 3.18: Faradaic efficiencies for bibenzyl (black), benzyl alcohol (BnOH, red) and benzaldehyde (PhCHO, blue) after 6-hour electrolysis under blue LED illumination. Bibenzyl production rate as a function of potential is also given (green).

No competing solvent oxidative processes were present in PAA electrolyses reported here, therefore, bibenzyl selectivity was predominantly controlled by photocurrent density provided the photoelectrode remained stable under the applied potential.

Similar photoelectrochemical Kolbe reactions have been performed at TiO_2 electrodes, using acetate and trifluoroacetate electrolytes in acetonitrile.[20, 123] Photocurrent densities of up to 1.2 mA cm^{-2} at 1.1 V vs Ag have been produced for the oxidation of potassium trifluoroacetate electrolytes, though no standard reference is given for comparison of electrode potentials and illumination conditions are very different. For the electrolysis of 80 mM tetrabutylammonium acetate at single-crystal TiO_2 electrodes, Kraeutler and Bard report a FE for ethane of 65% in 0.1 M tetrabutylammonium perchlorate electrolyte. Average photocurrent densities of 6.8 mA cm^{-2} at approximately +0.1 V vs Fc/Fc^+ (0 V vs $Ag/AgNO_3$ quasi reference as quoted) were recorded with irradiation of the TiO_2 photoelectrode by a 450 W Xe lamp.[219] Although photocurrent densities observed at $BiVO_4$ photoelectrodes in this work were significantly lower than those observed at TiO_2, Kolbe product selectivity was much higher (88% under standard conditions at +0.09 V vs Fc/Fc^+).

3.2.5 Photo-Kolbe Selectivity over Time

After optimisation of electrolytic cell conditions and formulation of a stable, accurate pseudo-reference electrode, reaction selectivity as a function of electrolysis time was considered. This was done with the aim of understanding effects of any oxygen leakage into the electrolytic cell and potential fouling of the electrode surface. Additionally, as photocurrents of up to 1 mA cm^{-2} had been obtained at relevant electrolysis potentials, shorter reaction times than 6 hours would still generate a quantifiable amount of products for GC analysis.

A controlled potential electrolysis of 1 M PAA neutralised with 0.05 equiv Et_3N was run for 6 hours at +0.09 V vs Fc/Fc^+ with aliquots taken every hour (Figure 3.19). Sharp increases in photocurrent were observed on restarting the electrolysis due to charging of the electrode caused by the large potential jump from open-circuit conditions to +0.09 V vs Fc/Fc^+.

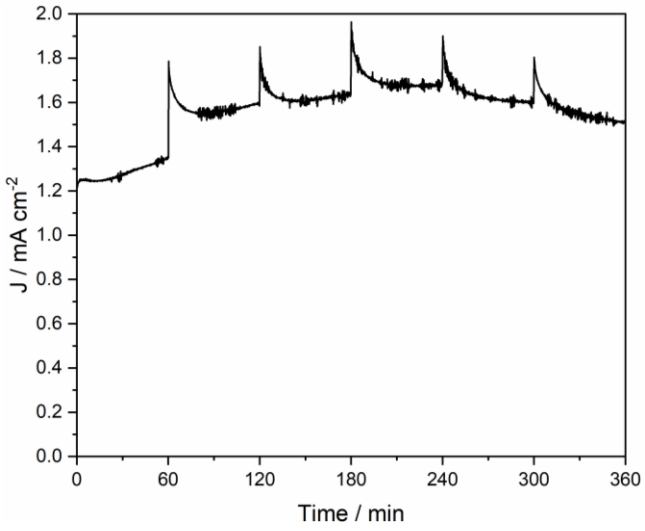

Figure 3.19: Controlled potential electrolysis at +0.09 V vs Fc/Fc^+ of a $BiVO_4$ photoelectrode in 1 M PAA with 0.05 equiv Et_3N. Electrolysis was paused and 200 µL aliquots were taken every hour.

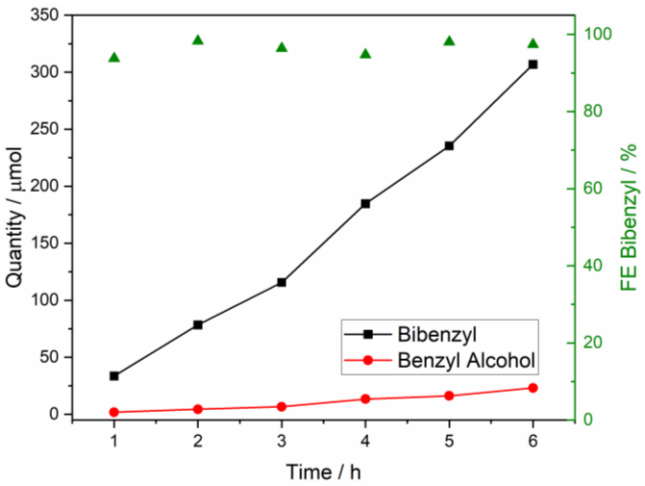

Figure 3.20: Time-dependent formation of bibenzyl (black) and benzyl alcohol (red) over a 6-hour electrolysis of 1 M PAA partially neutralised with 0.05 equiv Et_3N. Faradaic efficiency for bibenzyl is also given (green). Electrolyses were carried out under blue LED illumination at +0.09 V vs Fc/Fc^+.

Generation of both bibenzyl and benzyl alcohol was linear over the timescale of the electrolysis due to the vast excess of carboxylate remaining in the electrolyte (Figure 3.20). As bulk concentrations were relatively unchanged, so too would have been the concentration of carboxylate anions in the Helmholtz layer. Selectivity for bibenzyl remains greater than 90% at all time points, indicating that there is no time-dependence of product selectivity over the first 6 hours of reaction. The enhanced bibenzyl selectivity compared to the 88% measured previously was attributed to the increased photocurrent density resulting from electrode charging.

As product selectivity was independent of time over shorter electrolyses, it was clear that no significant fouling of the electrode occurred as the concentration of PAA does not change appreciably over the course of the reaction and that electrolysis products were stable. Additionally, as product quantities were detectable by GC after only short electrolysis times, further studies of product selectivity were carried out using 3 hour electrolyses as opposed to 6 hours.

3.2.6 Effect of Acid Concentration

The effects of phenylacetic acid and triethylamine concentrations on bibenzyl selectivity were determined through controlled potential electrolyses over 3 hours and GC analysis of product distributions.

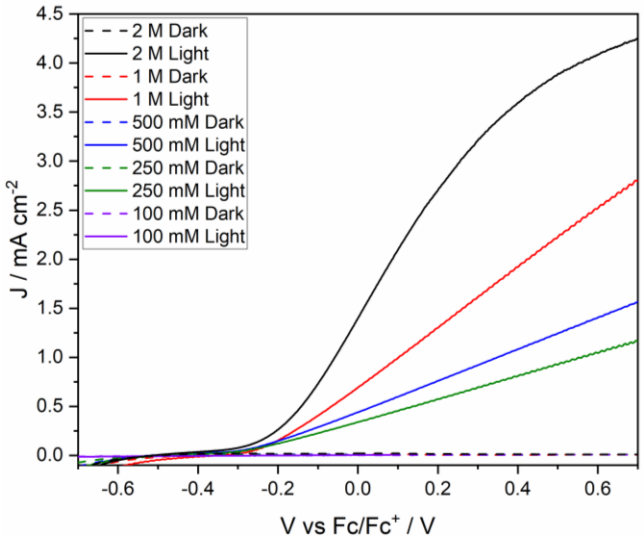

Figure 3.21: Linear sweep voltammograms of a $BiVO_4$ photoanode in 2 M (black), 1 M (red), 500 mM (blue), 250 mM (green) and 100 mM (violet) PAA electrolyte partially neutralised by addition of 0.05 equiv Et_3N.

As PAA concentration was decreased from 2 M to 100 mM, a significant drop off in photocurrent density was observed at all potentials (Figure 3.21). At 100 mM PAA, no photocurrent at all was observed, most likely due to an increase in cell solution resistance. Additionally, voltammogram shape changed from an increase to plateau for 2 M PAA, to overall Ohmic behaviour for 1 M PAA and lower concentrations. This was attributed to increased solution resistance from lower carboxylate concentrations.

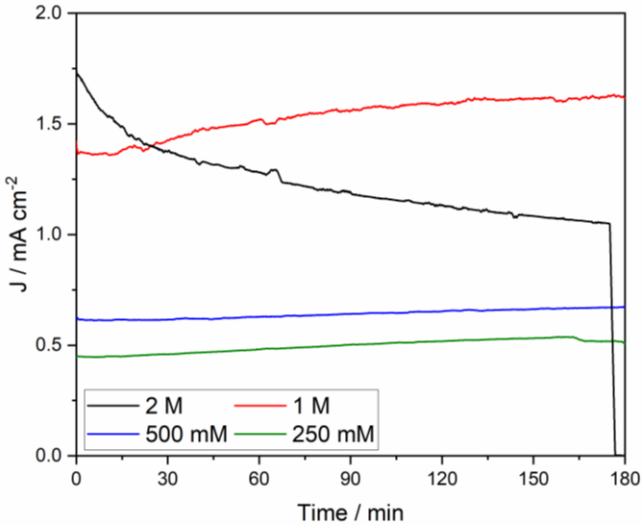

Figure 3.22: Controlled potential electrolyses at +0.09 V vs Fc/Fc^+ in 2 M (black), 1 M (red), 500 mM (blue) and 250 mM (green) PAA electrolyte solutions partially neutralised by addition of 0.05 equiv Et_3N. $BiVO_4$ photoelectrodes were illuminated by a blue LED array (32 mW cm^{-2}).

Controlled potential electrolyses at +0.09 V vs Fc/Fc^+ showed an identical trend in photocurrent to the LSVs, though only a 0.1 mA cm^{-2} difference in photocurrent density is observed between 500 and 250 mM. When using 2 M PAA electrolytes, a sharp decay in the photocurrent density is observed, below levels of 1 M electrolytes. This was attributed to poor photoelectrode stability in higher concentration electrolytes. The bibenzyl selectivity seemed to correlate with average photocurrent, suggesting that the rate of benzyl radical formation was a key factor in determining Kolbe product selectivity (Figure 3.23). By increasing the rate of radical formation, steady-state radical concentrations would be greater and therefore radical-radical coupling rates increased.

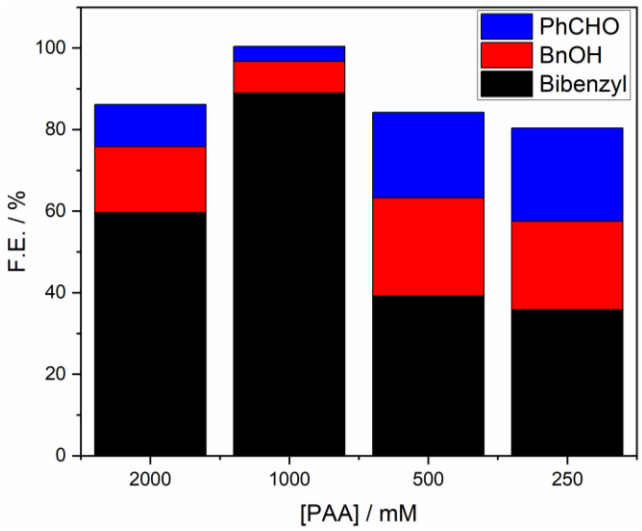

Figure 3.23: Faradaic efficiencies for bibenzyl (black), benzyl alcohol (BnOH, red) and benzaldehyde (PhCHO, blue) after 3-hour electrolysis at +0.09 V vs Fc/Fc^+ for different PAA electrolyte concentrations.

Under standard electrolysis conditions of 1 M PAA with 0.05 equiv Et_3N, a bibenzyl selectivity of 88% was achieved, with the other 12% of charge passed accounted for by non-Kolbe products - benzyl alcohol and benzaldehyde. Increasing acid concentration to 2 M resulted in lower bibenzyl and total FE, attributed to decomposition of the electrode in higher concentration electrolytes, consistent with CPE measurements. As acid concentration was decreased, the F.E. for bibenzyl dropped dramatically to around 39% for 500 mM and 35% for 250 mM PAA. Additionally, non-Kolbe products accounted for a much greater proportion of charge passed with benzyl alcohol F.E. measured at 22% and benzaldehyde F.E. at 21% for both 500 and 250 mM. The total F.E. was calculated assuming single-electron oxidation of phenylacetic acid gave each product. For 500 and 250 mM PAA electrolyte, total FE was some way below 100%, indicating possible multiple-electron oxidation processes. Benzyl alcohol and benzaldehyde can both be oxidised further to form benzoic acid which may have resulted in the 15-20% of charge passed not being accounted for. Gas chromatograms showed no clear peaks for alternative products, and analysis of a benzoic acid standard did not match the retention time of any peaks observed in chromatograms of reaction aliquots. The absence of higher oxidation products meant unaccounted for charge was attributed to a second oxidation of the intermediate radical to a carbocation.[126] Reaction of the carbocation with latent oxygen or water would then have produced the benzyl alcohol and benzaldehyde observed by GC.

For 1 M phenylacetic acid electrolytes, the total FE was attributed to the larger concentration of carboxylate ions in solution. The high carboxylate concentration in the bulk would have been mirrored by the composition of the Helmholtz layer at the electrode surface. Enhanced carboxylate concentrations at the surface may have promoted dissociation/desorption of intermediate benzyl radicals and promoted radical-radical coupling.

Decreased photocurrent densities and thus bibenzyl selectivity was attributed to an increased solution resistance in lower concentration PAA electrolytes (Table 3.3).

Table 3.3: Solution resistance taken from EIS measurements at 50 kHz for PAA electrolytes.

[PAA] / mM	Solution Resistivity / Ω m
1000	164.1
500	272.7
250	470.1

To account for changes in solution resistance on changing PAA concentration, a supporting electrolyte ($TBAPF_6$) was added to adjust the concentration of charged species to 50 mM, as with 1 M PAA electrolytes.

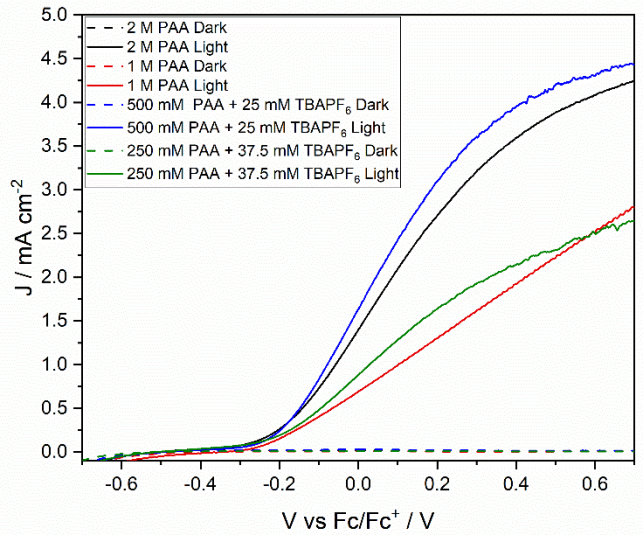

Figure 3.24: Linear sweep voltammogram of a $BiVO_4$ photoanode in 2 M PAA (black), 1 M PAA (red), 500 mM PAA + 25 mM $TBAPF_6$ (blue) and 250 mM +37.5 mM $TBAPF_6$ (green) electrolytes. All solutions were partially neutralised by addition of 0.05 equiv Et_3N relative to PAA. Voltammograms were recorded under blue LED illumination (32 mW cm^{-2}, solid) and in the dark (dashed).

After addition of $TBAPF_6$ supporting electrolyte, a significant increase in photocurrent density was observed, with 500 mM PAA electrolyte reaching up to 4.5 mA cm^{-2} at 0.7 V vs Fc/Fc^+ (Figure 3.24). Additionally, the photocurrent trace is remarkably similar to that of 2 M PAA with no added electrolyte. As a lower photocurrent density was observed for 250 mM PAA with 37.5 mM $TBAPF_6$ and 1 M it was proposed that 'saturation' of the photoelectrode surface with carboxylate anions was achieved in the 500 mM + 25 mM $TBAPF_6$ and 2 M PAA solutions. The overall increases observed on addition of a supporting electrolyte suggested that even at 1 M PAA, solution resistance was an inhibiting factor in photocurrent generation.

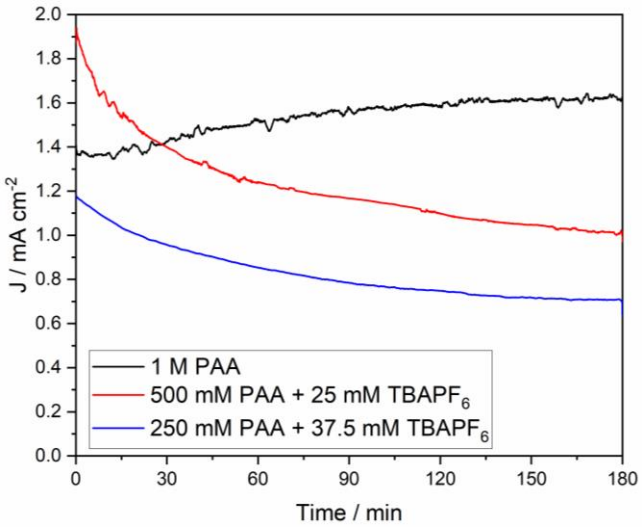

Figure 3.25: Controlled potential electrolyses at +0.09 V vs Fc/Fc^+ in 1 M PAA (black), 500 mM PAA + 25 mM $TBAPF_6$ (red) and 250 mM PAA + 37.5 mM $TBAPF_6$ (blue) electrolyte solutions. All electrolyte solutions were partially neutralised by addition of 0.05 equiv Et_3N with respect to PAA. $BiVO_4$ photoelectrodes were illuminated by a blue LED array (32 mW cm^{-2}).

Although photocurrent density increases were observed on addition of supporting electrolyte, the enhancement was not stable over time (Figure 3.25). For electrolytes with added $TBAPF_6$, a photocurrent density decay over time was observed to levels below that of 1 M PAA electrolyte. This was attributed to anion competition at the electrode surface reducing surface carboxylate concentration, with more pronounced effects as time passed due to the increased $TBAPF_6$ concentration relative to remaining carboxylate.

Table 3.4: Faradaic efficiencies for Kolbe and non-Kolbe products after electrolysis of mixed PAA-$TBAPF_6$ electrolytes at +0.09 V vs Fc/Fc^+ for 3 hours.

[PAA] / mM	[$TBAPF_6$] / mM	FE Bibenzyl / %	FE Benzyl Alcohol / %
500	12.5	29	66
250	37.5	25	52

After electrolysis, bibenzyl FE was much lower for electrolytes containing added $TBAPF_6$ (Table 3.4), in line with literature precedent for electrochemical Kolbe reactions of PAA. Electrolysis at platinum electrodes in methanolic solutions has shown a complete loss of Kolbe product after addition of only 13 mM sodium perchlorate ($NaClO_4$), again attributed to anion competition at the electrode surface.[220] Addition of further $TBAPF_6$ to 250 mM PAA electrolytes resulted in a slight decrease in both bibenzyl and benzyl alcohol FEs, though some Kolbe product was still observed, contrasting electrochemical examples at smooth Pt foils. The observation of Kolbe product for PEC reactions here, even at higher $TBAPF_6$ concentrations, was attributed to enhanced surface area of the porous $BiVO_4$ photoelectrode reducing the negative impact of anion competition by increased number of reaction sites. Additionally, as similar bibenzyl selectivity was observed for both PAA concentrations, there may be specific sites or crystal facets of $BiVO_4$ that strongly bind carboxylate anions which are not displaced by PF_6^-, allowing the Kolbe reaction to proceed even in the presence of $TBAPF_6$.

3.2.7 Effect of Triethylamine Concentration

Triethylamine concentrations between 0.1 – 0.025 equiv were used as a means of altering carboxylate anion concentrations in solution. As triethylamine has been employed as a sacrificial electron donor in PEC systems, low concentrations of triethylamine base relative to PAA were used. By using low base concentrations, the equilibrium would shift in favour of formation of the protonated amine and thus no residual amine would be available for oxidation during electrochemical measurements.

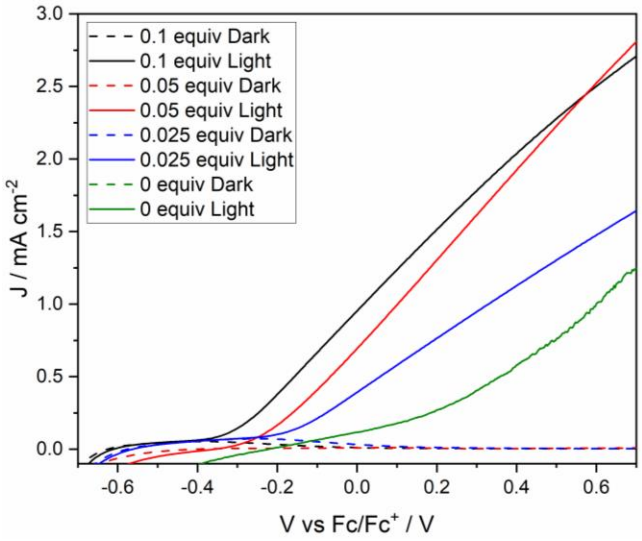

Figure 3.26: Linear sweep voltammograms of a $BiVO_4$ photoanode in electrolytes containing 0.01 (black), 0.05 (red), 0.025 equiv (blue) and 0 equiv (green) triethylamine (Et_3N) relative to PAA. Voltammograms were recorded at a scan rate of 10 mV s^{-1} in the dark and under blue LED illumiantion.

As Et_3N concentration was decreased a 50-80 mV anodic shift in the photocurrent onset potential was observed. The observed shift was attributed to a decreased concentration of phenylacetate anions in the Helmholtz layer decreasing band-bending within the space-charge region of the semiconductor. The equilibration of semiconductor Fermi level and electrochemical potential of the substrate would have resulted in greater electron transfer from the semiconductor to the electrolyte, increasing band bending. Photocurrent onset potentials typically fall around the flat-band potential of the semiconductor, therefore increased band bending at equilibrium would result in a more cathodic flat-band potentials and thus more cathodic onset potential.[221] The potential shift on reducing Et_3N concentration from 0.05 to 0.025 equiv was slightly larger than observed between 0.1 and 0.05 equiv possibly suggesting that a saturation concentration of phenylacetate anions can be obtained, at which point photocurrent onset potential is somewhat fixed.

Although a shift in onset potential was observed between 0.1 and 0.05 equiv Et_3N, the photocurrent generated is similar at all applied potentials. For 0.025 equiv Et_3N a drop of around 40% is observed at +0.7 V vs Fc/Fc^+. The drop in photocurrent may have arisen from the increased concentration of phenylacetic acid relative to phenylacetate anions,

resulting in a less well-defined carboxylate layer at the electrode surface. The formation of a defined carboxylate layer is critical to the rate and selectivity of Kolbe reactions.

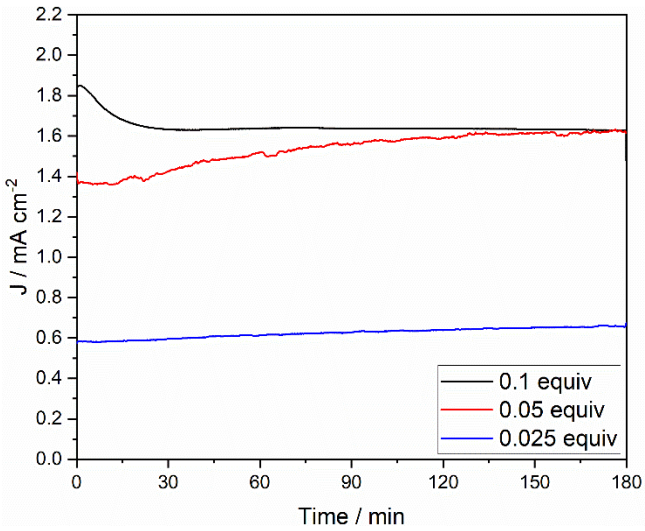

Figure 3.27: Controlled potential electrolyses at +0.09 V vs Fc/Fc^+ for phenylacetic acid electrolyte solutions containing 0.1 (black), 0.05 (red) and 0.025 (blue) equiv Et_3N.

Over 3 hours of electrolysis at +0.09 V vs Fc/Fc^+, photocurrents at each Et_3N concentration were reflective of those measured by LSV (Figure 3.27). As observed with voltammetry, 0.025 equiv Et_3N gave the lowest average photocurrent of 0.6 mA cm^{-2} and was consistent with currents measured by LSV. For 0.05 and 0.1 equiv Et_3N photocurrent densities, an initial difference of around 0.45 mA cm^{-2} was observed between the two electrolytes. However, over the course of the electrolysis a decay in photocurrent density was observed for 0.1 equiv electrolytes and a 0.2 mA cm^{-2} increase observed for 0.05 equiv Et_3N.

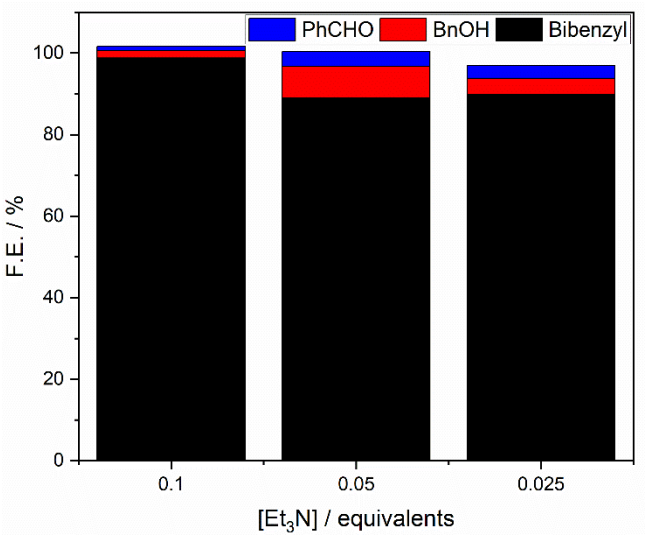

Figure 3.28: Faradaic efficiencies for bibenzyl (black), benzyl alcohol (BnOH, red) and benzaldehyde (PhCHO, blue) as a function of triethylamine concentration after 3 hour electrolysis at +0.09 V vs Fc/Fc^+.

Although average photocurrents were similar for 0.05 and 0.1 equiv Et_3N electrolytes, the highest bibenzyl selectivity was observed with 0.1 equiv Et_3N – 97% FE (Figure 3.28). The independence of selectivity on amine concentration suggested that the concentration of carboxylate in solution was not critical to driving bibenzyl selectivity, provided sufficient amine concentration to regenerate carboxylate anions (Figure 3.28). Additionally, although photocurrent density and carboxylate concentration were very similar for 0.025 equiv Et_3N and 250 mM PAA reactions, bibenzyl selectivity is much lower when using low acid concentrations, suggesting some role of the associated acid in determining the selectivity of the photoelectrochemical Kolbe reaction.

3.3 Bismuth Vanadate Photoelectrode Stability

3.3.1 Characterisation of Photoelectrodes After Electrolysis in 1 M PAA Electrolytes

An ideal photoelectrochemical system would be recyclable without a loss in product selectivity and photoelectrode activity. Understanding the degradation pathways of a catalyst are key to improving performance metrics such as recyclability and stability. For photoelectrochemical Kolbe reactions, a decay of electrode performance was observed with successive use of the same $BiVO_4$ photoelectrode in 1 M PAA electrolytes. The performance decay was exacerbated after electrolysis at more anodic potentials (Figure 3.29).

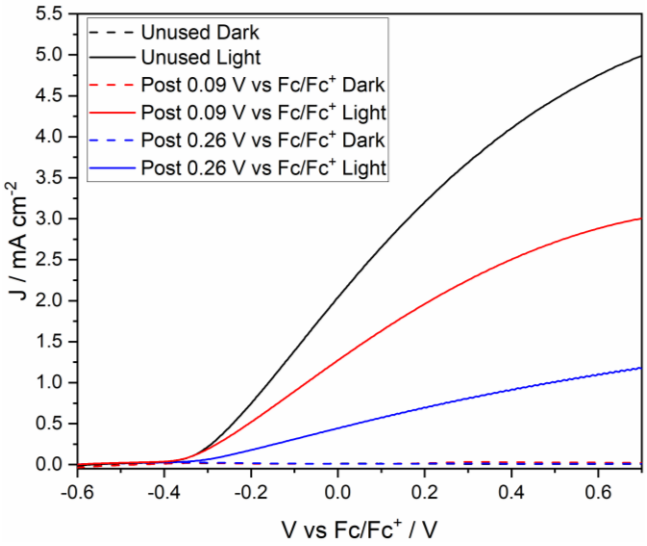

Figure 3.29: Linear sweep voltammograms of a $BiVO_4$ photoelectrode in 1 M PAA electrolyte before (black) and after electrolysis at +0.09 (red) and +0.26 V vs Fc/Fc^+. Voltammograms were recorded in the dark (dashed) and under blue LED illumination (32 mW cm^{-2}, solid).

To elucidate the mechanism of performance losses in $BiVO_4$ photoelectrode, electrodes were characterised by SEM, XRD and XPS after electrolysis and compared to a fresh electrode.

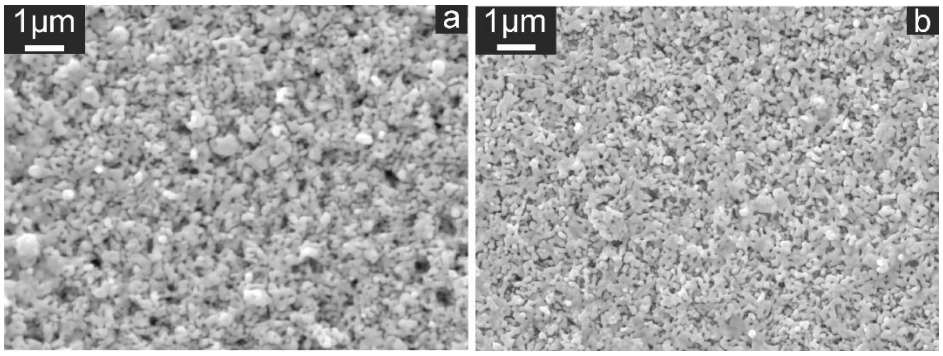

Figure 3.30: Plane SEM images of a $BiVO_4$ photoelectrode a) before and b) after 3 hour electrolysis in 1 M PAA partially neutralised with 0.05 equiv Et_3N.

No clear changes to surface structure or $BiVO_4$ feature size were observed by SEM after electrolysis (Figure 3.30). Feature sizes remained around 100-200 nm, meaning agglomeration of material was not a prominent deactivation pathway in this system.

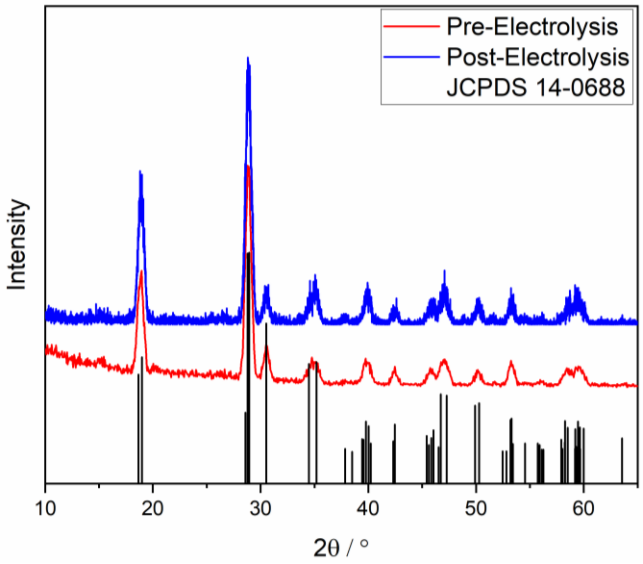

Figure 3.31: GI-XRD diffractogram of $BiVO_4$ photoelectrodes before (red) and after (blue) 3-hour electrolysis in 1 M PAA electrolyte partially neutralised by 0.05 equiv Et_3N. Reference data for monoclinic bismuth vanadate (black lines) is also given.

After electrolysis, X-ray diffractograms were consistent with the original sample, with no new peaks observed (Figure 3.31). This suggested that bulk monoclinic $BiVO_4$ was stable to electrolysis conditions, or that changes were on a small enough scale that they were not detected by GI-XRD measurements. Monoclinic $BiVO_4$ is the most thermodynamically stable phase of $BiVO_4$ therefore conversion to another polymorph, such as tetragonal $BiVO_4$, was unlikely.[222]

XPS analysis of a used $BiVO_4$ photoelectrode showed no evidence for peak shifts compared to the fresh sample (Table 3.5, Table 3.6). This suggested no new Bi and V species had been formed during electrolysis and that no change in oxidation state of bismuth or vanadium occurred at the electrode surface.

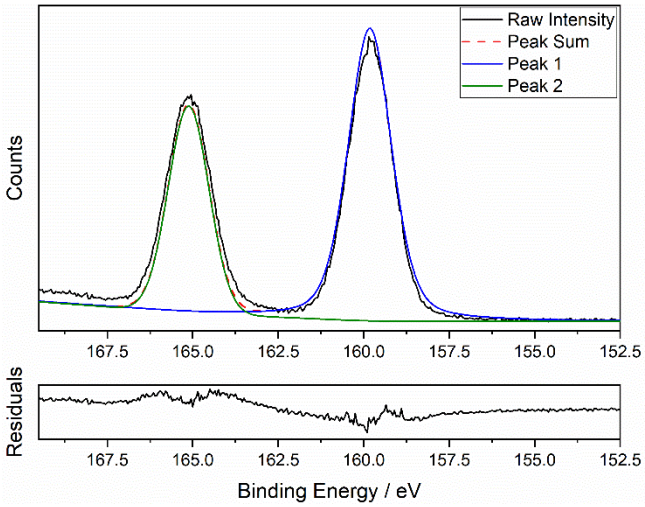

Figure 3.32: Bi 4f region of the XPS spectrum of a $BiVO_4$ photoelectrode after 3-hour electrolysis in 1 M PAA electrolyte partially neutralised by 0.05 equiv Et_3N.

Table 3.5: Summary of deconvoluted XPS signals in the Bi 4f region of a $BiVO_4$ photoelectrode after 3-hour electrolysis in 1 M PAA electrolyte partially neutralised by 0.05 equiv Et_3N.

Region	Peak	Species	Peak Position / eV	Peak FWHM / eV	Percentage Integration
Bi 4f	1	Bi^{3+} $4f_{7/2}$	159.8	1.5	63.7
	2	Bi^{3+} $4f_{5/2}$	165.1	1.4	36.3

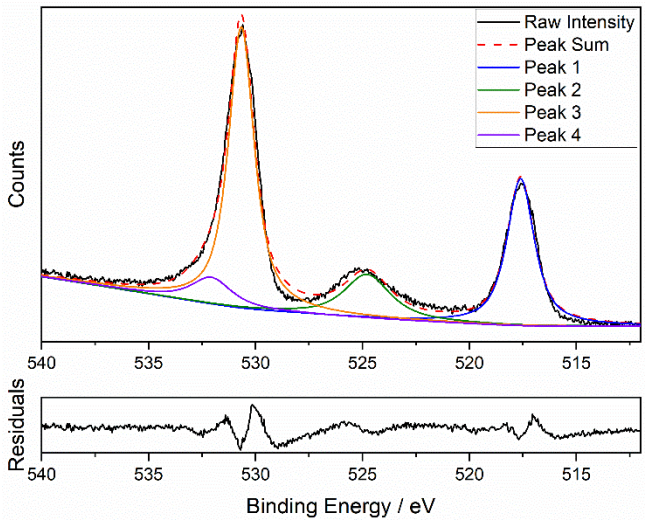

Figure 3.33: V 2p and O 1s region of the XPS spectrum of a $BiVO_4$ photoelectrode after 3-hour electrolysis in 1 M PAA electrolyte partially neutralised by 0.05 equiv Et_3N.

Table 3.6: Summary of deconvoluted XPS signals in the V 2p and O 1s regions of a $BiVO_4$ photoelectrode after 3-hour electrolysis in 1 M PAA electrolyte partially neutralised by 0.05 equiv Et_3N.

Region	Peak	Species	Peak Position / eV	Peak FWHM / eV	Percentage Integration
V 2p	1	V^{5+} $2p_{3/2}$	517.6	1.53	28.0
	2	V^{5+} $2p_{1/2}$	524.8	2.57	14.0
O 1s	3	Metal Oxide	530.7	1.44	50.4
	4	Hydroxide/Water	532.1	2.28	7.6

Quantitative XPS analysis of a $BiVO_4$ photoelectrode before and after electrolysis gave an initial surface Bi:V ratio of 1.00:1.94, with a relative loss of V and O after electrolysis (Table 3.7). The initial excess of vanadium and oxygen measured by XPS may have been explained by the formation of a V_2O_5 layer at the electrode surface. Any formation of crystalline V_2O_5 would have been detected by XRD unless quantities were below detection limits. Additionally, due to the thin $BiVO_4$ films, signal-to-noise ratio of GI-XRD diffractograms is quite poor. As no clear XRD evidence for vanadium oxides was observed, the origin of excess vanadium and oxygen at the electrode surface could not be determined conclusively. The surface stoichiometry was tentatively attributed to the formation of a vanadium rich electrode surface due to bismuth volatility during the annealing process.[174, 186] Excess vanadium at $BiVO_4$ surfaces have been observed by XPS, with changes in stoichiometry linked to improved performance. After manipulation of surface stoichiometry with sodium hydroxide, Bi enriched surfaces (Bi:V = 79:21) showed enhanced photocurrents for sulfite oxidation.[188] In depth analysis of the surface stoichiometry and its effects on the PEC Kolbe reaction could be an avenue for further research.

Table 3.7: XPS quantification data for a $BiVO_4$ photoelectrode surface before and after 3-hour electrolysis at +0.09 V vs Fc/Fc^+.

	Pre-electrolysis		Post-electrolysis	
Peak	Binding Energy / eV	Relative Quantity	Binding Energy / eV	Relative Quantity
Bi 4f	159.7	1.00	159.9	1.00
V 2p	517.6	1.94	517.6	1.67
O 1s	530.6	7.88	530.6	6.82
C 1s	285.0	1.48	285.0	1.78

Photocorrosion of $BiVO_4$ photoelectrodes generally proceeds by leaching of vanadium from the electrode.[223, 224] However, in non-aqueous media such as MeCN, suppression of $BiVO_4$ photocorrosion has been observed, therefore vanadium leaching here was not attributed to photocorrosion of the electrode.[112] Nevertheless, the loss of vanadium from the electrode surface may have caused performance losses in $BiVO_4$ photoelectrodes.

In addition to a relative loss of vanadium and oxygen, a slight increase in the amount of carbon on the sample was observed. Therefore, an alternative mechanism for performance losses was through fouling of the electrode surface by overoxidation of hydrocarbyl species such as the benzyl radical. The increase in carbon content observed by XPS could not be taken as conclusive proof of passivation during electrolysis as carbonaceous materials can be deposited during handling of the samples prior to analysis.

Pourbaix diagrams (Figure 3.34) of $BiVO_4$ in aqueous solution show that at low pH, as would be expected with high acid concentrations in the electrolyte, the anodic potential range over which the electrode is stable is extremely small; less than 1.0 V below pH 7.[225]

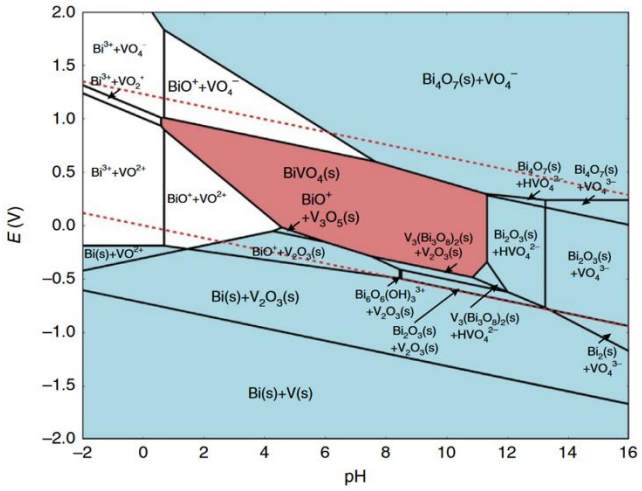

Figure 3.34: Pourbaix diagram for BiVO4 in aqueous solution. Dotted red lines indicate the hydrogen and oxygen evolution reactions. Figure was taken from Toma et al., Nat. Commun., 2016.[225]

As such, it was possible that the poor recyclability and stability of $BiVO_4$ photoelectrodes in PAA electrolytes resulted from a phase transition at 0.09 V vs Fc/Fc^+ during electrolysis. The relative loss of vanadium and oxygen after electrolysis, and further decay at higher potentials, indicated that electrolysis conditions lay outside the window of stability for $BiVO_4$. However, as pH is difficult to determine accurately in non-aqueous solution, it was difficult to establish a clear potential range over which $BiVO_4$ electrodes were stable in PAA electrolytes.

3.3.2 UV-Ozone Treatment of Bismuth Vanadate Photoelectrodes

Fouling of metal and metal oxide surfaces can be removed by treatments that oxidise the carbonaceous impurities to CO_2 or C-containing species that desorb. Methods such as electrochemical cleaning, chemical treatment and UV-ozone treatment have been used to remove carbonaceous impurities from gold electrodes and $Y:ZrO_2$ surfaces.[226, 227]

To remove any possible passivating organic material from $BiVO_4$ photoelectrodes, UV-ozone treatment was carried out for 5 minutes on a sample that had been used for electrolysis at +0.26 V vs Fc/Fc^+.

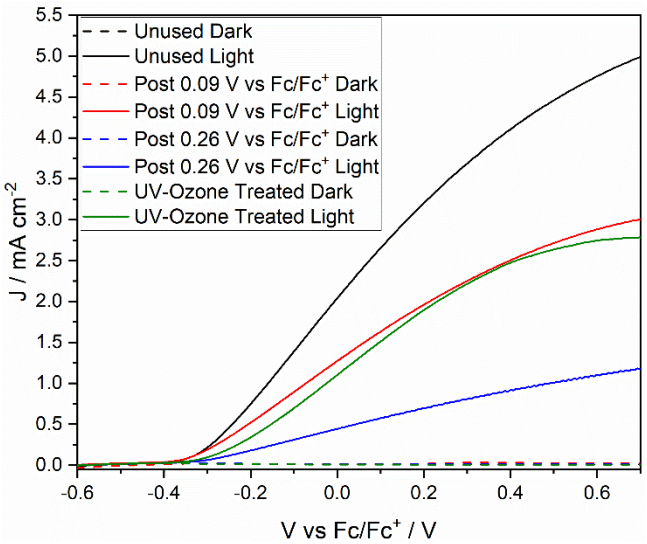

Figure 3.35: Linear sweep voltammograms of a $BiVO_4$ photoelectrode before (black) and after electrolysis of 1 M PAA electrolyte at 0.09 (red) and 0.26 V vs Fc/Fc^+ (blue), and after UV-ozone treatment for 5 minutes (green). Voltammograms were recorded in the dark (dashed) and under blue LED illumination (32 mW cm^{-2}, solid).

LSV measurements of the UV-ozone treated sample showed a reasonable performance improvement, with photocurrent densities increased by up to 1.5 mA cm^{-2} at +0.26 V vs Fc/Fc^+ (Figure 3.35). Despite the performance improvement, photoelectrode performance remained much worse than a fresh $BiVO_4$ photoelectrode. Degradation of $BiVO_4$ photoelectrodes was therefore attributed to two main pathways – fouling and vanadium leaching. Fouling accounted for some of the reversible photocurrent density losses observed, however irreversible photocurrent loss was attributed to vanadium leaching at the electrode surface.

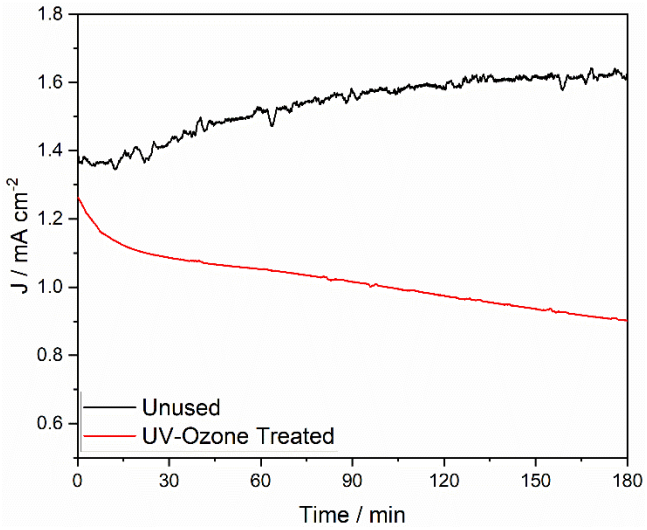

Figure 3.36: Controlled potential electrolysis of 1 M PAA partially neutralised with 0.05 equiv Et_3N at an unused $BiVO_4$ photoelectrode (black) and a UV-ozone treated photoelectrode (red).

A 0.2 mA cm^{-2} decrease in initial photocurrent density was observed for the UV-ozone treated sample during electrolysis (Figure 3.36). Over the course of the electrolysis, the discrepancy between the two photoelectrodes increases as a decay in photocurrent density is observed for the UV-ozone treated sample. This was tentatively attributed to further vanadium leaching during electrolysis reducing the PEC performance of the electrode.

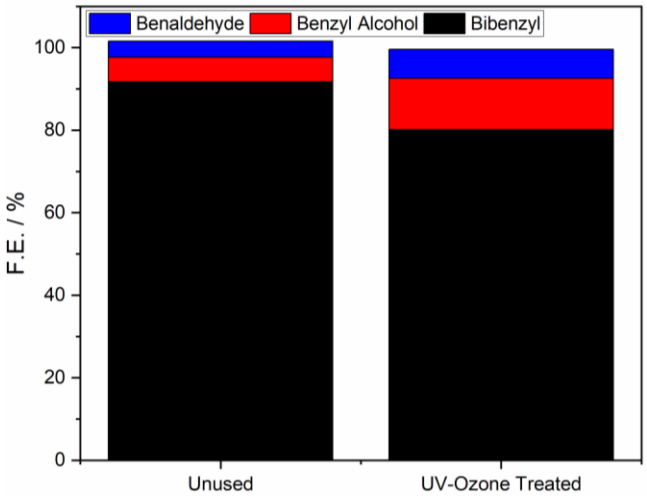

Figure 3.37: Faradaic efficiencies for bibenzyl (black), benzyl alcohol (red) and benzaldehyde (blue) after 3 hour electrolyses at an unused $BiVO_4$ photoelectrode and after UV-ozone treatment.

A slight decrease in bibenzyl selectivity of around 15% was observed after UV-ozone treatment. Although still a reasonably high selectivity (77%), the lower selectivity was attributed to the lower photocurrent density of the treated photoelectrode and further decay of electrode performance due to V leaching. Overall, UV-ozone treatment posed a reasonable method for restoring photoelectrode performance after electrolysis. However, due to the lower Kolbe product selectivity and decay in photocurrent density with time, further experiments were carried out using fresh $BiVO_4$ photoelectrodes as opposed to regenerated samples. As vanadium leaching seemed a prominent degradation pathway, complete regeneration of electrode activity was unlikely. Further work investigating the application of surface protecting layers or co-catalysts could help improve

photoelectrode stability to the optimised photoelectrochemical Kolbe conditions described.

3.4 Conclusions

In this chapter, a highly active photoelectrochemical Kolbe reaction system has been developed. Although good stability was observed under optimised conditions, at more forcing reaction conditions, such as higher acid concentrations and applied potentials, stability is much poorer. Selectivity up to 97% for bibenzyl was obtained at $BiVO_4$ photoelectrodes for electrolysis of 1 M PAA solutions partially neutralised by 0.1 equiv Et_3N.

PEC Kolbe reactions were shown to be sensitive to several factors including electrolytic cell parameters, applied potential and electrolyte composition. Improvements to FE for bibenzyl (88%) were observed at milder potential (+0.09 V vs Fc/Fc^+) on moving to blue LED illumination (32 mW cm^{-2}) in a one-compartment cell due to a combination of increased photocurrent density and smaller cell volume generating greater concentrations of benzyl radicals at steady state, favouring radical-radical coupling.

Selectivity generally followed photocurrent trends when altering applied potential and electrolyte composition, though lower bibenzyl selectivity (74%) was obtained at +0.26 V vs Fc/Fc^+ due to electrode deactivation at higher potentials. Similar electrode instability was observed for 2 M PAA electrolytes, as shown by decaying photocurrent density with time and total FEs lower than 100%. Deactivation of $BiVO_4$ photoelectrodes was attributed to a combination of electrode fouling and leaching of surface vanadium as observed by XPS. UV-ozone treatment could be used to restore photoelectrode performance but not to original photocurrent densities. Further work on electrode modifications could be carried out to improve electrode stability and activity through surface protecting layers and heterojunction formation.

4. Substrate Effects and Mechanistic Studies of the Photoelectrochemical Kolbe Reaction at $BiVO_4$ Photoelectrodes

4.1 Introduction

4.1.1 Substituent Effects in the Kolbe Electrolysis of Arylacetic Acids

In the Kolbe electrolysis of aliphatic carboxylic acids, substitution at the alpha-position has been shown to dictate selectivity between Kolbe and non-Kolbe pathways. Electron donating substituents stabilise the formation of a carbocation and therefore favour non-Kolbe pathways such as methoxylation reactions in methanolic solutions. For the electrolysis of phenylacetic acid, substitution at the alpha-position and around the aryl ring can influence electrochemical behaviour and product selectivity.

Recent work has documented oxidation potentials for phenylacetic acid, phenylacetate and several derivatives. Unsubstituted phenylacetic acid has an oxidation potential of 2.51 V vs SCE which is decreased to 1.27 V vs SCE after deprotonation to the carboxylate.[132] Aryl substitution tends to lower the oxidation potential of the carboxylate, typically by a few 10s of mV. However, for 4-methoxyphenylacetic acid (+0.99 V vs SCE), a significant shift in oxidation potential of the carboxylate is observed. This has been attributed to the strong electron donation activating the carboxylate for oxidation. The activation effect of methoxy substituents also lowers the oxidation potential of the intermediate radical (0.26 V vs SCE) compared to the unsubstituted phenylmethyl radical (0.73 V vs SCE). Electron-donating substituents thus favour 2-electron oxidation to the carbocation and preferential formation of methoxylated products in methanolic solutions.[228, 229]

Although changes to oxidation potential are observed on substitution of phenylacetate anions, there seems to be no correlation between oxidation potential and product selectivity in their electrolysis in methanolic solutions. Coleman *et al*. report the highest dimer selectivity for pentafluorophenylacetic acid (74%) followed by unsubstituted phenylacetic acid (68%) after electrolysis.[230] Other strongly electron withdrawing substituents, such as 4-CF_3 and 4-Cl, show lower dimer selectivity than the unsubstituted acid – 37 and 4% respectively. All mono-substituted arylacetic acids showed lower dimer selectivity and increased selectivity for methoxylated product, formed from reaction of the

carbocation and solvent. The highest selectivity for methoxylated products was observed for 4-methoxyphenylacetic acid, as expected based on oxidation potentials of the carboxylate and intermediate radical. However, product analysis was carried out after only 5% phenylacetate conversion, so the time dependence of product selectivity is unclear.

Some changes in selectivity were observed on changing from 4- to 3- to 2-substitution, namely that carbocation formation is favoured for 2-substituted PAAs. This correlation was observed for -CF_3 substituted PAAs (37, 30 and 24% for 4-, 3- and 2-substitution respectively) but not for methyl substituted, where dimer yields for 4- (38%) and 3-methylphenylacetate (40%) are similar.

In all cases of phenylacetic acid substitution, intermediate radicals have lower oxidation potentials than the carboxylate. Therefore, selective formation of the Kolbe product is kinetically driven. This is a significant reason for the use of high current densities and carboxylate concentrations in electrochemical examples. Indeed, at low current densities (3.2 mA cm^{-2}) at platinum electrodes in methanol, benzaldehyde (80%) is the major product of phenylacetate oxidation.[220]

For some arylacetic acids, direct oxidation of the aryl moiety has been observed in acetonitrile with added tetrabutylammonium perchlorate electrolyte (0.1 M).[231] For naphthyl and anthracylacetic acids, oxidation of the aryl moiety still leads to the formation of Kolbe products in a 'pseudo-Kolbe' reaction with reasonable selectivity – around 30%.[231] Preparative electrolyses of these acids were carried out in THF/MeOH mixtures, therefore mechanistic inferences from cyclic voltammetry measurements in acetonitrile may not hold. Measured oxidation potentials for aryl moieties lay around 0.5 V vs SCE more anodic than corresponding carboxylates (around 1.0 V vs SCE), therefore oxidation selectivity in these examples cannot solely be attributed to thermodynamic parameters. The pseudo-Kolbe reaction pathway has also been shown to proceed for methoxy-substituted arylacetic and aliphatic acids.[145, 228] Initial oxidation of the methoxy substituent is followed by an intramolecular dissociative electron transfer (IDET) to form the carbon centred radical. This radical then either dimerises, or, more likely, undergoes a second oxidation to the carbocation.

From existing electrochemical studies, no correlations between carboxylate oxidation potential and dimer selectivity are clear, therefore changes in reaction pathway are not solely thermodynamic in origin. Processes such as substrate adsorption are known

to play a key, if unclear, role in Kolbe electrochemistry, and may factor in deciding between conventional and pseudo-Kolbe pathways for arylacetic acids.[232]

4.1.2 Aims

In this chapter, the key aim was to expand mechanistic understanding of the Kolbe reaction at $BiVO_4$ electrodes, particularly the substrate effects of substituted phenylacetic acids on product selectivity. Initially, development focused on exploring the scope of photoelectrochemical Kolbe reactions with phenylacetic acid derivatives. Electrochemical measurements in acid electrolytes were combined with GC quantification of products to probe substituent effects on Kolbe product selectivity. Further characterisation of electrodes by EIS was used as an in situ probe of charge carrier behaviours to determine key limitations of bismuth vanadate as a photoelectrode material for PEC Kolbe reactions.

Comparison of photoelectrochemical systems between high and low acid concentration electrolytes was used as a mechanistic probe to investigate the nature of the radical intermediate at the electrode surface and subsequent effects on reaction pathways. Finally, impedance spectroscopy was used to characterise charge carrier behaviours within the electrode and correlate these between different electrolysis conditions.

4.2 Substituent Effects of the Photoelectrochemical Kolbe Reaction at $BiVO_4$ Photoelectrodes

4.2.1 Photoelectrochemical Kolbe Reaction of Phenylacetic Acid Derivatives

Once optimised photoelectrochemical conditions had been established, the scope of the photoelectrochemical Kolbe reaction at $BiVO_4$ photoelectrodes was explored to determine substituent effects on Kolbe product selectivity. Initially, phenylacetic acid derivatives with aryl substituents were employed as substrates for photoelectrochemical Kolbe reactions. The photoelectrochemical behaviour of substrates was initially investigated by LSV and CPE measurements to observe the effect of substituents on reaction kinetics. Electrolyses of phenylacetic acid derivatives were carried out once per substrate.

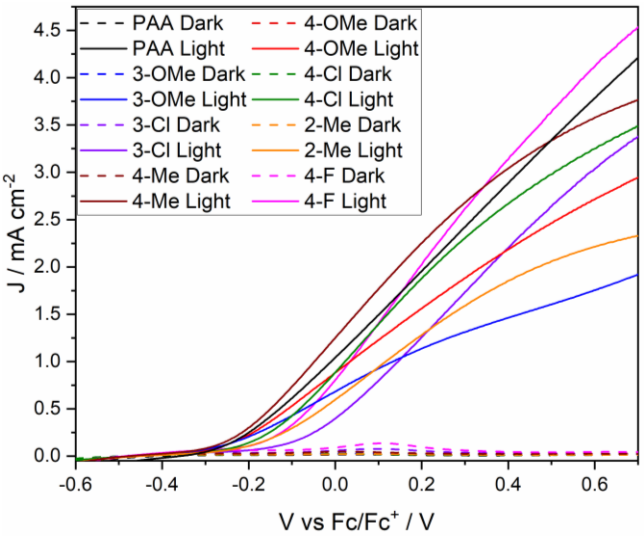

Figure 4.1: Linear sweep voltammograms of $BiVO_4$ photoelectrodes in 1 M electrolytes of substituted phenylacetic acids with 0.05 equiv Et_3N. Voltammograms were recorded in the presence (solid) and absence (dashed) of blue LED illumination.

From the linear sweep voltammograms (Figure 4.1), photocurrent onset potentials showed no clear correlation with electronic substituent effects, or oxidation potential of the carboxylate anions.[132] Electron-donating substituents 4-OMe and 4-Me showed the most cathodic onset potentials, whilst electron withdrawing 3-Cl exhibited the most anodic onset potential. Although a possible general trend of electron-donating substituents making onset potentials more cathodic, trends did not follow the extent of electron-withdrawing/donating of the substituent given by Hammett parameters, σ (Table 4.1).[233]

Table 4.1: Electrochemical oxidation potentials of carboxylate anions and photocurrent onset potentials measured by LSV and Hammett σ parameters for aryl-substituted phenylacetic acids.

Aryl Substituent	Oxidation Potential / V vs SCE[132]	Photocurrent Onset Potential / V vs Fc/Fc^+	σ
H	1.27	-0.32	0
4-Me	1.17	-0.35	-0.17
4-OMe	0.99	-0.34	-0.27
3-OMe	1.17	-0.33	0.12
4-Cl	1.25	-0.28	0.23
2-Me	-	-0.28	-
4-F	1.21	-0.21	0.06
3-Cl	-	-0.21	0.37

Cyclic voltammetry of several phenylacetate anions has shown changes in oxidation potential of up to 0.3 V vs SCE, however the same trends were not observed here, meaning changes to photocurrent onset potential were not due to changes in oxidation potential (E_{ox}) of the substrates. As onset potentials were relatively similar and changes were small, it was possible that these values were controlled by recombination of photogenerated charge carriers in the photoelectrode. The onset potential may have reflected the necessary potential to suppress recombination to a sufficient extent that oxidation of carboxylate was enabled. This may be indicative of Fermi level pinning by surface electronic states at the semiconductor-electrolyte interface. Fermi level pinning is described for a semiconductor-metal interface in Section 1.1.1, however similar effects can be observed when a high concentration of filled electronic states exist at the semiconductor surface. Fermi level pinning by surface states can be characterised by an independence of photovoltage on substrate redox potential.[30, 234] By approximating the photovoltage as the difference between the photocurrent onset potential and E_{ox} of the substrate, and assuming a consistent overpotential, a similar independence is observed here, suggesting Fermi level pinning dictates the photocurrent onset potential.[235]

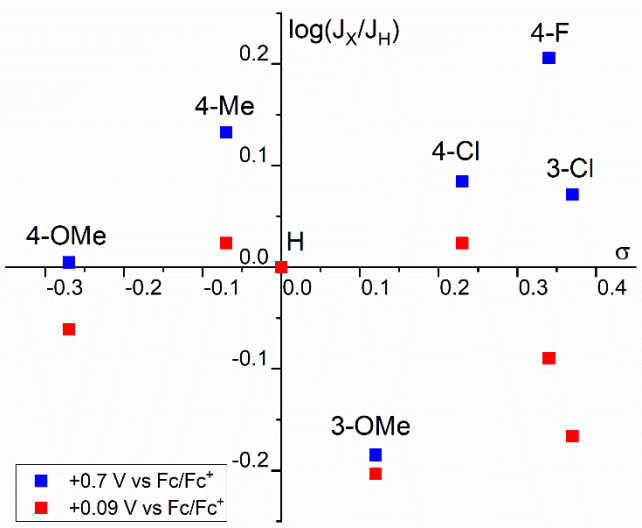

Figure 4.2: Hammett-style plot for photocurrent density at +0.09 (red) and +0.70 V vs Fc/Fc^+ (blue) of aryl-substituted phenylacetic acids.

No correlation between electronic substituent effects and photocurrent density was observed across aryl-substituted phenylacetic acids by LSV, as shown by Hammett-style plots of photocurrent density at +0.09 V and +0.70 V vs Fc/Fc^+ (Figure 4.2). The reaction kinetics at photoelectrodes are controlled predominantly by generation of charge carriers by absorption and recombination of electron-hole pairs.[31] As applied potential is

increased, recombination is suppressed by increasing the electric field gradient across the semiconductor, providing impetus for electron-hole separation by increasing band-bending. The band-bending is affected by the nature of the electrolyte due to the equilibration of E_F and E_{redox} of the substrate. At +0.09 V vs Fc/Fc^+, current-voltage characteristics are linear, meaning kinetics are mostly controlled by surface hole availability, which increases with applied potential due to suppression of electron-hole recombination. In this regime, electrode kinetics are likely dominated by recombination, rather than solely by substituent effects so no trends were observed at low applied potentials. However, no correlation was observed with photocurrent densities at +0.7 V vs Fc/Fc^+, either. Recombination rates are also acutely affected by the presence of defect states within the photoelectrode, therefore at low applied potentials, photocurrents may have been influenced by variable defect compositions in $BiVO_4$ photoelectrodes.

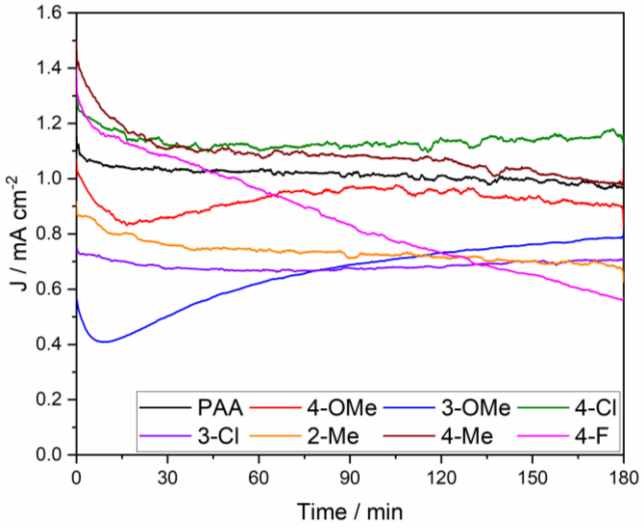

Figure 4.3: Controlled potential electrolyses of 1 M electrolytes of substituted phenylacetic acids containing 0.05 equiv Et_3N at +0.09 V vs Fc/Fc^+.

Controlled potential electrolyses of aryl-substituted acid electrolytes showed no clear photocurrent trends over 3 hours for electron-withdrawing or donating groups based on electronic substituent effects (Figure 4.3). In the literature, an independence of Kolbe dimer selectivity on electronic substituent effects has also been observed for electrochemical oxidations of substituted phenylacetate anions in methanol.[228, 236] However, excluding 4-F-PAA, time-averaged photocurrent densities for 3- and 2-substituted phenylacetic acids were lower than for 4-substituted derivatives. As 3- and 2-substituted phenylacetic acids will be less rod-like in shape it was possible that acid packing at the electrode surface was poorer, reducing surface carboxylate concentration and therefore

photocurrent density. As dimer selectivity generally increased with increasing photocurrent density, the poorer packing resulted in lower dimer yields for 3- and 2-substituted PAAs (Figure 4.4). At Pt electrodes, the electrochemical Kolbe reaction of α-silylacetic acids gives significantly poorer dimer yields as steric congestion of the silane was increased.[237]

Initial photocurrents at 0 minutes follow trends seen by LSV identically, however photocurrent decay of up to 0.2 mA cm^{-2} over the first 20 minutes was observed for all substituted acids. After the initial decay, most substituted phenylacetic acid electrolytes showed stable photocurrents over 3 hour electrolyses except for methoxy- and fluorophenylacetic acids. The photocurrent decay followed by plateau was attributed to possible charging of the electrode-electrolyte interface by accumulation of carboxylate anions. Accumulation of substrate at the electrode surface is matched by an accumulation of holes in the space-charge region of the photoelectrode, generating an enhanced photocurrent density for a short period.[66, 238] After the initial decay, the kinetics were then regulated by flux of photogenerated holes to the surface of the electrode.

For methoxy-substituted phenylacetic acids, photocurrent densities recovered after the initial decay before plateau at around 1.05 mA cm^{-2} for 4-OMe and 0.75 mA cm^{-2} for 3-OMe-PAA. Although reasonable photocurrent densities were recorded for these substrates, no Kolbe dimer production was observed. For methoxy-substituted phenylacetic acids, preferential oxidation of the methoxy substituent and subsequent rearrangement to give a benzylic radical or cation has been observed when using stoichiometric oxidants (such as cerium ammonium nitrate, CAN) as well as electrochemically at Pt electrodes.[228, 236, 239] It is known that carboxylate or intermediate radical oxidation can occur via oxidation of an oxidizable substituent, which can subsequently undergo intramolecular dissociative electron transfer (IDET) to give the expected radical intermediate or carbocation.[240] This pseudo-Kolbe reaction has been observed for both arylacetic and aliphatic carboxylic acids.[145, 231]

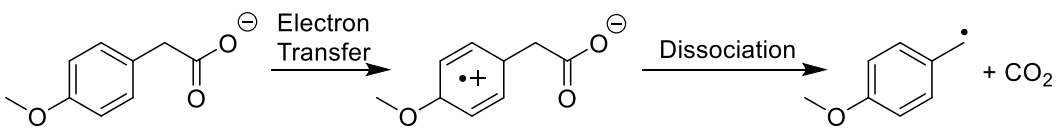

Scheme 4.1: Intramolecular dissociative electron transfer of 4-methoxyphenylacetic acid to yield the benzylic radical and CO_2.

Additionally, a second oxidation to the carbocation is observed, shown by formation of methoxylated products in methanolic solutions.[241] The oxidation potential of the 4-OMe substituted radical is only around 0.26 V vs SCE, therefore a second oxidation is extremely thermodynamically favourable.[229] In fixed potential electrolyses (Figure 4.3), the initial decay of photocurrent density was attributed to charging of the photoelectrode as before. As up to 60% total FE was obtained for alcohol and aldehyde side products, over-oxidation of the intermediate radical cation or subsequent benzyl radical was a competing pathway in conversion of methoxy-substituted PAAs.

For 4-F-PAA, a significant photocurrent density decay of 0.65 mA cm^{-2} was observed over a 3-hour electrolysis, suggesting possible electrode instability in fluorinated acid electrolytes.

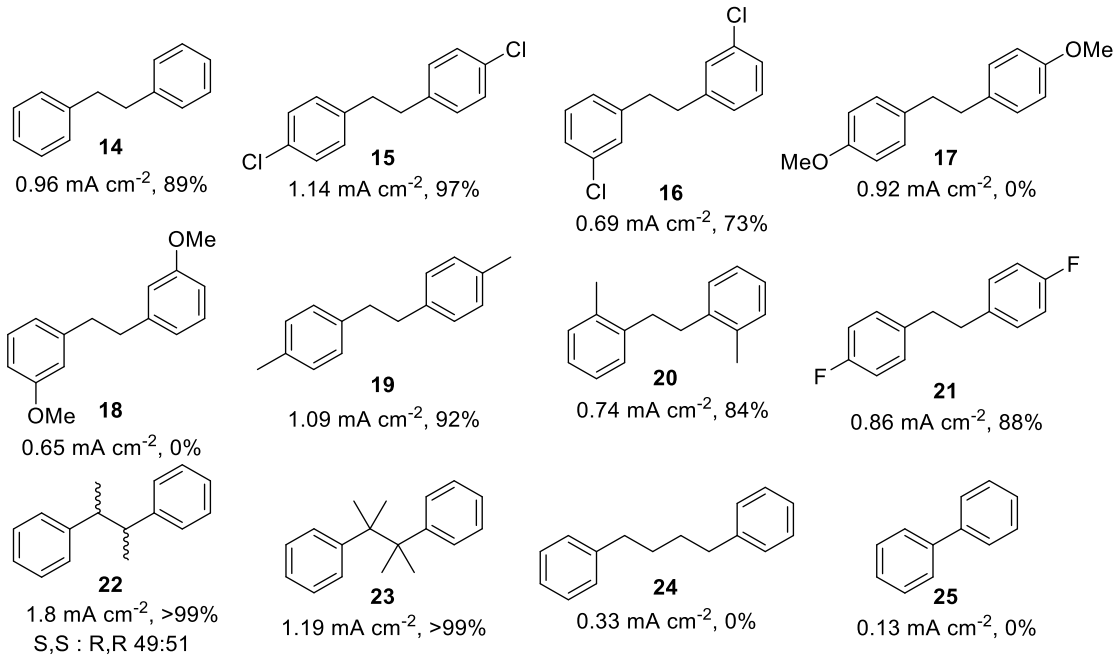

Figure 4.4: Time-averaged photocurrent densities and Faradaic efficiencies for Kolbe dimers of phenylacetic acid and derivatives. Products were analysed by GC and GC-MS after 3 hour electrolyses at +0.09 V vs Fc/Fc^+ under blue LED illumination.

Kolbe product selectivity remained high (>73%) for both electron-donating and electron-withdrawing substituents on the phenyl ring, except for methoxy-substituted acids (Figure 4.4). In general, dimer selectivity correlated with time-averaged photocurrent density, meaning the lowest dimer selectivity was observed for 3- and 2-substituted phenylacetic acids. As surface packing of acid is reduced for these substituents, lower

surface carboxylate concentrations resulted in lower photocurrent density and therefore lower steady state radical concentrations, disfavouring radical-radical coupling. Although small variation in $BiVO_4$ photoelectrode performance was observed by LSV in standard conditions using PAA, differences in FE were thought to be significant for most substrates as Kolbe product selectivity was either extremely high (>80%) or negligible (0%). In the case of 3-Cl-PAA, the effect of meta-substitution is significant due to the >10% drop in FE which could not have been accounted for by small electrode activity differences observed in batches of $BiVO_4$.

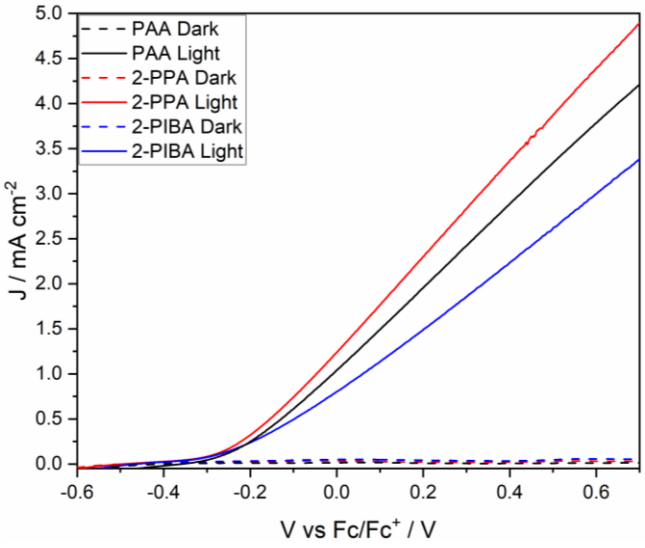

Figure 4.5: Linear sweep voltammograms of $BiVO_4$ photoelectrodes in electrolytes containing 1 M phenylacetic acid (PAA, black), 2-phenylpropionic (2-PPA, red) and 2-phenylisobutyric acids (2-PIBA, blue). Voltammograms were recorded in the presence (solid lines) and absence (dashed lines) of blue LED illumination.

α-substituted phenylacetic acids were also electrolysed to observe effects of intermediate radical stability on Kolbe product selectivity. Inductive effects of the α-methyl substituents should stabilise the intermediate radical, increasing its lifetime.

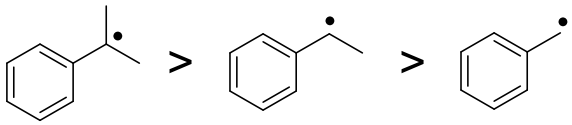

Scheme 4.2: Benzylic radical stability for dimethylbenzyl, methybenzyl and benzyl radicals.

Despite the increased steric bulk due to α-methyl substitution (Figure 4.5), a photocurrent density increase of 0.25 mA cm^{-2} at +0.09 V vs Fc/Fc^+ versus unsubstituted

phenylacetic acid was observed for 2-phenylpropionic acid. This suggested that the stability of the intermediate alkyl radical was more important in determining photocurrent density than the steric congestion on methyl substitution. In contrast, the photocurrent density in 2-phenylisobutyric acid electrolyte decreased by 0.34 mA cm^{-2} relative to PAA, suggesting that further steric congestion of the acid was a more important factor than radical stability in determining oxidation rate. For all acids, photocurrent onset potentials were approximately -0.3 V vs Fc/Fc^{+} despite lower oxidation potential for oxidation of the carboxylate for PPA (+1.07 V vs SCE) compared to PAA (+1.27 V vs SCE).[132] This suggested that either the onset potential was controlled by the electronic structure of the photoelectrode, or that oxidation did not proceed via the carboxylate anion.

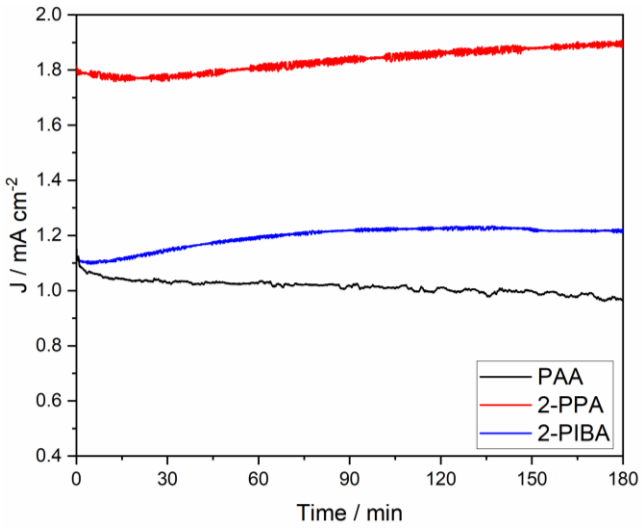

Figure 4.6: Controlled potential electrolyses of 1 M phenylacetic acid (PAA, black), 2-phenylpropionic (2-PPA, red) and 2-phenylisobutryic acid (2-PIBA, blue) electrolytes containing 0.05 equiv Et_3N at +0.09 V vs Fc/Fc^{+}.

Stable photocurrent densities of approximately 1.83 mA cm^{-2} and 1.19 mA cm^{-2} were recorded over 3 hours for electrolyses of 2-PPA and 2-PIBA electrolytes respectively. Compared to those measured by LSV, photocurrent density for PAA oxidation stabilised at around 1.0 mA cm^{-2}. Generation of secondary or tertiary intermediate radicals improved dimer selectivity to >99%, though rates of reaction with oxygen should be relatively similar (Figure 4.4).[242] For 2-PPA, a significant increase in photocurrent density to 1.8 mA cm^{-2} was observed, therefore improved selectivity here was assigned to the increased steady state concentration of intermediate radicals favouring coupling. The ratio of diastereomers was assigned from the two GC peaks observed in analysis.[243] Only a modest photocurrent density increase was observed for 2-PIBA oxidation (around 0.2 mA cm^{-2}), therefore

improved dimer selectivity was partially attributed to increased steady state radical concentration. Another important factor was possibly the packing of the radicals at the electrode surface. The increased steric bulk of 2-PIBA from the α-methyl substituents could enhance desorption rates of the radical from the electrode surface.

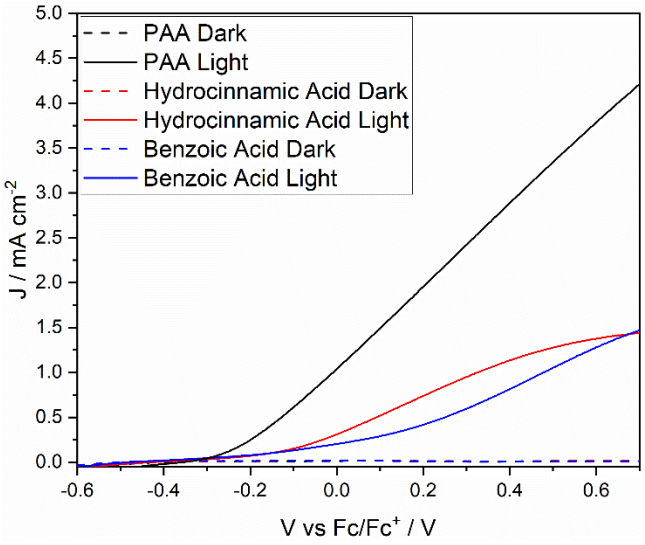

Figure 4.7: Linear sweep voltammograms of a $BiVO_4$ photoelectrode in 1 M electrolytes of hydrocinnamic (black) and benzoic (red) acids with 0.05 equiv Et_3N. Voltammograms were recorded in the presence (solid) and absence (dashed) of blue LED illumination.

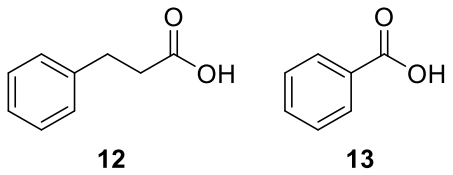

12 **13**

Figure 4.8: Structures of hydrocinnamic and benzoic acids.

Hydrocinnamic and benzoic acids were used as electrolytes for photoelectrochemical Kolbe reactions to assess the effects of radical stabilisation by the phenyl ring (Figure 4.8). For phenylacetic acid, the intermediate radical is stabilised by resonance with the π-system of the phenyl ring, extending the radical lifetime relative to benzoic and hydrocinnamic acids where no radical stabilisation by resonance is possible. For the phenyl radical produced by decarboxylation of benzoic acid, the unpaired electron populates an orbital that lies out of the plane of the π-system, thus no stabilisation of the radical is possible.[244]

LSV measurements of hydrocinnamic and benzoic acid electrolytes (Figure 4.7) show a photocurrent onset potential relatively consistent with PAA, 2-PPA and 2-PIBA (~-0.3 V vs Fc/Fc^+), however photocurrent densities were ~50% of values measured for PAA and 2-PIBA.

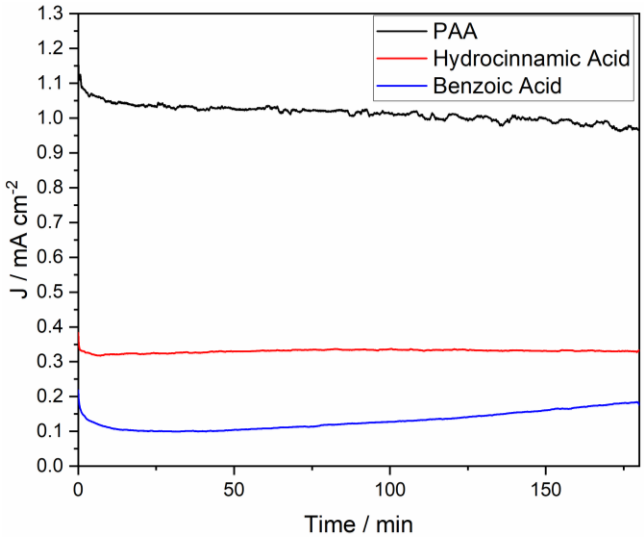

Figure 4.9: Controlled potential electrolyses of 1 M phenylacetic (black), hydrocinnamic (red) and benzoic (blue) acid electrolytes containing 0.05 equiv Et_3N at +0.09 V vs Fc/Fc^+.

During the initial 10 minutes of electrolysis, photocurrent density for benzoic acid oxidation decreased by 50%, but increased over the remaining 170 minutes of the electrolysis. An identical trend was observed during a 12-hour electrolysis of 1 M benzoic acid electrolytes (Figure 4.10). This phenomenon was also attributed to an initial carboxylate accumulation, similarly to aryl-substituted acids.

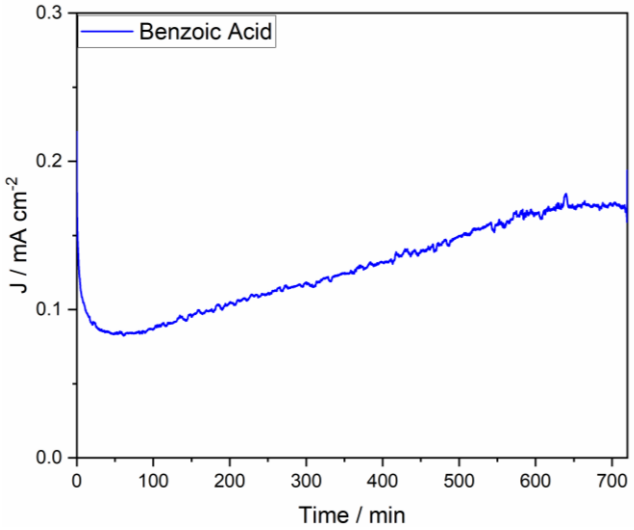

Figure 4.10: Controlled potential electrolysis of 1 M benzoic acid electrolyte containing 0.05 equiv Et_3N at +0.09 V vs Fc/Fc^+.

For benzoic acid, no evidence for the Kolbe product was observed by GC or GC-MS after 3-hour electrolysis. Due to the low photocurrent density (0.13 mA cm^{-2}), electrolysis was repeated over 12 hours to improve starting material conversion (Figure 4.10), however again no evidence for biphenyl was observed – no alternative products were observed by GC-MS either. Decarboxylation of benzoic acid would result in formation of the intermediate radical directly on the aromatic ring. As the intermediate phenyl radical is unstable, decarboxylation, and thus C-C coupling, is unfavourable. Carboxyl radicals generated from benzoic acid oxidation have been trapped in oxidative esterification reactions at platinum electrodes.[245, 246] Additionally, for Kolbe electrolysis of benzoic acid at Pt electrodes in acetonitrile containing naphthalene, only phenolic ester products were observed, suggesting formation of the phenyl radical ($C_6H_5^{\bullet}$) is unfavourable even at much higher current densities (~40 mA cm^{-2}) than generated in this work.

Unusually, no evidence of Kolbe products were observed with hydrocinnamic acid, despite aliphatic acids typically being favoured in classical Kolbe electrolysis.[211] As with oxidation of 4-OMe-PAA, an IDET mechanism would account for the absence of C-C coupled product. For the carboxylate oxidation mechanism, formation of the 2-phenylethyl radical should lead to at least some formation of the C-C coupled product, which was not observed here. In the IDET mechanism, rearrangement of the intermediate radical would not result in the 2-phenylethyl radical, meaning no C-C coupling could be achieved. The observation of 2-phenylethanol by GC suggests that the oxidative current arose from the more sluggish oxidation of the carboxylate directly, and that carbocation formation was favoured due to

the favourable thermodynamics and kinetics of a second electron oxidation in the presence of low radical concentrations. Additionally, assuming one electron pathways for all product formation did not account completely for the charge passed during electrolysis, therefore the possibility of multiple-electron oxidations seems likely.[247, 248]

In the context of extensive electrochemical Kolbe chemistry, there are several notable features of the photoelectrochemical reactions described here. Remarkably high Faradaic efficiencies for Kolbe C-C coupling are observed for a range of benzylic carboxylic acids at relatively low current density ca. > 1 mA cm^{-2}. For the electrochemical oxidation of phenylacetate at platinum electrodes, 80% selectivity for benzaldehyde is observed at 3.2 mA cm^{-2}.[228] In part, the high dimer selectivity is supported by use of acetonitrile avoiding competitive solvent oxidation, but clearly the relative adsorption of carboxylate anions and radical intermediates is critical to the observed selectivity. Overoxidation to the carbocation is not observed for the benzylic substrates investigated here, even within the porous environment of the $BiVO_4$ photoelectrode. The lower current density used here results in a lower surface density of holes than for typical electrochemical Kolbe coupling undertaken at > 100 mA cm^{-2} indicating that, under the studied conditions, rates of radical desorption are greater than rates of a second oxidation due to low concentrations of surface holes.

With respect to substrate scope, comparison of the FE and photocurrent of PAA and the α-methyl-substituted analogues PPA and PIBA show that whilst both PPA and PIBA show near quantitative C-C coupling, mono-methylation results in a particularly dramatic increase in photocurrent (Figure 4.4 and Figure 4.6). The increased FEs are consistent with greater stabilisation of the substituted radicals, but the differences in photocurrent and hence rate of reaction are not consistent with thermodynamic stability of the respective radicals or oxidation potentials of the carboxylates at metal electrodes. The data suggest that the increased steric bulk of dimethylation reduces the rate of oxidation due to weaker adsorption to the photoelectrode surface.

Furthermore, it is known that carboxylate or intermediate radical oxidation can occur via oxidation of an oxidizable substituent which can subsequently undergo intramolecular dissociative electron transfer (IDET) to give the expected radical intermediate or carbocation. Existing studies of photoelectrochemical Kolbe chemistry use acetic acids and TiO_2 photoanodes which is known to bind carboxylic acids strongly via the carboxylate group. This adsorption typically occurs through the presence of surface

hydroxyl groups, the density of which is known to vary with synthetic method.[249, 250] It is possible that $BiVO_4$ electrodes used here contain far fewer surface OH groups than TiO_2 electrodes in other PEC Kolbe studies, and thus carboxylate binding is much weaker.

Although direct oxidation of the carboxylate anion is more thermodynamically favourable (~1.2 V vs SCE versus ~2.3 V vs SCE for oxidation of the aryl moiety), the combination of photovoltage generated on illumination of the $BiVO_4$ electrode and applied potential exceed the oxidation potential for both pathways.[132]

The origin of the selectivity observed here could originate from IDET and initial oxidation of surface bound arene, which would explain the similar rates and selectivity for benzylic acid oxidations using $BiVO_4$ photoelectrodes. In cases where the IDET mechanism is unlikely, such as benzoic and hydrocinnamic acids, a stark drop in current is observed, indicating a shift from oxidation of the arene moiety to more sluggish direct oxidation of the carboxylate. This is corroborated by relative rate constants measured for oxidative pathways of PAA using cerium ammonium nitrate.[236]

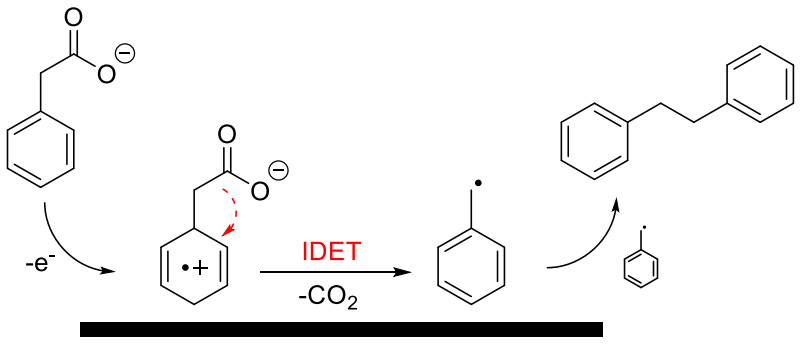

Figure 4.11: Proposed intramolecular dissociative electron transfer (IDET) mechanism for the photoelectrochemical Kolbe reaction of phenylacetate at $BiVO_4$ photoelectrodes. The dashed red line indicates rearrangement of the radical and loss of CO_2.

4.2.2 Cross-Coupling of Phenylacetic Acid and 2-Phenyliosbutyric Acid

Once the scope of Kolbe dimerization reactions had been studied, the heterocoupling of carbon centred radicals at $BiVO_4$ electrodes was attempted as selective C-C bond formation between two unique moieties is a valuable synthetic transformation. These types of reaction are typically carried out using Suzuki or Sonogoshira couplings

which employ expensive palladium complexes as catalysts.[251] Photocatalytic Kolbe cross-coupling reactions have been demonstrated using TiO_2 photocatalyst powders, however yields were relatively low for heterocoupled products, with product ratios dictated by steric congestion of the intermediate radical.[121] By applying a bias to $BiVO_4$ photoelectrodes it was hoped that a change in heterocoupling selectivity would be observed.

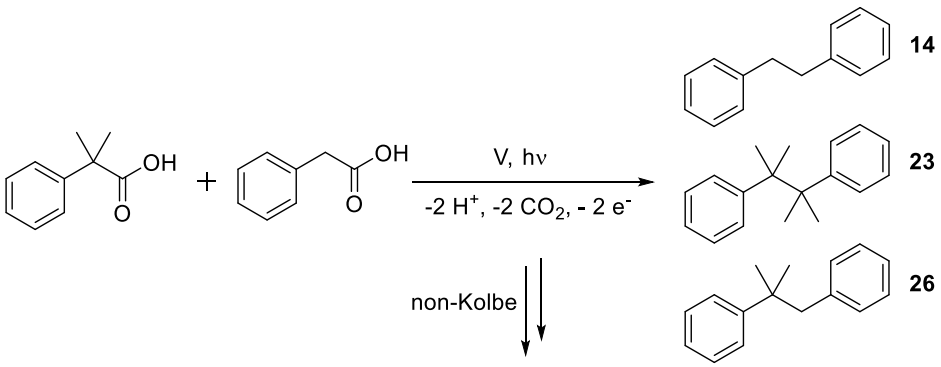

Scheme 4.3: Cross-coupling of 2-phenylisobutyric and phenylacetic acids under photoelectrochemical conditions.

To maximise the possibility of generating hetero-coupled products, phenylacetic acid and 2-phenylisobutyric acid were selected as substrates due to their similar current-voltage characteristics, suggesting comparable rates of radical formation (Scheme 4.3). Additionally, pKa values of both acids were similar (4.31 for PAA and 4.39 for 2-PIBA in water), meaning no preferential deprotonation of one acid was expected.

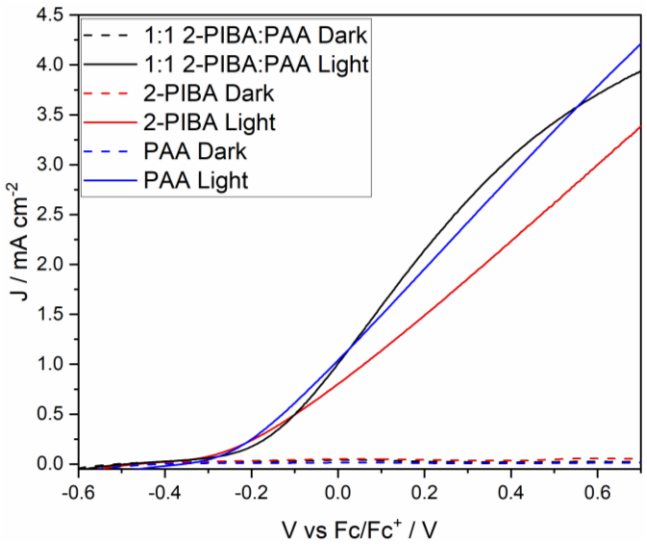

Figure 4.12: Linear sweep voltammogram of a $BiVO_4$ photoelectrode in 1 M 1:1 2-phenylisobutyric acid:phenylacetic acid (black), 2-phenylisobutyric (red) and phenylacetic acid (blue) electrolytes containing 0.05 equiv Et_3N. Voltammograms were recorded in the absence (dashed) and presence (solid) of 32 mW cm^{-2} blue LED array illumination.

LSV measurements of $BiVO_4$ photoelectrodes in pure and mixed acid electrolytes showed similar photocurrent densities between 1:1 2-PIBA:PAA and PAA electrolytes at all potentials (Figure 4.12). This possibly suggested preferential oxidation of PAA in the mixed electrolyte due to more facile electron transfer kinetics.

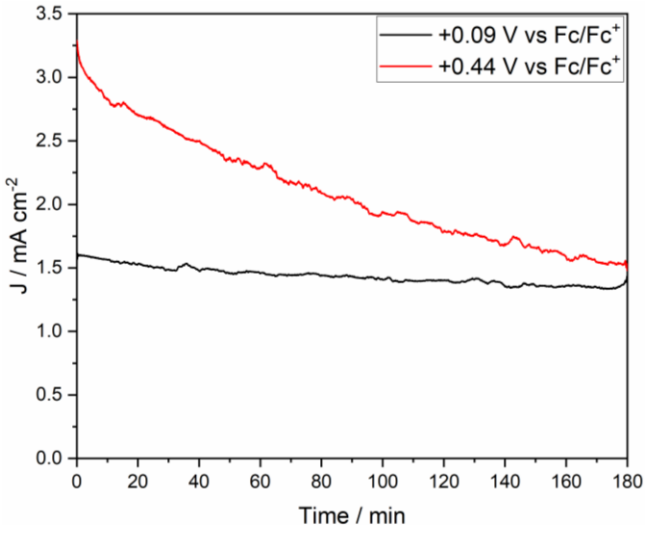

Figure 4.13: Controlled potential electrolysis of a 1 M 1:1 2-phenylisobutyric:phenylacetic acid electrolyte at a $BiVO_4$ photoelectrode under blue LED array illumination (32 mW cm^{-2}). Electrolyses were carried out at +0.09 (black) and +0.44 V vs Fc/Fc^+ (red). Electrolytes were partially neutralised by addition of 0.05 equiv Et_3N.

At +0.09 V vs Fc/Fc^+ a stable oxidative current of 1.5 mA cm^{-2} was observed, approximately 0.3 mA cm^{-2} greater than recorded for electrolysis of 2-PIBA electrolytes (Figure 4.13). For electrolysis at +0.44 V vs Fc/Fc^+, initial photocurrent density was much greater (3.2 mA cm^{-2}), though after 3 hours photocurrent densities were similar to those generated at +0.09 V vs Fc/Fc^+. The decay of photocurrent with time was attributed to electrode fouling or poor electrode stability at more anodic potentials. $BiVO_4$ photoelectrodes have been shown to be prone to photocorrosion under bias, particularly in aqueous media, with dissolution exacerbated by applied potential.[223, 252] The predominant mechanism for activity loss of $BiVO_4$ photoelectrodes is through leaching of vanadium, as shown in section 3.3.1.[253]

Although corrosion of the photoelectrode resulted in performance decrease, total FE for Kolbe and non-Kolbe products was 97% indicating that electrode instabilities were not caused by Faradaic processes (Table 4.2).

Table 4.2: Faradaic efficiencies for major C-C coupled products from the electrolysis of 1 M 1:1 2-phenylisobutyric:phenylacetic acid electrolytes.

V vs Fc/Fc^+ / V	Charge Passed / C	FE **14** / %	FE **23** / %	FE **26** / %
+0.09	241	63.2	5.9	26.8
+0.44	352	66.5	5.5	24.9

The formation of cross-coupled product was confirmed using GC data, as peaks for bibenzyl and dicumene were assigned based on retention times measured after electrolysis of pure 2-PIBA and PAA electrolytes. A third peak at 9.54 min was assigned to **26** based on GC-MS data. No direct observation of the molecular ion peak by mass spectrometry was obtained for **26**, but fragmentation patterns in GC-MS data confirmed the presence of the tropylium cation and a cumene fragment.

No potential dependence of product formation was observed, with an approximate 1:0.1:0.4 ratio of **14**:**23**:**26** obtained for electrolyses at +0.09 and +0.44 V vs Fc/Fc^+ (Table 4.2). Deviation from statistical distributions of products in Koble heterocoupling reactions are typically rationalised based on differences in oxidation potential. However, as the oxidation potential of 2-PIBA is lower than that of PAA, this would not account for the product distributions observed.[132, 254] This was reinforced by the independence of product

selectivity from applied potential. As bibenzyl was detected as the major product, and dicumene only seen in small yields, selectivity of hetero-coupling was controlled either by steric congestion of the intermediate radicals, or by preferential adsorption of PAA at the electrode surface.[255]

Exerting control over selectivity in mixed-acid electrolytes was not possible in equimolar conditions, however further work could be done, changing acid ratios in the starting electrolyte, and trying to form persistent radicals alongside transient to maximise cross-coupling selectivity. For the electrochemical cross coupling of methyl adipate and hexanoate at platinum electrodes, heterocoupling yields increase as excess of hexanoic acid is changed from 1:1 (36%) to 1:6 (58%).[256]

4.3 Photoelectrochemical Kolbe Reaction of 4-Chlorophenylacetic Acid at Low Electrolyte Concentration

4.3.1 Photoelectrochemical Kolbe Selectivity at 50 mM 4-Chlorophenylacetic Acid Concentration

For synthetic applications, a PEC system should demonstrate high product yields at high starting material conversions. For PEC Kolbe reactions described in previous sections, the large acid quantities mean impractically long reaction times were required for full conversion of starting material although no additional electrolyte is required. The effects of lower acid concentrations on product selectivity were therefore investigated by reducing acid concentration to 50 mM. To support the passage of charge through 50 mM acid solutions, a 0.1 M $TBAPF_6$ supporting electrolyte was added. The effects of supporting electrolyte on product selectivity were also investigated.

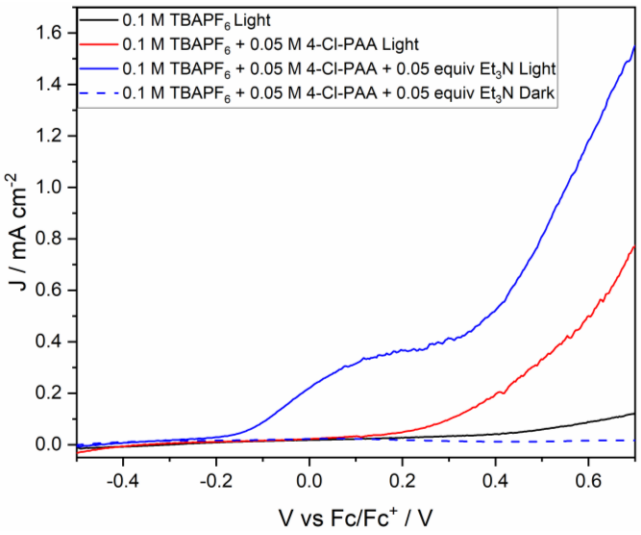

Figure 4.14: Linear sweep voltammograms of a $BiVO_4$ photoelectrode in 0.1 M $TBAPF_6$ (black), 0.1 M $TBAPF_6$ + 0.05 M 4-Cl-PAA (red) and 0.1 M $TBAPF_6$ + 4-Cl-PAA + 0.05 equiv Et_3N (blue) solutions under blue LED illumination. A scan of the full electrolyte solution in the absence of illumination is also given (blue, dashed). Scan rate 10 mV s^{-1}.

Significant changes to voltammogram shape were seen on reducing acid concentration to 50 mM 4-Cl-PAA (Figure 4.14). In the absence of acid, no significant oxidative photocurrents were generated below 0.4 V vs Fc/Fc^+ showing the oxidation of electrolyte is not in competition with carboxylate oxidation. PEC Kolbe studies of acetate oxidation at TiO_2 photoelectrodes have shown generation of photocurrents up to 3 mA cm^{-2} at 1.0 V vs Ag wire in methanolic $TBAPF_6$ solutions due to solvent oxidation.[123] After addition of 4-Cl-PAA, an oxidative photocurrent is generated above 0.1 V vs Fc/Fc^+, attributed to the direct oxidation of the acid. For 4-Cl-PAA solutions with added Et_3N, the voltammogram showed two distinct features; the first oxidative wave attributed to oxidation of deprotonated 4-Cl-PAA, known to have a lower oxidation potential than the associated acid, and the second feature associated with direct oxidation of the acid without deprotonation.[132] The oxidation of associated acid was prevalent due to the overall low concentration of Et_3N base.

After electrolysis for 24 hours at +0.24 V vs Fc/Fc^+, 4,4'-dichlorobibenzyl selectivity was poor, with only (5.5±1.8)% FE observed by NMR (Figure 4.15). In addition to the poor selectivity for 4,4'-dichlorobibenzyl, the total FE for Kolbe and non-Kolbe products was only 34%.

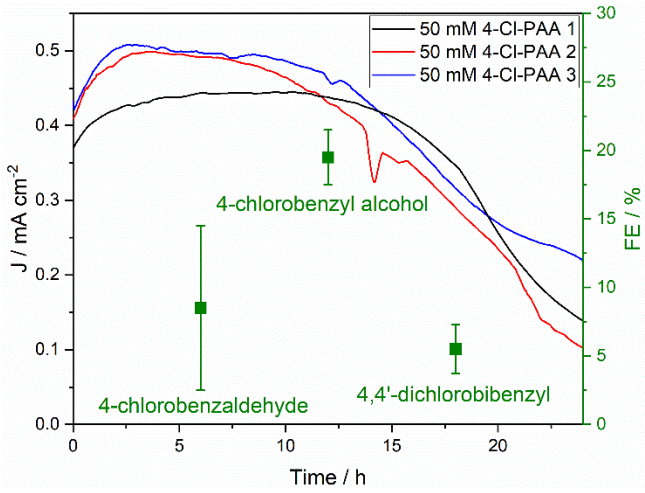

Figure 4.15: Sequential controlled potential electrolyses of 50 mM 4-Cl-PAA in 0.1 M $TBAPF_6$ supporting electrolyte at $BiVO_4$ photoelectrodes. The same photoelectrode was used for first (black), second (red) and third (blue) electrolyses. Faradaic efficiencies with error bars for major electrolysis products are shown (green).

The low FE for 4,4'-dichlorobibenzyl was attributed to the low photocurrent density (0.43 mA cm^{-2}) arising from low carboxylate concentration at the electrode surface and low steady state radical concentrations, disfavouring radical-radical coupling. Additionally, in aqueous media, supporting electrolytes have been shown to acutely affect Kolbe product selectivity for electrolysis of valeric acid at Pt electrodes.[195] In non-aqueous media, the oxidation of acetic and trifluoroacetic acids proceeds at photocurrent densities up to 3 mA cm^{-2} in the presence of $TBAPF_6$ supporting electrolyte.[123] Ethane and hexafluoroethane were detected as major products – though 1 M acid concentrations were used and no yields or Faradaic efficiencies were given. It was therefore assumed that, for the oxidation of 50 mM PAA at $BiVO_4$ photoelectrodes in this work, $TBAPF_6$ was not oxidised during photoelectrolysis, but provided anion competition to carboxylate binding at the photoelectrode surface.

The electrochemical reactions of Kolbe and non-Kolbe products was a potential contributor to the low total FE for electrolysis of 50 mM electrolytes. No evidence for 4-chlorobenzoic acid was observed by NMR, therefore successive oxidations of alcohol and aldehyde products were discounted. Electrolysis of 20 mM 4,4'-dichlorobibenzyl in 0.1 M $TBAPF_6$ supporting electrolyte showed negligible oxidative photocurrents (<0.02 mA cm^{-2}) and after 2 hours no loss of substrate was observed. As the concentration of 4,4'-dichlorobibenzyl in reaction mixtures would have been significantly lower than 20 mM,

parasitic oxidation of products was discounted as a possible reaction pathway. No competing Faradaic processes were present, therefore the low total FE for observed electrolysis products was attributed to multi-electron oxidations to form intermediate carbocations, in a two-electron, Hofer-Moest type oxidation.[257]

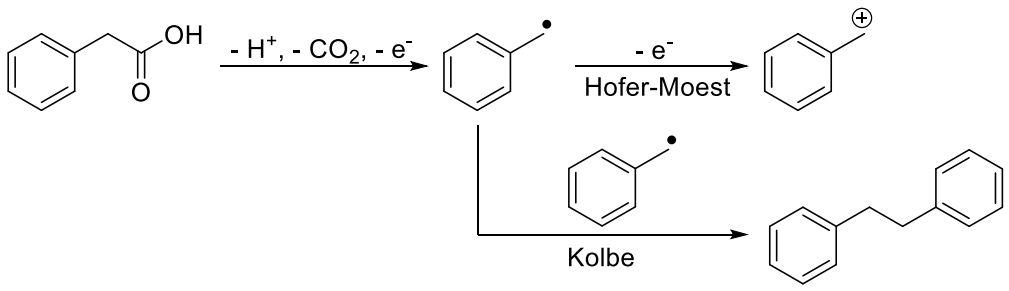

Scheme 4.4: Hofer-Moest and Kolbe reaction pathways for a benzyl radical generated by oxidative decarboxylation of phenylacetic acid.

4.3.2 Mechanistic Studies of the Photoelectrochemical Kolbe Reaction in Low Concentration Electrolytes

To assess the nature of low overall FEs in 50 mM 4-Cl-PAA solutions, Kolbe product selectivity was analysed as a function of charge passed. Passage of 0.5 F mol^{-1} relative to initial quantity of 4-Cl-PAA resulted in increased selectivity (20%) for dimer but with total FEs some way below 100% (Figure 4.16). Further oxidation (0.85 F mol^{-1}) showed no significant loss of selectivity for 4,4'-dichlorobibenzyl (19%) with a slightly increased selectivity for 4-chloro-benzyl alcohol (10%). The significant drop in dimer FE after 1.25 F mol^{-1} of charge was passed suggested that alcohol and aldehyde formation were more prevalent in the absence of excess 4-Cl-PAA. Additionally, the sharp increase in aldehyde FE after 1.25 F mol^{-1} was passed could have arisen from oxidation of 4-chlorobenzyl alcohol.

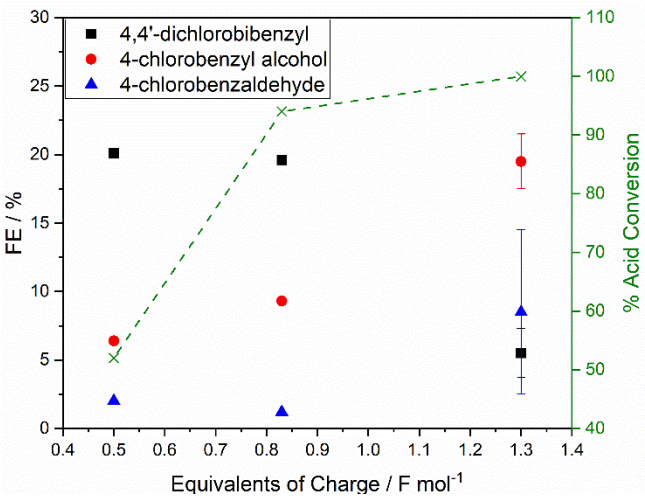

Figure 4.16: Faradaic efficiencies for Kolbe and non-Kolbe products after passage of different equivalents of charge. Electrolyses were carried out at +0.24 V vs Fc/Fc^+ in 50 mM 4-Cl-PAA with 0.05 equiv Et_3N solutions containing 100 mM $TBAPF_6$ supporting electrolyte. Percentage conversion of 4-Cl-PAA, as measured by NMR, is given in green.

Based on our findings and literature precedent, a proposed mechanism explaining Kolbe and non-Kolbe product formation was formulated for both low and high acid concentration conditions. In both cases of high and low acid concentration, oxidation yields an adsorbed benzylic radical on the photoelectrode surface. High acid concentrations in the electrolyte promote desorption of the intermediate radical through competitive adsorption at the $BiVO_4$ surface. The liberation of the radical into solution thus favours dimerization in solution, or reaction with oxygen/water to give non-Kolbe products, in line with EPR observations of free radicals observed in TiO_2 photocatalysis.[26] In 1 M 4-Cl-PAA electrolytes (Figure 4.17), dimer selectivity remains high (68%) after 24-hour electrolysis, though is some way below selectivity after 3 hours, possibly due to electrode fouling or poor electrode stability over longer timescales. Additionally, generation of oxygenated products in 3-hour electrolyses (Figure 4.4) can be accounted for by assuming only a one-electron oxidation, therefore over-oxidation of the intermediate radical is suppressed in high acid concentration electrolytes.

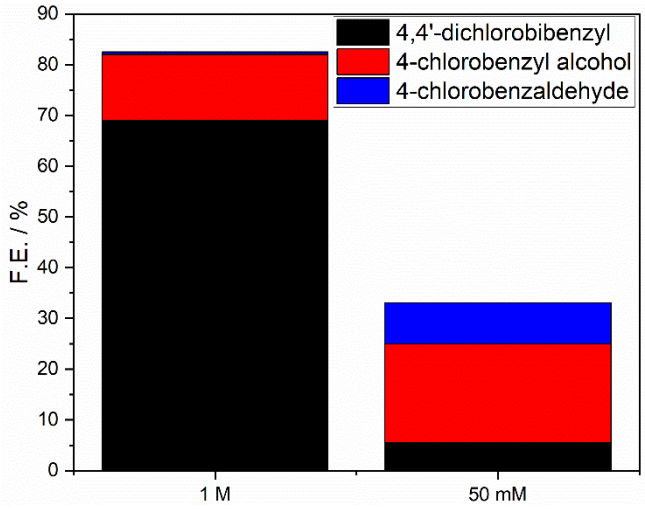

Figure 4.17: Faradaic efficiencies for Kolbe and non-Kolbe products after 24 hour electrolyses in 1 M 4-Cl-PAA/0.05 equiv Et_3N solutions with no added electrolyte and 50 mM 4-Cl-PAA/0.05 equiv Et_3N solutions containing 100 mM $TBAPF_6$. Electrolyses were carried out at +0.24 V vs Fc/Fc^+ under blue LED illumination.

In low concentration electrolytes, the relative lack of carboxylate for competitive adsorption or competition of PF_6^- adsorption means the radical remains adsorbed onto the photoelectrode surface for a longer time and can undergo further oxidation to the cation. At low acid conversions (0.5 – 0.85 F mol^{-1}, Figure 4.16), carboxylate concentration is sufficient to give okay Kolbe product selectivity (~20%). As conversion of acid proceeds, less carboxylate is available for competitive adsorption, leading to over-oxidation of the adsorbed radical or competitive oxidation of the alcohol. The carbocation produced then reacts with lattice oxygen, or residual water or oxygen to give oxygenated non-Kolbe products.[258, 259]

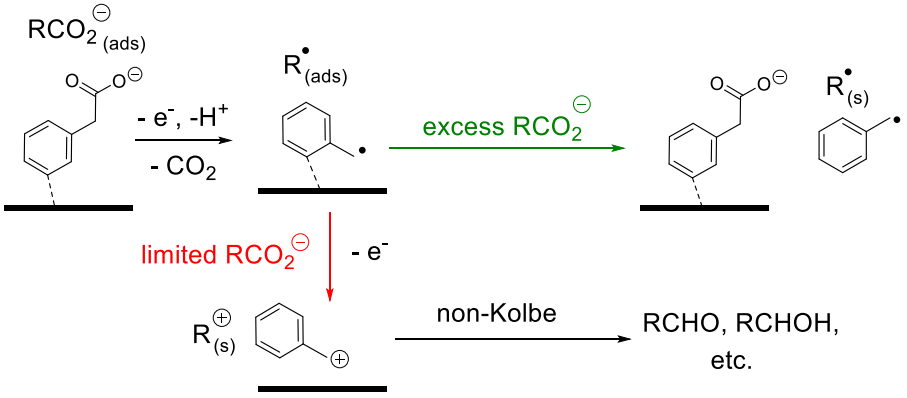

Scheme 4.5: Proposed mechanism for the dominant reaction pathways of phenylacetate oxidation in high and low acid concentration electrolytes.

Quantitative XPS analysis of the $BiVO_4$ photoelectrode surface after electrolysis shows a loss of V and O, so lattice oxygen may contribute to the formation of oxygenated products (Table 3.7). However, the amount of oxygen present in non-Kolbe products exceeds the amount present at the electrode surface based on approximate masses of $BiVO_4$. Reactions with residual water or molecular oxygen were thus a significant contributor to the formation of oxygenated products. This Hofer-Moest style oxidation accounted for the low total F.E.s in 50 mM acid electrolytes and the 15-20% loss of charge in <500 mM electrolytes (Figure 3.23).[126, 257] Multiple electron transfers may have been facilitated by the presence of PF_6^-, disrupting the electrochemical double layer and stabilising carbocation formation. Electrolysis of phenylacetate at platinum electrodes in methanol shows complete suppression of dimer formation after the addition of 5 mM sodium perchlorate due to competitive anion adsorption.[220]

4.4 Electrochemical Analysis of $BiVO_4$ Photoelectrodes in 4-Chlorophenylacetic Acid Electrolytes

4.4.1 Photon-to-Current Efficiency of the Photoelectrochemical Kolbe Reaction of 4-Chlorophenylacetic Acid

Thus far, mechanistic studies had been carried out in the context of the electrolyte, with interpretation of oxidation rates and product selectivity made. However, to fully understand the system, further characterisation of the $BiVO_4$ electrode was required to understand the quantum efficiency of the reaction and charge carrier behaviours within the semiconductor. PEC systems are commonly benchmarked through incident photon to current conversion efficiency (IPCE) measurements and photon-to-product metrics such as apparent quantum yield (AQY). These efficiencies are calculated as a function of incident wavelength or total irradiance. These measurements are also important for photosynthetic systems as poor photon-to-current efficiencies or catalysis can create a kinetic bottleneck caused by recombination of charge carriers in the bulk crystal or at surface states.

Blue LED array light sources used in this work emit with λ_{max} = 450 nm with a bandwidth of 80 nm. Emission spectra of LED arrays showed a roughly Gaussian distribution of wavelengths (Figure 3.2). For electrolysis of 4-Cl-PAA electrolytes at +0.09 V vs Fc/Fc^+, a photon to current quantum efficiency of 12.1% was calculated at 450 nm (32 mW cm^{-2}).

Table 4.3: Incident photon-to-current efficiencies for $BiVO_4$ photoelectrodes at +0.09 V vs Fc/Fc^+ in 1 M 4-Cl-PAA electrolytes.

Irradiance / mW cm^{-2}	Ave. Photocurrent @ +0.09 V vs Fc/Fc^+/ mA	Incident Photon-to-Current Efficiency / %
32.2	2.10	12.1
16.5	1.81	20.2
9.70	1.28	24.2

At lower irradiance values increased quantum efficiencies were calculated, suggesting photon saturation of the photoelectrode. Under saturation conditions, the generation of charge carriers occurs in such great quantity that recombination rates are increased. Despite the reduced quantum efficiency measured at an irradiance of 32.2 mW cm^{-2}, photocurrent densities were greater, meaning enhanced radical formation rates, radical concentration and therefore greater dimer selectivity based on previous results (Figure 4.4).

Based on a dimer selectivity of 99% for the oxidation of 4-Cl-PAA observed after 3 hours, the apparent quantum yield of the reaction can be calculated as 12.0% for irradiance of 32.2 mW cm^{-2}. Comparatively, for the PEC Kolbe reaction of acetate and trifluoroacetate at TiO_2 electrodes, an AQY of only 5% was observed.[123] In C-H amination reactions at Fe_2O_3 photoelectrodes, AQY was calculated at around 9.6%. In all cases of organic transformations at semiconductor photoelectrodes, the low AQY values can be rationalised by the low photon-to-current efficiencies typically observed. Recombination of charge carriers is a significant loss mechanism in these systems and thus lowers IPCE measurements. The slightly improved AQY observed in this work can be attributed to the unusually high product selectivity for C-C coupling.

4.4.2 Impedance Spectroscopy of $BiVO_4$ Electrodes in 1 M 4-Chlorophenylacetic Acid Electrolytes

Further characterisation of the photoelectrochemical Kolbe reaction at $BiVO_4$ photoelectrodes was carried out using electrochemical impedance spectroscopy (EIS) and Mott-Schottky analysis. By understanding charge carrier behaviours within the electrode, kinetic limitations of PEC reactions would become clear and insight into possible material improvements could be gained. Impedance spectra were initially fitted using a modified

Randles cell, with cell series resistance, R_s, bulk capacitance, C_{bulk}, and bulk charge transfer resistance, $R_{ct,bulk}$, elements to model charge transfer within the semiconductor (Figure 4.18). A second constant phase element and resistor in parallel were added to model charge transfer resistance, R_{ct}, and space-charge capacitance, Q_{SC}, at the electrode surface. A constant phase element was used in place of a traditional capacitor to account for frequency dispersions caused by the high porosity of the electrode.[260] Capacitance values can be calculated from constant-phase elements using:

$$C_{SC} = \frac{(Q_{SC}R_{ct})^{1/n}}{R_{ct}} \qquad \text{Equation 3}$$

Where C_{SC} is the space-charge capacitance and n is the constant phase element exponent, extracted from fitting of impedance data.[260] The impedance response of porous films can be understood through the use of transmission line models, however correlating a large number of model parameters to real chemical processes is often difficult.[65, 66] Similar equivalence cells have been used to model Fe_2O_3 photoelectrodes in photoelectrochemical C-H amination reactions in non-aqueous media.[116]

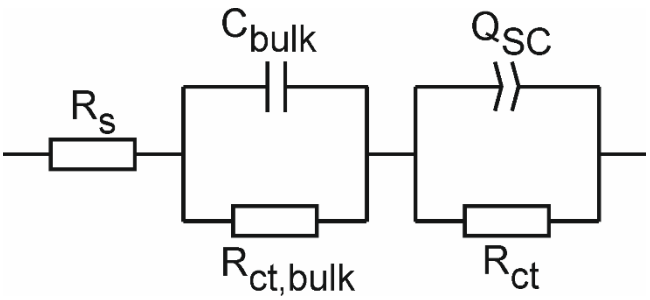

Figure 4.18: Equivalence cell used for modelling of impedance data for illuminated $BiVO_4$ photoelectrodes in 1 M 4-Cl-PAA electrolytes.

Impedance measurements were recorded under illumination of $BiVO_4$ photoelectrodes at 200 mV intervals. 4-Cl-PAA solutions were static during measurements as stirring resulted in noisy Nyquist plots.

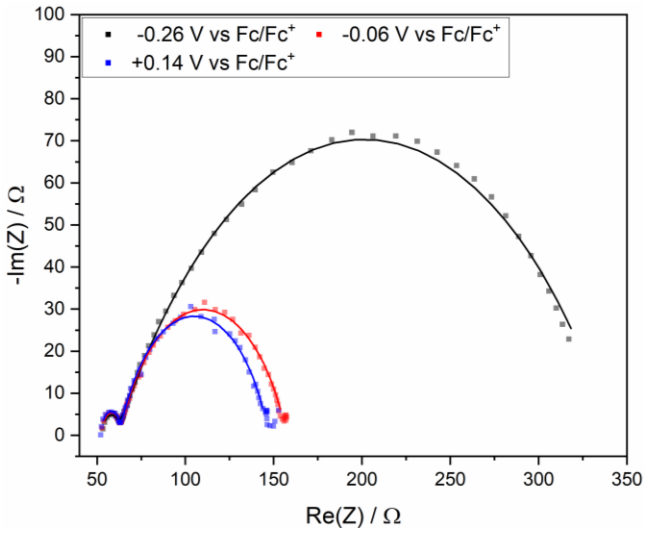

Figure 4.19: Electrochemical impedance spectra of an illuminated $BiVO_4$ photoanode in 1 M 4-Cl-PAA electrolyte at -0.26 (grey circles), -0.06 (red) and 0.14 (blue). Simulated impedance spectra are represented by the solid lines.

From the impedance measurements, two clear features were defined – one high frequency semicircle and one low frequency. The high frequency feature showed little to no potential dependence and was therefore attributed to the bulk of the photoelectrode. It was also possible that the high frequency semicircle corresponded to the FTO substrate, however EIS measurements with a blank FTO plate did not show a clear high frequency feature as with $BiVO_4$. Changes to applied bias are predominantly observed over the space-charge region of the semiconductor due to poor screening by low concentrations of charge carriers in the bulk. Thus, in the bulk region, changes to applied potential result in minimal changes to charge carrier behaviours.

Due to the variation observed with applied potential, the low frequency feature was attributed to charge carrier behaviours in the space-charge region of the semiconductor. As applied bias is made more anodic, a decrease in R_{CT} was observed, in combination with decreased C_{SC} (Table 4.4). The decreased R_{CT} values were expected based on the LSV data for electrodes (Figure 4.1), with photocurrent density increasing with applied potential.

Table 4.4: Parameters extracted from the fitting of impedance spectra for an illuminated $BiVO_4$ photoelectrode in 1 M 4-Cl-PAA electrolyte.

Potential vs Fc/Fc^+ / V	R_s / Ω	C_{bulk} / µF	$R_{ct,bulk}$ / Ω	C_{SC} / µF	R_{ct} / Ω
-0.26	53.12	0.972	8.226	380.8	280.8
-0.06	52.84	0.912	9.971	150.5	94.52
0.14	52.33	0.844	10.52	117.8	84.26

Decreasing C_{SC} values were tentatively attributed to depopulation of surface states as applied potential was increased. The term C_{SC} used in the equivalence cell was non-specific and therefore incorporated all phenomena within the space-charge region, including contributions from the Helmholtz capacitance and the capacitance of mid-gap surface states.[198, 261] As applied potential is increased, a corresponding increase in band bending is observed within the semiconductor. As the band bending increases, filled electronic energy levels in the mid-gap begin to empty, thus reducing C_{SC} as electrons are transported to the bulk (Figure 4.20).

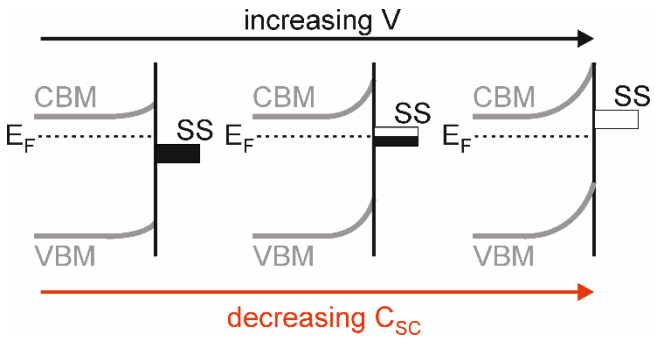

Figure 4.20: Effects of increasing applied potential on the Fermi level, E_F, and surface state population, SS, in a $BiVO_4$ photoelectrode. Surface state population is indicated in black.

The validity of impedance fitting using the equivalence cell shown in Figure 4.18 was tested by comparison of total resistance, R_{tot}, measured by LSV and calculated from Table 4.4.[49] For impedance measurements, R_{tot} was taken as the summation of all resistances ($R_s + R_{ct,bulk} + R_{ct}$). R_{tot} for LSV measurements was calculated using:

$$R_{tot} = \left(A_S \frac{dJ}{dV}\right)^{-1}$$

Where A_S is the electrode area, and dJ/dV is the differentiated voltammogram.

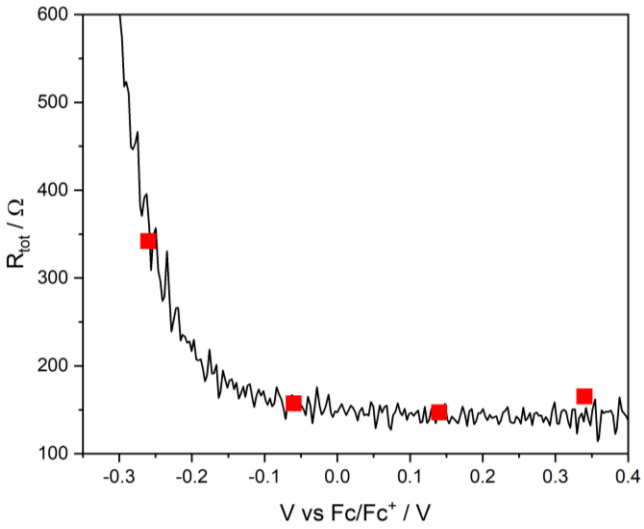

Figure 4.21: Total cell resistance values calculated from linear sweep voltammograms of a $BiVO_4$ photoelectrode in 1 M 4-Cl-PAA electrolyte (black line). R_{tot} values estimated from fitting of impedance spectra are also shown (red squares).

Excellent agreement between R_{tot} values was observed, suggesting that the equivalence cell used for fitting of impedance data was a valid model.

Mott-Schottky analysis was also carried out for $BiVO_4$ photoelectrodes to determine approximate flat-band potentials and compare these to photocurrent onset potentials.

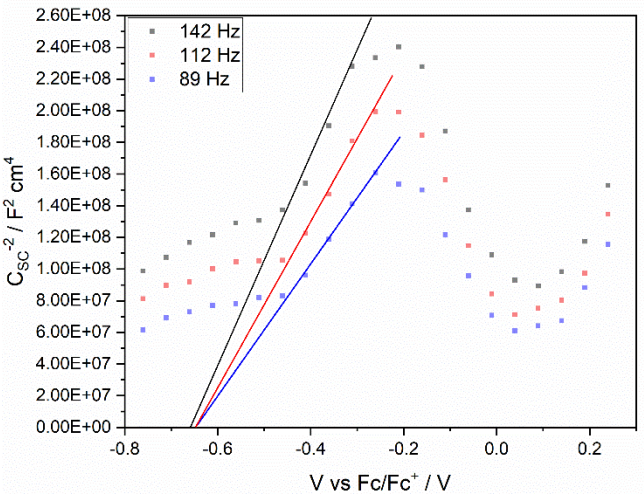

Figure 4.22: Mott-Schottky plots of a $BiVO_4$ photoelectrode in 1 M 4-Cl-PAA electrolytes at 142 (black), 112 (red) and 89 Hz (blue).

Up to -0.2 V vs Fc/Fc^+, the Mott-Schottky analysis of $BiVO_4$ electrodes followed expected behaviour, with increasing surface capacitance with applied potential. However, above this potential, an inversion of C_{SC} vs potential behaviour was observed. Similar behaviour has been observed for Fe_2O_3 nanorod electrodes, with inversion attributed to the nanostructuring at the electrode surface.[262] Application of the MS equation relies upon several assumptions, including one that the electrode surface is flat and planar. This assumption is broken for nanostructured or rough electrodes. Equally, an assumption is made that no other interfacial capacitances are present in the system (i.e., the Helmholtz capacitance is negligible). For donor densities greater than 10^{18} cm^{-3}, as are estimated for $BiVO_4$ electrodes here, the Helmholtz capacitance is significant and thus contributes to the measured surface capacitance. Sufficiently high donor densities (>10^{23} cm^{-3}) combined with significant Helmholtz capacitance can affect estimations of flat-band potential by decreasing the slope of the linear region.[198] As donor densities measured for $BiVO_4$ electrodes were only around 10^{19} cm^{-3}, flat-band potential estimations from the unmodified Mott-Schottky equation were taken as reasonable estimates.

Table 4.5: Flat band potentials and donor densities of $BiVO_4$ photoelectrodes extracted from Mott-Schottky analysis.

Frequency / Hz	Flat Band Potential vs Fc/Fc^+ / V	N_D (x10^{19})/ cm^{-3}
142	-0.645	1.18
112	-0.644	1.48
89	-0.649	1.82

An overpotential of around 350 mV can be estimated for the photoelectrochemical Kolbe reaction at $BiVO_4$ electrodes, taken as the difference between photocurrent onset and flat-band potentials.[116] Donor densities in $BiVO_4$ photoelectrodes used in this work correlate well at all frequencies, and show good agreement with literature values of around 10^{19} cm^{-3}.[70, 263] Donor density values were calculated using geometric area in absence of active surface area and a relative permittivity of ε = 86.

EIS measurements were repeated for a $BiVO_4$ photoelectrode in 50 mM 4-Cl-PAA solutions with added supporting electrolyte to compare charge carrier behaviours between the two systems. Impedance measurements were recorded in static solutions without stirring, therefore a significant diffusional component was observed in LSVs and Nyquist plots due to the low carboxylate concentration. As stirring rate can be variable on the

microscopic scale, attempts to agitate the solution and mimic electrolyses resulted in extremely noisy impedance spectra, particularly at low frequencies where mass transport elements dominate the impedance output.

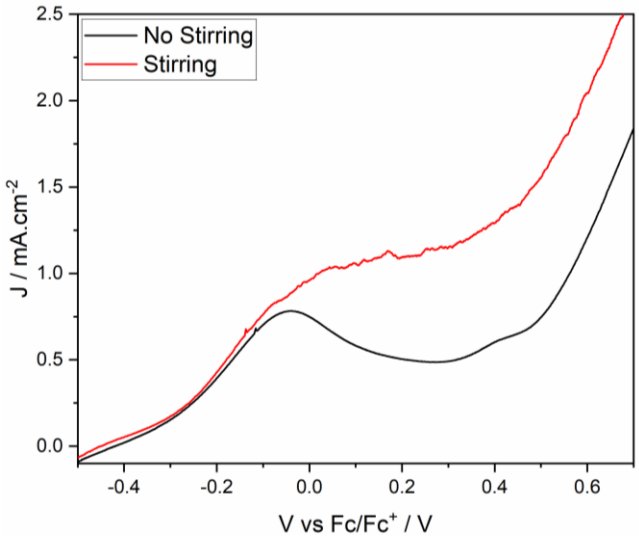

Figure 4.23: Linear sweep voltammogram of a $BiVO_4$ photoelectrode in unstirred (black) and stirred (red) 50 mM 4-Cl-PAA solutions containing 100 mM $TBAPF_6$ supporting electrolyte. Solutions were partially neutralised by addition of 0.05 equiv Et_3N. Voltammograms were recorded under blue LED illumination (32 mW cm^{-2}) at a scan rate of 100 mV s^{-1}.

In unstirred solutions, the oxidation of 4-Cl-PAA carboxylate anions was shown by the diffusion-controlled current peak at around -0.05 V vs Fc/Fc^+ (Figure 4.23). EIS measurements were therefore recorded at -0.06 V vs Fc/Fc^+ to interrogate charge transfer to the carboxylate anions (Figure 4.24).

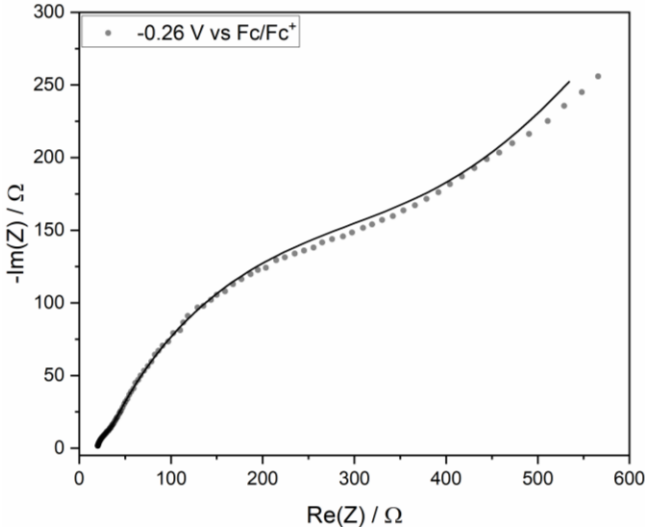

Figure 4.24: Electrochemical impedance spectrum of an illuminated $BiVO_4$ photoanode in 50 mM 4-Cl-PAA solution containing 100 mM $TBAPF_6$ supporting electrolyte at -0.26 V vs Fc/Fc^+. Solutions were partially neutralised by addition of 0.05 equiv Et_3N. Simulated impedance spectra are represented by the solid lines.

For the fitting of impedance spectra in 50 mM 4-Cl-PAA solutions, a similar equivalence cell as before was used, though a Warburg diffusion element, W_H, was included to account for the linear behaviour observed at low frequency caused by diffusion within the Helmholtz layer (Figure 4.25).

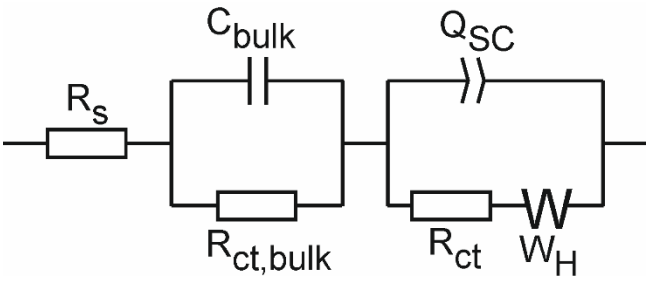

Figure 4.25: Equivalence cell used for the fitting of EIS spectra in 50 mM 4-Cl-PAA solutions.

As with 1 M 4-Cl-PAA solutions, two features were observed at higher frequencies, attributed to the same bulk and surface processes. However, in the lower concentration solution, a considerable overlap of the two features was observed suggesting more similar timescales for bulk and surface processes in electrolytes containing 50 mM 4-Cl-PAA. This may have also been caused by the significant increase in C_{bulk} in lower 4-Cl-PAA concentration solutions (Table 4.6).

Table 4.6: Parameters extracted from the fitting of impedance spectra for an illuminated $BiVO_4$ photoelectrode at -0.06 V vs Fc/Fc^+.

[4-Cl-PAA] / M	R_s / Ω	C_{bulk} / µF	$R_{ct,bulk}$ / Ω	C_{SC} / µF	R_{ct} / Ω
1	52.84	0.912	9.971	150.5	94.52
0.05	19.64	39.5	6.37	422.4	430.9

Generally, extracted parameters of the equivalence cells in 1 M and 50 mM 4-Cl-PAA electrolytes were similar, except for C_{bulk} which was around 2 orders of magnitude greater in lower acid concentrations. This was attributed to less extreme band bending caused by the reduction in carboxylate concentration at the electrode surface, and therefore reducing the flux of holes to the electrode surface. This change in band bending was reflected in the more anodic flat-band potential of -0.12 V vs Fc/Fc^+, as measured by Mott-Schottky analysis (Figure 4.26). Overall, the sluggish charge transfer kinetics in low acid concentration electrolytes were a result of increased bulk capacitance coupled with increased charge transfer resistance at the surface. The slower electron transfer and reduced carboxylate coverage at the electrode surface resulted in multiple-electron transfer pathways dominating and diminished dimer yields from radical-radical coupling.

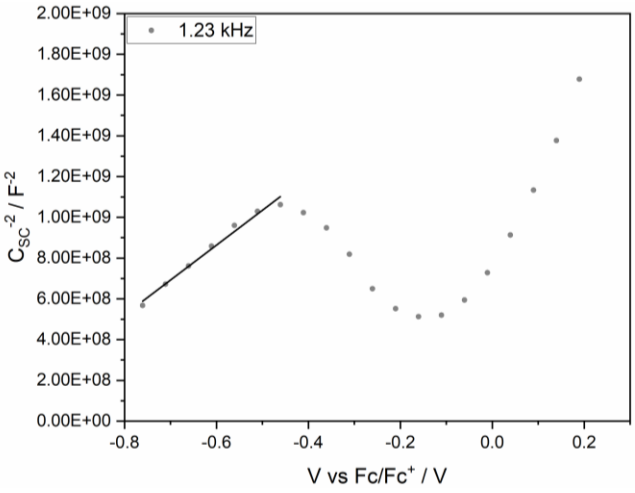

Figure 4.26: Mott-Schottky plots of a $BiVO_4$ photoelectrode in 50 mM 4-Cl-PAA solutions containing 100 mM $TBAPF_6$ supporting electrolyte at 1.23 kHz.

Due to the prevalence of the Warburg diffusion element at low frequency, Mott-Schottky plots were taken at around 1 kHz to isolate the space-charge capacitance. Flat-band potentials of $BiVO_4$ photoelectrodes in 50 mM 4-Cl-PAA solutions were measured at around -1.04 V vs Fc/Fc^+. When compared to the onset of the diffusion controlled oxidative current at ~-0.2 V vs Fc/Fc^+, an approximate overpotential of 0.8 V was calculated

for the oxidation of 4-Cl-PAA in the presence of $TBAPF_6$. The significant 0.4 V cathodic shift of E_{fb} on reducing 4-Cl-PAA concentration may have arisen from a non-negligible Helmholtz capacitance in these electrolytes due to the interference of PF_6^- anions on double layer formation.[198]

Although EIS measurements for 50 mM 4-Cl-PAA solutions were not truly operando characterisation as they were carried out in static solutions, the appearance of a diffusional element in the Nyquist plot suggested that electrode coverage by carboxylate was much lower than in 1 M 4-Cl-PAA solutions, for which this element was not observed. In 50 mM 4-Cl-PAA solutions, the poor electrode coverage, combined with sluggish charge transfer kinetics, resulted in lower steady-state radical concentrations which favoured over-oxidation of the intermediate radical and reduced dimer yields.

4.5 Conclusions

The scope of photoelectrochemical Kolbe reactions at $BiVO_4$ photoelectrodes was interrogated, including some attempts at radical-radical cross coupling reactions. In general, dimer selectivity was observed to follow photocurrent trends, with dimer selectivity up to 97% observed for aryl-substituted acids. For methoxy-substituted acids, a second oxidation to the carbocation is favoured due to the lower oxidation potential of the intermediate radical. Formation of the carbocation resulted in the observation of no dimerised product for these substrates. Based on the absence of dimer product for methoxyphenylacetic and hydrocinnamic acids, as well as reduced photocurrent for more sterically bulky arylacetic acids, we propose an intramolecular dissociative electron transfer mechanism predominates under our standard conditions.

Cross-coupling of radicals generated by oxidation of phenylacetic and 2-phenylisobutyric acids showed steric control of selectivity, with 67% selectivity obtained for bibenzyl and only 6% for dicumene, despite the lower oxidation potential of 2-PIBA. Increasing the electrolysis potential showed no effect on cross-coupling selectivity as radical-radical coupling selectivity was controlled predominantly by steric congestion of radical intermediates or preferential adsorption of PAA, as dimethylation results in weaker adsorption to the photoelectrode surface.

Attempts to reduce starting acid concentrations to improve conversion of starting material resulted in significant loss of selectivity for 4,4’-dichlorobibenzyl (~5%). Oxidation

of supporting electrolyte or product decomposition were discounted, as no appreciable oxidative photocurrents were measured in 0.1 M $TBAPF_6$ or 20 mM 4,4'-dichlorobibenzyl solutions. The effects of PF_6^- anions on electrochemical double layer formation could not be discounted, however, and disruption of the electrochemical double layer by these anions likely accounts for the loss of selectivity.

Higher selectivity (20%) was obtained when 4-chlorophenylacetic acid was below 100%, suggesting excess carboxylate in solution was key for enhancing Kolbe product selectivity. A mechanism for the formation of Kolbe and oxygenated products was proposed, with competitive adsorption of intermediate radicals and carboxylate anions at the electrode surface. Adsorption of intermediate radicals in low acid concentration electrolytes resulted in over-oxidation to the carbocation and increased selectivity for oxygenated products.

Impedance spectroscopy of 1 M and 50 mM 4-Cl-PAA solutions showed that a combinatorial effect of poorer electrode coverage by carboxylate and more sluggish charge transfer kinetics resulted in poorer dimer selectivity at low acid concentrations. The reduction in steady-state radical concentration as a result of these changes meant over-oxidation of the intermediate radical was favoured over dimerization and competitive alcohol oxidation could occur.

5. Conclusions and Future Work

Herein is presented an electrostatic spray pyrolysis methodology for the synthesis of reproducible bismuth vanadate photoelectrodes for photoelectrochemical Kolbe reactions of carboxylic acids. A thorough optimisation of oxidative decarboxylation reactions was undertaken to maximise phenylacetic acid (PAA) oxidation rates and radical-radical coupling selectivity. Analysis of the reaction system was focused on understanding key mechanistic processes and defining further research to optimise photoelectrochemical transformations.

Initial deposition of pre-synthesised $BiVO_4$ nanoparticles yielded poor performance electrodes, with photocurrent density of less than 0.2 mA cm^{-2} for PAA oxidation due to a poor electrical contact at the FTO/$BiVO_4$ interface. When depositing precursor complexes at high temperatures, significant performance improvements were seen, with a 3-fold increase in photocurrent density with deposition temperatures of 450 °C. Deposition solvent systems were shown to affect $BiVO_4$ photoelectrode performance due to poor solubility of vanadyl acetylacetonate in alcoholic solvents, resulting in inhomogeneous deposition and significant quantities of V(IV) within the electrode. The presence of V(IV) was initially observed by LSV before confirmation using XPS. Changing the solvent system to EtOAc:DMSO resulted in deposition of high-performance, reproducible electrodes with photocurrent density > 1.0 mA cm^{-2}. Best activity was observed with electrodes deposited at 350 °C for 30 minutes, with an optimal trade-off between absorption characteristics and charge transfer through electrode.

Although high PEC performance, reproducible $BiVO_4$ photoelectrodes were prepared using the electrostatic spray pyrolysis apparatus detailed, further optimisation of the set-up could be carried out to improve reproducibility even more. Several components were prepared in-house, though these could be replaced with commercial alternatives such as Luer fittings and engineered nozzles. Additionally, although some solvent system optimisation was carried out, further research could be undertaken to explore the relationships of film thickness and porosity with solvent boiling point, as detailed for electrospray deposition of polymer systems. Optimisation of $BiVO_4$ photoelectrodes may be subjective, with different electrode requirements for specific reactions, therefore the ease of adjusting electrospray parameters makes it an ideal candidate for the preparation of metal oxide photoelectrodes.

When using $BiVO_4$ photoelectrodes for PEC Kolbe reactions of PAA, bibenzyl selectivity was heavily dependent upon electrolytic cell set-up and illumination source. Initially a 2-component cell was used to eliminate any parasitic reactions of products, however moving to a one-compartment cell and a smaller cell volume resulted in an increased bibenzyl selectivity from 28 to 88%. This increase was attributed to a combination of improved photocurrent density due to shorter electrode spacing, and better sealing of the electrolytic cell from the ambient atmosphere. Improvements were also observed when using a blue LED array (32 mW cm^{-2}) instead of solar simulated AM1.5G (100 mW cm^{-2}) due to the higher proportion of emitted photons absorbed by the photoanode. As applied potential was increased, bibenzyl selectivity increased up to +0.26 V vs Fc/Fc^+ where selectivity dropped to 76%. This was a result of poor photoelectrode stability at higher applied potentials. UV-ozone treatment remedied some of the performance losses after electrolysis as some fouling material was present at the electrode surface. Not all PEC performance was recovered, however, due to irreversible vanadium leaching from the surface, as confirmed by XPS analysis. Bibenzyl selectivity was also shown to depend heavily on acid concentration, but less so on amine concentration. On decreasing acid concentration to 250 mM, a photocurrent density drop was observed due to increased solution resistance, resulting in around a 30% drop in bibenzyl Faradaic efficiency (FE). When decreasing acid concentration bibenzyl selectivity dropped by around 30% due to decreased photocurrent density and thus lower intermediate radical concentrations. Amine concentration seemed to have less effect on reaction selectivity, though FE for bibenzyl increased on addition of 0.01 equiv base. Generally, provided sufficient amine and PAA concentrations, bibenzyl was produced with high selectivity as the stability of a defined carboxylate layer at the electrode surface was a significant factor in maintaining photocurrents.

The diminishing PEC performance of $BiVO_4$ electrodes somewhat reduces their viability for these reactions, therefore further research on alternative, visible-light absorbing semiconducting materials could reveal a more stable photoanode material. Additionally, modification of $BiVO_4$ through doping or co-catalyst deposition could be used as a method for improving PEC performance as well as stability. The scope of PEC Kolbe reactions could also be explored in alternative solvents, including methanol – a popular choice in electrochemical Kolbe reactions. The effects of solvent on the product selectivity could be used to further elucidate the key factors determining radical-radical coupling selectivity.

Exploration of substituent effects of PAA derivatives showed no correlation between electronic substituent effects of aryl substituents and dimer selectivity, with dimer FE shown to depend on photocurrent density. Diminished photocurrent density was observed when using 2- and 3-substituted arylacetic acids. It was hypothesised that the less rod-like shape caused worse packing of carboxylate anions at the electrode surface, reducing effective carboxylate concentration and therefore photocurrent density. Lower photocurrent density for these acids thus resulted in lower dimer FEs. For example, 4-Cl-PAA gave a photocurrent density of 1.14 mA cm^{-2} and dimer selectivity of 97%, whilst 3-Cl-PAA gave 0.69 mA cm^{-2} and 73% respectively. A similar trend was observed for 4-Me-PAA (1.09 mA cm^{-2}, 92%) and 2-Me-PAA (0.74 mA cm^{-2}, 84%), though the difference was less. No dimer formation was observed when using methoxy substituted PAAs because electron donation of the substituent lowers the oxidation potential of the intermediate radical, favouring two-electron oxidation to a carbocation. Electrolysis of α-methyl substituted PAA demonstrated that increased radical stabilisation yielded higher homocoupling selectivity, even in cases where photocurrent density was not increased significantly, suggesting adsorption strength of the substrate played a critical role in the selectivity of dimer formation. Additionally, reduced photocurrent densities and dimer yields were observed when using 2- and 3-substituted arylacetic acids, attributed to poorer packing of the aryl groups at the electrode surface. Based on presented results and literature precedent, an intramolecular dissociative electron transfer mechanism was proposed, with initial oxidation of the aryl moiety followed by decarboxylation. This mechanism was known for the oxidation of methoxy-substituted acids at metallic electrodes and some larger arylacetic acids. The proposed mechanism accounts for the absence of product formation when using aliphatic acids such as hydrocinnamic acid. This mechanism has not been observed for simple arylacetic acids at metallic electrodes due to the lower oxidation potential of the carboxylate anion versus the aryl moiety. Therefore, this mechanism is possibly unique to semiconductor photoelectrodes, or $BiVO_4$.

On lowering the 4-Cl-PAA concentration and adding supporting electrolyte reduced the FE for dimer formation. Initial passage of fewer equivalents of charge showed significantly higher dimer FEs and since no parasitic redox reactions of the product were present, FE decreases attributed to changing selectivity in the absence of excess acid and anion competition from PF_6^- anions in the supporting electrolyte. Further understanding of the adsorption-desorption equilibrium of surface bound carboxylate may prove important in oxidative decarboxylation reactions for future use in photo- and photoelectrochemical C-

C and C-X bond formations, such as Giese coupling of a radical and an alkene. Further exploration of photoelectrochemical Giese reactions could be used to assess whether conclusions drawn in this thesis apply to radical-alkene couplings. PEC Giese chemistry may also alleviate issues concerning low acid concentration electrolytes by eliminating the need for radical-radical coupling.

Impedance analysis revealed that for lower acid concentrations, the diminished photocurrent density correlated with a significant increase in bulk capacitance and increased charge transfer resistance at the electrode surface. This was attributed to reduced carboxylate concentrations at the electrode surface, resulting in less extreme band bending and therefore poorer electron-hole separation within the semiconductor. As stirring of electrolyte solutions gave rise to noisy impedance data, these measurements were not true operando characterisation of the reaction system. Further EIS measurements could be carried out with more precise agitation of solutions to maintain mass transport rates of carboxylate and provide an adequate model of PEC Kolbe reactions. EIS and IMPS studies could also be used to identify key kinetic bottlenecks within the semiconductor and direct electrode modifications to further optimise PEC Kolbe reactions, or other transformations. Additionally, further operando characterisation, in particular *in situ* EPR studies, could be used to validate the mechanism proposed for PEC Kolbe reactions. The differentiation of adsorbed and free radical species would give further insight into the nature of radical species formed in PEC Kolbe reactions.

Overall, this thesis presents an initial interrogation of photoelectrochemical oxidative decarboxylation reactions at a visible-light absorbing semiconductor, $BiVO_4$. The findings of this work help to further develop the understanding of synthetic photoelectrochemical systems and enable the application of semiconductor photoelectrodes to organic transformations.

6. Experimental

6.1 Materials and Reagents

Ammonium metavanadate was purchased from Fisons Scientific Apparatus. Ethylenediaminetetraacetic acid was purchased from Avocado. Bismuth (III) 2-ethylhexanoate and vanadyl (IV) acetylacetonate were purchased from Alfa Aesar. Dimethylsulfoxide was purchased from Fisher Scientific. Ferrocene (98%) was purchased from Aldrich and further purified by sublimation. FTO glass, bismuth nitrate pentahydrate, triethylamine (≥99.5 %), 2-methyl, 4-methyl, 4-methoxy and 3-methoxyphenylacetic acid, benzoic and hydrocinnamic acids were purchased from Sigma-Aldrich. Phenylacetic acid (98.5 %) was purchased from Acros Organics. 3-chloro, 4-chloro and 4-fluorophenylacetic acid, 2-phenylisobutyric and 2-phenylpropionic acids were all purchased from Fluorochem. Tetrabutylammonium hexafluorophosphate was purchased from Fluka and was recrystallised in ethanol prior to usage. 4,4'-Dichlorobibenzyl was purchased from Merck Life Sciences.

Chloroform-d, ethyl acetate, ethanol and acetonitrile were obtained from Sigma-Aldrich. Dichloromethane, isopropanol and toluene were purchased from VWR International. Acetonitrile was dried using an Innovative Technology PureSolv Solvent Purification System and stored with molecular sieves (4 Å). Deionised water was purified using a Milli-Q water purification system.

6.2 Instrumentation and Methods

6.2.1 BET Surface Area Analysis

BET (Brunauer-Emmett-Teller) surface area analysis of hydrothermally-synthesised $BiVO_4$ nanoparticles were carried out using a Micromeritics Tristar 3000 Porosimeter. Approximately 100 mg of $BiVO_4$ powder was dried at 80 °C for 6 hours and degassed with nitrogen prior to adsorption measurements.

6.2.2 Controlled Potential Electrolyses

Controlled potential electrolyses were carried out using either a BioLogic SP-150 or BASi EC Epsilon potentiostat in a 3-electrode configuration. A 1 or 2-compartment electrolytic cell was loaded with a $BiVO_4$ working electrode, Pt wire counter electrode and either a Pt or Ag wire reference electrode (Figure 3.3, Figure 3.5, Figure 3.7). Electrolytic

cells were charged with up to 20 mL dry, degassed electrolyte solution in MeCN and further purged with a flow of N_2 or Ar gas. Electrolyses were carried out at specified potentials for a minimum of 3 hours under blue LED array illumination (32 mW cm^{-2}).

6.2.3 Cyclic and Linear Sweep Voltammetry

Cyclic and linear sweep voltammograms were recorded on either a BioLogic SP-150 or BASi EC Epsilon potentiostat in a 3-electrode configuration. A 1 or 2-compartment electrolytic cell was loaded with a $BiVO_4$ working electrode, Pt wire counter electrode and either a Pt or Ag wire reference electrode. Cyclic voltammograms were recorded between -0.3 – 1.0 V vs reference for up to 10 cycles at a scan rate of 10 mV s^{-1} in the dark and under blue LED array illumination (32 mW cm^{-2}). Linear sweep voltammograms were recorded between -0.5 – 1.0 V vs reference at a scan rate of 10 mV s^{-1} in the dark and under blue LED array illumination (32 mW cm^{-2}).

6.2.4 Diffuse Reflectance UV-vis Spectroscopy

Diffuse reflectance spectra of $BiVO_4$ powders were recorded using an Ocean Optics HR2000+ spectrometer with Mikropak DH-2000-BAL UV-VIS-NIR light source. Spectra were recorded and averaged over 10 scans with 5 second integration time. Reference spectra were collected using a flat polystyrene standard in the dark and under illumination. $BiVO_4$ powders were sandwiched between two glass microscope slides to prepare a flat surface. The top slide was removed prior to spectra being recorded.

6.2.5 Electrochemical Impedance Spectroscopy

Electrochemical impedance spectroscopy (EIS) measurements were recorded using a BioLogic SP-150 potentiostat in a 3-electrode, 1-compartment electrolytic cell containing a $BiVO_4$ working electrode, a Pt wire counter electrode and an Ag wire reference electrode isolated in a Luggin capillary. Data were collected using an a.c. potential amplitude of 10 mV between 500 kHz – 50 mHz, with 10 points per frequency decade. Applied voltage was increased in 200 mV steps between -0.66 – 0.54 V vs Fc/Fc^+ in the dark and under illumination by a blue LED array (32 mW cm^{-2}). Mott-Schottky analysis was recorded between -0.76 – 0.74 V vs Fc/Fc^+ in 75 mV steps. Measurements were recorded between 100 kHz – 100 mHz with a sinus amplitude of 10 mV.

6.2.6 Electrostatic Spray Pyrolysis

An illustration and schematic of the electrospray apparatus are given in Figure 6.1 and Figure 6.2. A Chemyx Fusion 100 syringe pump was used to pump solutions through 1/16th in. inner diameter tubing. Solutions were mixed in a 3D-printed PEEK Y-piece (Roboze 3D Parts) prior to deposition from a flattened Braun Sterican metal syringe needle (0.8 x 120 mm, shortened to 110 mm). Glass beads were prepared by Ms Abigail Mortimer (University of York). Applied voltage and temperature controllers were made by Mr Chris Rhodes (University of York). All tubing was adhered using Araldite ARA-400007 Rapid epoxy resin. Deposition was carried out only under conditions where a stable cone-jet spraying mode was formed (Figure 2.1). Expulsion of air bubbles from tubing was carried out by flowing solution through the tubing with simultaneous inversion of the metal nozzle. Confirmation of air bubble removal was made once solution flow through the nozzle was uninterrupted for at least 5 seconds. Prior to application of the potential difference, a droplet of deposition solution was formed at the glass bead to ensure consistent cone-jet formation. The deposition area after formation of the cone-jet was consistently a 2 cm diameter circle that was centred with respect to the centre of the unmasked area of FTO.

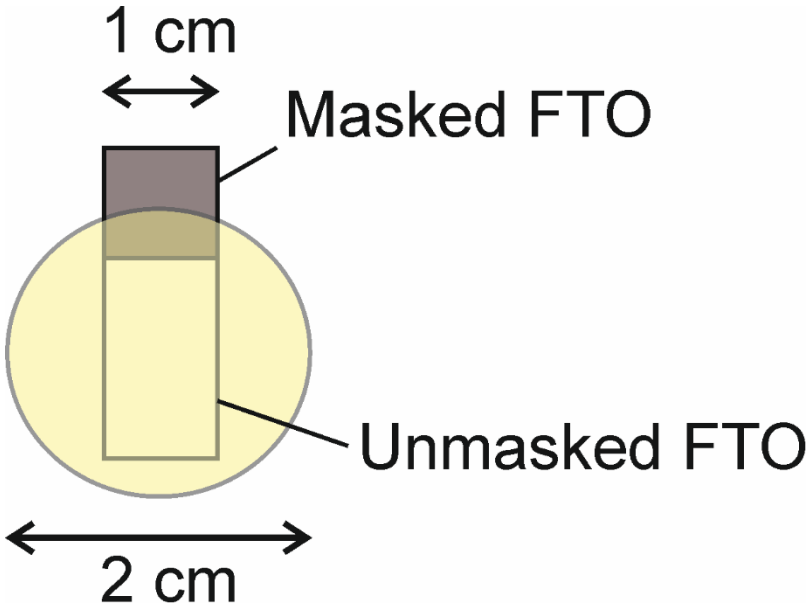

Figure 6.1: Illustration and approximate dimensions of electrospray deposition area used for the preparation of $BiVO_4$ photoelectrodes. The deposition area was centred on the unmasked portion of FTO.

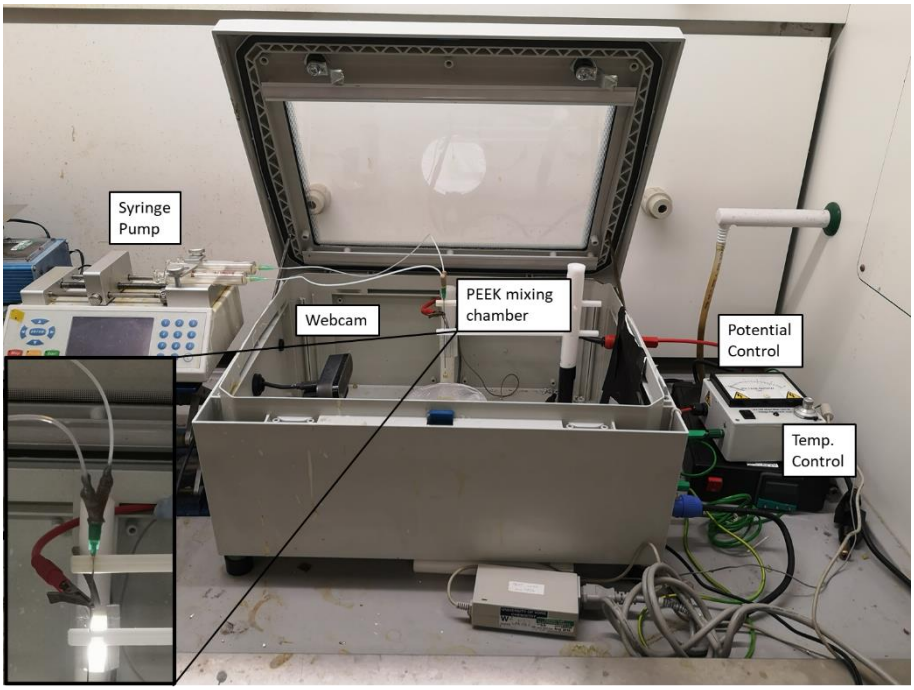

Figure 6.2: Schematic of the electrospray deposition set-up and PEEK mixing chamber (inset) used for preparation of $BiVO_4$ photoelectrodes.

6.2.7 Gas Chromatography

Gas chromatography was carried out partially by Dr Scott Hicks (University of York). Product mixtures were methylated (Section 6.4.1) and then analysed using a ThermoTrace 1300 GC gas chromatograph, with the GC inlet held at 280 °C. Separation of products was achieved using a fused silica capillary column (Rxi-17, 30 m x 0.25 mm I.D. x 0.25 µm film thickness), with an oven temperature program as follows: 50 °C (0.5 min) to 90 °C at 100 °C min^{-1}, then 300 °C (1 min) at 15 °C min^{-1}. A hydrogen carrier gas was used at a flow of 1.5 mL min^{-1}. Products were detected using a flame ionisation detector held at 330 °C.

For analysis of headspace gases, a 50 µL aliquot of the cell headspace was taken after 3-hour electrolysis of 1 M PAA solutions at +0.09 V vs Fc/Fc^+. Measurements were made with an Agilent Technologies 7820A gas chromatograph, with a thermal conductivity detector (TCD), fitted with a Carboxen 1010 PLOT 30 m x 0.53 mm capillary column. Argon was used as the carrier gas at a flow rate of 2 mL/min with a split ratio of 10:1 and a 50 µL manual injection. The initial oven temperature was held at 100 °C for 2 minutes and was increased at a rate of 25°C/min to 250°C and held at this temperature for 2 minutes, with a total run time of 10 minutes. Injection temperature was 200°C and the detector temperature was 250°C.

6.2.8 Gas Chromatography-Mass Spectrometry

GC-MS was carried out by Mr Karl Heaton (University of York). Measurements were recorded on a JEOL AccuTOF GCx-plus mass spectrometer coupled to an Agilent 7890B GC system containing a Phenomenex ZB-5MS plus column (30 m x 0.25 mm x 0.25µm). Chromatography conditions were identical to those described in section 6.2.7.

6.2.9 Grazing Incidence X-Ray Diffraction

Grazing Incidence X-Ray Diffraction measurements were carried out on a Rigaku SmartLab X-Ray diffractometer with a Cu Kα source (λ = 1.5406 Å). The incident X-ray beam was held at 0.5° whilst 2θ was scanned between 5 - 75° in 0.05° steps.

6.2.10 Mass Spectrometry

Electrospray ionisation mass spectrometry (ESI-MS) was collected by Mr Karl Heaton on a Bruker microTOF Electrospray Mass Spectrometer. Samples were submitted as methylated mixtures in 1:1 DCM:MeOH. The methylation of reaction mixtures is described in section 6.4.1.

6.2.11 NMR Spectroscopy

Solution ^{1}H NMR spectra were recorded on a JEOL ECX400 (400 MHz) spectrometer. Samples were dissolved in $CDCl_3$ containing dimethylterephthalate (10 mg mL^{-1}) and peaks referenced to the residual $CHCl_3$ solvent peak.

6.2.12 Powder X-ray diffraction

Powder X-ray diffractograms (p-XRD) were recorded using a Bruker D8 X-ray Diffractometer with a Lynxeye detector and Cu Kα source (λ = 1.5406 Å). Samples were held on an Al disk and measurements recorded between 5 – 90° with a step size of 0.02°.

6.2.13 Scanning Electron Microscopy

Scanning electron micrographs were recorded on a JEOL 7800 F Prime Field Emission Scanning Electron Microscope. Images were taken under an acceleration voltage of 10 kV at 10 mm working distance. Backscattered electrons were detected using the lower electron detector (LD). Prior to imaging all samples were coated with a Pd/Pt alloy

(10 nm) using a JEOL JFC 2300 HR High Resolution Fine Coater to prevent sample charging under the electron beam. Electrical connections were made between sample surfaces and aluminium stubs with Agar Scientific conductive silver paint. Imaging resolution and quality was limited by sample charging in spite of measures to reduce this. EDS measurements were recorded using two Oxford Instruments UltiMax 170 Silicon Drift Detector Energy Dispersive X-Ray Spectrometers. The incident electron beam was held at 10 keV.

6.2.14 UV-ozone cleaning

UV-ozone treatment of $BiVO_4$ photoelectrodes was done using an Ossila UV-Ozone cleaner for 5 minutes at 25.0 °C.

6.2.15 UV-vis Transmittance Spectroscopy

UV-vis transmittance spectra of $BiVO_4$ electrodes were recorded using an Ocean Optics HR2000+ spectrometer with Mikropak DH-2000-BAL UV-VIS-NIR light source. Spectra were recorded and averaged over 10 scans with 5 second integration time and a boxcar width of 30. Reference spectra were collected using a cleaned FTO plate standard in the dark and under illumination.

6.2.16 X-Ray Photoelectron Spectroscopy

X-ray photoelectron spectroscopy was carried out by Dr Ben Coulson at the University of York. XPS experiments were performed in an ultrahigh vacuum system with a base pressure of $<3 \times 10^{-10}$ mbar using a monochromated Al Kα source at 1486.6 eV (Omicron XM 1000) and a power of 220 W. An aperture diameter of 6 mm was used with the sample normal at 22.5° to both the X-ray source and the entrance optics of the hemispherical energy analyser (Omicron EA 125). XPS spectra were referenced to adventitious carbon peak at 284.8 eV. Peak deconvolution and fitting was carried out manually using XPSPEAK4.1 software.

6.3 Chapter 2 Experimental

6.3.1 Hydrothermal Synthesis of $BiVO_4$ Nanoparticles

Bismuth vanadate nanoparticles were synthesised according to a literature procedure.[169] Bismuth nitrate pentahydrate (4.85 g, 10 mmol) and EDTA (2.93 g, 10 mmol) were dissolved in 2 M HNO_3 (100 mL) and stirred for 30 minutes. Ammonium

metavanadate (1.17 g, 10 mmol) was added and stirring continued for 2 hours to give a pale-yellow solution. Teflon-lined autoclaves were filled with the reaction solution and heated to 90 °C for 6 hours (5 °C min^{-1}). After heating, synthesised particles were separated by centrifugation (4000 rpm, 30 minutes) before washing with deionised water and ethanol sequentially. Particles were dried at 70 °C overnight.

6.3.2 Cleaning of Fluorine-doped Tin Oxide Glass

FTO slides (10 x 30 mm) were cleaned by soaking in Piranha solution (3:1 H_2SO_4:H_2O_2) for 1 hour at room temperature before rinsing sequentially with deionised water and ethanol. Substrates were then dried under a flow of N_2 gas, and a 10 x 15 mm area masked with tin foil. After use, Piranha solution was neutralised to approximately pH 7 by slow addition of sodium hydrogen carbonate.

6.3.3 Electrostatic Spray Pyrolysis of $BiVO_4$ Nanoparticles

As-synthesised $BiVO_4$ nanoparticles were suspended in 9:1 isopropanol:dimethylsulfoxide (10 mg mL^{-1}) and passed through 1/16th in. inner diameter tubing at a flow rate of 0.03 mL min^{-1}. The nanoparticle suspension was flowed through a metal nozzle held at 8 kV potential difference to the baseplate. The suspension was then deposited onto a cleaned FTO substrate held at 140 °C for 30 minutes. After deposition, yellow $BiVO_4$ nanoparticle films were calcined in air at 450 °C for 2 hours to yield the final photoelectrodes.

6.3.4 Electrostatic Spray Pyrolysis of Bismuth 2-ethylhexanoate and Vanadyl Acetylacetonate in Ethyl Acetate:Co-Solvent Mixtures

Bismuth 2-ethylhexanoate (319.3 mg, 0.5 mmol) and vanadyl acetylacetonate (132.2 mg, 0.5 mmol) were dissolved separately in 1:1 mixtures of ethyl acetate and co-solvent (50 mL, Table 6.1). Precursor solutions were loaded into 2 mL glass syringes and air bubbles expelled before attachment to tubing. Solutions were flowed through 1/16th in. inner diameter tubing by syringe pump and mixed in a 3D-printed PEEK mixing chamber at a specified flow rate. The mixed precursor solution was flowed through a metal nozzle held under an applied potential and sprayed onto cleaned, heated FTO substrates. FTO substrates were masked by tin-foil to leave 1.5 x 1 cm exposed for deposition. After deposition, films were annealed in air at 450 °C for 2 hours to give the final yellow photoelectrodes. Deposition parameters are given in Table 6.1.

Table 6.1: Co-solvents and deposition parameters for the electrospray deposition of $BiVO_4$ photoelectrodes.

EtOAc co-solvent	Deposition Temperature / °C	Flow Rate / mL min^{-1}	Applied Voltage / kV	Deposition Time / min
Ethanol	300 - 450	0.03	9.5	30
Isopropanol	450	0.015 - 0.05	7.5	18 - 120
Dimethylsulfoxide	350 - 450	0.03	8.5	15 - 45

6.3.5 Linear Sweep Voltammetry of 1 M Phenylacetic Acid Electrolytes

Phenylacetic acid (13.62 g, 100 mmol) was dried in vacuo in an ampoule and dissolved in dry, degassed MeCN (100 mL). 0.05 equiv dry triethylamine (0.21 mL, 1.5 mmol) was added to 30 mL of the stock phenylacetic acid solution. A 2-compartment electrolytic cell was degassed by a N_2 flow and charged with 20 mL phenylacetic acid-triethylamine solution in the working electrode compartment and 5 mL in the counter electrode compartment.

A 3-electrode configuration was used with a $BiVO_4$ working electrode, a Pt counter electrode, and a Pt wire reference electrode. Voltammograms were recorded between -0.76 – 1.24 V vs Fc/Fc^+ reference at a scan rate of 10 mV s^{-1}. Measurements were recorded in the dark and under illumination by a solar-simulated irradiation source (100 mW cm^{-2}) or a blue LED array (32 mW cm^{-2}).

6.3.6 Ferrocene/Ferrocenium Electrochemical Reference

After electrochemical measurements, the potential of the Ag wire pseudo-reference electrode was referenced to the ferrocene/ferrocenium redox couple. Ferrocene (7.4 mg, 0.04 mmol) was added to the electrolytic cell containing remaining PAA electrolyte. TBAPF6 (309.9 mg, 0.8 mmol) The $BiVO_4$ working electrode was replaced with a platinum wire. Voltammograms were recorded between -0.1 – 0.5 V vs Ag wire at a scan rate of 50 mV s^{-1} for one cycle (Figure 6.3). The reference potential, V_{Ref}, for the ferrocene/ferrocenium redox couple was calculated using:

$$V_{Ref} = \frac{(V_{p,a} + V_{p,c})}{2} \qquad \text{Equation 4}$$

Where $V_{p,a}$ is the potential at peak anodic current and $V_{p,c}$ is the potential at peak cathodic current.

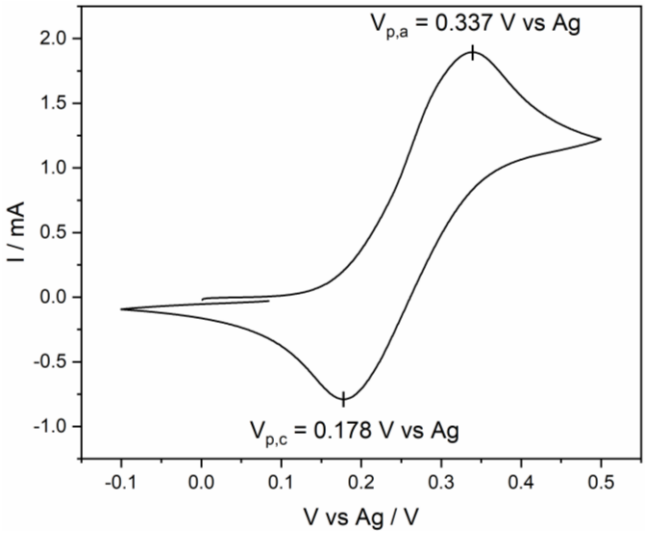

Figure 6.3: Cyclic voltammogram of 5 mM ferrocene in MeCN containing 0.1 M $TBAPF_6$ supporting electrolyte.

6.4 Chapter 3 and 4 Experimental

6.4.1 Methylation of Carboxylic Acids with Trimethylsilyldiazomethane (2.0 M in hexanes) for GC Analysis

A 40 µL aliquot of electrolyte after electrolysis was diluted by 1 in 50 in 1:1 dichloromethane:methanol. A 1 mL aliquot of the dilution was taken and trimethylsilyldiazomethane (2.0 M in hexanes, 30 µL) was added to the aliquot and left to react for 30 minutes in the dark. After methylation, aliquots were dried *in vacuo*, redissolved in 1:1 dichloromethane:methanol (1 mL) and filtered through a .22 µm syringe filter to remove solid particulates. For each electrolysis, 3 GC samples were prepared, each injected 3 times to average out dilution and instrumental errors.

6.4.2 GC Calibration Curves of Bibenzyl, Benzyl Alcohol and Benzaldehyde

Solutions of bibenzyl, benzyl alcohol and benzaldehyde were made to known concentrations in 1:1 DCM:MeOH. GC chromatograms were recorded in triplicate for all concentrations of each product (3 samples, 3 injections each).

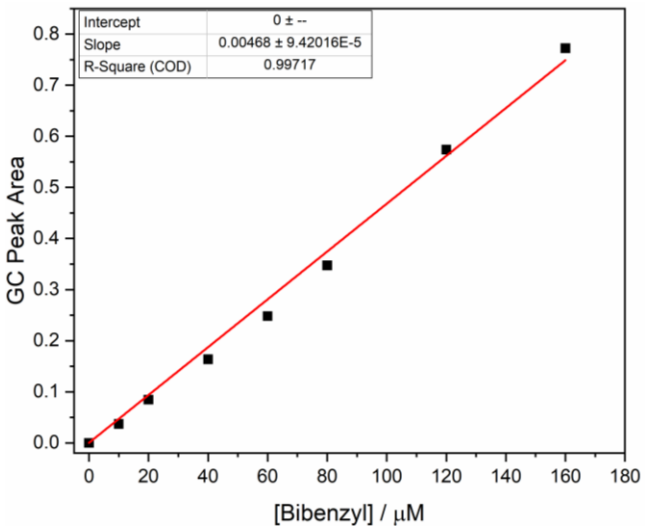

Figure 6.4: GC calibration curve of bibenzyl.

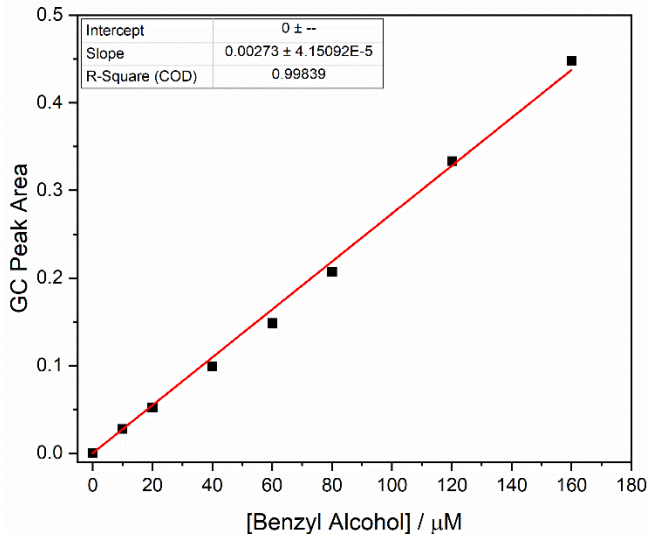

Figure 6.5: GC calibration curve for benzyl alcohol.

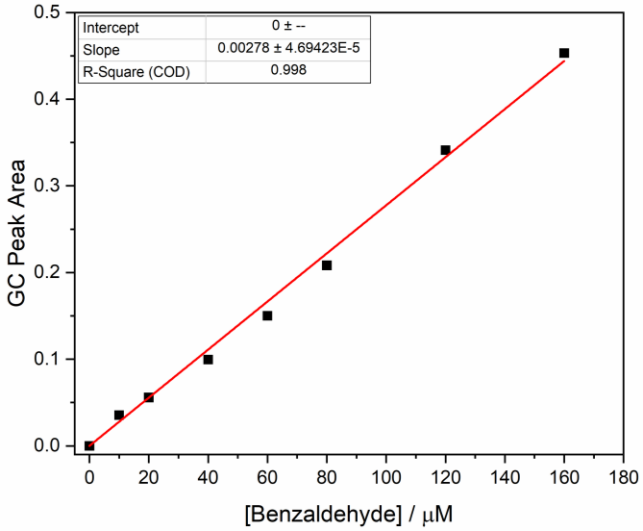

Figure 6.6: GC calibration curve for benzaldehyde.

6.4.3 General Procedure for Controlled Potential Electrolysis of Phenylacetic Acid Derivatives

A known amount of phenylacetic acid derivative (up to 30 mmol) was dried in a Schlenk tube and dissolved in dry, degassed MeCN (up to 30 mL). 0.05 equiv dry triethylamine (up to 0.21 mL, 1.5 mmol) was added to the stock phenylacetic acid solution. The Schlenk tube was then sealed with a rubber septum and N_2 balloon. A 1- or 2-compartment electrolytic cell containing a magnetic stirrer bar was degassed for 5 minutes with N_2 flow and charged with phenylacetic acid-triethylamine solution. After addition of electrolyte (8 – 20 mL), the headspace of electrolytic cells were degassed for a further 5 minutes and reactions carried out for 3 hours under a static atmosphere of nitrogen unless stated. Further degassing of the solution was not carried out to prevent electrical contact of the electrolyte solution and metallic components of the electrodes.

A 3-electrode configuration was used with a $BiVO_4$ working electrode, a Pt counter electrode, and a Pt wire reference electrode. Electrolyses were carried out at specified potentials for up to 6 hours under blue LED array (32 mW cm^{-2}) or AM1.5G illumination (100 mW cm^{-2}). Products were methylated, analysed by gas chromatography, and compared to external standards.

For time-dependent product analysis, the electrolysis was paused and 100 μL aliquots of the electrolyte were taken each hour for 6 hours.

Schematics of electrolytic cells used are given in Figure 3.3, Figure 3.5 and Figure 3.7.

Table 6.2: Electrolysis parameters and for the oxidation of phenylacetic acid derivatives and GC retention times of products in photoelectrochemical Kolbe reactions. X denotes no product observation by GC-MS.

Substrate	[Acid] / M	[Et_3N] / equiv	Dimer t_R / min	Alcohol t_R / min	Aldehyde t_R / min	Potential / V vs Fc/Fc^+
Phenylacetic Acid	0.25 - 1	0.025 – 0.1	8.88	5.09	4.55	-0.26 - 0.54
4-Chloro-phenylacetic Acid	1	0.05	11.94	X	X	0.09
3-Chloro-phenylacetic Acid	1	0.05	11.73	X	X	0.09
4-Methoxy-phenylacetic Acid	1	0.05	X	7.32	7.12	0.09
3-Methoxy-phenylacetic Acid	1	0.05	X	6.56	5.72	0.09
4-Methyl-phenylacetic Acid	1	0.05	10.23	6.23	5.81	0.09
2-Methyl-phenylacetic Acid	1	0.05	10.34	5.97	5.34	0.09
4-Fluoro-phenylacetic Acid	1	0.05	8.71	X	X	0.09
2-Phenylpropionic Acid	1	0.05	9.36, 9.26	X	X	0.09
2-Phenylisobutyric Acid	1	0.05	10.95	X	X	0.09
Hydrocinnamic Acid	1	0.05	X	5.46	X	0.09
Benzoic Acid	1	0.05	X	4.09	X	0.09
Phenylacetic Acid/2-Phenyl-isobutyric Acid	0.5/0.5	0.05	8.86, 9.54, 10.95	X	X	0.09 - 0.54

6.4.4 Apparent Quantum Yield Measurements for Phenylacetic Acid Oxidation

4-chlorophenylacetic acid (1.71 g, 10 mmol) was dissolved in dry, degassed MeCN (10 mL). 0.05 equiv triethylamine (0.07 mL, 0.5 mmol) was added. The electrolytic cell was charged with 8 mL phenylacetic acid-triethylamine solution.

A 3-electrode configuration was used with a $BiVO_4$ working electrode, a Pt counter electrode, and an Ag wire reference electrode isolated in a Luggin capillary. Controlled potential electrolyses were carried out at +0.09 V vs Fc/Fc^+ for 1 minute under blue LED illumination (λ = 450 nm) at 80, 120 and 160 mm from the working electrode (32, 17 and 10 mW cm^{-2}).

Incident Photon to current efficiency (IPCE) was calculated as the ratio of electrons passed per second to the total number of photons irradiating the electrode.

$$Electron\ No. = \frac{ItN_A}{F} \qquad \text{Equation 5}$$

Where I is the photocurrent in A, t is the time in seconds, N_A is Avogadro's number and F is the Faraday constant (96485 C mol^{-1})

$$Incident\ Photon\ No. = \frac{Y_e A \lambda}{hc} \qquad \text{Equation 6}$$

Where Y_e is the irradiance at the photoelectrode in W cm^{-2}, A is the geometric electrode area, λ is the incident photon wavelength (assumed 450 nm here), h is Planck's constant and c is the speed of light in a vacuum.

Apparent quantum yield (AQY) was calculated as the IPCE multiplied by the product selectivity for the Kolbe product.

For the electrolysis of 1 M 4-Cl-PAA under 32.2 mW cm^{-2} irradiance:

$$Electron\ No. = \frac{2.1\ mA\ \times 1\ s\ \times 6.022 \times 10^{23}}{96485\ s\ A\ mol^{-1}} = 1.31 \times 10^{16}$$

$$Photon\ No. = \frac{32.2\ mW\ cm^{-2} \times 1.5\ cm^2 \times 450 \times 10^{-9}\ m}{6.63 \times 10^{-34}\ m^2\ kg\ s^{-1}\ 3 \times 10^8\ m\ s^{-1}} = 1.085 \times 10^{17}$$

$$PCE = \frac{1.3 \times 10^{16}}{1.085 \times 10^{17}} \times 100\% = 12.1\%$$

$$AQY = 12.1\% \times 0.99 = 12.0\%$$

6.4.5 Controlled Potential Electrolysis of 4-Chlorophenylacetic Acid containing 100 mM Tetrabutylammonium Hexfluorophosphate Supporting Electrolyte

4-chlorophenylacetic acid (85.3 mg, 0.5 mmol) and tetrabutylammonium hexafluorophosphate (0.39 g, 1.0 mmol) were dissolved in dry, degassed MeCN (10 mL) in a Schlenk tube. 0.05 equiv triethylamine (0.1 mL, 0.25 M, 0.025 mmol) was added. The electrolytic cell was charged with 8 mL of acid-triethylamine solution and further degassed for 5 minutes with Ar flow. Once degassed, the continuous Ar flow was replaced with an Ar balloon to maintain the headspace of the cell.

A 3-electrode configuration was used with a $BiVO_4$ working electrode, a Pt counter electrode, and an Ag wire reference electrode isolated in a Luggin capillary. Controlled potential electrolyses were carried out at +0.24V vs Fc/Fc^+ for 8-24 hours under blue LED array illumination (32 mW cm^{-2}).

After electrolysis, product mixtures were dried *in vacuo* and redissolved in toluene (10 mL). The mixture was filtered, and extracts dried *in vacuo*. Extracted products were then redissolved in $CDCl_3$ containing dimethylterephthalate (10 mg mL^{-1}) as an internal standard and analysed by ^1H NMR. Products were not isolated and were analysed as mixtures quantified by characteristic ^1H NMR signals.

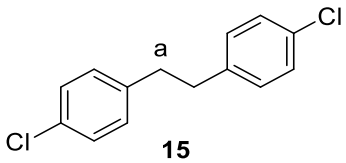

15

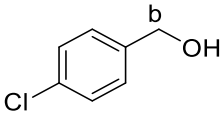

27

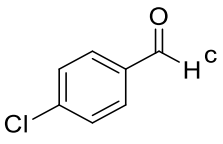

28

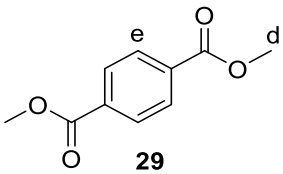

29

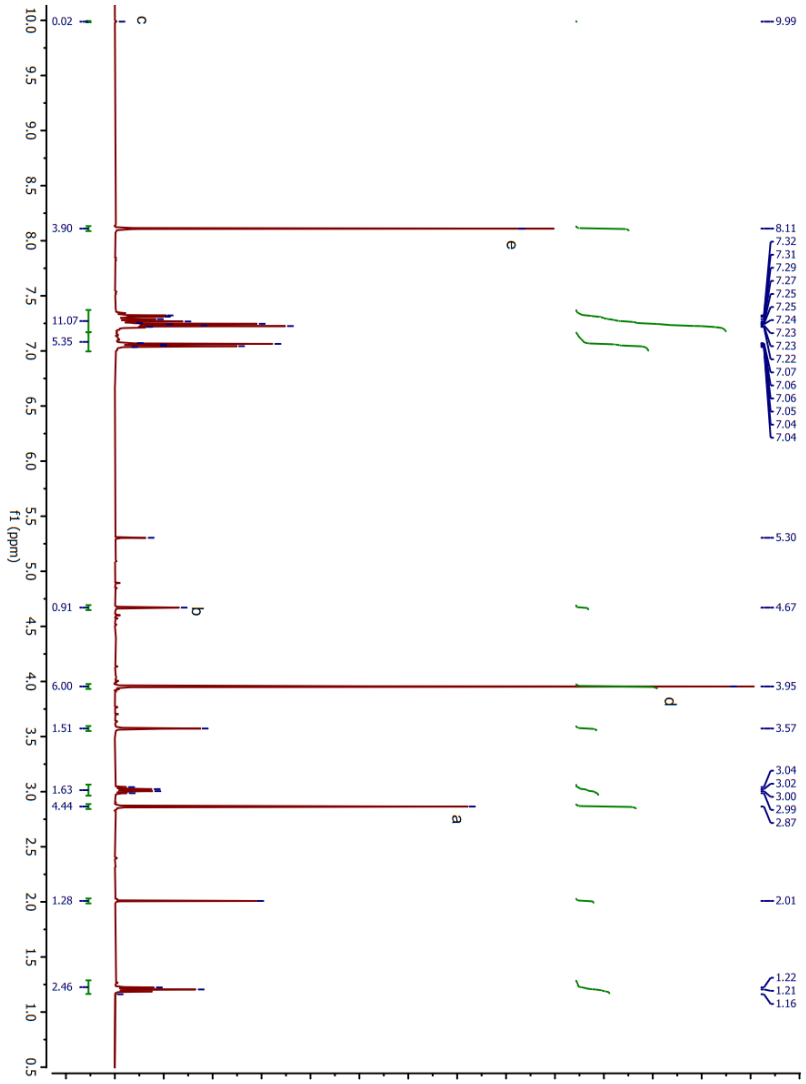

^{1}H NMR (400 MHz, $CDCl_3$) δ 9.99 (s, 1H, **28** C*H*O), 8.11 (s, 4H, **29** arene C*H*), 7.32-7.04 (m, 20 H, multiple products, aromatic C*H*), 5.30 (s, 1 H, dichloromethane), 4.67 (s, 2H, **27** CH_2OH), 3.95 (s, 6H, **29** CH_3), 3.57 (s, 2H, 4-chlorophenylacetic acid CH_2COOH), 3.04-2.99 (q, *J* = 8 Hz, 6H, triethylamine), 2.87 (s, 4H, **15** CH_2), 2.01 (s, 3H, acetonitrile), 1.22-1.16 (t, *J* = 8 Hz, 9H, triethylamine).

6.4.6 24 Hour Controlled Potential Electrolysis of 1 M 4-Chlorophenylacetic Acid Electrolytes

4-chlorophenylacetic acid (1.71 g, 10 mmol) was dissolved in dry, degassed MeCN (10 mL). 0.05 equiv triethylamine (0.07 mL, 0.05 mol) was added. The electrolytic cell was charged with 8 mL of acid-triethylamine solution and further degassed for 5 minutes with

Ar flow. The continuous Ar flow was removed and replaced by an Ar balloon to maintain the headspace of the cell.

A 3-electrode configuration was used with a $BiVO_4$ working electrode, a Pt counter electrode, and an Ag wire reference electrode isolated in a Luggin capillary. Controlled potential electrolyses were carried out at +0.09 V vs Fc/Fc^+ for 24 hours under blue LED array illumination (32 mW cm^{-2}).

6.4.7 Electrochemical Impedance Spectroscopy of 50 mM 4-Chlorophenylacetic Acid Electrolytes

4-chlorophenylacetic acid (85.3 mg, 0.5 mmol) and tetrabutylammonium hexafluorophosphate (0.39 g, 1.0 mmol) were dissolved in dry, degassed MeCN (10 mL). 0.05 equiv triethylamine (0.1 mL, 0.25 M, 0.025 mmol) was added. The electrolytic cell was charged with 8 mL of acid-triethylamine solution and further degassed for 5 minutes with Ar flow.

A 3-electrode configuration was used with a $BiVO_4$ working electrode, a Pt counter electrode, and an Ag wire reference electrode isolated in a Luggin capillary. Electrochemical impedance measurements were recorded between 500 kHz – 50 mHz for 10 points per decade with a sinus amplitude of ±10 mV. Measurements were recorded at 200 mV increments between -0.66 – 0.54 V vs Fc/Fc^+ under blue LED array illumination. Data above 0.14 V vs Fc/Fc+ were omitted as corrosion of the electrode occurred at these potentials, which could not be interpreted with the equivalence cell used. Mott-Schottky analysis was recorded between -0.76 – 0.74 V vs Fc/Fc^+ at frequencies between 100 kHz – 100 mHz with a sinus amplitude of ±10 mV. All Mott-Schottky measurements were recorded in the dark.

6.4.8 Electrochemical Impedance Spectroscopy of 1 M 4-Chlorophenylacetic Acid Electrolytes

4-chlorophenylacetic acid (1.71 g, 10 mmol) was dissolved in dry, degassed MeCN (10 mL). 0.05 equiv triethylamine (0.07 mL, 0.05 mol) was added. The electrolytic cell was charged with 8 mL of acid-triethylamine solution and further degassed for 5 minutes with Ar flow.

A 3-electrode configuration was used with a $BiVO_4$ working electrode, a Pt counter electrode, and an Ag wire reference electrode isolated in a Luggin capillary. Electrochemical

impedance measurements were recorded between 500 kHz – 50 mHz for 10 points per decade with a sinus amplitude of ±10 mV. Measurements were recorded at 200 mV increments between -0.66 – 0.54 V vs Fc/Fc^+ under blue LED array illumination. Due to the presence of a sole diffusion-controlled peak, only data from -0.06 V vs Fc/Fc^+ were shown. Mott-Schottky analysis was recorded between -0.76 – 0.74 V vs Fc/Fc^+ at frequencies between 100 kHz – 100 mHz with a sinus amplitude of ±10 mV. All Mott-Schottky measurements were recorded in the dark.

Abbreviations and Terms

2-PIBA – 2-phenylisobutyric acid

2-PPA – 2-phenylpropionic acids

acac – acetylacetonate

Ag/AgCl – Silver/Silver Chloride Electrode

$Ag/AgNO_3$ – Silver/Silver Nitrate Reference Electrode

AQY – Apparent Quantum Yield

$BiVO_4$ – Bismuth Vanadate

BnOH – Benzyl Alcohol

C_3N_4 – Carbon Nitride

CBM – Conduction Band Minimum

C_{bulk} – Bulk Capacitance

C_{dl} – Double Layer Capacitance

CdS – Cadmium Sulfide

CE – Counter Electrode

CeO_2 – Cerium Dioxide

CoPi – Cobalt Phosphate

CPE – Constant Phase Element

C_{SC} – Space Charge Capacitance

$CsPbBr_3$ – Caesium Lead Bromide

C_{SS} – Surface State Capacitance

CV – Cyclic Voltammetry

CVD – Chemical Vapour Deposition

DMF – Dimethylformamide

DMSO – Dimethyl Sulfoxide

d-PEC – Decoupled Photoelectrochemistry

DRUVS – Diffuse Reflectance UV-Vis Spectroscopy

E – Electric Field Strength

e^- - electron

EDS – Energy Dispersive X-ray Spectroscopy

EDTA – Ethylenediamine Tetraacetic Acid

E_F – Fermi Level

$E_{F,n}$ – Quasi-Fermi Level for Electrons

$E_{F,p}$ – Quasi-Fermi Level for Holes

E_{fb} – Flat Band Potential

E_g – Band Gap

EIS – Electrochemical Impedance Spectroscopy

EM – Electron Microscopy

E_{ox} – Oxidation Potential

EPR – Electron Paramagnetic Resonance Spectroscopy

equiv – equivalents

E_{red} – Reduction Potential

E_{redox} – Equilibrium Redox Potential

ESI-MS – Electrospray Ionisation Mass Spectrometry

Et_3N – Triethylamine

EtOAc – Ethyl Acetate

EtOH – Ethanol

Fc/Fc^+ - Ferrocene/Ferrocenium Redox Couple

FE – Faradaic Efficiency

Fe_2O_3 – iron (III) oxide/hematite

FTO – Fluorine-doped Tin Oxide

FWHM – Full-width Half-maximum

GC – Gas Chromatography

GC-MS – Gas Chromatography-Mass Spectrometry

GI-XRD – Grazing Incidence X-ray Diffraction

h^+ - hole

HFIP – Hexafluoroisopropanol

IDET – Intramolecular Dissociative Electron Transfer

IMPS – Intensity Modulated Photocurrent Spectroscopy

IMVS – Intensity Modulated Photovoltage Spectroscopy

IPCE – Incident-Photon-to-Current Conversion Efficiency

i-PEC – Interfacial Photoelectrochemistry

iPrOH – Isopropanol

IR – Infra-Red Spectroscopy

IrO_2 – Iridium Dioxide

ITO – Indium-doped Tin Oxide

k – rate constant

k_{rec} – Recombination Rate Constant

LED – Light Emitting Diode

LSV – Linear Sweep Voltammetry

MeCN – Acetonitrile

MS – Mott-Schottky

ND – Donor Density

NHE – Normal Hydrogen Electrode

NHPI – N-Hydroxyphthalimide

NHS – N-Hydroxysuccinimide

NMR – Nuclear Magnetic Resonance Spectroscopy

NP – Nanoparticle

PAA – Phenylacetic Acid

PEC - Photoelectrochemical

PEEK – Polyether Ether Ketone

PhCHO – Benzaldehyde

PLD – Pulsed Laser Deposition

Pt-Ti – Platinised Titanium

Pt-TiO_2 – Platinised Titania

p-XRD – Powder X-ray Diffraction

Q_{SC} – Space Charge Constant Phase Element

R_{CT} – Charge Transfer resistance

$R_{ct,bulk}$ – Charge Transfer Resistance in Bulk Semiconductor

RE – Reference Electrode

RHE – Reversible Hydrogen Electrode

R_S – System Resistance

R_{tot} – Total Resistance

R_{trap} – Charge Trapping Resistance

bpy – 2,2'-bipyridyl

RuO_2 – Ruthenium Dioxide

SCE – Saturated Calomel Electrode

SEM – Scanning Electron Microscopy

SET – Single Electron Transfer

SHE – Standard Hydrogen Electrode

SnO_2 – Tin Oxide

SS – Surface State

TAS – Transient Absorption Spectroscopy

$TBAPF_6$ – Tetra-n-butylammonium hexafluorophosphate

TiO_2 – Titanium Dioxidde

UV – Ultra-Violet

V – Potential

VBM – Valence Band Maximum

WE – Working Electrode

W_H – Warburg Diffusion Element of the Helmholtz Region

WO_3 – Tungsten Trioxide

WSC – Space Charge Width

XAS – X-ray Absorption Spectroscopy

XPS – X-ray Photoelectron Spectroscopy

XRD – X-ray Diffraction

$Y:ZrO_2$ – Yttrium-doped Zirconium Oxide

Z_{Im} – Imaginary Component of Impedance

Z_{Re} – Real Component of Impedance

References

1. C. Torborg and M. Beller, *Adv. Synth. Catal.*, 2009, **351**, 3027-3043.
2. P. T. Anastas, M. M. Kirchhoff and T. C. Williamson, *Appl. Catal. A-Gen.*, 2001, **221**, 3-13.
3. N. S. Lewis and D. G. Nocera, *Proc. Natl. Acad. Sci. U.S.A.*, 2006, **103**, 15729-15735.
4. M. Asif and T. Muneer, *Renew. Sust. Energ. Rev.*, 2007, **11**, 1388-1413.
5. M. I. Blanco, *Renew. Sust. Energ. Rev.*, 2009, **13**, 1372-1382.
6. H. D. Roth, *Angew. Chem. Int. Ed. Engl.*, 1989, **28**, 1193-1207.
7. A. Albini and M. Fagnoni, *ChemSusChem*, 2008, **1**, 63-66.
8. G. Ciamician, *Science*, 1912, **36**, 385-394.
9. J. M. R. Narayanam and C. R. J. Stephenson, *Chem. Soc. Rev.*, 2011, **40**, 102-113.
10. C. K. Prier, D. A. Rankic and D. W. C. MacMillan, *Chem. Rev.*, 2013, **113**, 5322-5363.
11. M. Reckenthäler and A. G. Griesbeck, *Adv. Synth. Catal.*, 2013, **355**, 2727-2744.
12. D. W. Manley and J. C. Walton, *Beilstein J. Org. Chem.*, 2015, **11**, 1570-1582.
13. A. Kudo and Y. Miseki, *Chem. Soc. Rev.*, 2009, **38**, 253-278.
14. A. Fujishima and K. Honda, *Nature*, 1972, **238**, 37.
15. Y. Yang, S. W. Niu, D. D. Han, T. Y. Liu, G. M. Wang and Y. Li, *Adv. Energy Mater.*, 2017, **7**, 26.
16. S. S. M. Bhat and H. W. Jang, *ChemSusChem*, 2017, **10**, 3001-3018.
17. I. Roger, M. A. Shipman and M. D. Symes, *Nat. Rev. Chem.*, 2017, **1**, 0003.
18. B. Kraeutler and A. J. Bard, *Nouv. J. Chim*, 1979, **3**, 31.
19. B. Kraeutler and A. J. Bard, *J. Am. Chem. Soc.*, 1978, **100**, 2239-2240.
20. B. Kraeutler and A. J. Bard, *J. Am. Chem. Soc.*, 1977, **99**, 7729-7731.
21. H. Kolbe, *Liebigs Ann. Chem.*, 1849, **69**, 257-294.
22. I. Izumi, F.-R. F. Fan and A. J. Bard, *J. Phys. Chem.*, 1981, **85**, 218-223.
23. B. Klahr, S. Gimenez, F. Fabregat-Santiago, J. Bisquert and T. W. Hamann, *J. Am. Chem. Soc.*, 2012, **134**, 16693-16700.
24. L. M. Peter, *J. Solid State Electrochem.*, 2013, **17**, 315-326.

25. C. Zachäus, F. F. Abdi, L. M. Peter and R. van de Krol, *Chem. Sci.*, 2017, **8**, 3712-3719.

26. D. W. Manley, R. T. McBurney, P. Miller, R. F. Howe, S. Rhydderch and J. C. Walton, *J. Am. Chem. Soc.*, 2012, **134**, 13580-13583.

27. A. Hainer, N. Marina, S. Rincon, P. Costa, A. E. Lanterna and J. C. Scaiano, *J. Am. Chem. Soc.*, 2019, **141**, 4531-4535.

28. M. Cardona and F. H. Pollak, *Phys. Rev.*, 1966, **142**, 530-543.

29. J. K. Cooper, S. Gul, F. M. Toma, L. Chen, Y.-S. Liu, J. Guo, J. W. Ager, J. Yano and I. D. Sharp, *J. Phys. Chem. C*, 2015, **119**, 2969-2974.

30. A. J. Bard, A. B. Bocarsly, F. R. F. Fan, E. G. Walton and M. S. Wrighton, *J. Am. Chem. Soc.*, 1980, **102**, 3671-3677.

31. L. M. Peter, in *Photocatalysis: Fundamentals and Perspectives*, The Royal Society of Chemistry, 2016, pp. 1-28.

32. S. R. Morrison, *Electrochemistry at semiconductor and oxidized metal electrodes*, Plenum, New York, 1980.

33. L. J. Brillson, *Surf. Sci. Rep.*, 1982, **2**, 123-326.

34. W. Schottky, in *Semiconductor Devices: Pioneering Papers*, World Scientific, 1991, pp. 381-381.

35. V. P. Zhdanov and B. Kasemo, *Physica E: Low-dimensional Systems and Nanostructures*, 2011, **43**, 1486-1489.

36. Z. Zhang and J. T. Yates, *Chem. Rev.*, 2012, **112**, 5520-5551.

37. H. Gerischer, *Surf. Sci.*, 1969, **18**, 97-122.

38. H. Gerischer, *J. Electrochem. Soc.*, 1966, **113**, 1174.

39. K. H. Beckmann and R. Memming, *J. Electrochem. Soc.*, 1969, **116**, 368-373.

40. R. N. Hall, *Phys. Rev.*, 1952, **87**, 387.

41. W. Shockley and W. Read Jr, *Phys. Rev.*, 1952, **87**, 835.

42. D. Vanmaekelbergh and F. Cardon, *Electrochim. Acta*, 1992, **37**, 837-846.

43. B. J. Morgan and G. W. Watson, *J. Phys. Chem. C*, 2010, **114**, 2321-2328.

44. Z. M. Jarzebski, *J. Electrochem. Soc.*, 1976, **123**, 299C.

45. M. Anpo and M. Che, in *Advances in catalysis*, Elsevier, 1999, vol. 44, pp. 119-257.

46. U. Diebold, *Surf. Sci. Rep.*, 2003, **48**, 53-229.

47. N. S. Lewis, *Annu. Rev. Phys. Chem.*, 1991, **42**, 543-580.

48. B. Klahr, S. Gimenez, F. Fabregat-Santiago, J. Bisquert and T. W. Hamann, *Energ. Environ. Sci.*, 2012, **5**, 7626-7636.

49. B. Klahr, S. Gimenez, F. Fabregat-Santiago, T. Hamann and J. Bisquert, *J. Am. Chem. Soc.*, 2012, **134**, 4294-4302.

50. A. Kahraman, M. B. Vishlaghi, I. Baylam, A. Sennaroglu and S. Kaya, *J. Phys. Chem. C*, 2019, **123**, 28576-28583.

51. D. Vanmaekelbergh, A. R. d. Wit and F. Cardon, *J. Appl. Phys.*, 1993, **73**, 5049-5057.

52. Y. Yang, J. Gu, J. L. Young, E. M. Miller, J. A. Turner, N. R. Neale and M. C. Beard, *Science*, 2015, **350**, 1061-1065.

53. P. Riente and T. Noel, *Catal. Sci. Technol.*, 2019, **9**, 5186-5232.

54. F. F. Abdi and R. van de Krol, *J. Phys. Chem. C*, 2012, **116**, 9398-9404.

55. S. Hernandez, G. Gerardi, K. Bejtka, A. Fina and N. Russo, *Appl. Catal. B-Environ.*, 2016, **190**, 66-74.

56. T. Lindgren, H. Wang, N. Beermann, L. Vayssieres, A. Hagfeldt and S.-E. Lindquist, *Sol. Energy Mater. Sol. Cells*, 2002, **71**, 231-243.

57. A. Elhage, A. E. Lanterna and J. C. Scaiano, *ACS Sustain. Chem. Eng.*, 2018, **6**, 1717-1722.

58. D. K. Gosser, *Cyclic voltammetry: simulation and analysis of reaction mechanisms*, VCH New York, 1993.

59. W. P. Gomes and D. Vanmaekelbergh, *Electrochim. Acta*, 1996, **41**, 967-973.

60. E. von Hauff, *J. Phys. Chem. C*, 2019, **123**, 11329-11346.

61. A. J. Bard, L. R. Faulkner, J. Leddy and C. G. Zoski, *Electrochemical Methods: Fundamentals and Applications*, Wiley, New York, 1980.

62. E. A. Ponomarev and L. M. Peter, *J. Electroanal. Chem.*, 1995, **397**, 45-52.

63. L. Bertoluzzi and J. Bisquert, *J. Phys. Chem. Lett.*, 2012, **3**, 2517-2522.

64. P. M. Hoffmann, G. Oskam and P. C. Searson, *J. Appl. Phys.*, 1998, **83**, 4309-4323.

65. J. Bisquert, G. Garcia-Belmonte, F. Fabregat-Santiago, N. S. Ferriols, P. Bogdanoff and E. C. Pereira, *J. Phys. Chem. B*, 2000, **104**, 2287-2298.

66. F. Fabregat-Santiago, G. Garcia-Belmonte, J. Bisquert, A. Zaban and P. Salvador, *J. Phys. Chem. B*, 2002, **106**, 334-339.

67. B. M. Klahr and T. W. Hamann, *J. Phys. Chem. C*, 2011, **115**, 8393-8399.

68. L.-k. Tsui, M. Saito, T. Homma and G. Zangari, *J. Mater. Chem. A*, 2015, **3**, 360-367.

69. K. Gelderman, L. Lee and S. W. Donne, *J. Chem. Educ.*, 2007, **84**, 685.

70. S. Xie, T. Zhai, Y. Zhu, W. Li, R. Qiu, Y. Tong and X. Lu, *Int. J. Hydrogen Energy*, 2014, **39**, 4820-4827.

71. E. A. Ponomarev and L. M. Peter, *J. Electroanal. Chem.*, 1995, **396**, 219-226.

72. L. Bertoluzzi and J. Bisquert, *J. Phys. Chem. Lett.*, 2017, **8**, 172-180.

73. D. Cardenas-Morcoso, A. Bou, S. Ravishankar, M. García-Tecedor, S. Gimenez and J. Bisquert, *ACS Energy Lett.*, 2020, **5**, 187-191.

74. M. Chiesa, E. Giamello and M. Che, *Chem. Rev.*, 2010, **110**, 1320-1347.

75. L. Liu, Z. Chen, J. Wang, D. Zhang, Y. Zhu, S. Ling, K.-W. Huang, Y. Belmabkhout, K. Adil, Y. Zhang, B. Slater, M. Eddaoudi and Y. Han, *Nat. Chem.*, 2019, **11**, 622-628.

76. M. D. Hernandez-Alonso, I. Tejedor-Tejedor, J. M. Coronado, M. A. Anderson and J. Soria, *Catal. Today*, 2009, **143**, 364-373.

77. X. Yan, Y. Xu, B. Tian, J. Lei, J. Zhang and L. Wang, *Appl. Catal. B-Environ.*, 2018, **224**, 305-309.

78. Y. C. Zhang, H. N. Zhang, A. A. Liu, C. C. Chen, W. J. Song and J. C. Zhao, *Journal of the American Chemical Society*, 2018, **140**, 3264-3269.

79. M. F. Lichterman, S. Hu, M. H. Richter, E. J. Crumlin, S. Axnanda, M. Favaro, W. Drisdell, Z. Hussain, T. Mayer, B. S. Brunschwig, N. S. Lewis, Z. Liu and H. J. Lewerenz, *Energ. Environ. Sci.*, 2015, **8**, 2409-2416.

80. O. Zandi and T. W. Hamann, *Nat. Chem.*, 2016, **8**, 778-783.

81. V. Chechik, E. Carter and D. Murphy, *Electron paramagnetic resonance*, Oxford University Press, New York, 2016.

82. M. Graetzel and R. F. Howe, *J. Phys. Chem.*, 1990, **94**, 2566-2572.

83. D. C. Hurum, A. G. Agrios, K. A. Gray, T. Rajh and M. C. Thurnauer, *J. Phys. Chem. B*, 2003, **107**, 4545-4549.

84. M. Nilges and J. H. Freed, *Chem. Phys. Lett.*, 1981, **82**, 203-207.

85. R. Venkatesan, S. Velumani, M. Tabellout, N. Errien and A. Kassiba, *J. Phys. Chem. Solids*, 2013, **74**, 1695-1702.

86. G. D. Watkins, *Phys. Solid State*, 1999, **41**, 746-750.

87. R. F. Howe and M. Gratzel, *J. Phys. Chem.*, 1987, **91**, 3906-3909.

88. R. F. Howe and M. Gratzel, *J. Phys. Chem.*, 1985, **89**, 4495-4499.

89. T. Berger, M. Sterrer, O. Diwald, E. Knozinger, D. Panayotov, T. L. Thompson and J. T. Yates, *J. Phys. Chem. B*, 2005, **109**, 6061-6068.

90. C. Di Valentin, G. Pacchioni, A. Selloni, S. Livraghi and E. Giamello, *J. Phys. Chem. B*, 2005, **109**, 11414-11419.

91. T. R. Gordon, M. Cargnello, T. Paik, F. Mangolini, R. T. Weber, P. Fornasiero and C. B. Murray, *J. Am. Chem. Soc.*, 2012, **134**, 6751-6761.

92. G. Xi and J. Ye, *Chem. Commun.*, 2010, **46**, 1893-1895.

93. H. Fan, D. Wang, L. Wang, H. Li, P. Wang, T. Jiang and T. Xie, *Appl. Surf. Sci.*, 2011, **257**, 7758-7762.

94. B. A. Coles and R. G. Compton, *J. Electroanal. Chem.*, 1983, **144**, 87-98.

95. C. Di Valentin and A. Selloni, *Journal of Physical Chemistry Letters*, 2011, **2**, 2223-2228.

96. C. A. Mesa, L. Francàs, K. R. Yang, P. Garrido-Barros, E. Pastor, Y. Ma, A. Kafizas, T. E. Rosser, M. T. Mayer, E. Reisner, M. Grätzel, V. S. Batista and J. R. Durrant, *Nat. Chem.*, 2020, **12**, 82-89.

97. J. Deng, Q. Zhang, X. Lv, D. Zhang, H. Xu, D. Ma and J. Zhong, *ACS Energy Lett.*, 2020, **5**, 975-993.

98. S. Corby, R. R. Rao, L. Steier and J. R. Durrant, *Nature Reviews Materials*, 2021, DOI: 10.1038/s41578-021-00343-7.

99. D. Ma, A. Liu, S. Li, C. Lu and C. Chen, *Catal. Sci. Technol.*, 2018, **8**, 2030-2045.

100. S. Das, K. Murugesan, G. J. Villegas Rodríguez, J. Kaur, J. P. Barham, A. Savateev, M. Antonietti and B. König, *ACS Catal.*, 2021, **11**, 1593-1603.

101. B. Pieber, J. A. Malik, C. Cavedon, S. Gisbertz, A. Savateev, D. Cruz, T. Heil, G. Zhang and P. H. Seeberger, *Angew. Chem. Int. Ed.*, 2019, **58**, 9575-9580.

102. Y.-Y. Liu, D. Liang, L.-Q. Lu and W.-J. Xiao, *Chem. Commun.*, 2019, **55**, 4853-4856.

103. X. Zhu, Y. Lin, J. San Martin, Y. Sun, D. Zhu and Y. Yan, *Nat. Commun.*, 2019, **10**, 2843.

104. J. P. Barham and B. König, *Angew. Chem. Int. Ed.*, 2020, **59**, 11732-11747.

105. D. I. Enache, J. K. Edwards, P. Landon, B. Solsona-Espriu, A. F. Carley, A. A. Herzing, M. Watanabe, C. J. Kiely, D. W. Knight and G. J. Hutchings, *Science*, 2006, **311**, 362-365.

106. Y. J. Zhang, G. H. Zhao, Y. N. Zhang and X. F. Huang, *Green Chem.*, 2014, **16**, 3860-3869.

107. H. Tsunoyama, H. Sakurai, Y. Negishi and T. Tsukuda, *Journal of the American Chemical Society*, 2005, **127**, 9374-9375.

108. H. Tateno, Y. Miseki and K. Sayama, *ChemElectroChem*, 2017, **4**, 3283-3287.

109. R. Arcas, E. Peris, E. Mas-Marzá and F. Fabregat-Santiago, *Sustain. Energ. Fuels*, 2021, **5**, 956-962.

110. H. M. L. Davies and D. Morton, *J. Org. Chem.*, 2016, **81**, 343-350.

111. J. H. Wang, X. B. Li, J. Li, T. Lei, H. L. Wu, X. L. Nan, C. H. Tung and L. Z. Wu, *Chem. Commun.*, 2019, **55**, 10376-10379.

112. T. Li, T. Kasahara, J. He, K. E. Dettelbach, G. M. Sammis and C. P. Berlinguette, *Nat. Commun.*, 2017, **8**, 390.

113. H. Tateno, Y. Miseki and K. Sayama, *Chem. Commun.*, 2019, **55**, 9339-9342.

114. H. Tateno, Y. Miseki and K. Sayama, *Chem. Commun.*, 2017, **53**, 4378-4381.

115. Z. H. Li, L. Luo, M. Li, W. S. Chen, Y. G. Liu, J. R. Yang, S. M. Xu, H. Zhou, L. N. Ma, M. Xu, X. G. Kong and H. H. Duan, *Nat. Commun.*, 2021, **12**, 13.

116. L. Zhang, L. Liardet, J. Luo, D. Ren, M. Grätzel and X. Hu, *Nat. Catal.*, 2019, **2**, 366-373.

117. L. M. Peter, K. G. U. Wijayantha and A. A. Tahir, *Faraday Discuss.*, 2012, **155**, 309-322.

118. B. Lamm, B. J. Trześniewski, H. Döscher, W. A. Smith and M. Stefik, *ACS Energy Lett.*, 2018, **3**, 112-124.

119. Y. K. Zhao, C. Y. Deng, D. J. Tang, L. Y. Ding, Y. C. Zhang, H. Sheng, H. W. Ji, W. J. Song, W. H. Ma, C. C. Chen and J. C. Zhao, *Nat. Catal.*, 2021, **4**, 684-691.

120. D. W. Manley, R. T. McBurney, P. Miller, J. C. Walton, A. Mills and C. O'Rourke, *J. Org. Chem.*, 2014, **79**, 1386-1398.

121. D. W. Manley and J. C. Walton, *Org. Lett.*, 2014, **16**, 5394-5397.

122. B. Giese, *Angew. Chem. Int. Ed.*, 1983, **22**, 753-764.

123. V. A. Grinberg, V. V. Emets, A. D. Modestov, N. A. Maiorova, E. V. Ovsyannikova, O. V. Bukhtenko and D. A. Maslov, *Russ. J. Electrochem.*, 2017, **53**, 217-222.

124. H.-J. Schäfer, in *Electrochemistry IV*, Springer, 1990, pp. 91-151.

125. A. Vijh and B. Conway, *Chem. Rev.*, 1967, **67**, 623-664.

126. M. C. Leech and K. Lam, *Acc. Chem. Res.*, 2020, **53**, 121-134.

127. X. Ma, D. F. Dewez, L. Du, X. Luo, I. E. Markó and K. Lam, *J. Org. Chem.*, 2018, **83**, 12044-12055.

128. S. Hamid, I. Ivanova, T. H. Jeon, R. Dillert, W. Choi and D. W. Bahnemann, *J. Catal.*, 2017, **349**, 128-135.

129. J. W. Hilborn and J. A. Pincock, *Journal of the American Chemical Society*, 1991, **113**, 2683-2686.

130. A. Vijh and B. Conway, *Fresenius' Zeitschrift für analytische Chemie*, 1967, **230**, 81-95.

131. B. E. Conway and M. Dzieciuch, *Can. J. Chem.*, 1963, **41**, 38-54.

132. L. Capaldo, L. Buzzetti, D. Merli, M. Fagnoni and D. Ravelli, *J. Org. Chem.*, 2016, **81**, 7102-7109.

133. G. Stork, A. Meisels and J. Davies, *Journal of the American Chemical Society*, 1963, **85**, 3419-3425.

134. C. P. Andrieux, F. Gonzalez and J.-M. Savéant, *Journal of the American Chemical Society*, 1997, **119**, 4292-4300.

135. D. Muck and E. Wilson, *J. Electrochem. Soc.*, 1970, **117**, 1358.

136. N. Sato, T. Sekine and K. Sugino, *J. Electrochem. Soc.*, 1968, **115**, 242-246.

137. B. E. Conway and M. Dzieciuch, *Can. J. Chem.*, 1963, **41**, 55-67.

138. K. Neubert, M. Schmidt and F. Harnisch, *ChemSusChem*, 2021, **14**, 3097-3109.

139. J. D. Wadhawan, F. J. Del Campo, R. G. Compton, J. S. Foord, F. Marken, S. D. Bull, S. G. Davies, D. J. Walton and S. Ryley, *J. Electroanal. Chem.*, 2001, **507**, 135-143.

140. L. Eberson and G. Ryde-Petterson, *Chemischer Informationsdienst*, 1973, **4**, no-no.

141. L. Eberson, 1976.

142. G. E. Hawkes, J. H. P. Utley and G. B. Yates, *J. Chem. Soc., Perkin Trans. 2*, 1976, DOI: 10.1039/P29760001709, 1709-1716.

143. R. Linstead, B. Shephard and B. Weedon, *J. Chem. Soc.*, 1952, 3624-3627.

144. D. L. Muck and E. R. Wilson, *J. Electrochem. Soc.*, 1970, **117**, 1358-1362.

145. M. Galicia, M. A. González-Fuentes, D. P. Valencia and F. J. González, *J. Electroanal. Chem.*, 2012, **672**, 28-33.

146. M. Galicia and F. González, *J. Electrochem. Soc.*, 2002, **149**, D46.

147. T. Dickinson and W. Wynne-Jones, *Trans. Faraday Society*, 1962, **58**, 382-387.

148. R. Beranek, *Angew. Chem.-Int. Edit.*, 2019, **58**, 16724-16729.

149. Y. Liang, T. Tsubota, L. P. A. Mooij and R. van de Krol, *J. Phys. Chem. C*, 2011, **115**, 17594-17598.

150. H. Jiang, H. Dai, X. Meng, L. Zhang, J. Deng, Y. Liu and C. T. Au, *Journal of Environmental Sciences*, 2012, **24**, 449-457.

151. H. Jiang, H. Dai, X. Meng, K. Ji, L. Zhang and J. Deng, *Appl. Catal. B-Environ.*, 2011, **105**, 326-334.

152. A. Tavakoli, M. Sohrabi and A. Kargari, *Chem. Pap.*, 2007, **61**, 151-170.

153. P. G. Jamkhande, N. W. Ghule, A. H. Bamer and M. G. Kalaskar, *J. Drug Deliv. Sci. Tech.*, 2019, **53**, 101174.

154. G. Talasila, S. Sachdev, U. Srivastva, D. Saxena and S. S. V. Ramakumar, *Energy Reports*, 2020, **6**, 1963-1972.

155. X. Liu, Y. Liu, J. Su, M. Li and L. Guo, *Int. J. Hydrogen Energy*, 2015, **40**, 12964-12972.

156. A. Duret and M. Gratzel, *J. Phys. Chem. B*, 2005, **109**, 17184-17191.

157. P. S. Patil, *Mater. Chem. Phys.*, 1999, **59**, 185-198.

158. A. Jaworek, *J. Mater. Sci.*, 2007, **42**, 266-297.

159. G. L. Messing, S. C. Zhang and G. V. Jayanthi, *J. Am. Ceram. Soc.*, 1993, **76**, 2707-2726.

160. J. H. Bang and K. S. Suslick, *Adv. Mater.*, 2010, **22**, 1039-1059.

161. A. Jaworek and A. T. Sobczyk, *J. Electrostat.*, 2008, **66**, 197-219.

162. A. H. Syafiza, M. S. A. Puteri and M. H. Azizi, 2013.

163. C. H. Chen, E. M. Kelder and J. Schoonman, *J. Power Sources*, 1997, **68**, 377-380.

164. C. H. Chen, E. M. Kelder, M. J. G. Jak and J. Schoonman, *Solid State Ionics*, 1996, **86-88**, 1301-1306.

165. T. M. Pang, P. D. Prewett and L. Gowland, *Thin Solid Films*, 1982, **88**, 219-224.

166. I. Taniguchi, R. C. van Landschoot and J. Schoonman, *Solid State Ionics*, 2003, **156**, 1-13.

167. I. Taniguchi, R. C. van Landschoot and J. Schoonman, *Solid State Ionics*, 2003, **160**, 271-279.

168. N. M. Muhammad, A. M. Naeem, N. Duraisamy, D.-S. Kim and K.-H. Choi, *Thin Solid Films*, 2012, **520**, 1751-1756.

169. W. Sun, M. Xie, L. Jing, Y. Luan and H. Fu, *J. Solid State Chem.*, 2011, **184**, 3050-3054.

170. T. W. Kim and K.-S. Choi, *Science*, 2014, **343**, 990-994.

171. F. F. Abdi, T. J. Savenije, M. M. May, B. Dam and R. van de Krol, *J. Phys. Chem. Lett.*, 2013, **4**, 2752-2757.

172. C. Karunakaran, S. Kalaivani, P. Vinayagamoorthy and S. Dash, *Mater. Sci. Semicond. Process.*, 2014, **21**, 122-131.

173. M. Yabuta, A. Takeda, T. Sugimoto, K. Watanabe, A. Kudo and Y. Matsumoto, *J. Phys. Chem. C*, 2017, **121**, 22060-22066.

174. M. A. Zurbuchen, J. Lettieri, S. J. Fulk, Y. Jia, A. H. Carim, D. G. Schlom and S. K. Streiffer, *Appl. Phys. Lett.*, 2003, **82**, 4711-4713.

175. K. Sivula, F. Le Formal and M. Grätzel, *ChemSusChem*, 2011, **4**, 432-449.

176. R. S. Neves, E. D. Robertis and A. J. Motheo, *Electrochim. Acta*, 2006, **51**, 1215-1224.

177. C. H. Griffiths and H. K. Eastwood, *J. Appl. Phys.*, 1974, **45**, 2201-2206.

178. H. Cheng, Q. Liu, J. Yang, S. Ma and R. L. Frost, *Thermochim. Acta*, 2012, **545**, 1-13.

179. N. Mahrez, S. Bendenia, K. Marouf-Khelifa, I. Batonneau-Gener and A. Khelifa, *Compos. Interfaces*, 2015, **22**, 403-417.

180. M. Karunakaran, S. P. Nunes, X. Qiu, H. Yu and K.-V. Peinemann, *J. Membr. Sci.*, 2014, **453**, 471-477.

181. W. A. Phillip, B. O'Neill, M. Rodwogin, M. A. Hillmyer and E. Cussler, *ACS Appl. Mater. Interfaces*, 2010, **2**, 847-853.

182. J. K. Cooper, S. E. Reyes-Lillo, L. H. Hess, C.-M. Jiang, J. B. Neaton and I. D. Sharp, *J. Phys. Chem. C*, 2018, **122**, 20642-20652.

183. P. S. Shinde, A. Annamalai, Ju H. Kim, Sun H. Choi, Jae S. Lee and Jum S. Jang, *Sol. Energy Mater. Sol. Cells*, 2015, **141**, 71-79.

184. L. Zhang, D. Chen and X. Jiao, *The Journal of Physical Chemistry B*, 2006, **110**, 2668-2673.

185. C. D. Wagner, *J. Electron. Spectrosc. Relat. Phenom.*, 1983, **32**, 99-102.

186. G. Hernandez-Cuevas, J. R. Leyva Mendoza, P. E. García-Casillas, C. A. Rodríguez González, J. F. Hernandez-Paz, G. Herrera-Pérez, L. Fuentes-Cobas, S. Díaz de la Torre, O. Raymond-Herrera and H. Camacho-Montes, *J. Adv. Ceram.*, 2019, **8**, 278-288.

187. A. Sakunthala, M. V. Reddy, S. Selvasekarapandian, B. V. R. Chowdari and P. C. Selvin, *Energ. Environ. Sci.*, 2011, **4**, 1712-1725.

188. D. Lee, W. Wang, C. Zhou, X. Tong, M. Liu, G. Galli and K.-S. Choi, *Nat. Energy*, 2021, **6**, 287-294.

189. S. B. Beil, D. Pollok and S. R. Waldvogel, *Angew. Chem. Int. Ed.*, 2021, **60**, 14750-14759.

190. D. Pollok and S. R. Waldvogel, *Chem. Sci.*, 2020, **11**, 12386-12400.

191. L. Cao, Q. Luo, J. Chen, L. Wang, Y. Lin, H. Wang, X. Liu, X. Shen, W. Zhang, W. Liu, Z. Qi, Z. Jiang, J. Yang and T. Yao, *Nat. Commun.*, 2019, **10**, 4849.

192. S. Cherevko, A. R. Zeradjanin, A. A. Topalov, N. Kulyk, I. Katsounaros and K. J. Mayrhofer, *ChemCatChem*, 2014, **6**, 2219-2223.

193. M. Selt, R. Franke and S. R. Waldvogel, *Org. Process Res. Dev.*, 2020, **24**, 2347-2355.

194. M. Dörr, J. L. Röckl, J. Rein, D. Schollmeyer and S. R. Waldvogel, *Chemistry*, 2020, **26**, 10195-10198.

195. C. Stang and F. Harnisch, *ChemSusChem*, 2016, **9**, 50-60.

196. G. Nuding, F. Voegtle, K. Danielmeier and E. Steckhan, *Synthesis*, 1996, **1996**, 71-76.

197. A. Matzeit, H. J. Schäfer and C. Amatore, *Synthesis*, 1995, **1995**, 1432-1444.

198. A. Hankin, F. E. Bedoya-Lora, J. C. Alexander, A. Regoutz and G. H. Kelsall, *J. Mater. Chem. A*, 2019, **7**, 26162-26176.

199. B. J. Trześniewski and W. A. Smith, *J. Mater. Chem. A*, 2016, **4**, 2919-2926.

200. T. W. Kim, Y. Ping, G. A. Galli and K.-S. Choi, *Nat. Commun.*, 2015, **6**, 8769.

201. K. R. Tolod, S. Hernández, M. Castellino, F. A. Deorsola, E. Davarpanah and N. Russo, *Int. J. Hydrogen Energy*, 2020, **45**, 605-618.

202. M. Quertenmont, I. Goodall, K. Lam, I. Markó and O. Riant, *Org. Lett.*, 2020, **22**, 1771-1775.

203. A. Petti, M. C. Leech, A. D. Garcia, I. C. A. Goodall, A. P. Dobbs and K. Lam, *Angew. Chem. Int. Ed.*, 2019, **58**, 16115-16118.

204. X. Ma, X. Luo, S. Dochain, C. Mathot and I. E. Markò, *Org. Lett.*, 2015, **17**, 4690-4693.

205. J. Knolle and H. J. Schäfer, *Electrochim. Acta*, 1978, **23**, 5-8.

206. A. Kütt, S. Tshepelevitsh, J. Saame, M. Lõkov, I. Kaljurand, S. Selberg and I. Leito, *Eur. J. Org. Chem.*, 2021, **2021**, 1407-1419.

207. C. A. Unsworth, B. Coulson, V. Chechik and R. E. Douthwaite, *J. Catal.*, 2017, **354**, 152-159.

208. M. Cherevatskaya, M. Neumann, S. Füldner, C. Harlander, S. Kümmel, S. Dankesreiter, A. Pfitzner, K. Zeitler and B. König, *Angew. Chem. Int. Ed.*, 2012, **51**, 4062-4066.

209. Y. Dai, P. Ren, Y. Li, D. Lv, Y. Shen, Y. Li, H. Niemantsverdriet, F. Besenbacher, H. Xiang, W. Hao, N. Lock, X. Wen, J. P. Lewis and R. Su, *Angew. Chem. Int. Ed.*, 2019, **58**, 6265-6270.

210. S. L. Upstone, *Encyclopedia of analytical chemistry*, 2000, **1699**, 1714.

211. G. S. Pande and S. N. Shukla, *Electrochim. Acta*, 1961, **4**, 215-231.

212. A. Wiebe, T. Gieshoff, S. Möhle, E. Rodrigo, M. Zirbes and S. R. Waldvogel, *Angew. Chem. Int. Ed.*, 2018, **57**, 5594-5619.

213. K. Izutsu, *Electrochemistry in Nonaqueous Solutions*, Wiley-VCH Verlag GmbH, 2009.

214. G. Gritzner and J. Kuta, *Pure Appl. Chem.*, 1984, **56**, 461-466.

215. M. P. S. Mousavi, S. A. Saba, E. L. Anderson, M. A. Hillmyer and P. Bühlmann, *Anal. Chem.*, 2016, **88**, 8706-8713.

216. C.-M. Li, I. M. Robertson, M. L. Jenkins, J. L. Hutchison and R. C. Doole, *Micron*, 2005, **36**, 9-15.

217. C. G. Chen, H. Q. Lin and Z. Q. Huang, *Acta Phys-Chim. Sin.*, 1992, **8**, 1-3.

218. M. K. Chantooni and I. M. Kolthoff, *J. Phys. Chem.*, 1973, **77**, 1-7.

219. I. Kolthoff and F. Thomas, *J. Phys. Chem.*, 1965, **69**, 3049-3058.

220. J. P. Coleman, J. H. P. Utley and B. C. L. Weedon, *J. Chem. Soc. Chem. Comm.*, 1971, DOI: 10.1039/C29710000438, 438-439.

221. B. R. Horrocks, M. V. Mirkin and A. J. Bard, *J. Phys. Chem.*, 1994, **98**, 9106-9114.

222. S. D. Dolić, D. J. Jovanović, K. Smits, B. Babić, M. Marinović-Cincović, S. Porobić and M. D. Dramićanin, *Ceram. Int.*, 2018, **44**, 17953-17961.

223. S. Y. Zhang, M. Rohloff, O. Kasian, A. M. Mingers, K. J. J. Mayrhofer, A. Fischer, C. Scheu and S. Cherevko, *J. Phys. Chem. C*, 2019, **123**, 23410-23418.

224. D. K. Lee and K. S. Choi, *Nat. Energy*, 2018, **3**, 53-60.

225. F. M. Toma, J. K. Cooper, V. Kunzelmann, M. T. McDowell, J. Yu, D. M. Larson, N. J. Borys, C. Abelyan, J. W. Beeman, K. M. Yu, J. Yang, L. Chen, M. R. Shaner, J. Spurgeon, F. A. Houle, K. A. Persson and I. D. Sharp, *Nat. Commun.*, 2016, **7**, 12012.

226. L. M. Fischer, M. Tenje, A. R. Heiskanen, N. Masuda, J. Castillo, A. Bentien, J. Émneus, M. H. Jakobsen and A. Boisen, *Microelectron. Eng.*, 2009, **86**, 1282-1285.

227. M. de Ridder, R. G. van Welzenis and H. H. Brongersma, *Surf. Interface Anal.*, 2002, **33**, 309-317.

228. J. P. Coleman, R. Lines, J. H. P. Utley and B. C. L. Weedon, *J. Chem. Soc., Perkin Trans. 2*, 1974, DOI: 10.1039/P29740001064, 1064-1069.

229. B. Sim, P. Milne, D. Griller and D. Wayner, *Journal of the American Chemical Society*, 1990, **112**, 6635-6638.

230. J. P. Coleman, R. Lines, J. H. Utley and B. C. Weedon, *J. Chem. Soc., Perkin Trans. 2*, 1974, 1064-1069.

231. J. P. Coleman and L. Eberson, *J. Chem. Soc. Chem. Comm.*, 1971, 1300-1301.

232. M. P. Soriaga, P. H. Wilson, A. T. Hubbard and C. S. Benton, *J. Electroanal. Chem.*, 1982, **142**, 317-336.

233. C. Hansch and A. Leo, *Substituent constants for correlation analysis in chemistry and biology*, Wiley, 1979.

234. H. Lewerenz, *J. Electroanal. Chem.*, 1993, **356**, 121-143.

235. C. Li, T. Hisatomi, O. Watanabe, M. Nakabayashi, N. Shibata, K. Domen and J.-J. Delaunay, *Energ. Environ. Sci.*, 2015, **8**, 1493-1500.

236. W. S. Trahanovsky, J. Cramer and D. W. Brixius, *J. Am. Chem. Soc.*, 1974, **96**, 1077-1081.

237. A. V. Shtelman and J. Y. Becker, *J. Org. Chem.*, 2011, **76**, 4710-4714.

238. E. Y. Liu, J. E. Thorne, Y. He and D. Wang, *ACS Appl. Mater. Interfaces*, 2017, **9**, 22083-22087.

239. D. D. Tanner and S. A. Osman, *J. Am. Chem. Soc.*, 1968, **90**, 6572-6574.

240. S. Antonello and F. Maran, *Chem. Soc. Rev.*, 2005, **34**, 418-428.

241. S. D. Ross and M. Finkelstein, *J. Org. Chem.*, 1969, **34**, 2923-2927.

242. B. Maillard, K. U. Ingold and J. C. Scaiano, *J. Am. Chem. Soc.*, 1983, **105**, 5095-5099.

243. R. Bigler, K. A. Mack, J. Shen, P. Tosatti, C. Han, S. Bachmann, H. Zhang, M. Scalone, A. Pfaltz, S. E. Denmark, S. Hildbrand and F. Gosselin, *Angew. Chem. Int. Ed.*, 2020, **59**, 2844-2849.

244. J. Hioe and H. Zipse, *Org. Biomol. Chem.*, 2010, **8**, 3609-3617.

245. D. Hayrapetyan, V. Shkepu, O. T. Seilkhanov, Z. Zhanabil and K. Lam, *Chem. Commun.*, 2017, **53**, 8451-8454.

246. J. Wilshire, *Aust. J. Chem.*, 1963, **16**, 432-439.

247. A. Studer and M. Bossart, *Tetrahedron*, 2001, **48**, 9649-9667.

248. S. Rosca, G. Stanciu, R. Stan, M. Ungureanu, S. I. Rosca and S. Mataka, *Rev. Chim.*, 2006, **57**, 276-280.

249. X. Wang, J. C. Yu, P. Liu, X. Wang, W. Su and X. Fu, *J. Photoch. Photobio., A*, 2006, **179**, 339-347.

250. C.-M. Huang, G.-T. Pan, P.-Y. Peng and T. C. K. Yang, *J. Mol. Catal. A: Chem.*, 2010, **327**, 38-44.

251. I. Kanwal, A. Mujahid, N. Rasool, K. Rizwan, A. Malik, G. Ahmad, S. A. A. Shah, U. Rashid and N. M. Nasir, *Catalysts*, 2020, **10**, 443.

252. Y. Kuang, Q. Jia, G. Ma, T. Hisatomi, T. Minegishi, H. Nishiyama, M. Nakabayashi, N. Shibata, T. Yamada, A. Kudo and K. Domen, *Nat. Energy*, 2016, **2**, 16191.

253. S. P. Berglund, D. W. Flaherty, N. T. Hahn, A. J. Bard and C. B. Mullins, *J. Phys. Chem. C*, 2011, **115**, 3794-3802.

254. P. F. Levy, J. E. Sanderson and L. K. Cheng, *J. Electrochem. Soc.*, 1984, **131**, 773-777.

255. R. C. Petersen, M. Finkelstein and S. D. Ross, *J. Org. Chem.*, 1967, **32**, 564-567.

256. W. Greaves, R. Linstead, B. Shephard, S. Thomas and B. Weedon, *J. Chem. Soc.*, 1950, 3326-3330.

257. H. Hofer and M. Moest, *Liebigs Ann. Chem.*, 1902, **323**, 284-323.

258. J. F. Montoya, J. Peral and P. Salvador, *ChemPhysChem*, 2011, **12**, 901-907.

259. S. Civiš, M. Ferus, M. Zukalová, A. Zukal, L. Kavan, K. D. Jordan and D. C. Sorescu, *J. Phys. Chem. C*, 2015, **119**, 3605-3612.

260. M. E. Orazem and B. Tribollet, *New Jersey*, 2008, 383-389.

261. R. De Gryse, W. P. Gomes, F. Cardon and J. Vennik, *J. Electrochem. Soc.*, 1975, **122**, 711-712.

262. L. M. Peter, Gurudayal, L. H. Wong and F. F. Abdi, *J. Electroanal. Chem.*, 2018, **819**, 447-458.

263. D.-D. Qin, T. Wang, Y.-M. Song and C.-L. Tao, *Dalton Trans.*, 2014, **43**, 7691-7694.